ABSTRACT

Title of Document: ADVANCE MATERIALS AND PROCESSES FOR INTEGRATED MICROCIRCUIT TECHNOLOGY.

Yves T. Ngu, PhD, 2008

Directed By: Professor Martin Peckerar, Department of Electrical and Computer Engineering

Improvements in technology, as we get closer and closer to the limits of Moore's law, require the use of a holistic design approaches as a new paradigm in value creation for future technologies. In light of these limitations, technology innovations should focus not only on shrinkage but also on a combination of exotic materials and novel designs. This idea constitutes the frame work of the research work presented in this thesis. The work focuses on the study of novel micro-circuit ideas founded on material processes, integrations and device structures.

This work begins with a hydrated Ruthenium oxide and activated carbon based electrochemical energy cell is introduced. Multiple electrode materials, packaging approaches and electrolyte composition are investigated. The performances of the various devices are evaluated. The studies on the fabrication of the novel electrochemical energy cell yielded encouraging results where the most promising cell is the Graphite-Zinc cell.

Subsequently, the examination of a novel $Al_xGa_{1-x}N$ alloy device structure and growth method that enables simultaneous dual UV-wavelength band detection. A clear roadmap to the creation of a dual UV-wavelength detector array, based on confined epitaxial growth, is offered. The growth mechanism involved in the confined epitaxial growth approach, which enables the stacking of active layers with varying stoichiometry, is introduced. Electrical and optical evaluations of the fabricated detectors proves the diode nature of the detectors; while, spectral sensitivity curves demonstrate dual UV-wavelength sensitivity of the detector array.

Finally, an inexpensive and effective sub-wavelength lithography technique based on a novel mask is studied. The concept behind the mask is to substitutes the conventional clear and opaque mask by a “dot array” mask making use of plasmonic waves. The mask is then utilized for far-filed imaging within a traditional stepper. Mask principals, fabrication approach and characterization of the printed patterns are presented. Contact windows were exposed with critical dimensions down to 110nm using 248nm incident radiation. While the exposure times are slightly longer than usual, the imaged patterns appear to be a cooperative effect of scattering from multiple apertures. The absence of a few random apertures does not distort the printed patterns.

ADVANCED MATERIALS AND PROCESSES FOR INTEGRATED MICROCIRCUIT TECHNOLOGY.

By

Yves T. Ngu.

Dissertation submitted to the Faculty of the Graduate School of the
University of Maryland, College Park, in partial fulfillment
of the requirements for the degree of
Doctor of Philosophy
2008

Advisory Committee:
Professor Martin Peckerar, Chair
Professor Pamela Abshire
Professor Neil Goldsman
Professor Kristine Rosfjord
Professor Aristos Christou

© Copyright by
Yves T. Ngu
2008

Dedication

I would like to dedicate this dissertation to my lovely wife Christelle and my two beautiful daughters Zorah and Chloe, who represent my greatest inspiration in life.

To my wise parents and handsome brothers

You Always Believed in me.

I Love you all

Acknowledgements

While I am the one receiving a degree, the accomplishments in this dissertation would not be possible without significant contributions from my colleagues, friends and family.

I would like to express my indebtedness and gratefulness to my academic advisor Professor Martin Peckerar for his support and guidance over the past 3 years, as well as my Dissertation Committee; Professor Neil Goldsman, Professor Pamela Abshire, Professor Kristine Rosfjord and Professor Aristos Christou.

I was privileged to collaborate with numerous talented individuals throughout my research at the University of Maryland. I would like to thank Dr. Mario Dagenais for his contribution to my research experience. From the Naval Research Laboratory, I would like to acknowledge Dr. Daniel Lowy, Dr. Lenny Tender, Dr. Chip Eddy and Dr. Richard Henry. From collaboration with the Laboratory of Physical Science, I would like to recognize Mr. Mike Khbeis and Dr. George Metze. Through collaboration with the NASA-Goddard Space Flight Center, I had the opportunity to work with a tremendous engineer, Dr. Shahid Aslam. Through my extensive cleanroom work I had the privilege to learn some tricks of the trade from Mr. Tom Loughran and Mr. John Hummel. I would like to recognize Mr. John Berry and Dr. John Melngailis for their collaboration and dedication in supplying me with my sub-wavelength aperture masks.

I would also like to extent my approbation and tribute to Dr. David Haynes for his profound impetus and eternal nurturing. Thanks for always being there when it was needed the most. David, your encouragement has always filled my heart with joy and enthusiasm to continue to strive for my dreams. You are truly special.

Special reverence to my late father Mr. Mathias Ngu, whose spirit I am sure is with me always; rest in peace Dad. Thanks to my Mum, for all her noble upbringing and self-sacrificing love, guidance, support and encouragement. Thanks to my siblings, Gerry and Anicer (Caroline) and the little ones, for their belief in me.

I would like to thank the love of my life, my wife Christelle and my two daughters Zorah and Chloe. It is a dream come true to achieve this degree, which I share with them. Christelle, thanks for your wholehearted love and ingenuous comfort. Thanks for being a part of my life to see me through every thick and thin life has to offer. I would like to thank Mr. and Mrs. Teuma for their encouragements and love as well as the entire Teuma family.

As a member of the Analog and Mixed-Signal Laboratory at the University of Maryland, College Park, I would like to recognize my colleagues: Dr. Seokjin Kim, Kwangsik Choi, Kanyogoro Esau, Dr. Sanaz Adl, Jimmy Wienke, Jeff Allnut, Po-Hsin Chen, Scott Bauman, Keir Lauritzen and Mahsa Dornajafi. I am grateful for their help, support and invaluable inputs. A special thank you goes out to Dr. Zeynep Dilli for her tireless contribution to the analysis of the electrochemical energy cell.

Last but not least, I would like to thank the entire PROMISE family at the Graduate School Office, University of Maryland, especially Dr. Johnetta Davis for always looking out for me.

Thanks to Almighty God for giving me strength, health and mental fortitude to successfully travel this PhD journey.

To those listed above and those I may have forgotten: Thank You.

Sincerely,

Yves Ngu

Table of Contents

Dedication ii

Acknowledgements iii

Table of Contents v

List of Tables ix

List of Figures x

CHAPTER 1: INTRODUCTION 1

1.1 Motivation 1
1.2 Dissertation Objectives 2
1.2.1 Electrochemical energy cell 2
1.2.2 Novel AlGaN based UV detector 2
1.2.3 Sub-wavelength aperture lithography technique 4
1.3 Unique Contributions 5
1.4 Dissertation Structure 8

CHAPTER 2: ELECTROCHEMICAL ENERGY CELL 10

2.1 Major Contribution 10
2.2 Introduction 11
2.3 Background 15
2.3.1 Batteries 15
2.3.2 Capacitors 21
2.4 Cell characterization techniques 30
2.4.1 Cyclic Voltammetry 30
2.4.2 Constant Current Charging 31
2.4.3 Cell Polarization 33
2.4.4 Constant Voltage / Current Charging - Resistive Discharge 33
2.4.5 Self Discharge 34
2.4.6 Device Demo 34
2.5 Electrode Material 35

2.6 Gold coated glass slide cells 38
2.6.1 Structure 38
2.6.2 Characteristics 40
2.6.3 Discussion 45
2.7 Gold coated aluminum cells 47
2.7.1 Structure 47
2.7.2 Characteristics 49
2.7.3 Discussion 51
2.8 Graphite-Zinc cells 52
2.8.1 Structure 52
2.8.2 Characteristics 56
2.8.3 Discussion 67
2.9 Graphite-Lead cells 68
2.9.1 Structure 68
2.9.2 Characteristics 69
2.9.3 Discussion 73
2.10 Electro-Chemistry of Rechargeable Cells 74
2.10.1 Lead Acid 74
2.10.2 Ruthenium Oxide 75
2.11 Competitive Technologies 76
2.12 Conclusion 82

CHAPTER 3: DUAL UV-WAVELENGHT IMAGING ARRAY 85

3.1 Major Contribution 85
3.2 Introduction 86
3.3 Background 91
3.3.1 Photodetectors figures of merit 91
3.3.2 Photoconductive detectors 92
3.3.3 Schottky barrier and metal-semiconductor-metal (MSM) photodiodes 93
3.3.4 p-n or p-i-n junction photodiodes 95
3.3.5 Focal plane arrays 97
3.4 Structure of Dual-Color UV Imaging Array 99
3.4.1 Pixel Composition 99
3.4.2 $Al_xGa_{1-x}N$ Growth Technique 102
3.4.3 Lift-Off Process 108
3.4.4 System Assembling 109
3.5 Fabrication Process Flow 111
3.5.1 Mask Design 112
3.5.2 Fabrication Steps 115
3.5.3 Processing Guide 121
3.6 Testing 124
3.6.1 Electrical Evaluation 124
3.6.2 Optical Evaluation 125
3.6.3 Imager Evaluation 129

3.7 Conclusion 130

CHAPTER 4: SUB-WAVELENGTH LITHOGRPHY TECHNOLOGY 132

4.1 Major Contribution 132
4.2 Introduction 132
4.3 Background 134
4.3.1 Single aperture 136
4.3.2 Array of holes 139
4.3.3 Effect of aperture shape 140
4.3.4 Transmission mechanism 141
4.4 Mask Fabrication and Experiment 143
4.4.1 FIB Tools 143
4.4.2 Mask Patterns 147
4.5 Results 149
4.6 Discussion 159
4.7 Conclusion 164

CHAPTER 5: CONCLUSION 166

5.1 Summary of Accomplishments 166
5.1.1 Electrochemical energy cell 166
5.1.2 Dual UV-wavelength detector array 168
5.1.3 Sub-wavelength lithography technique 169
5.2 Unique Contribution 171
5.3 Future Work 174
5.3.1 Electrochemical energy cell 174
5.3.2 Dual UV-wavelength detector array: Reduced leakage and Avalanche diodes 175
5.3.3 Sub-wavelength lithography technique 176

Appendix A: $Al_xGa_{1-x}N$ absorption thickness calculations 177

Appendix B: Fabrication Process for Dual-Color UV Detector Array 180

Bibliography 185

List of Tables

Table 1: Powder Composition 40

Table 2: Summary of calculated capacitance values 41

Table 3: Open circuit voltage of gold coated aluminum cells 49

Table 4: Electrolyte composition (in percent per volume) 55

Table 5: V_{OC} of devices made with electrolyte E0-6 56

Table 6: Self discharge / V_{OC} of single and double stacked cell using electrolyte E0 58

Table 7: Comparison of properties of cell E0GZ11 when new (fresh) and after voltage charging at 1.4V for 2 hours 65

Table 8: Open circuit voltage of Graphite-Lead cells and charging voltages........ 70

Table 9: Comparison of properties of cell E0GP1, E6GP1 (missing fresh cell data) and E7GP1 when new (fresh) and after multiple voltage charging at their respective voltages. The three cells have electrolyte with varying pH, E0GP1 (4pH), E6GP1 (1pH) and E7GP1 (5pH) 72

Table 10: Lithium cell comparison to Graphite-Zinc and Graphite-Lead cells........ 79

Table 11: Rockwell PICNIC chip properties (from Rockwell) 111

Table 12: Characteristics of detectors........ 125

Table 13: Magnification calculation 147

Table 14: Magnification used to write patterns 148

Table A1: Mass attenuation coefficient 178

Table A1: Summary of absorption calculations........179

List of Figures

Figure 1: Electrochemical energy cell within sensor mote 13

Figure 2: Schematic of Faradaic processes (from electrochem). 13

Figure 3: Schematic of non-Faradaic process (from electrochem). 14

Figure 4: Procedures for charging batteries; (a) constant current; (b) constant voltage (from M. Dell). 19

Figure 5: Procedures for charging batteries; (a) taper current; (b) constant-current – constant-voltage (from M. Dell). 20

Figure 6: Ragone plot of various energy storage devices (from R. Kotz). 25

Figure 7: (A) Von Helmholtz capacitor model of the double-layer. (B) Gouy-Chapman diffuse layer model of the double-layer. (C) Stern model of the double-layer incorporating a coupled diffuse layer charge distribution, with corresponding drops of potential shown. (D) Overall model of the double-layer showing presence of solvent molecules (from B. E. Conway). 28

Figure 8: Comparison of ideal and real cyclic voltammograms (from E. Frackowiak). 31

Figure 9: Current charging experimental setup (from Cooper Bussman); (a) circuit setup; (b) charging potential 32

Figure 10: Constant voltage / current charging followed by resistive discharge........ 34

Figure 11: Voltammetry plot of modified carbon electrodes (from J. M. Miller). 36

Figure 12: Planar electrochemical cell; (a) profile showing the interface; (b) overall structure of the device 39

Figure 13: Voltage vs. time plots from constant current charging; (a) Mix 1 device; (b) Mix 2 device. 42

Figure 14: Voltage vs. time plots from constant current charging; (a) Activated carbon device; (b) Ruthenium oxide device. 43

Figure 15: Voltammograms of samples (a) Mix 1 (10:1 $RuO_2.xH_2O$ and AC), (b) Mix 2 (1:1 $RuO_2.xH_2O$ and AC) measured at 20 mV/s.. 44

Figure 16: Hypothesized cell mechanism (a) Equivalent circuit, (b) Cell layer interaction 46

Figure 17: Schematic of gold coated aluminum cells 48

Figure 18: Schematic of triple stacked gold coated aluminum cells 48

Figure 19: Voltage versus time plot of voltage charged cell then resistively discharged through 10KΩ resistive load. 50

Figure 20: Voltage versus time plot of voltage charged cell then resistively discharged through 10KΩ resistive load and self discharged. 50

Figure 21: Schematic of graphite-zinc single cell 53

Figure 22: Schematic of graphite-zinc double stacked cell. 53

Figure 23: Picture of a Graphite-Zinc packaged cell. 54

Figure 24: Overpotential dependence on amount of electrolyte given identical load; bottom left E0GZ7 (10 drops of electrolyte); top right E0GZ8 (15 drops of electrolyte) 59

Figure 25: E0GZ8 overpotential drop at varying resistive loads 60

Figure 26: E1GZ1 overpotential drop at varying resistive loads 60

Figure 27: Cell E0GZ7 charged with 100µA for 1 hour then discharged 61

Figure 28: Single graphite-zinc cell 100KΩ load discharge 62

Figure 29: Single graphite-zinc cell 10KΩ load discharge (experience self-recharge) 63

Figure 30: Double stacked graphite-zinc starts with 100µA charging (for 30sec) followed by self-discharge 64

Figure 31: Double stacked graphite-zinc cell 5KΩ load discharge 64

Figure 32: Graphite-Zinc cell (E0GZ11) voltage charged at 1.4V for 2 hours resistive load (9.92KΩ) discharge 66

Figure 33: Slow discharge for cell E0GZ12 67

Figure 34: Graphite-Lead cell structure 69

Figure 35: Graphite-Lead cell (E0GP1) resistive load (9.92KΩ) discharge as fresh / new cell and after 3 hour charging at 0.7V 71

Figure 36: Graphite-Lead cell (E0GP1) resistive load (9.92KΩ) discharge as fresh / new cell and after subsequent charging 71

Figure 37: Graphite-Lead cell (E6GP1) resistive load (9.92KΩ) discharge after subsequent charging 72

Figure 38: Graphite-Lead cell (E7GP1) resistive load (9.92KΩ) discharge as fresh / new cell and after subsequent charging 73

Figure 39: Resistive load (1KΩ) discharge of a 1.5V hearing aid battery 77

Figure 40: Structure of folded Graphite-Zinc cell (E0FD) 81

Figure 41: Resistive load (29.83KΩ) discharge of folded Graphite-Zinc cell (E0FD1) 82

Figure 42: (a) and (b) Lattice constant 'a' and 'c' for $Al_xGa_{1-x}N$ random alloys measured by high resolution X-ray diffraction at room temperature (solid lines) and calculated for T=0K (dashed lines) (from M. E. O. Ambacher). 89

Figure 43: (a) Open circuit voltage of photoconductive photodiode (from J. Yamaura), (b) geometry and bias of a photoconductor (from M. Razeghi). 93

Figure 44: Device structure of (a) a vertical Schottky barrier detector (from Q. Chen), (b) a MSM Schottky detector showing incident light under front and back illumination (from M. Razeghi). 95

Figure 45: Schematic representation of (a) p-n junction photodiode (from M Razeghi), (b) p-i-n junction photodiode (from J. D. Brown). 96

Figure 46: Imaging array, (a) and (b) pictures of a 32x32 GaN/AlGaN photodiode array (from J. D. Brown), (c) hybrid UV Focal Plane Array (FPA), indium bump interconnects to a silicon CMOS read out integrated circuit (from P. Lamarre). 98

Figure 47: Structure of two-color UV photodiode arrays with one band in UVa and the other band in UVb. The "A" pixel will respond to one band and "B" pixels will respond to another band. The green grid lines are the n-Ohmic contacts. 99

Figure 48: Absorption percentage as a function Al mole fraction and thickness of $Al_xGa_{1-x}N$ layer. 100

Figure 49: Aluminum Mole Fraction in $Al_xGa_{1-x}N$ (from F. Yun). 101

Figure 50: Schematic of growth technique (from R. F.Davis) of (a) LEO growth through a window in SiO2 and laterally over the mask. (b) PE growth from GaN seed laterally off the sidewalls and vertically off the stripe. (c) TEM of LEO GaN film. (d) TEM of PE grown GaN film. 104

Figure 51: Dark-filed XTEM micrograph of dislocation structure in confined epitaxy grown homoepitaxially on a continuous GaN film on sapphire. Dislocation density reduction from $4.4*10^9/cm^2$ to $6.3*10^8/cm^2$ 106

Figure 52: MicroRaman data showing strain reduction in selectively grown GaN material. Blue curve is for continuous GaN layer beneath the selective epitaxy region and black curve is for a free-standing GaN substrate (presumably strain free). Selectively grown mesas show approximately 50% reduction in strain. Inset shows laser spot size relative to selectively grown mesa size. (Data courtesy of Orest Glembocki, NRL) 107

Figure 53: General two layer lift-off procedure (from Stanford Nanofabrication). . 109

Figure 54: GDS image of two pixels (pixel B on the left and pixel A on the right) with all dimensions in µm. 115

Figure 55: Phase I of processing flow 118

Figure 56: Phase II of processing flow 119

Figure 57: Schematic of flip chip bonding (from Wikepidia); (a) pads are metalized on the surface of the chips; (b) solder dots are deposited on each of the pads; (c), (d) and (e) chips are flipped and positioned so that the solder balls are facing connectors on the external circuitry; (f)solder balls are then remelted; (g) and (h) mounted chip is “underfilled” 120

Figure 58: Cross section schematic of a typical flip chip mounting (from Wikepidia). 121

Figure 59: Micrograph of detector pixels after completion of Phase I of the fabrication process flow 122

Figure 60: Micrograph of detector pixels after completion of Phase II of the fabrication process flow 124

Figure 61: Current vs. Voltage plots of Color 1 and Color 2 pixels 125

Figure 62: Setup of optical evaluation of pixels 126

Figure 63: IV characteristics of diodes in absence (dark) and presence (light) of UV-illumination. 127

Figure 64: $Al_{.2}Ga_{.8}N$ detector (Color 1) current at various UV-wavelengths with diodes biased at -1.5V 128

Figure 65: GaN detector (Color 2) current at various UV-wavelengths with diodes biased at -1.5V 129

Figure 66: System setup for imager evaluation 130

Figure 67: Conventional mask versus “Dot Array” mask 133

Figure 68: Diffraction and typical transmission spectrum of visible light through a subwavelength hole in an infinitely thin perfect metal film (from H. A. Bethe)...... 135

Figure 69: Transmission spectraof a single aperture (d= 440nm) surrounded by (A) rings with sinusoidal cross section and (B) a square array of dimples (h=180nm). Left insets, focus ion beam images of typical samples; right insets, cross sections of the hole and corrugation (from T. Thio). 138

Figure 70: Real-space model of charge displacement at the metal surface and associated electric fields of SP modes at level crossing (from T. Thio)................. 138

Figure 71: Contact printing application (a) Schematic of the lithographic setup. (b) Image of hole array fabricated by Focused Ion Beam etching. The diameter of the holes is 160nm and the lattice constant is 320nm (from Srituravanich).................. 139

Figure 72: AFM image of the transferred dot array pattern (from Srituravanich)... 140

Figure 73: Measured transmissivity (transmission divided by open air fraction) spectra for 3 different hole arrays (from K. L. Van der Molen). 141

Figure 74: Schematic view of the axes of the SEM and the FIB optical columns relative to the sample normal in a Dualbeam 620. The angle θ is the tilt angle between the optical axes of the SEM, θ_{max} is the fixed angle between the optical axes of the FIB and SEM colums and E the eucebtric point (from F. Machalett) 144

Figure 75: Schematic diagram of the FIB/SEM dual beam system (from T. Kalvas). 144

Figure 76: FIB milling on one position for a prolonged dwell time (from O. Wilhelmi). 146

Figure 77: SEM images of arrays of sub-wavelength apertures; (a) Array of a 10x10 apertures with 320nm hole spacing; (b) array of 3x3 apertures with 280nm hole spacing; (c) array of 10x10 apertures with single correctional hole with 300nm hole spacing; (d) array of 10x10 apertures with 3x3 array of correctional holes all with 300nm hole spacing 149

Figure 78: Illustration of ASML QML Stepper.. 151

Figure 79: SEM image of resolved pattern with X and Y measurement; (a) resolved 10x10 array with 280nm hole spacing x = 676.5nm; y = 672.4nm; (b) resolved 7x7 array with 260nm hole spacing x = 409.2nm; y = 603.6nm; (c) resolved 5x5 array with 220nm hole spacing x = 276.0nm; y = 259.4nm 153

Figure 80: SEM image of resolved pattern with X and Y measurement; (a) resolved 3x3 array with 280nm hole spacing x = 187.5nm; y = 187.5nm; (b) resolved 3x3 array with 220nm hole spacing x = 110.2nm; y = 96.56nm 154

Figure 81: Effect of correctional holes on edge acuity; (a) resolved 10x10 array with an added single diagonal aperture; (b) resolved 10x10 array with an added 3x3 correctional array 155

Figure 82: Feature size stability analysis, feature size vs. hole spacing in 10x10 arrays at different doses 156

Figure 83: Feature size stability analysis, feature size vs. focus of 7x7 arrays with varying hole spacing (nm) 157

Figure 84: SEM images of 10x10 arrays with 240nm hole spacing and missing apertures; (a) Mask of 10x10 array missing 10 apertures; (b) Mask of 10x10 array missing 20 apertures; (c) Mask of 10x10 array missing 40 apertures; (d) resolved pattern missing 10 apertures; (e) resolved pattern missing 20 apertures; (f) resolved pattern missing 30 apertures 158

Figure 85: Illustration of Plasmon coupling to sub-wavelength apertures (from W. L. Barnes). 160

Figure 86: Calculated pattern of light emerging from a single slit surrounded by a finite array of grooves (from W. L. Barnes). 160

Figure 87: FDTD simulation of the electric field around the silver field; (a) electric field in the x-direct (along the silver field); (b) electric field in the z-direction (perpendicular to the silver film); (c) electric field magnitude 163

Figure 88: Mini-pixel layout; (a) approximately 6µm across; (b) approximately 3µm across 176

Figure A1: Absorption as a function of depth of penetration and the $Al_xGa_{1-x}N$ alloy stoichiometry……………………………………………………………………..179

CHAPTER 1: INTRODUCTION

1.1 Motivation

Technology has gained a more predominant role in today's society. From cell phones to mp3 players, technology is continuously transforming our culture. The common trend is to push for smaller, cheaper, multi-functionality types of technology innovations. This trend was at the heart of Dr. Meyerson (IBM fellow, VP and Chief Technologist at IBM Corporation) keynote address at the 42nd Design Automated Conference (DAC). During his address, while talking about the issue of "How Does One Define 'Technology' Now That Classical Scaling Is Dead?" Dr. Meyerson pointed out that: "Holistic design is a new paradigm in value creation." In effect, he believes that "This is a synthesis of material and design architecture approaches. Integrating new materials and process technologies with novel system architectures is essential to advancing technology. "

The work described in this thesis goes along Dr. Meyerson vision of technology innovation as it generates technology advancement by pursuing novel micro-circuit ideas through focusing on material processes, integrations and device structures. There are three main studies examined in this thesis. The studies herein presented look at a hydrated ruthenium oxide and activated carbon based electrochemical energy cell, a novel $Al_xGa_{1-x}N$ alloy device structure and growth method as well as an inexpensive and effective sub-wavelength apertures lithography technique.

1.2 Dissertation Objectives

1.2.1 Electrochemical energy cell

This thesis touches upon a strategy to develop an electrochemical energy cell based on hydrated ruthenium oxide and activated carbon for power storage and delivery. The generation of this electrochemical cell focuses on properties of electrode materials and device structure. Moreover, emphases will be placed on the use of a unique dielectric and a high effective electrode surface area as well as a novel cell structure. The development will target:

- The analysis of different electrode materials and their behavior in my electrolyte environment.

- Unique dielectrics/electrolytes via the use of powdery hydrated ruthenium oxide and activated carbon within an acidic electrolyte.

- Characterization techniques to determine the performance of various electrochemical cells structures and composition.

1.2.2 Novel AlGaN based UV detector

This thesis concentrates on demonstrating the feasibility of utilizing a novel III-V nitride semiconductor growth technique (confined epitaxial growth) jointly developed and patented by the University of Maryland and the Naval Research Laboratory (NRL) in the fabrication of a dual ultraviolet (UV)-wavelength photodetector array. Advancements made in the fabrication procedure necessary to enable confined epitaxial growth will directly serve as guidelines to the improvement

of UV detectors as well as devices based on III-V nitride semiconductors. This research will explore the following areas:

a) **Building a detector array.** Integrating the confined epitaxial growth technique in the development of photodetectors requires the use of a bi-layer lift-off process. In this study the bi-layer lift-off method, photoresit/LOL 2000 (lift off lithography), is calibrated for the appropriate structure and the tools used. To successfully incorporate the growth method in the fabrication process of $Al_xGa_{1-x}N$ based photodetectors, this thesis focuses on three steps necessary to develop an UV detector array:

    - Establishing a process flow optimized for detection in the wavelength bands of interest (dual UV-wavelength band detector pixels).

    - Designing lithographic masks to implement the process flow.

    - Executing process sequence at the FabLab cleanroom, University of Maryland, and at outside vendors (Hionix, Naval Research Laboratory and Teledyne).

b) **Building the interface for detection.** The UV detector pixels generate a current in response to the detected signal. In order to record the detected signal, an interface between the detectors and a data acquisition unit has to be developed; composed of the following parts:

    - Identifying a Read-Out Integrated Circuit (ROIC) that matches in shape and size with my designed array.

- Mounting the ROIC to the designed detector array to enable back side illumination.

- Controlling the data acquisition unit

c) **Testing the array.** The dual-color array is characterized to establish its proper functioning. The detectors within the array are tested electrically and optically. Then, the entire unit is evaluated to establish the proper functioning of the complete readout and driver system. The various tests focus on three areas:

- Electrical evaluation

- Optical Evaluation

- System evaluation

1.2.3 Sub-wavelength aperture lithography technique

A mask making method using arrays of sub-wavelength apertures to create an inexpensive sub-wavelength resolution lithography mask is presented. Rather than creating a mask with continuous clear and opaque regions, a “dot array” mask is utilized to explore the use of sub-wavelength aperture array for far-field imaging. Such an analysis requires the targeting of the following task:

- Fabrication of the array of sub-wavelength apertures via focus ion beam milling.

- Transmission characterization, this is done by examining how well the transmitted light can pattern photoresist while the mask is used in a conventional stepper.

- Understanding the robustness of such a mask. In other words, what happens if some apertures do not go all the way through the mask film?

1.3 Unique Contributions

The electrochemical energy cell research work presented in this thesis touches upon an area not much explored; that of using hydrated ruthenium oxide and activated carbon as electrode materials in powder form. This research work, furthermore, contributes to the work done in the field of UV detector fabrication and characterization as well as in the area of $Al_xGa_{1-x}N$ alloy film growth which would enhance the performance of III-nitride dependent devices. In addition, the research conducted on the array of sub-wavelength apertures for lithography applications adds to the knowledge pool in sub-wavelength aperture far-field imaging work. These different research endeavors offer unique contributions along the following lines:

Electrochemical Energy Cell

I present a variety of electrochemical energy cells structures. These cells show the viability of powder ruthenium oxide and activated carbon use as electrode material [1, 2]. This deviates from the conventional use/deposition of these materials when applied as electrode; notably, sputtering, evaporation or pressed with a binder. I have

developed a thin, flexible electrochemical cell (battery) that can be easily integrated into a general flexible electronics matrix [3]. My claimed contributions are these:

a) I have created electrodes that have a high surface area as power is generated at the electrode surface.

b) I implemented the cells with an electrolyte that is as close to pH-neutral (7) as possible to prevent rapid dissolution of the electrode materials or package sealing materials while favoring the needed redox reactions.

c) I have enabled the reaction chemistry to proceed as close to equilibrium as possible to allow electrically driven reversibility (re-charging).

d) I have targeted the weight and volume of the cells to be as light and low volume as possible as well as flexible.

Dual UV-Wavelength Imaging Array

I introduce a simultaneous dual UV-wavelength detector array. This thesis outlines the fabrication process flow to generate the detector array and implements the process flow to generate a detector array. The design of this array is enabled by my development of a novel fabrication process flow that depends on a modified lift-off process, a patented confined epitaxy growth method for III-nitride semiconductors and a creative detector staking approach. These guiding principles pave the way for the following contribution to the field:

- My presented lift-off lithography process applied to the conditioning/patterning of the area needed for active $Al_xGa_{1-x}N$ growth

demonstrates the importance of the confined epitaxial growth process in the quality improvement of grown $Al_xGa_{1-x}N$ layers [4, 5].

- My presented fabrication process flow for the generation of an array of dual UV-wavelength detectors demonstrates simultaneous dual UV-wavelength band detection. This is the first demonstration of such capability, uncovered by the research described in this thesis.

- My lift-off lithography process in conjunction with my presented UV detector device structure (the stacking of two $Al_xGa_{1-x}N$ active layers) offers a road map for the development of other devices based on $Al_xGa_{1-x}N$ alloys

Sub-Wavelength Lithography Technology

I present a novel mask, a "Dot Array" mask. This mask is based on inexpensive and effective array of sub-wavelength apertures for use in a conventional stepper for far field imaging [6]. A multitude of square patterns are shown in this thesis to establish some of the mechanisms involve in this sub-wavelength transmission phenomenon. The guiding principles of the construction and calibration of the mask lay the ground for the following contribution to the field:

- I developed of a mask writing technique where a beam writer is presented with a smaller writing area without requiring the shrinkage of the expected printed pattern or the loss of resolution.

- I have conducted the first use and demonstration of far-field imaging capability of an array of sub-wavelength apertures [7].

1.4 Dissertation Structure

This thesis is organized as follows: Chapter 1 has covered the motivation, objectives and contribution of this thesis work. Chapter 2 examines and contrasts the mode of operation of capacitor and batteries. Then, figures of merit of both types of devices are presented as well as the test setups required for their characterization. Following that, different electrochemical cells are scrutinized from a structural and composition standpoint. Their charging and discharging behaviors is also presented. The electro chemistries involved in conventional batteries and in my battery are analyzed. Ultimately, the electrochemical flexible battery I fabricated is compared and contrasted to different commercially available battery systems.

Chapter 3 presents an introduction to ultraviolet detector figures of merit, mode of operations and existing imaging arrays based on $Al_xGa_{1-x}N$. Furthermore, the chapter presents the confined epitaxy growth technique applied to $Al_xGa_{1-x}N$ alloy. This is followed by a presentation of my dual UV-wavelength detector array fabrication process flow. The mask used in executing the fabrication process flow and the characterization of the array is covered.

Chapter 4 discusses mechanism of light transmission through a sub-wavelength aperture and array of apertures. Then, the sub-wavelength aperture array mask's fabrication method is introduced as well as the different mask patterns explored. Following that, transmission performances are qualified via the use of scanning electron microscope (SEM) images of the resolved mask patterns. The chapter closes with an analysis of surface plasmon and how they relate to the far field imaging phenomenon on which my "Dot Array" mask relies. Finally, Chapter 5 offers some

closing remarks with a summary of the findings of all three research areas as well as an enumeration of this thesis work unique contribution to various fields of interest. In closing, some potential expansions to the work presented in this thesis are offered.

CHAPTER 2: ELECTROCHEMICAL ENERGY CELL

2.1 Major Contribution

This chapter introduces a variety of electrochemical energy cells describing the structure and fabrication of a thin, flexible electrochemical cell (a battery) that can be easily integrated into a general flexible electronics matrix. The guiding principles of construction are these:

a) I have created electrodes that have a high surface area as power is generated at the electrode surface.

b) I implemented the cells with an electrolyte that is as close to pH-neutral (7) as possible to prevent rapid dissolution of the electrode materials or package sealing materials while favoring the needed redox reactions [3].

c) I have enabled the reaction chemistry to proceed as close to equilibrium as possible to allow electrically driven reversibility (re-charging).

d) I have targeted the weight and volume of the cells to be as light and low volume as possible as well as flexible.

I achieved (a) through the use of nano-particulate RuO_x as a cathode material [1]. I assure permeability of the RuO_x mass by compounding it with graphite nano-

particles. This also lowers the internal resistance of the cell. The compound forms a screenable conducting paste that can be applied as a thin film over a flexible substrate (like polypropylene).

To accomplish (b) I use an ethylene glycol base to which I add a buffered HNO_3 solution. The buffering and dilution process creates a pH 5 mixture. This electrolyte is applied as droplets over the RuO_x/activated carbon paste, forming a gel-like mixture. A counter-electrode of either zinc or lead is pressed over the gel. The RuOx/electrolyte/metal foil cell has an electrochemistry close to that of a lead-acid battery and the redox reaction responsible for power generation is close to equilibrium, allowing for electrically driven re-charging. This also satisfies requirement (c). A second plastic sheet is placed over the whole assemblage and the assemblage is sealed. All the materials used are flexible. The resulting RuOx/graphite-electrolyte-metal foil cell is thinner than 0.5mm, and a typical zinc anode cell weighs less than 1g – satisfying requirement (d).

2.2 Introduction

The Maryland Smart Dust Project is an interdisciplinary research project at the University of Maryland at College Park that focuses on the development of ad-hoc sensor networks that utilize very small wireless sensor nodes. The project centers largely on the development of intelligent sensor nodes which have volumes of much less than a cubic centimeter, and are often referred to as Smart Dust. The class of smart dust systems that are targeted is aimed at short communication and sensing distances (less than 10 meters) and low power wireless sensing nodes (less than

1mw). To achieve this, unique transceiver and processor circuits have been designed and fabricated as well as novel antennas and energy storage and harvesting systems.

This chapter's focal point is on the development of the energy storage component of the sensor nodes. The component is an electrochemical energy cell that enables efficient energy storage and delivery within a compact volume. The cell should allow for easy integration (in terms of "form, fit and function") into arbitrarily designed sensor "motes" to meet energy storage specifications for low-power ad hoc distributed networks. The cell is to be charged by a "rectenna" (RF power conversion into current). In a sense, the cell is charge by a current source and delivers its stored charge upon request to a sensor system. Figure 1 illustrates where the electrochemical energy cell fits within the sensor mote. Electrochemical energy can be stored in two inherently different ways: through electron transport as observed in a battery (in the case of redox reaction or Faradaic process) or through non-Faradic means (with no electron transport between the electrode) as in the case of a double-layer capacitor where the storage of electric charge and energy is electrostatic [8]. A Faradaic process is related to electron transfer across a metal electrolyte interface, with reduction or oxidation of species present at the interface (see Figure 2). A non-Faradaic process involves the accumulation of charges at the metal/solution interface (see Figure 3).

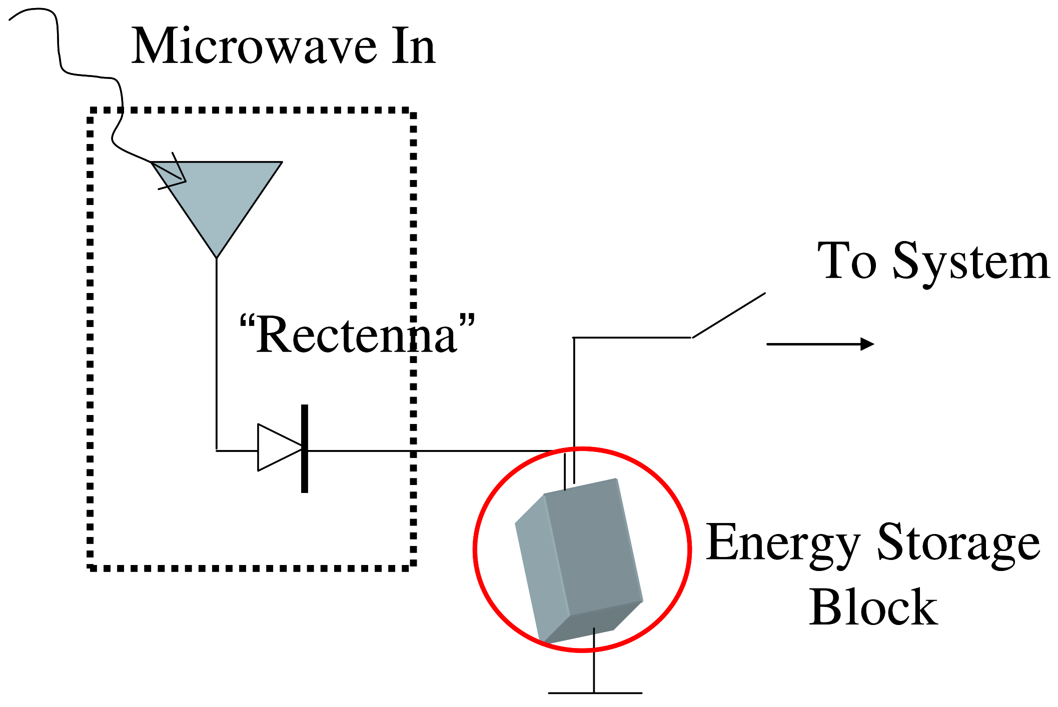

Figure 1: Electrochemical energy cell within sensor mote

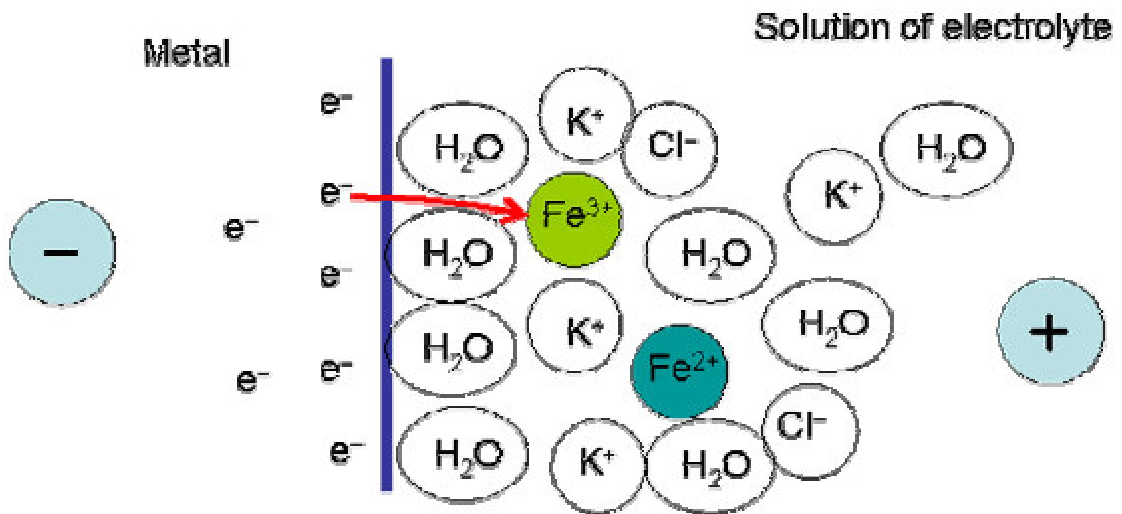

Figure 2: Schematic of Faradaic processes (from electrochem).

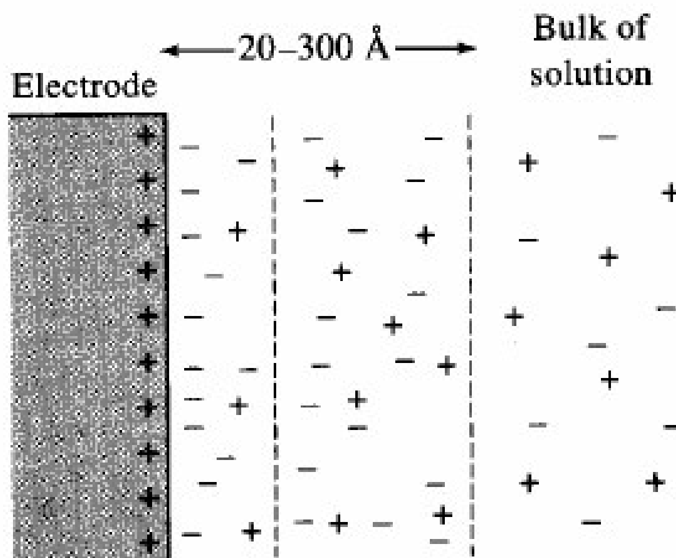

Figure 3: Schematic of non-Faradaic process (from electrochem).

The performance characteristics of energy devices are fundamentally determined by the structural and electrochemical properties of electrode materials as well as the choice of electrolyte. Multiple designs and packaging approaches were investigated throughout the design of the energy cell. The cell's structures, materials, electrolytes, packaging and performances will be discuss in this chapter and examined in the up-coming Sections. First, Section 3 will offer an overview of energy cells and the difference between capacitors and batteries. Next, Section 4 will cover various electrochemical cell characterization approaches. Section 5 will discuss properties and behavior of electrode materials. Subsequently, Section 6, 7, 8 and 9 will offer an in-depth analysis, in chronological order, of the cells designed for this project. Finally, Section 9 will present a summary of the cells' performances, a discussion of these results as well as concluding remarks.

2.3 Background

2.3.1 Batteries

The first battery was fabricated by Alessandro Volta 200 years ago. It was made out of a pile of silver/copper and zinc, and the separator was cloth saturated with brine [9]. The term 'battery' originally implied a group of 'cells' in a series or parallel arrangement; however, nowadays, it is understood to mean either a single cell or a group of cells. A battery is a device for the storage of electrical energy in the form of chemicals and for the re-conversion of these chemicals into direct-current electricity. While very complex, the processes taking place at the electrodes can be represented, to a first approximation, by simple electrochemical equations. During discharge, the equation describes a chemical reduction process (capture of electrons) at the positive electrode and an oxidation process (loss of electron) at the negative electrode [9]. During charging, the processes at the electrodes are a reversal of the processes that take place during discharge.

An electrochemical reaction or electrode process refers to the electron transfer between an electronic conductor and some species in an electrolytic phase. For this transfer to proceed on a continuous basis requires a second electrode process in which electron transfer takes place in the opposite direction to ensure electroneutrality [10]. Electrons can be transferred to and from an electronic conductor such as an electrolyte.

An electrochemical cell can be characterized by three figures of merit, its available capacity, its available energy and the power it can deliver.

- Capacity is the number of coulombs or ampere hours delivered. For purpose of comparison, one can calculate specific capacity which is the capacity divide by the weight of the cell and given in Ah/Kg. A volume-based specific capacity can also be calculated in units of Ah/dm^3.

- The amount of practical available energy depends on the manner in which the cell is discharge and is determined by:

$$E = \int_0^t (V * I) dt \quad \textbf{(1)}$$

Where t refers to the total discharge time, V is the potential across the cell and I the current flowing out of the cell. The units of energy are either joules (i.e. watt seconds) or watt hours (1 Wh = 3600J). Energy density (also referred to as specific energy) is used for comparison purposes and is either weight-based (Wh/Kg) or volume-based (Wh/dm^3).

- Power delivered, P, relates to the level of discharge current drawn from a cell by an external load resistance. It is define as the product of the flowing current and the associated cell potential:

$$P = V * I \quad \textbf{(2)}$$

For purpose of comparison, the most convenient parameter is power density quoted in W/Kg or W/dm^3.

The more electrolyte and electrode material there is in the cell, the greater the capacity of the cell. As a result, for cells having the same exact chemistry, a small cell

has less capacity than a larger cell although they display the same open-circuit voltage. Furthermore, the available capacity of a battery depends upon the rate at which it is discharged as well as the discharge conditions such as the magnitude of the current, the duration of the current, temperature, and other factors. This dependence exists because of the chemical reactions within the cells. If a battery is discharged at a relatively high rate, the available capacity will be lower than expected. The battery capacity that battery manufacturers display on a battery is the product of 20 hours multiplied by the maximum constant current that a new battery can supply for 20 hours at 68 F° (20 C°), down to a predetermined terminal voltage per cell [11].

Batteries are generally divided into two broad classes:

- *Primary batteries* are designed to deliver a single discharge. The chemical transformations responsible for the electrical energy are irreversible. Once the initially available reactants are used-up they can not be easily restored.

- *Secondary batteries* are designed to be rechargeable. The chemical transformations responsible for the electrical energy can be reversed by electrical means.

A secondary battery is charged by passing direct-current (d.c.) electricity through the battery in order to reverse the discharge process. An electrochemical reduction reaction occurs at the negative electrode. It usually brings about the formation of a metal, while electrochemical oxidation of the active material takes place at the positive electrode [9]. In effect, the charging of a battery is an electrolytic

process. As a result, if current continues to flow through the battery after charging is complete (i.e. active material of the electrode is fully converted to its original state), the cell enters an overcharge regime. Overcharging will lead to the electrolyte being decompose electrochemically. For an aqueous electrolyte, water is lost by electolysis and needs to be replaced to preserve the optimal performance of the cell.

Four fundamental approaches are used for charging a secondary battery [9]:

- *Constant current charging*, this method utilizes a constant current throughout the charging process (see Figure 4(a)). Special attention needs to be paid to the current level used. The use of a current that is too small would lead to a very slow charging while using a current that is too large would lead to degassing of the electrolyte.

- *Constant voltage charging*, this method utilizes a constant voltage throughout the charging process. In such a setting, the sourced current is established by the voltage difference between the battery and the charging source. The current starts high and decreases almost exponentially as charging proceeds (see Figure 4(b)). Hence, it takes a long time to fully charge the battery.

- *Taper-current charging*, this method utilizes a design in which the current starts off high and decreases progressively as the battery voltage increases (see Figure 5(a)).

- *Constant-current constant-voltage charging*, this method utilizes, first, a constant current to charge the battery up to a pre-determined voltage at which gassing is likely to take place. Then, the voltage is held constant and the

current can then decline exponentially as in the case of *constant-voltage charging* (see Figure 5(b)).

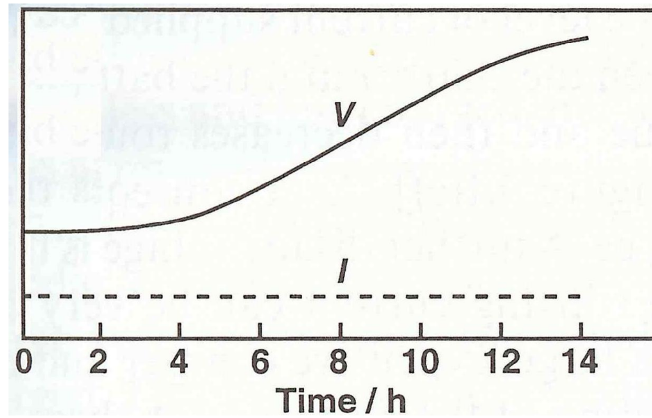

(a)

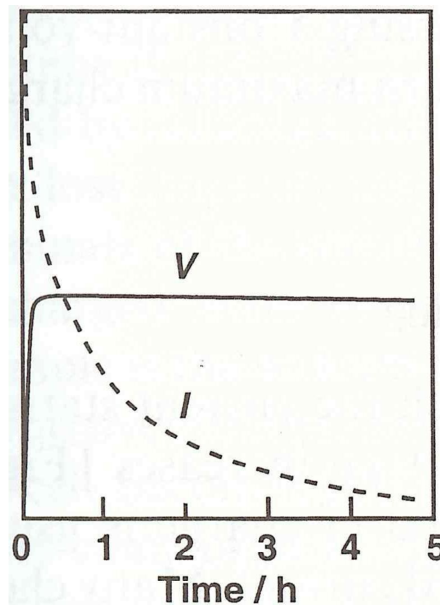

(b)

Figure 4: Procedures for charging batteries; (a) constant current; (b) constant voltage (from M. Dell).

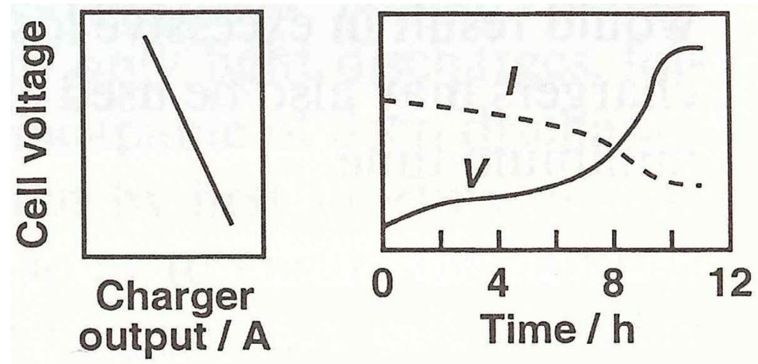

(a)

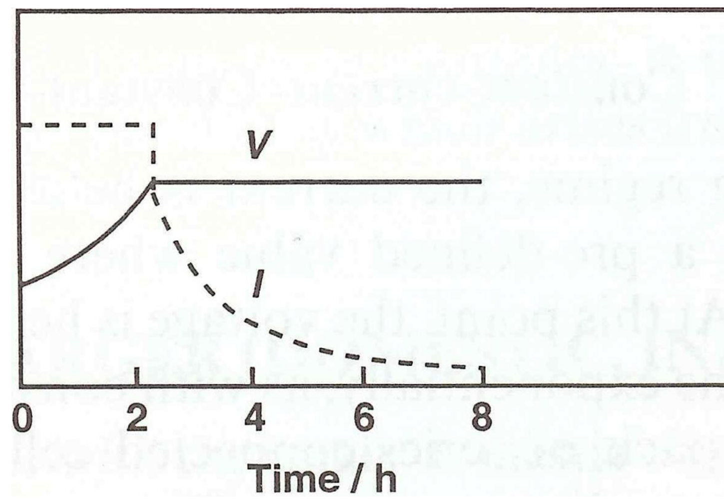

(b)

Figure 5: Procedures for charging batteries; (a) taper current; (b) constant-current – constant-voltage (from M. Dell).

2.3.2 Capacitors

Electrical capacitors or condensers (as they are sometimes referred to) are electric circuit elements used to temporarily store electricity or electrical energy. They are usually comprised of three essential parts:

- Two electrical conductors
- A separator
- A dielectric

The electrical conductors are usually metal plates separated and insulated from each other by a dielectric. The plates are charged with equal amounts of positive and negative electrical charges. The capacity of an electrical capacitor is the ratio of the quantity of electricity and the voltage across the device. That is to say that the capacity of a capacitor depends on the amount of electricity (charge) it will hold at a certain voltage which can be expressed as follows:

$$C = \frac{Q}{V} \tag{3}$$

Where Q is the quantity of electricity (charge), V the voltage across the device and C the capacity expressed in Farad (F).

In order to increase the charge storage capability (capacitance) of capacitors, one must use a dielectric layer that is thin, pinhole free ("ideally" self-organizing); furthermore, the dielectric constant should be high and the effective surface area of the electrode should be large. There exist a fixed relationship between the nature of the dielectric, the area of the plate and the distance between the plates. The relationship is best described as follows:

$$C = \frac{0.0885 * K * A}{t} \tag{4}$$

Where A is the area (in cm^2) of the plate, t is the distance between the plates (in cm) and K refers to dielectric constant. The dielectrics may be found in liquid, solid or gaseous form or even in a combination of these forms depending on the capacitor. Some dielectrics commonly used include paper, glass, sulphur and vegetable oil. It is customary to identify capacitors in accordance with the dielectric used; for instance, there are oil capacitors, paper capacitors and air capacitors. However, there are other types of capacitors, notably, electrolytic capacitors and electrochemical capacitors.

Electrolytic Capacitors

An electrolytic capacitor is similar to any type of electrical capacitor since it is made of two conducting surfaces separated by a dielectric medium. The difference from the conventional double metallic plate capacitor resides in that only one of its conducting surfaces is a metallic plate while the other is an electrolyte or chemical compound. The dielectric utilized is a very thin oxide of the metal which makes up the one metallic plate used in the device [12].

The electrolytic capacitor must always be connected in such a way that the electrolyte is the negative electrode. This will allow only a small current flow through the capacitor. Leakage current is generated in the electrolytic capacitor from the fact that in addition to the metal film emitting electrons, the electrolyte is also able to emit some electrons from the ions. This leakage current is determined by the field strength (due to the applied potential), the oxide film at the metal surface and the conductivity

of the electrolyte. Electrolytes of low conductivity (high specific resistance) display low leakage current because of the reduced number of ions. However, these electrolytes downside is that they increase the resistance effectively in series with the capacitor.

The capacity of electrolytic capacitors can be augmented by increasing the surface of a given type of anode or by roughening the plain surface. Capacitors with a plain anode surface are referred to as plain foil capacitors while those with a roughen surface are called etched foil capacitors. Most present day electrolytic capacitors are made with etched surface anode structures [12]. The roughening of the surface can be done various ways among which, sand blasting, scratching with rotating brushes, mechanical embossing and chemical etching with acids and salts of acids. Capacitors that are made-out of an hydrous oxide material generate their capacity mostly from Faradaic charge storage as oppose to double-layer charge storage (non-faradaic process).

Electrochemical Capacitors

Electrochemical capacitors are referred to by a host of names: supercapacitor, ultracapacitor or electrochemical double-layer capacitor. The denomination ‘supercapacitor’ is commonly used although it is the trade name of the first commercial devices made by Nippon Electric Company. The term ‘ultracapacitor’ is also frequently used, originating from devices made by Pinnacle Research Institute (PRI). These different terms will be used interchangeably through out this thesis.

The concept of a high energy density, electrochemical double-layer capacitor is relatively recent. The first patent was issued in 1957 and the first attempt to commercialize such devices was in 1969 by SOHIO. Early electrochemical capacitors used compressed carbon particulate and an aqueous electrolyte, generating a cell voltage of 1V. They were intended for low power applications as smaller and longer life substitutes for batteries. The first high power electrochemical capacitors were developed for military applications in the early 1980's by the Pinnacle Research Institute for the US military. These devices were made out of ruthenium/tantalum oxide electrodes with sulfuric acid as the electrolyte.

Electrochemical capacitors have an unusually large storage capacity relative to their size compare to what would be expected from traditional electrostatic capacitors of equal size. The availability of high-power electrochemical capacitors represents a new class of energy technology that fills the gap that exists among other energy storage devices. The Ragone plot of Figure 6 (graphical representation of energy and power capabilities of different technologies) illustrates the position occupied by electrochemical capacitors.

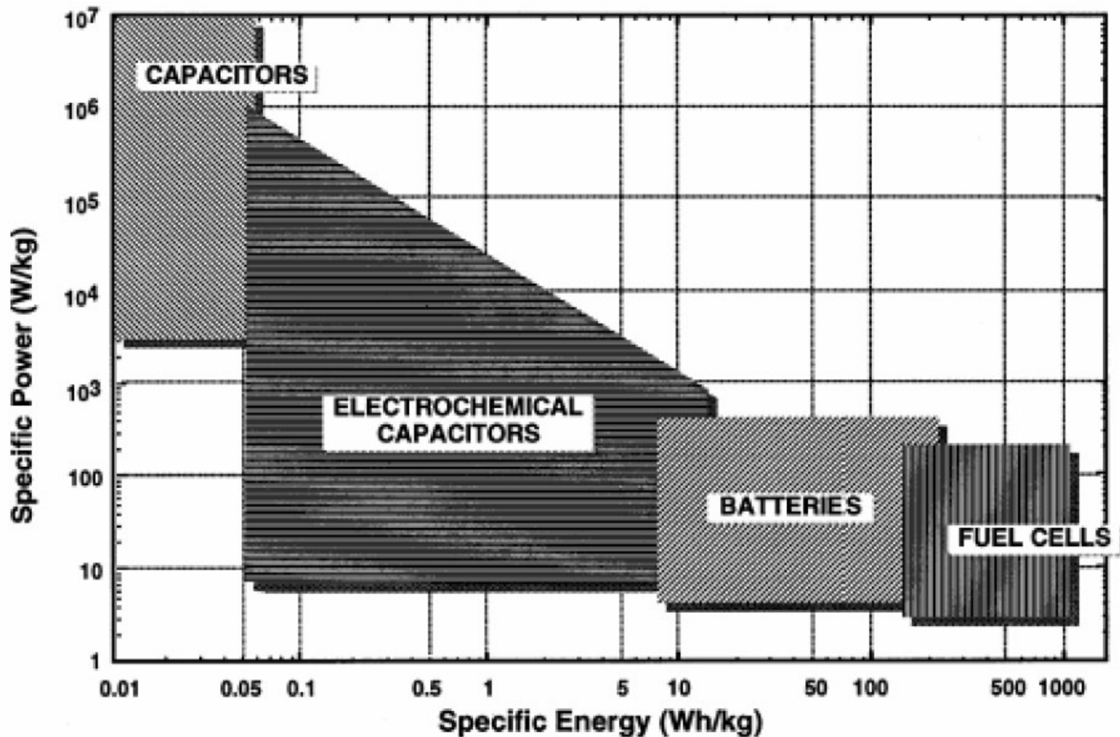

Figure 6: Ragone plot of various energy storage devices (from R. Kotz).

In the 1970's, B. E. Conway, at the University of Ottawa, discovered that an extremely fast redox reaction was possible at the surface of some low resistivity oxides. This discovery led to the creation of an electrochemical capacitor based on the intercalation of hydrogen ions (protons) into a surface to produce charge separation [13]. The success of this approach depends on the existence of a source of hydrogen ions in the electrolyte solution; hydroxide and acid yield the best results especially sulfuric acid and potassium hydroxide. Sulfuric acid (H_2SO_4) has the highest conductivity among acid solutions and good low temperature performance. These properties make it the electrolyte of choice.

There are really two types of “supercapacitance” [14]:

- Double layer capacitance: due to charge separation
- Pseudocapacitance: due to faradaic adsorption or discharge of electrons (redox reactions)

Double-layer capacitance arises from the potential-dependence of the surface density of charges stored electrochemically at the interfaces of the capacitor. The charge found at the capacitor electrode, be it a metal or graphite surface, is either a deficit or an excess of conduction-band electrons in the near-surface area of the solution/metal interface. The capacitor counterbalancing charges are provided by accumulated anions or cations of the electrolyte which provides the other side of the double-layers interface [15]. The double-layer capacitance comes from the traditional ideas of Von Helmholtz and of Gouy; according to which, double-layer of separated charges (+ and -) is generated across an electrified interface. The electric double-layer capacitor accumulates and supplies electric energy by physical adsorption of ions. Adsorption is a process that occurs when a gas or liquid solute accumulates on the surface of a solid or a liquid (adsorbent), forming a molecular or atomic film (the adsorbate) [16].

Multiple models have been proposed for the double-layer. The first model was that of Von Helmholtz, in 1853, who visualized it as a double array of charges comparable to that on the plates of a capacitor [17]; this view is illustrated in Figure 7(a). In the early 1900’s, Gouy noticed that the capacitance was not constant; instead, it was determined by the ionic concentration and the applied potential. To explain this observation Gouy suggested that thermal motion kept the ions from

accumulating on the surface of the electrode, instead forming a diffuse space charge as shown on Figure 7(b). In 1924, Stern modified the Gouy-Chapman model by adding a compact layer as well as Gouy's diffuse layer. The compact Stern layer consisted of a layer of specifically adsorbed ions [18]. This model is illustrated in Figure 7(c) where the layer of adsorbed ions at the electrode surface is referred to as the Helmholtz plane and beyond that you have a diffuse layer identifying the closest approach of the diffuse ions to the electrode. The current model includes the action of the solvent; layer of solvent are present within the Helmholtz layer at the surface of the electrode, see Figure 7(d).

Although some surface oxidation/reduction also occurs in a double layer capacitance as one would expect in a battery, these reaction are restricted to one or two monolayer on the electrode surfaces. Unlike ordinary batteries, a chemical reaction is not used. Hence, overall behavior of the device is compatible with that of a capacitor. The main differences between the electrical energy of a battery and that of a capacitor is that the cell voltage of a capacitor continuously declines during discharge for electrostatic reason while for an ideal battery, the voltage remains almost constant during discharge (up to 95 to 99% consumption of charge capacity) for thermodynamic reasons.

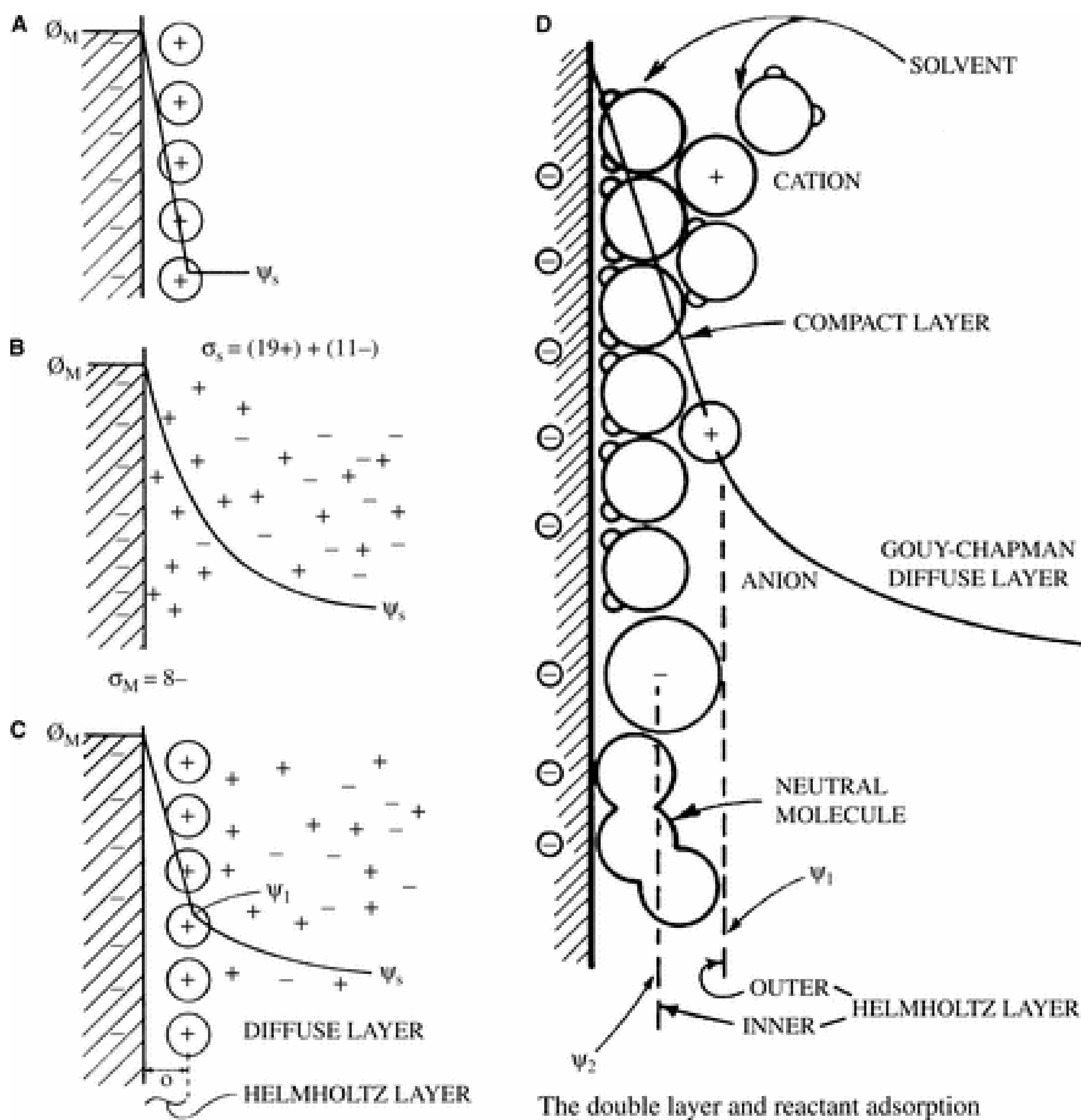

Figure 7: (A) Von Helmholtz capacitor model of the double-layer. (B) Gouy-Chapman diffuse layer model of the double-layer. (C) Stern model of the double-layer incorporating a coupled diffuse layer charge distribution, with corresponding drops of potential shown. (D) Overall model of the double-layer showing presence of solvent molecules (from B. E. Conway).

Pseudocapacitance arises at an electrode surface where a completely different charge-storage mechanism applies. Ruthenium oxide (RuO_2) is one of the best illustration of a pseudocapacitive material [19]. RuO_2 is an electroactive oxide that yields to Faradaic behavior; Ru^{2+}, Ru^{3+} and Ru^{4+} couple in the redox reaction. The oxidized and reduced form of a redox part are identified as forming a redox couple. Electrochemically formed Ruthenium oxide films that are hydrous more readily exhibit redox pseudocapacitance [14]. The situation required for a pseudocapacitance to occur is when the potential at which a charge is being passed is a function of the integrated charge accumulated. Thus a pseudocapacitance can be associated with either a redox reaction for which potential is a (log) function of the ratio of activities of the oxidized and reduced species or with a process of progressive occupation of surface sites on an electrode by an underpotential-deposited (UPD) species. UPD is a phenomenon of electrodeposition of a species (usually reduction of a metal cation to a solid metal) at a potential less negative than the equilibrium potential for the reduction of this metal [20].

Pseudocapacitance occurs in cases where Faradaic charge transfer processes lead to passage of extents of charge (q). These charges, for thermodynamic reasons, depend on potential, ideally constant electrode potential [21]. For instance, processes which are associated with pseudocapacitance include redox processes in liquid or solid solutions where the electrode potential is a function of the log of the ratio of reductant converted to oxidant (or vice-versa) in a redox system. In a pseudocapacitor, as opposed to an ideal double-layer capacitor, charging and discharging takes place through Faradaic processes involving electron transfer across

the electrode/solution interface. Since the process occurs at an electrode/solution interface, an additional (typically much smaller) double-layer capacitance also exist in a parallel setup with the pseudocapacitor and is non-Faradaically charged with changing potential [21].

2.4 Cell characterization techniques

There are multiple techniques to measure the performance of an energy cell (battery or capacitor). The different figures of merits that are targeted in the various techniques have been presented in the previous section. This section focuses on the measurement techniques used through out this chapter to establish the performance of the diverse energy cells that were fabricated throughout this thesis work.

2.4.1 Cyclic Voltammetry

Cyclic voltammetry offers a measure of electrochemical cell's charge-response relative to a change in voltage; as a result, it provides a way of evaluating capacitance. In a cyclic-voltammogram the charging and discharging of a capacitor at any potential, in the charging sweep, provides information on the kinetics of the process. Reversal of the direction of sweep directly leads to an opposite discharging current passing at approximately the same potential, provided the process is kinetically reversible [15]. Differently said, a voltammogram that displays a "mirror-image" anodic and cathodic depicts a reversible reaction. An irreversible process will have two different charge and discharge profiles where the ends of which do not meet up. An ideal capacitor (no internal resistance) would display a rectangular shaped cyclic voltammetry curve whereas electrochemical capacitors display a parallelogram

shape with irregular peaks as illustrated in Figure 8 (curve 4). The peaks are proof of redox reactions (pseudocapacitance).

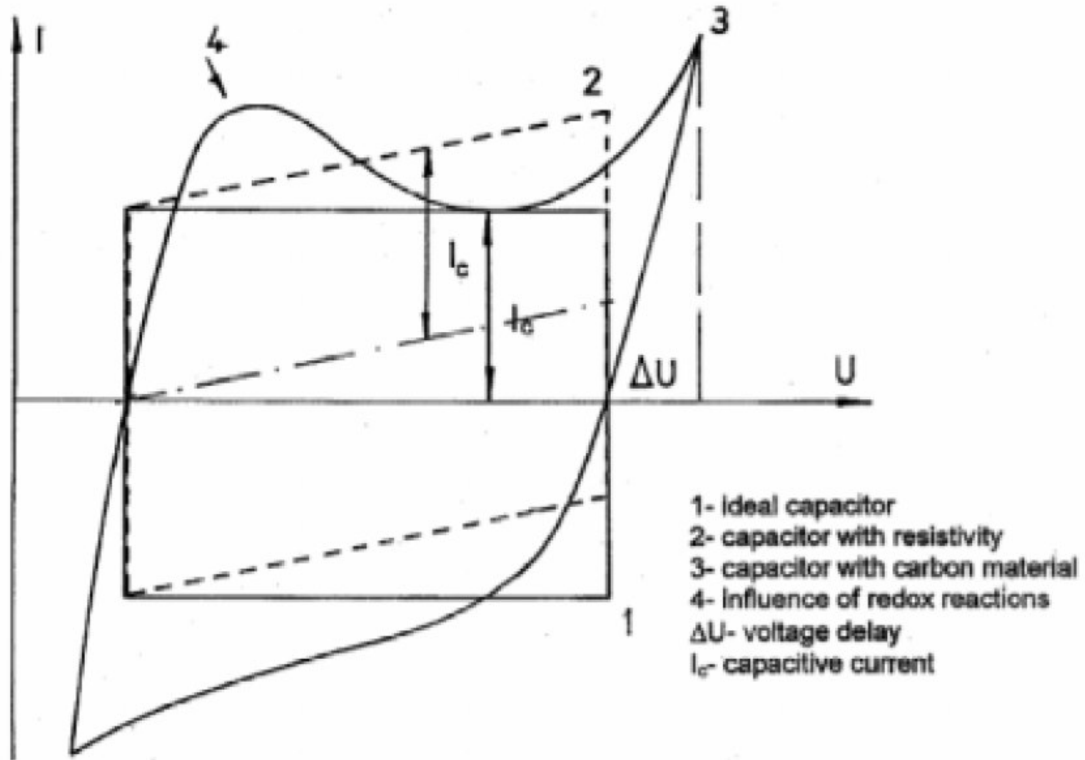

Figure 8: Comparison of ideal and real cyclic voltammograms (from E. Frackowiak).

2.4.2 Constant Current Charging

Constant current charging uses a predetermined constant current to charge the device under test, while the voltage across the device's leads is being monitored. For a typical capacitor, the voltage during charging starts at a non-zero voltage (V_i), increases semi linearly to a working voltage and then settles. The initial voltage and the slope of the voltage curve are then used to determine the internal series resistance (R_s) of the device and the overall capacitance, through Equations 10 and 11, where I is the set constant current, ΔV the change in voltage over some time interval, Δt.

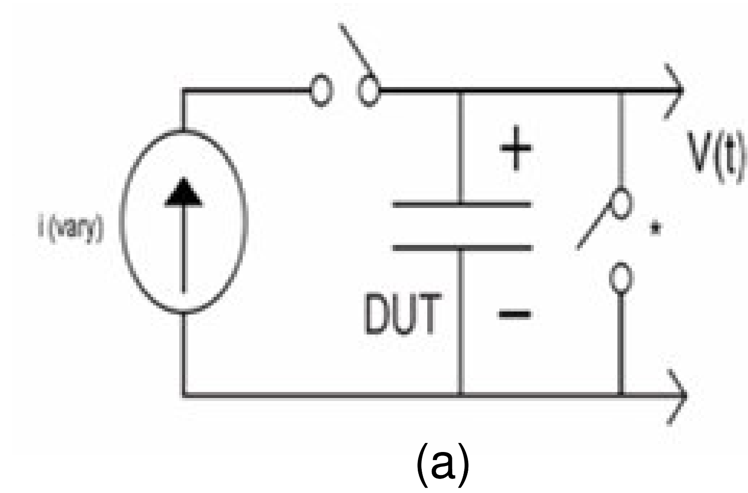

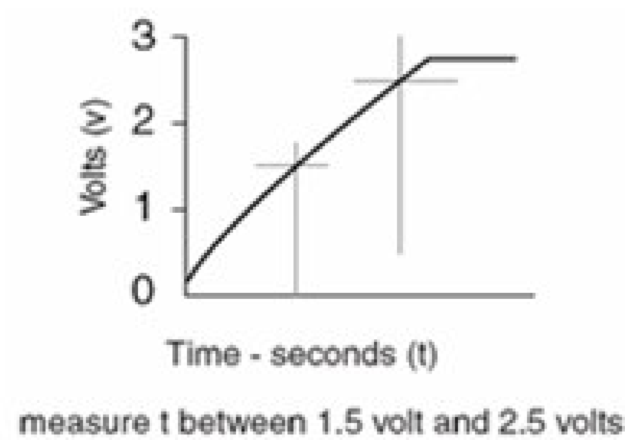

Figure 9: Current charging experimental setup (from Cooper Bussman); (a) circuit setup; (b) charging potential

$$R_S = \frac{V_i}{I} \tag{5}$$

$$C = I * \frac{\Delta t}{\Delta V} \tag{6}$$

2.4.3 Cell Polarization

Polarization of a device is the time honored method of analyzing a battery. The device is discharged such that voltage is stepwise reduced from open circuit voltage to 0.1 V. Rate of change of voltage is determined by the units of mV/s. In such a setting, the current sourced by the cell is recorded. Then, voltage and power plotted vs. current.

2.4.4 Constant Voltage / Current Charging - Resistive Discharge

Constant voltage / current charging is used to condition a cell prior to load discharge or self-discharge. The cell is initially charged by the voltage / current source. Then the device under test (DUT) is used to run a resistive load. A schematic of such a setup is presented in Figure 10 where source referrers to either a voltage supply or a current supply. The potential across the load is monitored with a parameter analyzed (as a function of time) and the associated current supplied by the DUT can be determined from ohms law. The current integral over the discharge (equation 7) is a measure of charge delivered.

$$\int idt \qquad (7)$$

If the charging unit is removed in Figure 10, one can determine the driving capability of a new cell (not previously discharge or charged) as well as that of an older cell (previously discharged or charged).

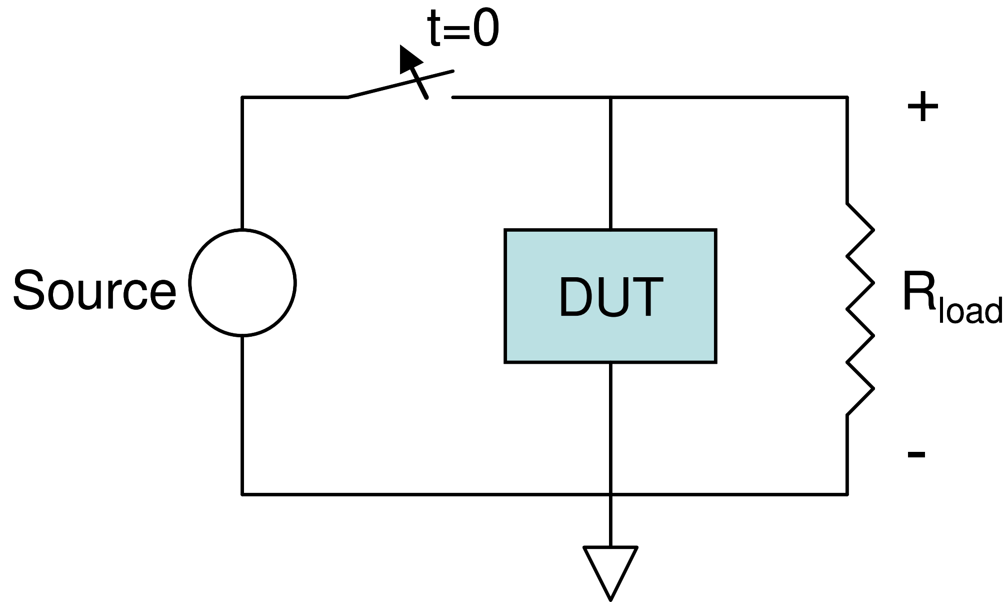

Figure 10: Constant voltage / current charging followed by resistive discharge

2.4.5 Self Discharge

In self discharge, the potential across the cell is measured periodically with no load attached. This is done with fresh cells, cycled cells and charged cells. The measurements identify the cells ability to hold charge or shelf-life. The cells' potential will drop if there is any leakage current or internal short.

2.4.6 Device Demo

The device demo focuses on some of the application requirements. The energy cell is targeted for "rectenna" charging. Hence, in addition to simple current charging (from a current source), the cells are also charged via a "rectenna". Furthermore, the resistive load is substituted with a low power ring oscillator. This is to demonstrate the cells' ability to drive a non linear load.

2.5 Electrode Material

For electrochemical devices, the electrode materials play a critical role in determining the electrical properties. They will dictate the various redox reactions that could occur in the case of a battery or a pseudocapacitor. In the case of a double-layer electrochemical capacitor, charge storage is a surface process; hence, the surface characteristics of the electrode greatly influence the capacitance of the cell. Some of the key electrode parameters are the following:

- Conductivity
- Pore size distribution
- Density
- Pore volume
- Wettability
- Particle size and shape
- Thickness
- Binders additives

Given its relatively inexpensiveness, carbon is the most widely used electrode material. Electrochemical cells have used as electrode material high surface materials such as graphite, activated carbon, carbon nanotube, carbon composite, and carbon aerogels/foams [22, 23]. Treatment of activated carbon materials influences the porous structure of the electrode surface, and it is the accessibility of the pores to the electrolyte that is important since the pores areas represent the effective surface of the

electrode. The mobility of the ions within the pores is dissimilar to the mobility of ions in the bulk of the electrolytic solution,

Pseudocapacitive effects are often found to occur on the surface of activated carbons. The level of pseudocapacitance (redox reactions) can be improved by modifying the carbon to increase its surface functionality. For instance, the capacitance of activated carbon is enhanced by treatment with ruthenium oxides [24]. The resulting voltammetry of such a carbon cure is illustrated in Figure 11.

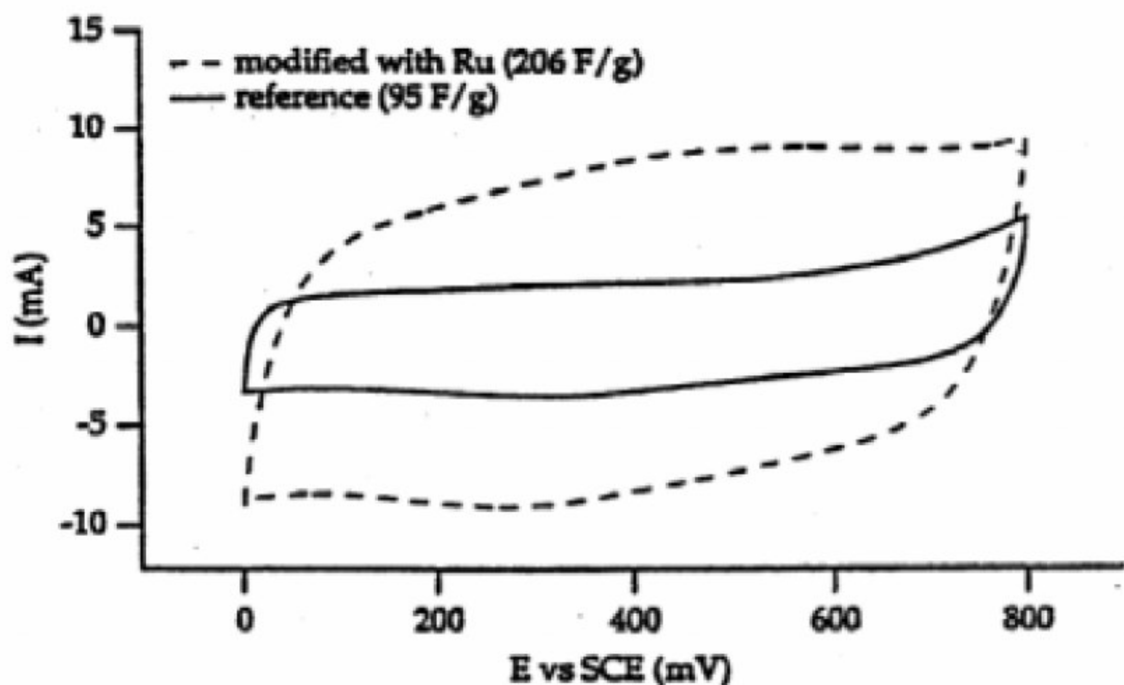

Figure 11: Voltammetry plot of modified carbon electrodes (from J. M. Miller).

Hydrated form of ruthenium oxide ($RuO_2.xH_2O$) has been shown to be an outstanding electrode material for electrochemical capacitors [19, 25, 26]. The electrodes of such devices were obtained by sputtering the Ruthenium or using a binder (mostly Teflon) to hold the particles in place. The conductivity of the electrode is very important for the power density of an electrochemical double-layer capacitor.

Conductivity is inversely proportional to particle size; as a result, a material of higher surface area gives way to an increased resistance. The use of binding material also affects conductivity; consequently, power performance is improved with a decreased percentage of binder [24].

The latter conclusion establishes the base of the investigation within this thesis. In this Chapter, I describe the studies on the fabrication of a new electrochemical cell based on hydrated ruthenium oxide ($RuO_2.xH_2O$) and activated carbon (AC). The hydrated ruthenium oxide is capable of generating higher capacitances than the anhydrous amorphous phase and it holds great promise as electrode material in supercapacitors [27]. The electrochemical cell I introduce are based on modified designs approaches [1-3]. Instead of reducing the percentage of binder used, I totally eliminate the binder, thereby enabling each particle of the electrode (activated carbon or hydrated ruthenium oxide) to be wetted by the electrolyte.

In order to keep the particles in place, the cell structure requires the use of acid resistant filter paper (glass fiber) to contain the electrode particles, to serve as separator and to soak-in the electrolyte. The use of acid resistant filter paper stamps from the fact that the solution employed is acidic (i.e. boric, nitric, phosphorous and sulfuric acids). This electrochemical capacitor cell structure enables efficient energy storage in a compact volume as well as an easy integration (in terms of “form, fit and function”) into arbitrarily designed sensor “motes”. The up-coming sections present the principals of my novel cell applied to multiple types of cells using various electrode materials, electrolyte composition, cell structures and packaging approaches.

2.6 Gold coated glass slide cells

2.6.1 Structure

The key component of the electrochemical cell was packaging; how to contain the sulfuric acid and the various powders as well as how to deposit the powder. The base structure on which the gold coated glass slide electrochemical cells were fabricated utilizes one electrode made out of silicon coated with gold while the other electrode is made out of a glass slide coated with gold. It was important to examine how well the powder electrode would perform on a planar structure.

Figure 12(a) and (b) offer schematics of the planar structure. Figure 12(a) presents the individual components of the electrochemical cell. On top of a silicon die coated with gold, a paste made-out of powder (ruthenium oxide and/or activated carbon) and sulfuric acid is smeared. Then filter paper (glass fibers) is place on the paste and impregnated with some more sulfuric acid, finally, a glass slide totally covered with gold is placed on the filter paper.

The gold layer is used to provide good conducting contacts and because gold is one of the rare metals that does not extensively react with sulfuric acid. Figure 12(b) shows how the cell is sealed. A non-conducting epoxy (wax) is used to seal the cell. It should be noted that the non-conducting epoxy actually covers all four sides of the cell (only three covered sides are represented in the illustration). The contacts to the electrolyte and the powder are provided on the side of the silicon die and on top of the glass slide (that is why the glass slide needs to be totally coated with gold to generate a conducting path between the front and back of the gold coated glass slide).

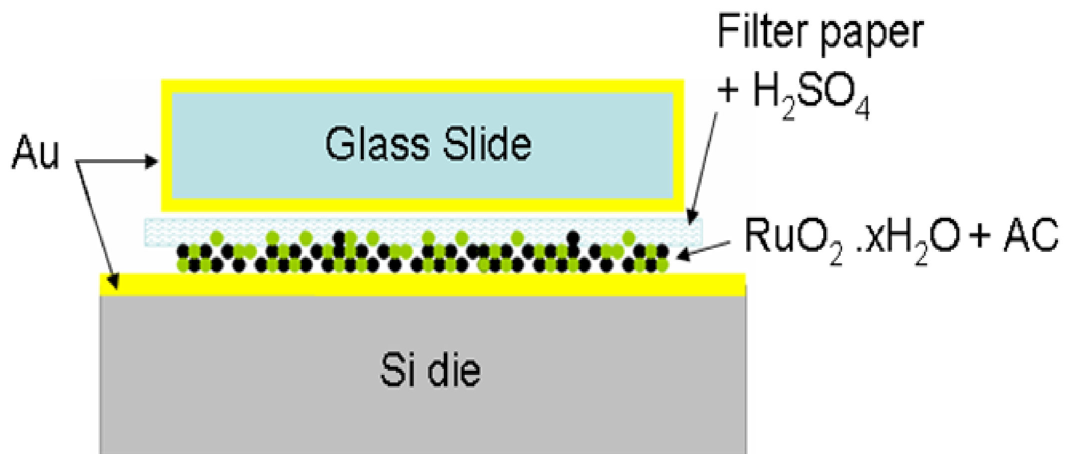

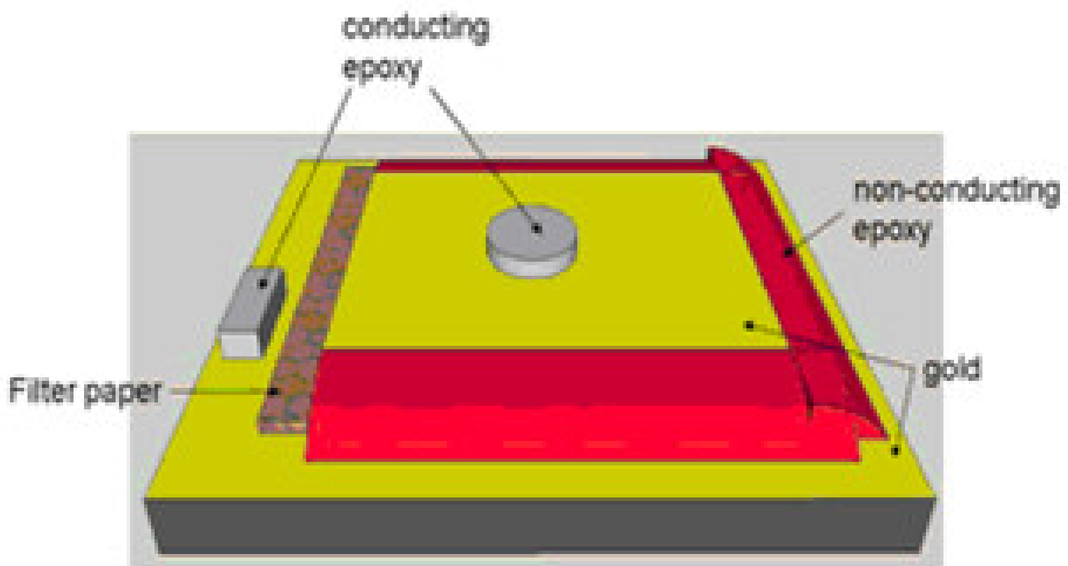

Figure 12: Planar electrochemical cell; (a) profile showing the interface; (b) overall structure of the device

The powder composition was varied to establish its effect on the overall capacitance. The powder composition for each device fabricated is tabulated in Table 1. Four types of devices were fabricated. *Mix 1* and *2* are devices where the powder used is a mixture of ruthenium oxide and activated carbon; with *Mix 1* having 10:1 composition by weight while *Mix 2* is 1:1 by weight. The other two devices AC and $RuO_2.xH_2O$ only have one compound; activated carbon and ruthenium oxide, respectively.

Table 1: Powder Composition

Device Name	**Powder Composition**
Mix 1	$RuO_2.xH_2O$ + AC (10:1 by weight)
Mix 2	$RuO_2.xH_2O$ + AC (1:1 by weight)
AC	AC (active carbon) only
$RuO_2.xH_2O$	$RuO_2.xH_2O$ only

2.6.2 Characteristics

Constant current charging results

The four devices described in Table 1 were measured via current charging. The resulting plots are shown in Figure 13 and Figure 14. Plots in Figure 13(a) and (b) have the same shape as Figure 9(b). This provides evidence for the capacitive nature of devices *Mix 1 and 2* (mixture of ruthenium oxide and activated carbon). The plots resulting from devices containing only AC or ruthenium oxide, Figure 14(a) and (b) respectively, show weak capacitive behavior. The largest capacitive values were obtained for *Mix 1 and 2*.

Cyclic Voltammetry (CV) results

The scan rate used for the CV measurements was 20mV/s. I found that device capacitance extracted from CV measurements is typically greater as the scan rate is decreased. My scan rate is, however, much larger than scan rates commonly reported in literature [23, 28]. The average capacitance was determined from the cyclic voltammetry plots using Equation 13

$$C = \frac{\Delta I}{S} \tag{8}$$

where S represents the scan rate ($\Delta V/\Delta t$) and ΔI the average current at a set potential value which, in my experiments, is the same as the voltage between the two electrodes of the device. CVs were recorded in two-electrode geometry, with the working entrance of the instrument connected to the electrode in contact with ruthenium oxide, while the counter and reference entrances were connected to the gold layer in contact only with the sulfuric acid. Scans were acquired in the potential range from -0.8 to +0.8 V versus the counter electrode. Typical voltammograms are shown in Figure 15.

The capacitive values for all four devices and their internal series resistance are tabulated in Table 2. The area (cm^2) used for approximating the capacitance per unit area is the projected geometric surface area (rather than effective surface area).

Table 2: Summary of calculated capacitance values

Device Name	Capacitance from I charging [mF/cm^2]*	Capacitance from CV [mF/cm^2]*	Internal Series Resistance [Ω]
Mix 1	27.5	50	500
Mix 2	3	4.5	18
AC	1.2	2.2	510
$RuO_2.xH_2O$	0.2	0.3	1000

* Projected geometric area.

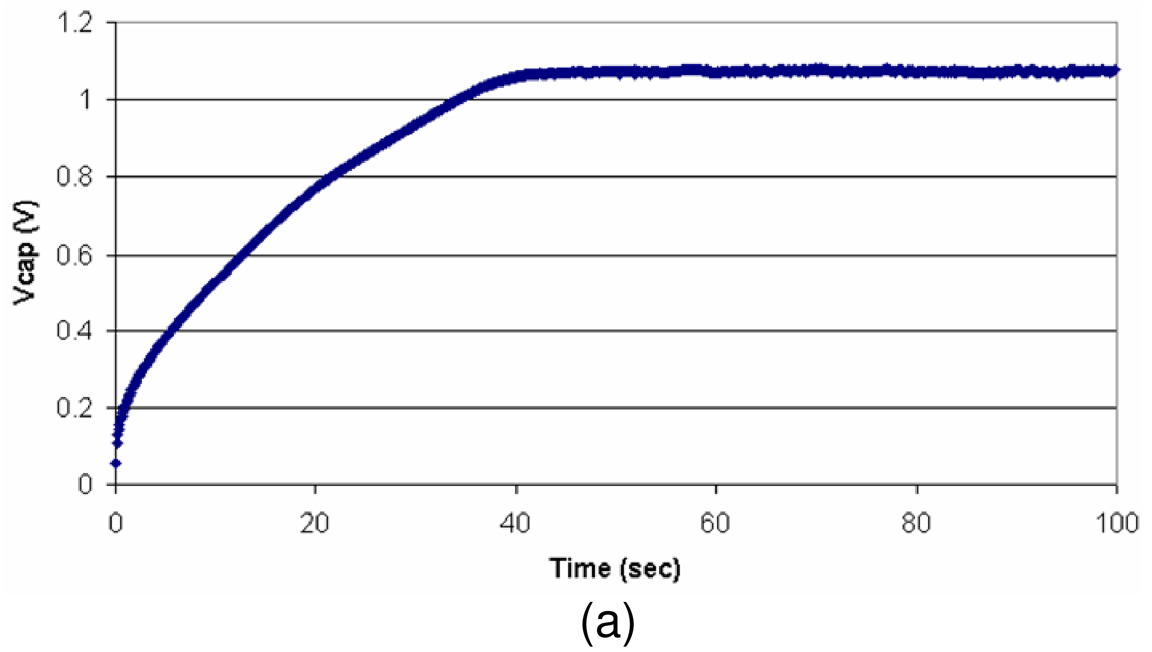

(a)

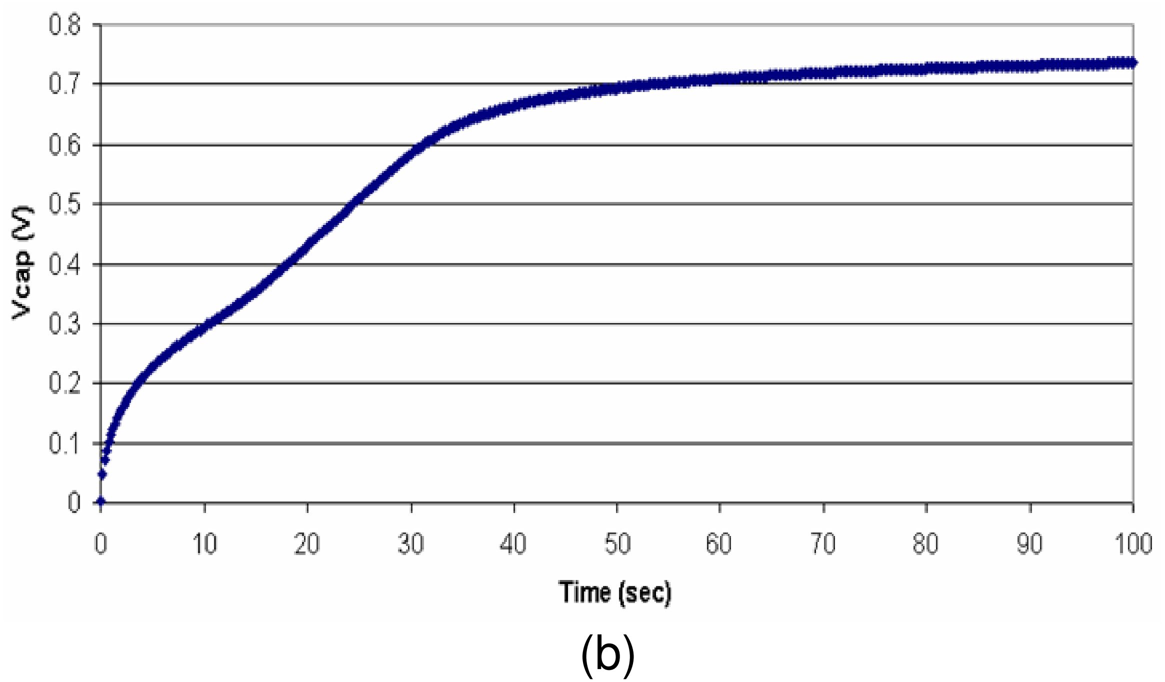

(b)

Figure 13: Voltage vs. time plots from constant current charging; (a) Mix 1 device; (b) Mix 2 device.

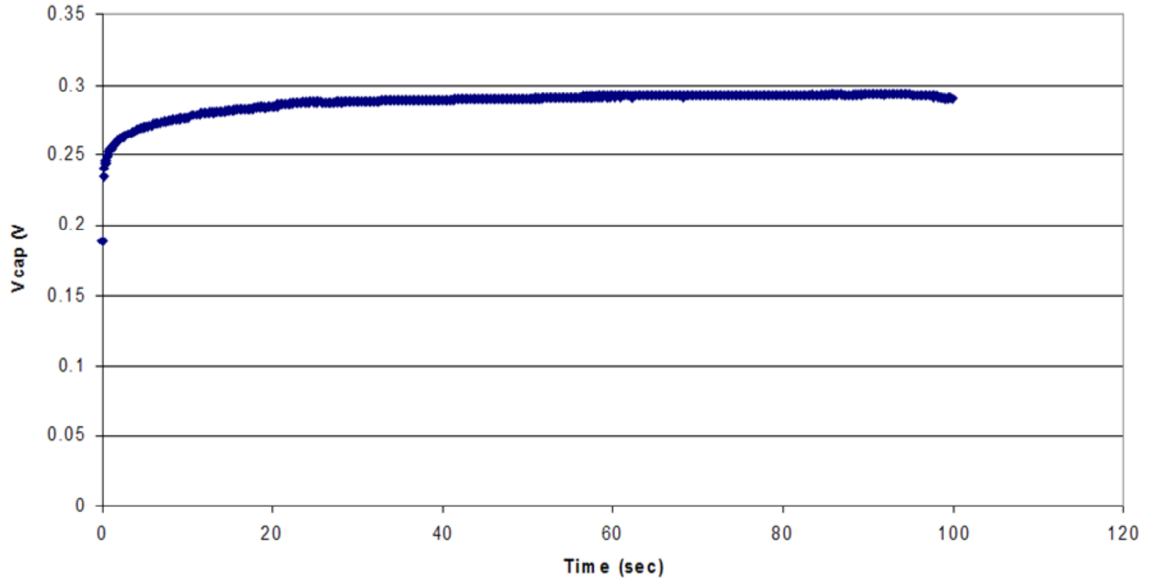

(a)

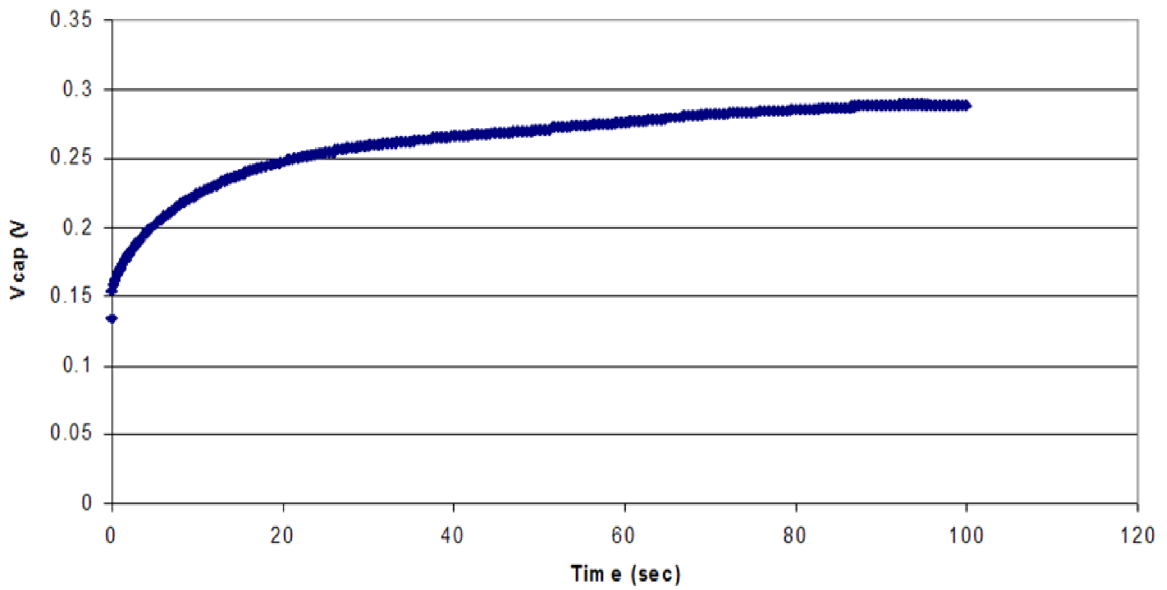

(b)

Figure 14: Voltage vs. time plots from constant current charging; (a) Activated carbon device; (b) Ruthenium oxide device.

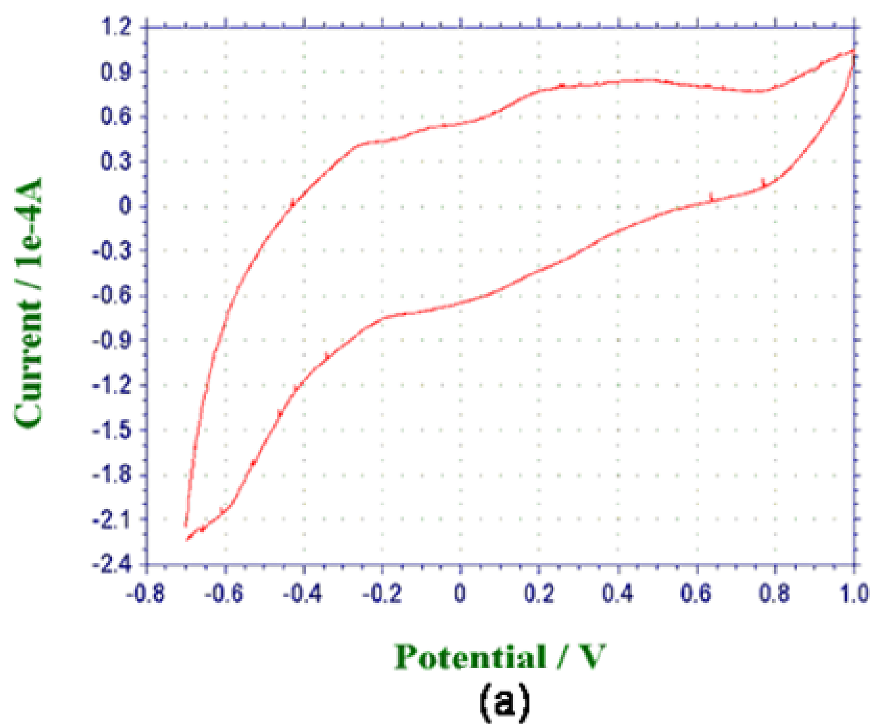

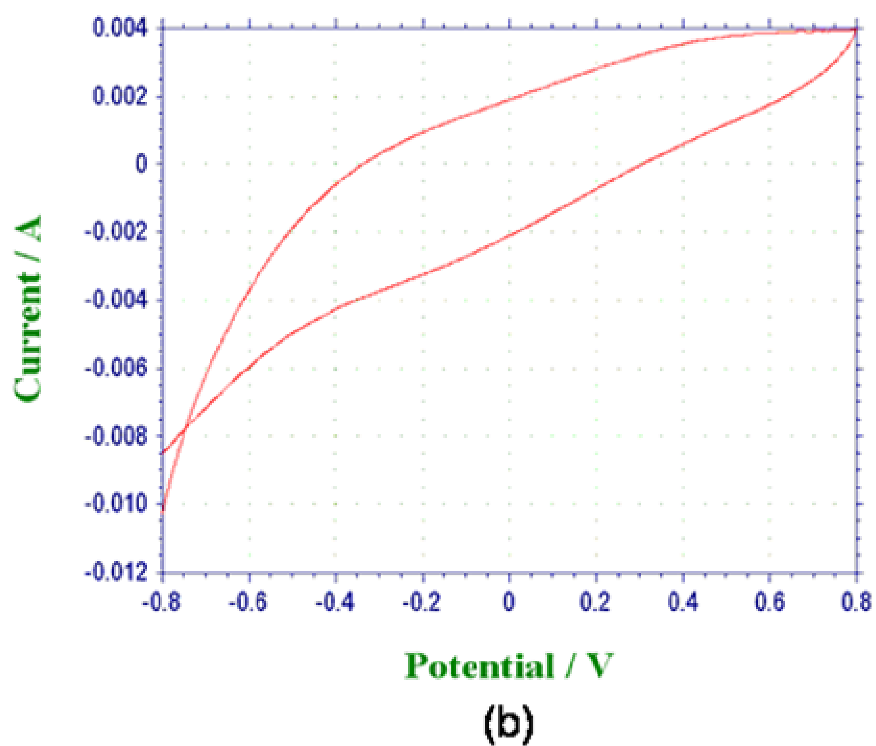

Figure 15: Voltammograms of samples (a) Mix 1 (10:1 $RuO_2.xH_2O$ and AC), (b) Mix 2 (1:1 $RuO_2.xH_2O$ and AC) measured at 20 mV/s

2.6.3 Discussion

From results in Table 2, the following conclusion can be drawn on the capacitance value relative to the composition of the powder [1]:

- $RuO_2.xH_2O$ + AC; 10:1, w/w (Mix 1) Lead to the device with the greatest capacitance
- $RuO_2.xH_2O$ + AC; 1:1, w/w (Mix 2) Lead to device with a "Good" capacitance
- AC only devices had moderate capacitance
- $RuO_2.xH_2O$ only devices had a very low capacitance

The capacitance of the electrochemical cells especially for Device Mix 1 is quite high because of the nature of the cell. An equivalent circuit of the electrochemical cell is shown in Figure 16(a) while Figure 16(b) illustrates some of the internal interactions in the cell. The capacitance of Mix 1 is high because the device is an asymmetric cell, as opposed to the conventional approach, with identical electrodes. The conventional approach is based on a design which leads to two capacitors in series. In this arrangement, the maximum capacitance is half the capacitance of one electrode, provided that the two electrodes are perfectly matched.

I bypass this drop in capacitance by creating just one electrode, for which the capacitance is C. This resulting capacitance is at least twice that of an equivalent symmetric device. The second metal is in contact with the electrolyte and at that metal a redox reaction occurs. This can be noted in the CV plots by the peaks in both forward and reverse sweeps (which correspond to oxidation and reduction, respectively). The redox reaction is represented in the equivalent circuit by the V_i

voltage source. In the hypothesized cell mechanism presented in Figure 16, the $RuO_2.xH_2O$ is oxidized at the gold interface by the presence of the sulfuric acid. Then, ionic motion carries charge to the counter electrode where a reduction occurs. The asymmetric nature of the electrodes enables the presence of such a redox reaction within the cell.

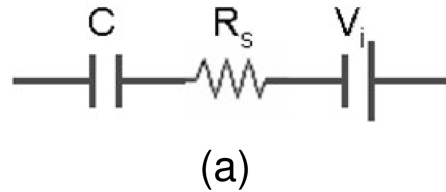

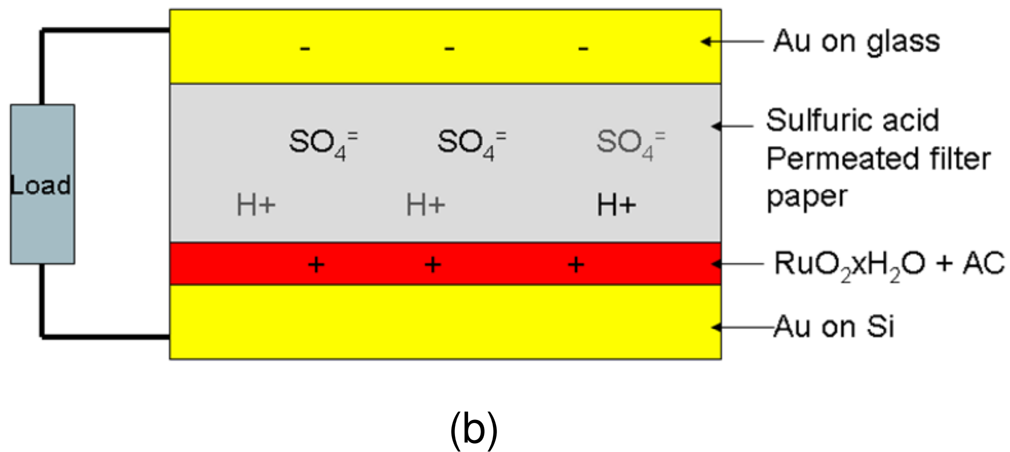

Figure 16: Hypothesized cell mechanism (a) Equivalent circuit, (b) Cell layer interaction

Furthermore, the redox reaction was confirmed experimentally. Once the devices were assembled and prior to any form of charging, a voltage of 120 to 200 mV could be recorded across the device terminals. Furthermore, once charged and then left unloaded for multiple weeks, the device voltage settles back to that original voltage. Multiple cells can be stacked either in series or in parallel to increase the driving strength of the system.

There is an interaction between ruthenium oxide and activated carbon since the mixed devices yield much greater capacitance values than the single compound devices. As the amount of hydrated ruthenium oxide increases (greater amount in the weight ratio) the capacitance value increases. That is evident by the *Mix 1* (10:1 by weight) devices having greater capacitance values than *Mix 2* devices (1:1 by weight). One difficulty with the cell structure presented in Figure 12 is packaging. With time, the non-conducting epoxy (wax) gave way and the electrolyte leaked out of the cell. In addition, getting reliable gold coverage along the side of the glass slide prove to be problematic. The next section covers the subsequent cell structure use to circumvent the packaging concerns.

2.7 Gold coated aluminum cells

2.7.1 Structure

In addressing some of the challenges posed by the gold coated glass slide cells (wax failure and low conduction of leads) a gold coated aluminum cell was developed. An illustration of the cell structure is presented in Figure 17. As solution, the wax was replaced by an acid resistant paint (ABOCOAT 8501-1 from Abatron, Inc.) and the glass slide replaced by aluminum sheet coated with gold. The acid resistant paint (epoxy) was used to seal the four corners of the cell. Once cured (over a period of 2 days at room temperature), the epoxy was dry to the touch and rigid.

The gold layer was applied to protect the aluminum sheet from being attacked by the sulfuric acid (electrolyte). The aluminum leads also enable easier electrical contact (biasing) of the electrolyte since the charges could be conducted straight through the electrode as oppose to along the surface as was the case with the gold

coated glass slide electrodes. The ease in conductivity favored a stacking of multiple cells within a single package. Three different types of devices were fabricated (single cell, *T1*, double stacked cell, *T2*, and triple stacked cell, *T3*). Figure 18 shows the schematic of triple stacked cell sealed on all four sides by the acid resistant paint.

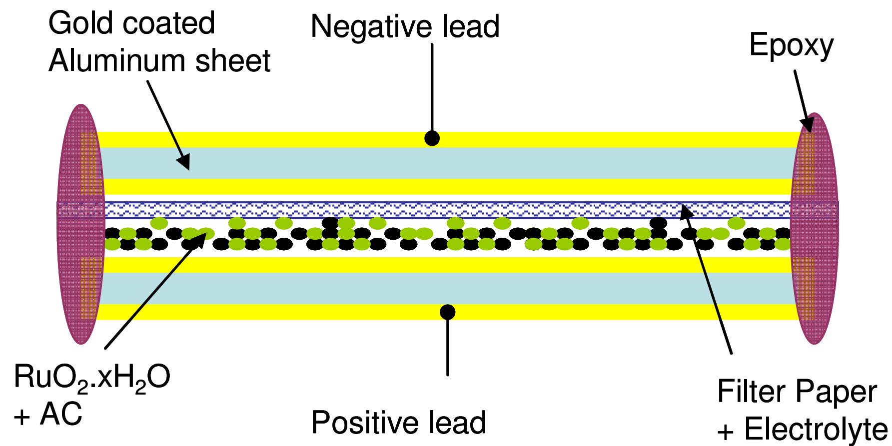

Figure 17: Schematic of gold coated aluminum cells

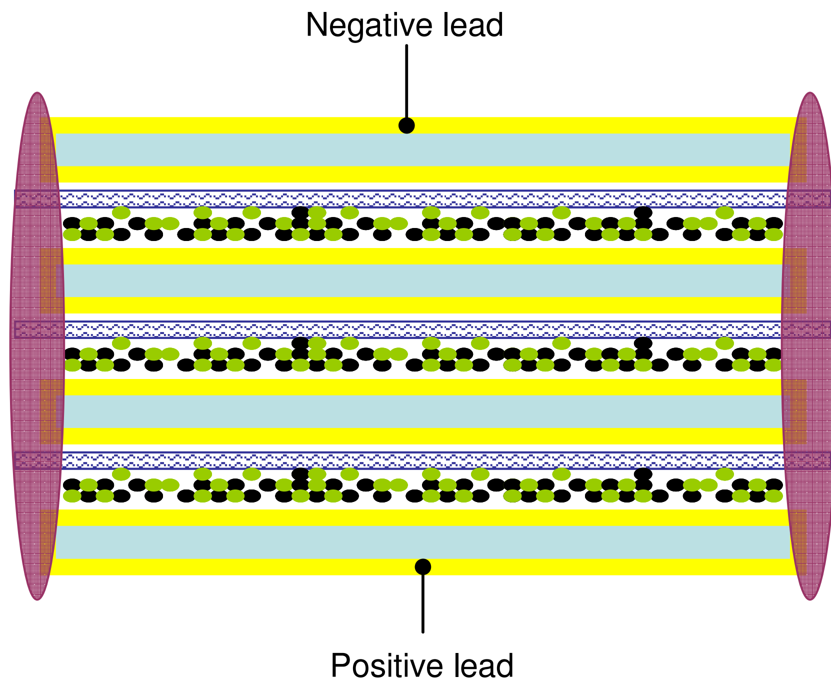

Figure 18: Schematic of triple stacked gold coated aluminum cells

2.7.2 Characteristics

The cells are, effectively, connected in series within the stacked devices. The open circuit voltage (V_{OC}, no load attached across the leads) of each device is different. Using a voltmeter, the open circuit voltages were determined for each of the devices and tabulated in Table 3. The three types of cells were voltage charged according to the setup describe in Figure 10. The charging period lasted 60sec and the charging voltages for *T1*, *T2* and *T3* were 0.9V, 1.8V and 2.8V, respectively. The charging voltage applied in all cases was different because the greatest concern in determining the charging voltage is to make sure that at the applied voltage the electrolyte (sulfuric acid) does not break down and form hydrogen and oxygen gas. In a single cell, this would occur at voltages higher than 1V; to be on the safe side, 0.9V was considered and multiple of that number were taken for the multiple cell devices.

Once the devices were charged for 60sec, they were discharged through a 10KΩ resistive load. The resulting voltage versus time plot is displayed in Figure 19. Figure 20 offers a comparison of the self discharge nature of the cell and the resistive load discharge (10KΩ). In the legend, the suffix *Self* and *Load* identify self discharge and load discharge, respectively. In all cases, the cells are charged at the potential determined earlier.

Table 3: Open circuit voltage of gold coated aluminum cells

Cell Name	T1	T2	T3
V_{OC} (V)	0.45V	0.89	1.40V

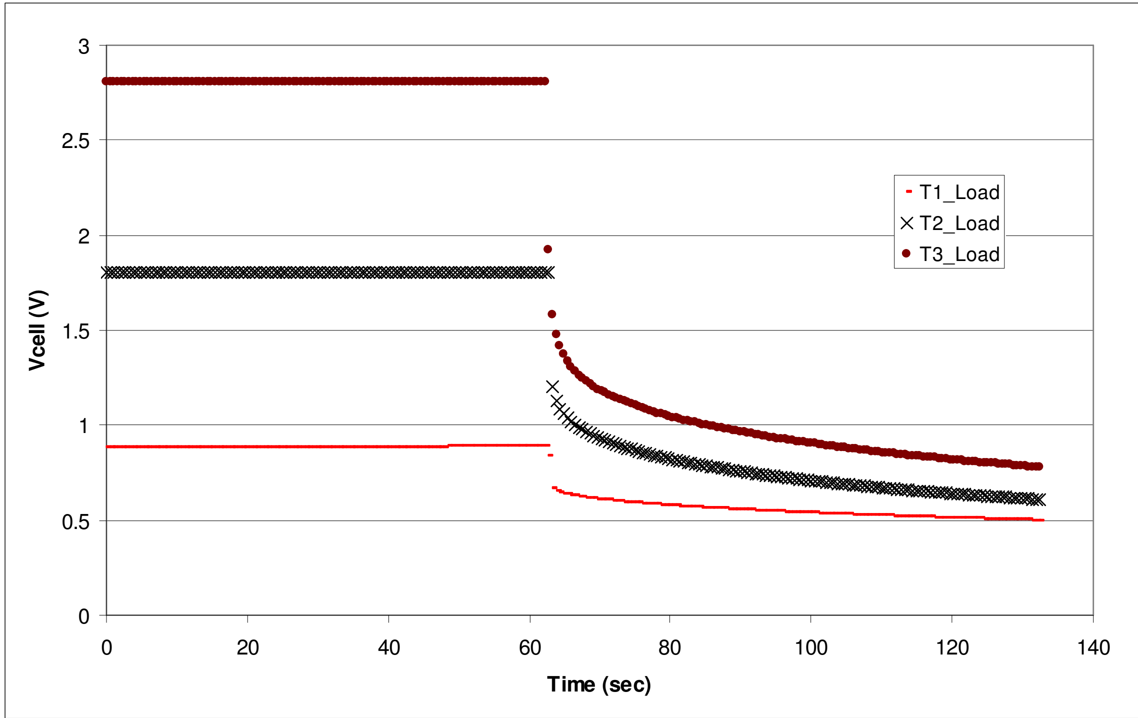

Figure 19: Voltage versus time plot of voltage charged cell then resistively discharged through 10KΩ resistive load.

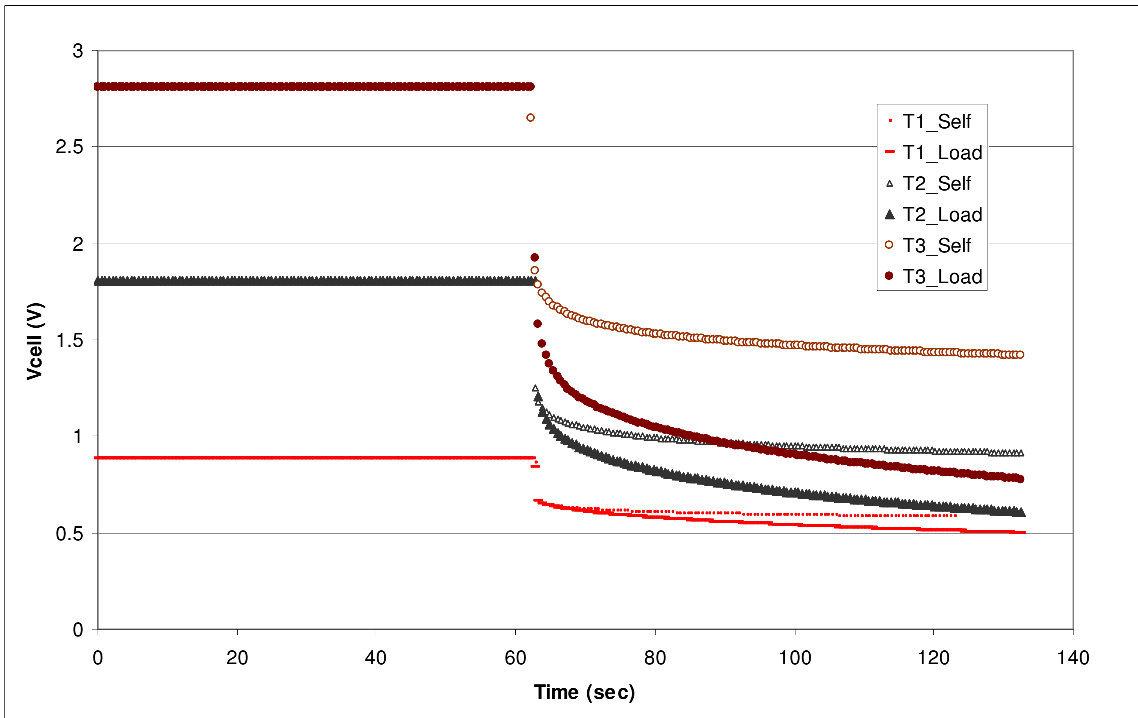

Figure 20: Voltage versus time plot of voltage charged cell then resistively discharged through 10KΩ resistive load and self discharged.

2.7.3 Discussion

From the open circuit voltage of the different devices (see Table 3) one can notice that the potential of the stack cell does add up as one would expect from cells in series. The increase in device voltage is accompanied by a reduction in device volume relatively to having individual cells connected in series. The volume reduction is due to the fact that stacked cells used less gold coated aluminum sheets compare to the number required for an equivalent number of individual cells. For instance, *T3* uses four gold coated aluminum sheets (see Figure 18) as opposed to six sheets for an equivalent three individual cells in series. The devices can be charged and then discharge through a load as seen in Figure 19. The direct comparison of a charged devices' discharge through a resistive load and via internal leakage is illustrated in Figure 20 where the load discharge plots are all lower than the self discharge plots. This points towards energy storage during charging. However, the cells have a considerable amount of leakage.

The gold coated aluminum cell display some interesting initial potential. The initial potential that is observed right after the device is assembled is due to redox reactions occurring within the cell. Unfortunately, the reactions involve the aluminum layer. The aluminum sheet is not well protected by the layer of gold. This is because the gold layer is not thick enough and the gold and aluminum did not bound well (gold pilling-off). In order to resolve these obstacles, a conducting material non-reactive with sulfuric acid needs to be used as cell electrode and / or the electrolyte needs to be changed to one less corrosive. These two approaches were investigated via the use of various less corrosive electrolytes and the use of graphite sheets. The weaker electrolytes also made it possible to use zinc sheets in the cell. The following

section looks at the graphite-zinc cells. With the Graphite based cells, I targeted battery behavior of the cell as oppose to the capacitive behavior of the (as was the case with the two cells presented in the previous two sections).

2.8 Graphite-Zinc cells

2.8.1 Structure

The study on my new Graphite-Zinc electrochemical energy cell (battery), based on a powdery mix of hydrated ruthenium oxide ($RuO_2.xH_2O$) and activated carbon (AC), yielded great results. One of the challenges presented by the gold coated aluminum cell is the sub-optimal performance of the gold coat which leads to the sulfuric acid corroding the aluminum. To overcome this hurdle, I fabricated the graphite-zinc cell utilizing a weaker electrolyte (so the zinc will not corrode).

The cell is implemented via the use of asymmetric electrodes; the asymmetry is both in material and electrolyte interface (see Figure 21). The electrode materials are zinc and graphite sheets. The graphite electrode is covered with a mixture of hydrated ruthenium oxide and activated carbon with 5 drops of electrolyte (drops dispensed with Fisherbrand transfer pipets *cat No 13-711-9A*) to form a paste. Each drop of dispensed electrolyte is approximately $5/30^{th}$ of a milliliter. A glass fiber filter paper is used as separator; it is impregnated with 5 or 10 drops of electrolyte depending on the cell. The entire cell is contained within a Lexan package that is acid resistant and sealed using its adhesive layer, and then the edges of the cell are melted shot with Methylane Chloride to ensure that nothing leaks out. The cell stacking approach described in the previous section was modified according to Figure 22. Inside the

cell, the contact between the zinc and graphite sheet is established via mechanical pressure exerted by the packaging.

Various electrolytes were investigated based on varying concentration of ethylene glycol, ammonium hydroxide, boric acid, nitric acid, de-ionized water and phosphorous acid, see Table 4. The ammonium hydroxide solution used for E0-6 has a concentration of 20% (~ 7% ammonia to 93% water, by % weight). The boric acid (crystals) was dissolved in water (5g in 100cc for a pH 5) and the citric acid was 3mg/ml. All the electrolyte mixtures were conducted at room temperature.

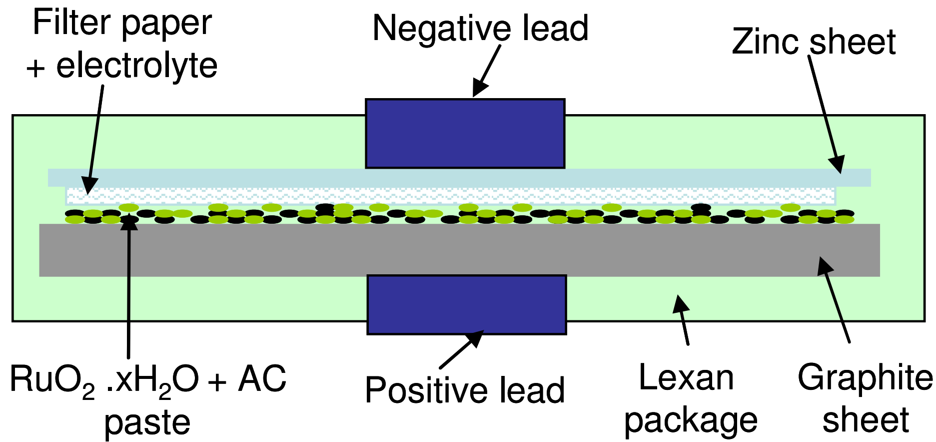

Figure 21: Schematic of graphite-zinc single cell.

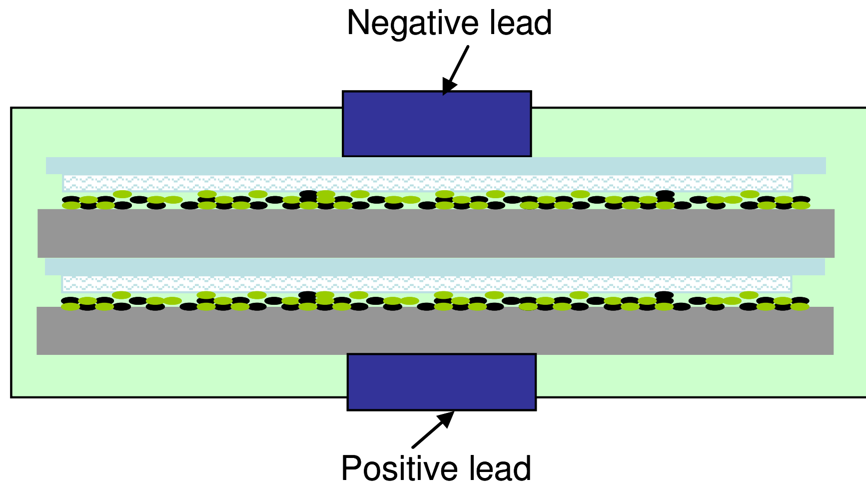

Figure 22: Schematic of graphite-zinc double stacked cell.

The picture of a graphite-zinc cell is displayed in Figure 23. The side shown in the picture is the graphite side. The cell has leads attached to the both electrode by means of conducting epoxy (cured at room temperature). The effective active area of the cell (location of the powder paste) is circled in Figure 23. The white contour around the graphite sheet is the filter paper extending beyond the graphite sheet to ensure that the electrodes do not touch each other.

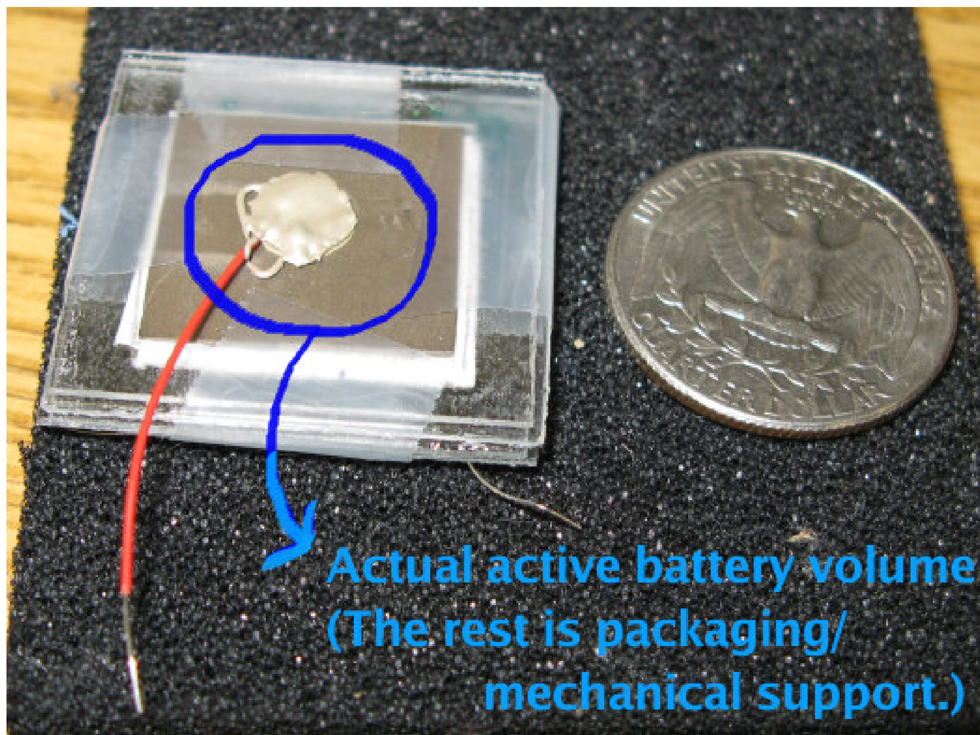

Figure 23: Picture of a Graphite-Zinc packaged cell.

Table 4: Electrolyte composition (in percent per volume)

	Electrolyte0 (E0)	Electrolyte1 (E1)	Electrolyte2 (E2)	Electrolyte3 (E3)	Electrolyte4 (E4)	Electrolyte5 (E5)	Electrolyte6 (E6)	Electrolyte7 (E7)
Ethylene Glycol	80%	32.7%	32.7%	32.7%	32.7%	32.7%	32.7%	25%
Ammonium Hydroxide	5%	1%	1%	1%	1%	1%	1%	4%
DI Water	0%	60%	57%	52%	60%	57%	52%	65.6%
Boric Acid (Chrystal)	10%	7%	10%	15%	0%	0%	0%	0%
Citric Acid	5%	0%	0%	0%	0%	0%	0%	0%
Phosphorous Acid	0%	0%	0%	0%	7%	10%	15%	5.4%
PH	5	6	6	5	1	1	1	4

2.8.2 Characteristics

A set of cells were made with the electrolytes E0-6 and their open circuit voltage were measured. The resulting potential across these cells over a period of 43 days are recorded in Table 5. In this table, the device naming nomenclature is as follows; ExGZy, where Ex identifies the electrolyte used (i.e. E0-6), GZ refers to the fact that it is a Graphite-Zinc cell and y is the number of the cell. The data in Table 5 shows that not all cells maintain their original potential or maintain a constant potential over weeks beside cells E0GZ6 and E1GZ1. Cell potential identified by --- corresponds to V_{OC}s' that were too unstable to be measured.

As a result, most of the Graphite-Zinc cells analyses were conducted on devices made with either electrolyte E0 or E1. The double stacked cell devices were only made with electrolyte E0. All of the E0 and E1 based cells kept a stable open circuit voltage beyond the 45 days mentioned in Table 5. In fact the first graphite-zinc cells have been operational for about 8 months now.

Table 5: V_{OC} of devices made with electrolyte E0-6

Cell Name	Day 1	Day 7	Day 37	Day 43
E0GZ6	1.12V	1.10V	1.10V	1.10V
E1GZ1	1.16V	0.88V	0.87V	0.88V
E2GZ1	1.24V	0.59V	---	---
E3GZ1	1.20V	1.04V	0.49V	---
E4GZ1	1.36V	1.27V	1.04V	0.86V
E5GZ1	1.34V	1.30V	0.87V	0.73V
E6GZ1	1.35V	1.11V	---	---

Additional single and double stacked devices were fabricated using electrolyte E0. Theses devices were subjected to the following tests:

- Self discharge: The potential across the cell is measured periodically with no load attached (V_{OC} measurements). This was done with fresh cells, cycled cells and charged cells.

- Overpotential measurement: This is a shift in the potential across the electrode from its equilibrium value (V_{OC}) as a result of current flow. This occurs when a resistive load is placed across the leads of a cell.

- Cell charging: A constant current is applied to the cell and the voltage across it is monitored. For an ideal capacitor, the voltage will first increase linearly before saturating at its working potential.

- Load discharge: A load is attached across the cell and the potential is monitored. This was done with fresh cells (just fabricated), cycled cells (previously load discharged) and charged cells (current charged and voltage charged).

<u>Self-Discharge</u>

The potentials obtained from the self discharge of the E0 based cells over multiple weeks are tabulated in Table 6. In the table, the "fresh" single cell is a cell that was never subjected to any load discharge or current charging, while the "tested" cells have been subjected, multiple times, to both current charging and load discharges. The potential across each cell remains very stable over multiple weeks

even for the multiply-tested cells. The potential across the double stacked cells starts at 1.60V which is less than the voltage across two cells in series. Overtime, the voltage across the stacked cell drops very drastically compare to single cells. The low voltage and the subsequent drop over time is attributed to the fact that the electrolyte is migrating from one part of the cell to the other such that overtime all the electrolyte would have made its way to one side (bottom cell).

Table 6: Self discharge / V_{OC} of single and double stacked cell using electrolyte E0

Cell Type	Day 1	Day 7	Day 14	Day 22	Day 31
Single (fresh)	1.18V	1.19V	1.19V	1.17V	1.15V
Single (tested)	1.13V	1.05V	1.09V	1.08V	1.11V
Double Stacked (tested)	1.60V	1.57V	1.36V	1.36V	1.25V

Overpotential

It was noticed that higher electrolyte amount reduces overpotential drop and increases amount of energy delivered to a load. This is most evident in Figure 24 where the shift in voltage across cell E0GZ7 and E0GZ8 as a result of current flowing through an attached load is shown. The plot at the bottom left is that of E0GZ7 while the one at the top right is that of E0GZ8. The difference between the two cells is that E0GZ8 has more electrolyte solution, 5 drops to make up the paste and 10 drops to wet the filter paper for a total of 15 drops, as opposed to the E0GZ7 cell that has a total of 10 drops (5 for the paste and 5 in the filter paper). To observe the cell overpotential response for different loads, the following procedure was used:

1. Measure potential across the device with no load for about 60 seconds
2. Attach a resistive load, measure potential for 30-60 seconds

3. Remove the resistive load, measure potential for about 60 seconds
4. Attach the next load and repeat.

Since the “discharge” period is very short the cells’ potential comes back up to their original level (cell regenerates) prior to the next discharge. Only single cells made with electrolyte E0 and E1 (E0GZ8 and E1GZ1) were tested and the cells’ overpotential plots are shown in Figure 25 and Figure 26; respectively. In each figure, the load attached during that time period is written below the corresponding drop in voltage. It should be noted that all the cells are able to supply higher current for lower loads, even though the overpotential drop is higher for lower loads. A comparison between Figure 25 and Figure 26 demonstrates that cell E1GZ1 recovers slower than E0GZ8. However, E1GZ1 exhibits much lower overpotential drop (difference in voltage across a device while it is resistively loaded and not loaded).

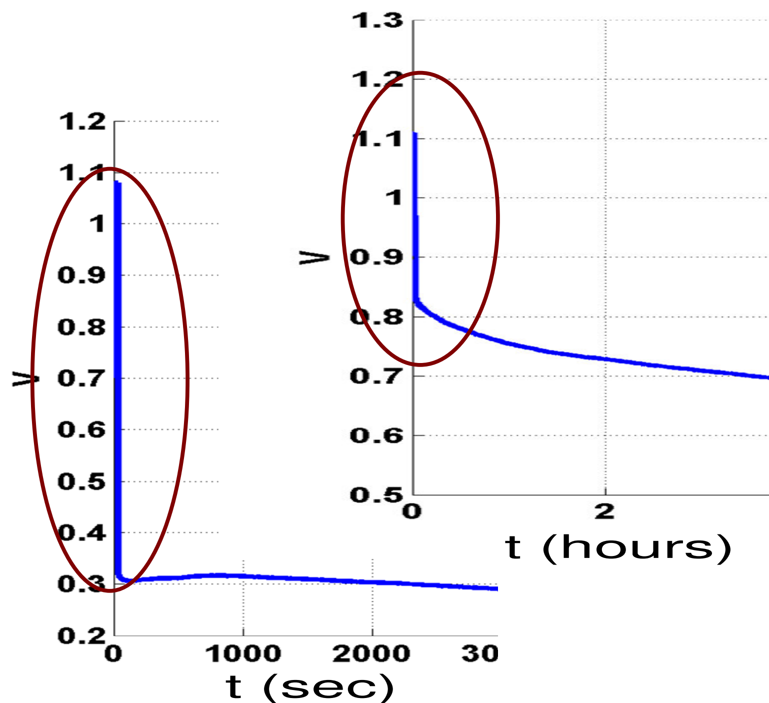

Figure 24: Overpotential dependence on amount of electrolyte given identical load; bottom left E0GZ7 (10 drops of electrolyte); top right E0GZ8 (15 drops of electrolyte)

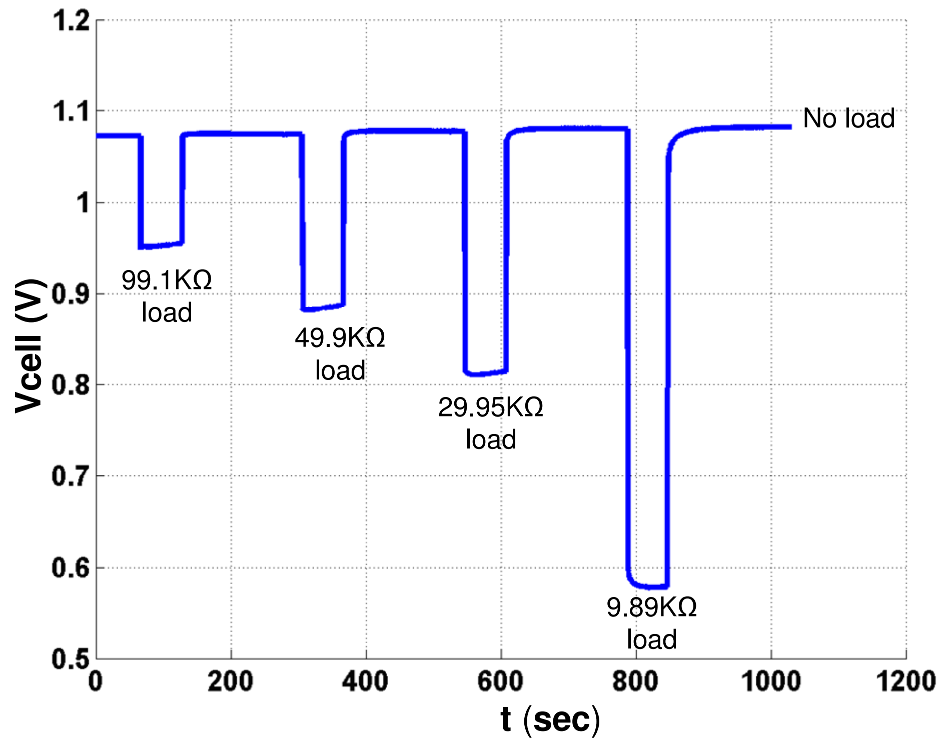

Figure 25: E0GZ8 overpotential drop at varying resistive loads

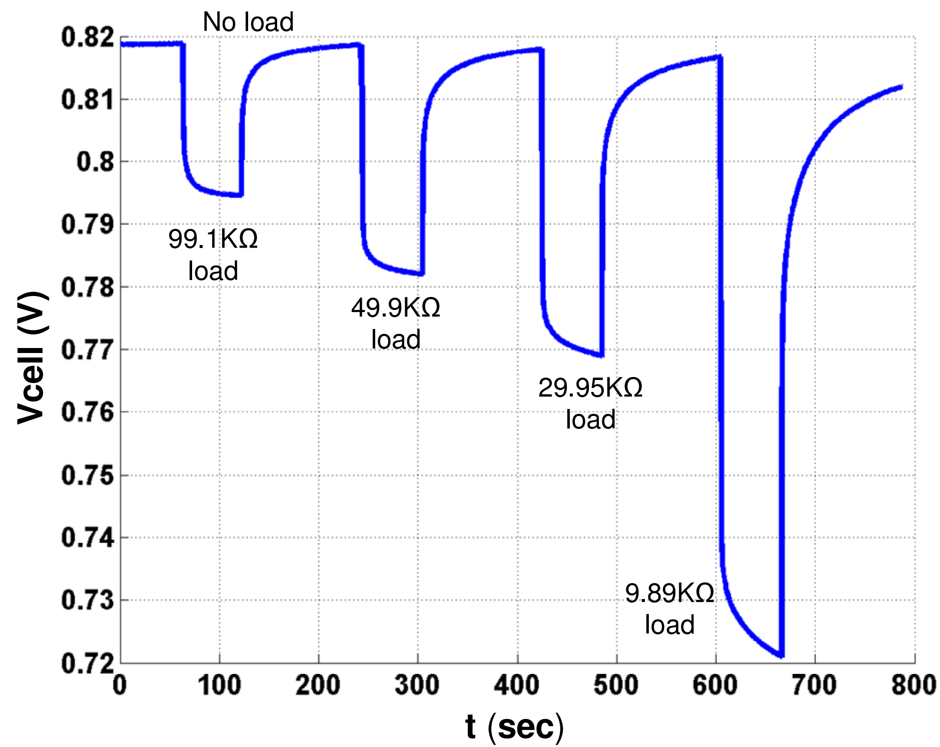

Figure 26: E1GZ1 overpotential drop at varying resistive loads

Cell Charging / Discharging

Current charging and resistive load discharging tests were conducted. A constant 100µA current was applied to the cell. Once the source was removed and the cell potential would decrease (leakage) then “stabilize”. Figure 27 illustrates this observation by representing the cell’s potential during constant charging followed by the relaxation period (no load). The cell capacitance was estimated from the slope od the charging potential to be about 4.5F.

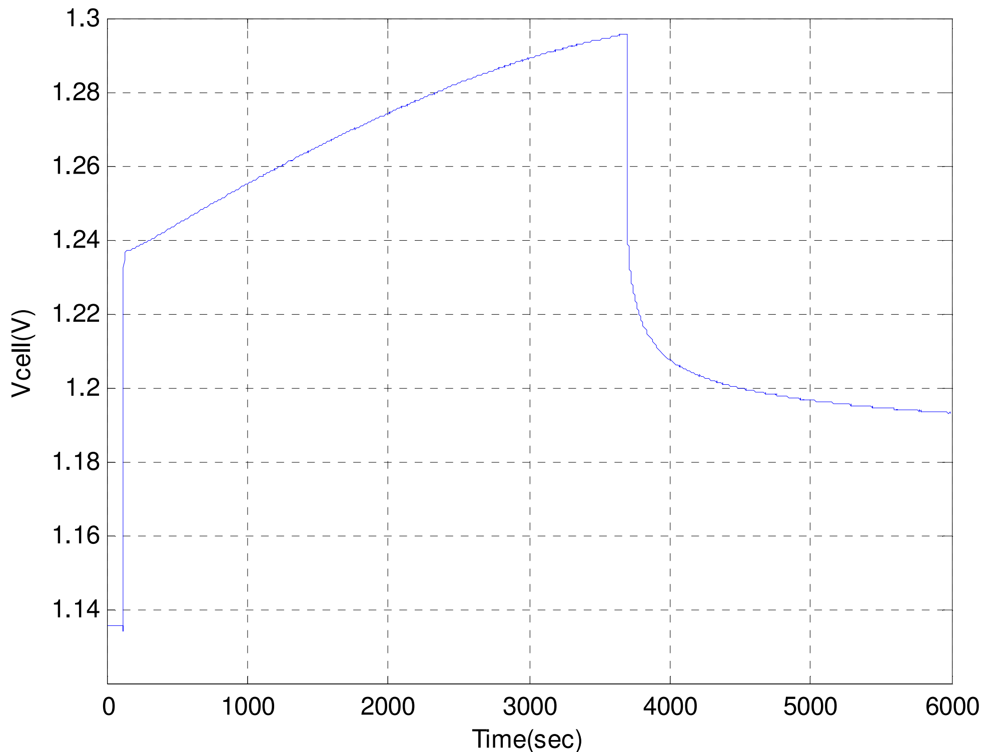

Figure 27: Cell E0GZ7 charged with 100µA for 1 hour then discharged

Cell E0GZ8 was discharged with a 100KΩ load; the resulting plot is presented in Figure 28. The initial voltage of the cell is 1.2V and the cell potential during discharge is monitored for $2^{1/2}$ hours. At a later time, the same run was done with a

10KΩ load; the result is plotted in Figure 29. In both runs, while discharging the cell, I have observed cell regeneration. In Figure 28, the potential across the cell drops below 0.75V during discharge and with the load still connected, the potential rises and remains around 0.8V for more that an hour. The same behavior is displayed in Figure 29 under 10KΩ load discharge.

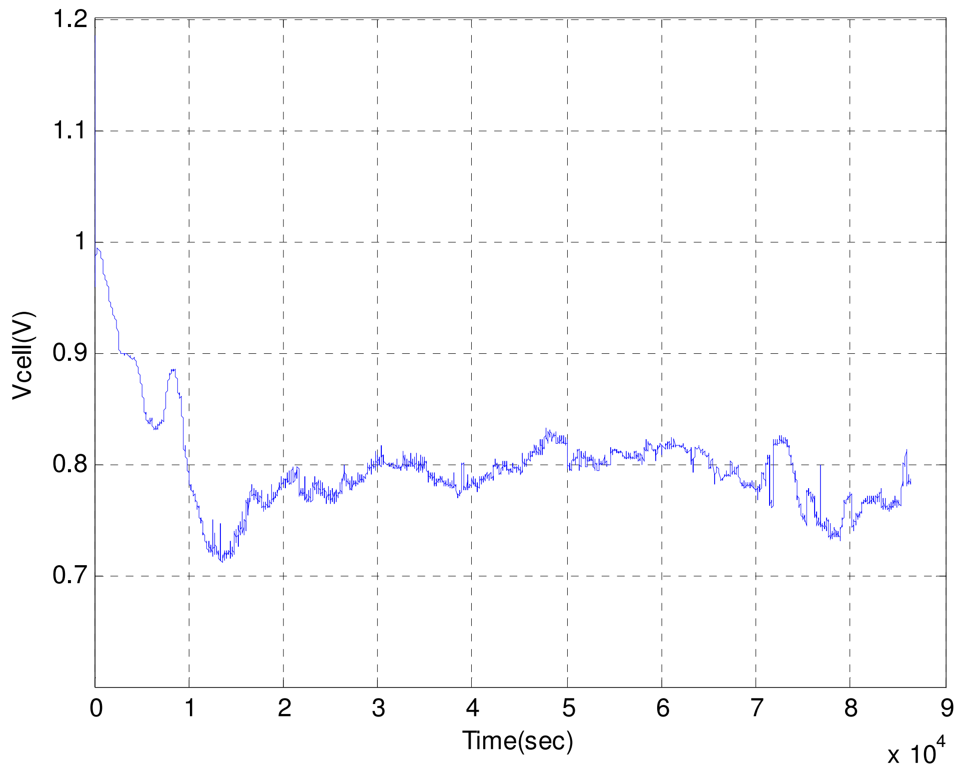

Figure 28: **Single graphite-zinc cell 100KΩ load discharge**

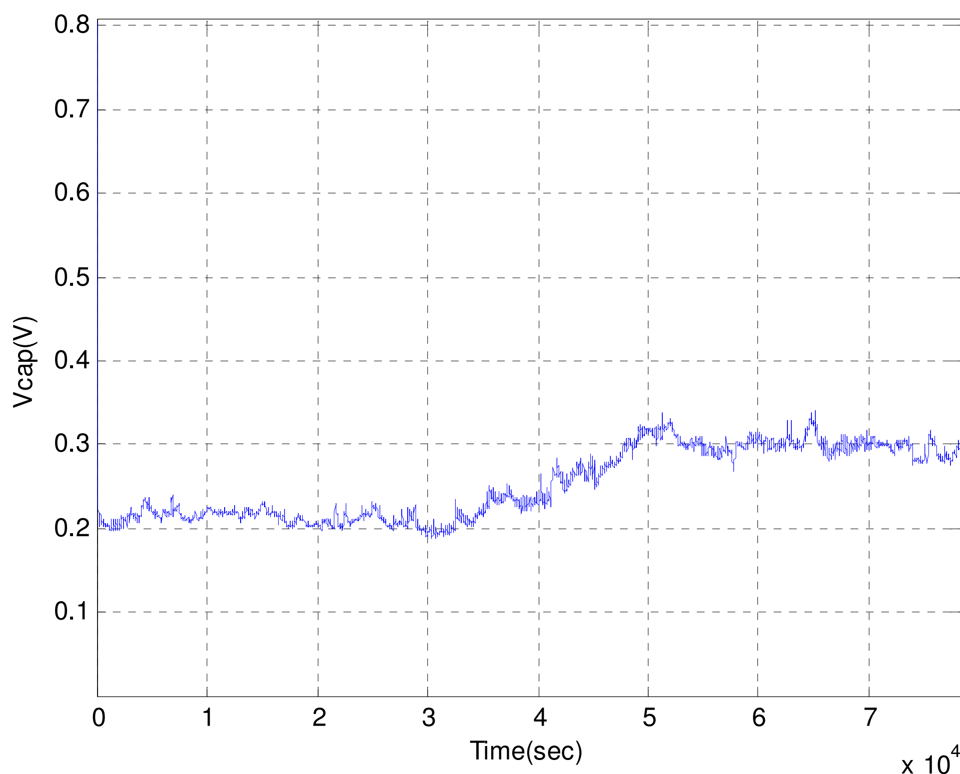

Figure 29: Single graphite-zinc cell 10KΩ load discharge (experience self-recharge)

An electrolyte E0 based double stacked cell was discharged with a 100KΩ load and 5KΩ load and the recorded cell discharge potentials are shown in Figure 30 and Figure 31; respectively. In Figure 30, the discharge was conducted after a 60sec 100μA current charging. During current charging, the potential across the cell increases to 1.8V. Once the 100KΩ load is connected and the current source is disconnected, the cell potential stays above 1.6V (internal potential presented in Table 6 on Day 1) and then decays. For the data in Figure 31, no prior charging of the cell was conducted and the initial voltage of the cell was 1.6V.

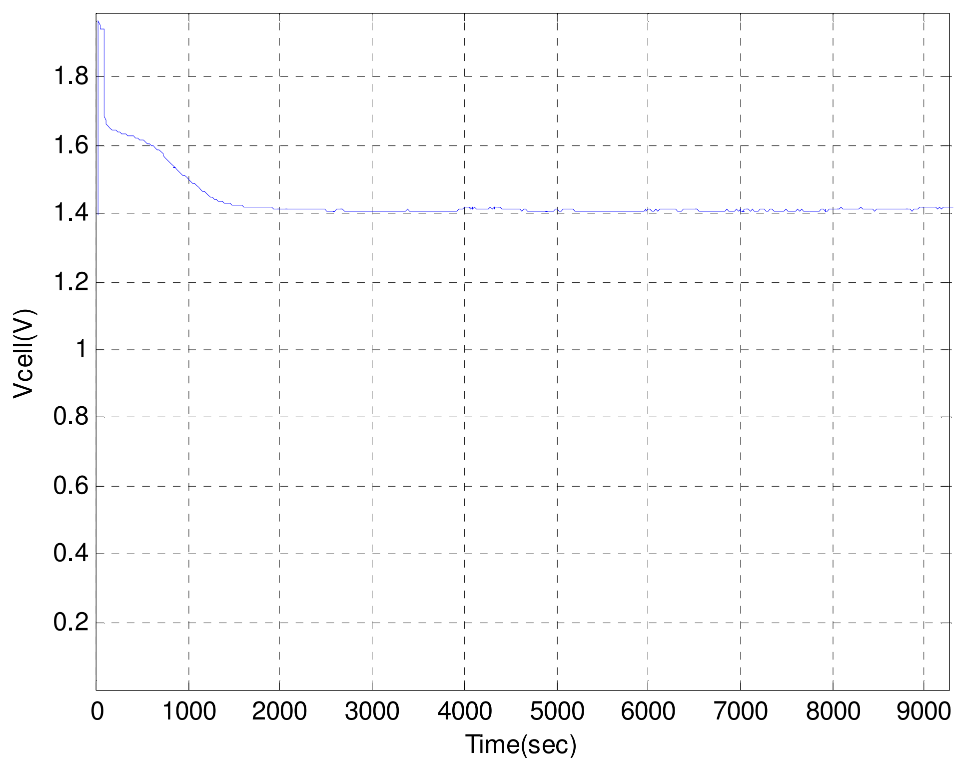

Figure 30: Double stacked graphite-zinc starts with 100µA charging (for 30sec) followed by self-discharge

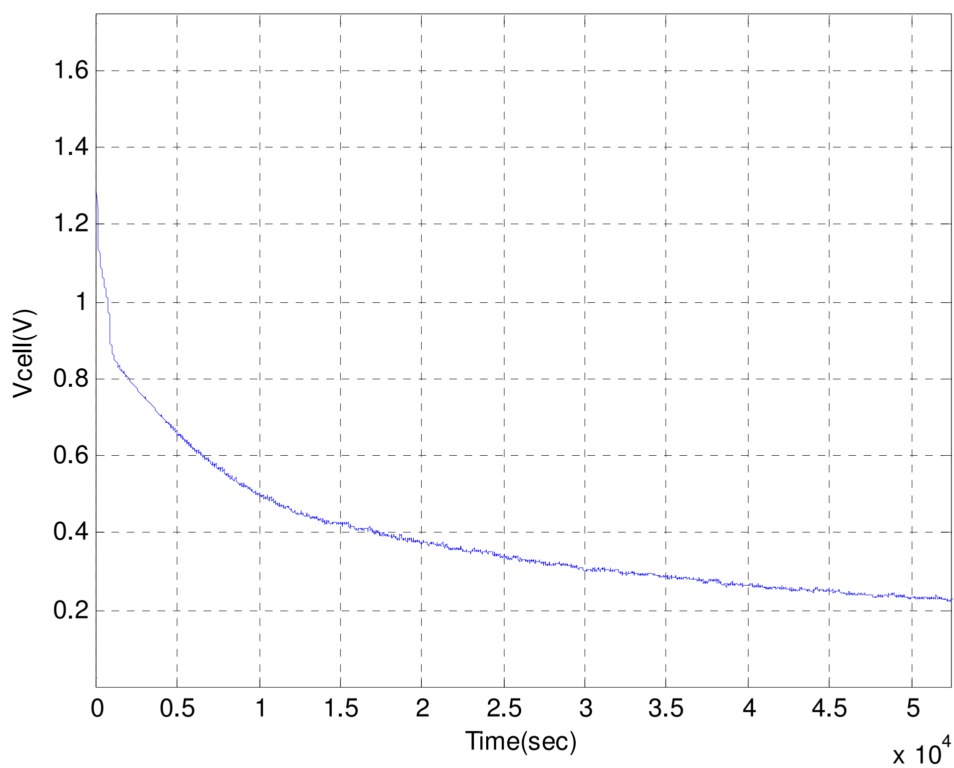

Figure 31: Double stacked graphite-zinc cell 5KΩ load discharge

A single cell using electrolyte E0 (Cell E0GZ11) was discharge by a resistive load (9.92KΩ) for 1.2 hours, right after assembly, then the cell was voltage charged at a potential of 1.4V for 2 hours followed by an identical resistive discharge. The resulting curves from both discharges are presented in Figure 32. *Fresh* identifies a new cell not previously charged or discharged while *Charged* refers to the charged cell. In both cases, the same cell is used. Comparing the curves in Figure 32 one can see that once the cell is charged, it has a higher capacity than when it was fresh / new (see Table 7).

Table 7: Comparison of properties of cell E0GZ11 when new (fresh) and after voltage charging at 1.4V for 2 hours

	Fresh Cell	**Charged Cell**
Starting voltage (V)	1.16	1.21
End voltage (V)	0.83	0.86
Discharge time (hours)	1.26	1.26
Capacity (mA.h)	0.108	0.115

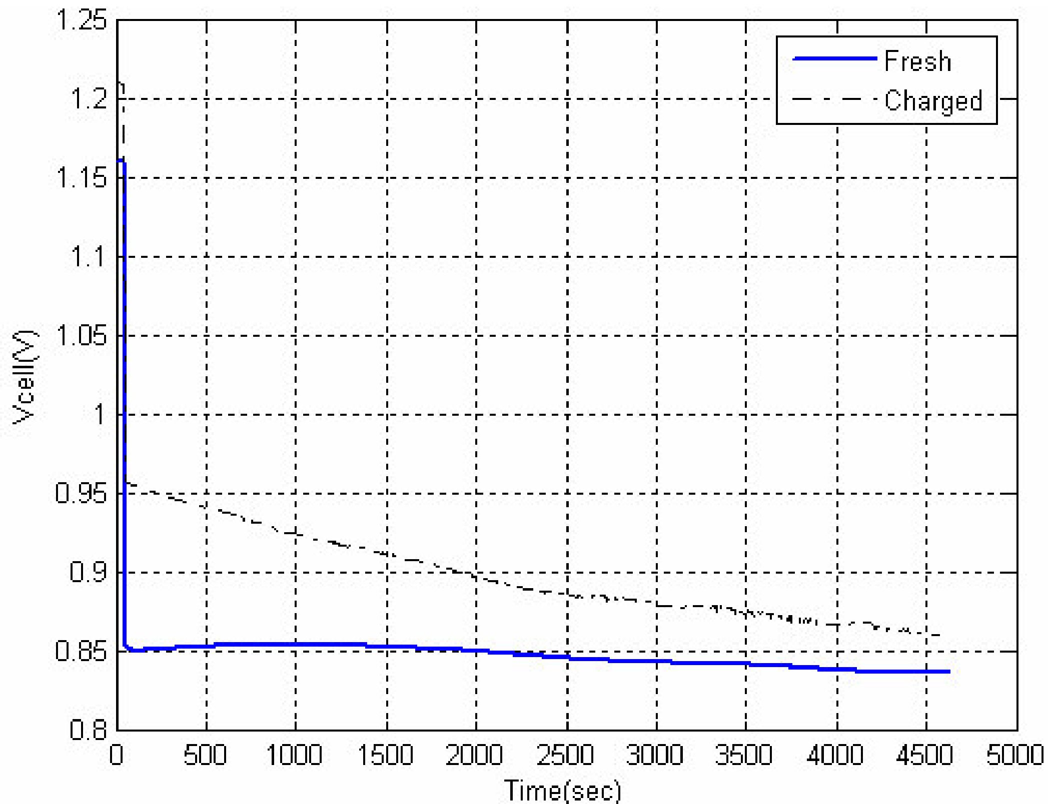

Figure 32: Graphite-Zinc cell (E0GZ11) voltage charged at 1.4V for 2 hours resistive load (9.92KΩ) discharge

Slow Discharge

I discharged a fresh cell (E0GZ12) across a 46.5 KΩ load over nearly 5 days in an attempt to obtain the total capacity of the cell by draining it. Figure 33 shows that I did not succeed in draining the cell, which still maintained nearly all of its fresh loaded potential after 113.6 hours (4.73 days). Subsequent discharge at smaller loads did not completely deplete the cell either. Thus far, the total capacity observed from this cell is 2.62 mA.h (or 10.13 J). I approximate the weight of the active components of the cell to be ~0.5g (ignoring the weight of the lexan packaging) this corresponds to a gravitic capacity of ~5240 mA.h/kg. Or considering a cell volume of 0.3175 cm^3 (volume of the electrolyte), the volumetric capacity is 8.25 mA.h/cm^3.

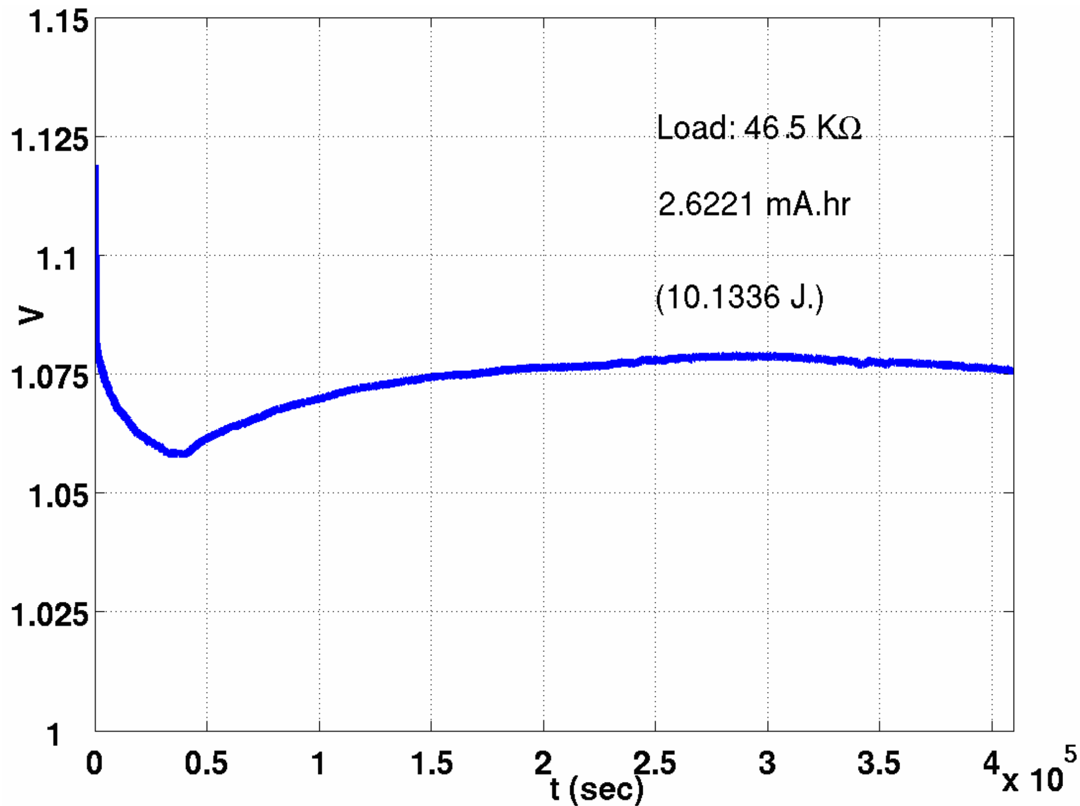

Figure 33: Slow discharge for cell E0GZ12

2.8.3 Discussion

The Graphite-Zinc cells were conceived as a solution to problems encountered by gold coated aluminum sheet cells; notably, the acid corroding the aluminum beneath the gold layer. Furthermore, the Graphite-Zinc cells simplify the assembly process of the cells in the sense that acid resistant paint (requiring 48hours curing time) was no longer needed to seal the cells. Instead, the cell is made with adhesive coated Lexan sheets and is, further, sealed with Methylane Chloride (the entire process takes less than 5 minutes).

The Graphite-Zinc cells had their highest and most stable potential when electrolyte E0 was used. This is due to the use of Boric acid which in addition to Ethylene Glycol provides a buffer to stop corrosion of the zinc electrode. The amount of electrolyte used, 10 drops versus 15 drops, affected the cells' behavior as the

increased amount of electrolyte not only reduces the internal resistance in the cell but provides more reagents to yield greater capacity (lower overpotential).

The charging of the cells was very successful both when charged with current or voltage. The charging with voltage requires that the charging potential be greater than the cells' natural potential (V_{OC} when cell is new/fresh). The charging performance and discharge capacity where only observed when the cell had a powdery mix of hydrated ruthenium oxide and activated carbon. In absence of the powder, the developed potential across the cell could not deliver any current when the cells were fresh or after charging attempts. Hence, the observed characteristics of the Graphite-Zinc cell are related to an electrolyte and powder mixture interaction; as evident from the varying performances for devices made with different electrolytes.

The chemistry within the Graphite-Zinc cell mimics that of typical lead acid (Lithium Manganese) batteries. Before diving (in a subsequent section) into a close look of the chemistry within the Graphite-Zinc cell, it is of importance to first look at a Graphite-Lead cell. Such a cell should merge the properties of my Graphite-Zinc cell and those of conventional lead acid batteries. This investigation is conducted in the next section.

2.9 Graphite-Lead cells

2.9.1 Structure

The Graphite-Lead cell has a structure similar to that of the Graphite-Zinc cell as seen in Figure 34. Three different electrolytes (E0, E6 and E7) were used to assemble the cell. I was interested in seeing how these cells compare to the Graphite-Zinc cells. Electrolyte E0 was chosen because it was the base electrolyte used for

most of the Graphite-Zinc cells, electrolyte E6 was chosen to look at the effect of a strongly acidic electrolyte (1pH) while electrolyte E7 offered an electrolyte with an acidity level between the previous two (4pH).

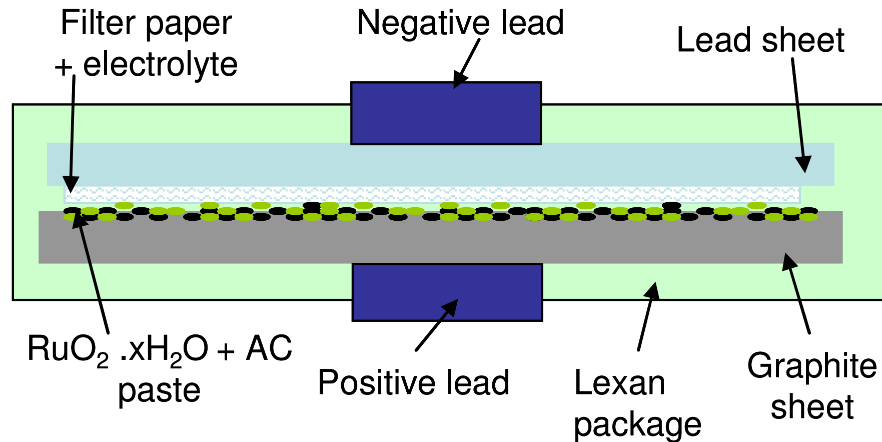

Figure 34: Graphite-Lead cell structure

2.9.2 Characteristics

Resistive load discharge of fresh cells as well as of voltage charged and resistive load discharges are the approaches used to characterize the Graphite-Lead cells (E0GP1, E6GP1 and E7GP1). The open circuit voltage of each of the cells and their corresponding charging potential are tabulated in Table 8. The charging voltage was chosen based on the cell's V_{OC} value to which approximately 0.2V is added. For instance, the V_{OC} of E0GP1 was 0.527V, as a result, the cell was charged at 0.7V. The voltage across E0GP1, E6GP1 and E7GP1 during load discharge was recorded for fresh cells and after voltage charging. Figure 35 shows a plot of the voltage across E0GP1 when the cell is fresh and compares it to that of the same cell after voltage charging. The charged cell has a higher voltage. The cell was subsequently charged a couple more times with different duration (see Table 9 for the exact charging time of each cell and runs). As an example, for E0GP1, charge 1 lasted 3 hours, charge 2

lasted 2 hours while charge 3 lasted 4hours. The resistive load discharge of the fresh cell is compare to that of the three charging condition in Figure 36. The characteristics of the different runs are listed in Table 9.

It should be noted in Figure 36 that after charge 1, the subsequent charging steps do not increase the driving capability of the cell. The internal reactions of the cells have been initialized. From that point on all the discharges are reproducible; hence, the cell is stable. Cell E6GP1 and E7GP1 display different (greater than E0GP1) V_{OC} values because of the strength (lower pHs) of their electrolytes. E6GP1 has the most acidic electrolyte (1pH) and also the greatest V_{OC}. However, the same initialization process occurs after repeated charging. Figure 37 and Figure 38 display the discharge curves of E6GP1 and E7GP1; respectively. Figure 37 does not have a curve for the fresh/new for cell E6GP1 and there are neither fresh cell data for E6GP1 in Table 9; this is because the recorded data was corrupted and could not be recovered. However, charging E6GP1 yielded a greater cell potential than its original V_{OC} and the charging cycles generated identical discharge curves.

Table 8: Open circuit voltage of Graphite-Lead cells and charging voltages

Cell Name	E0GP1	E6GP1	E7GP1
V_{OC} (V)	0.527	0.89	0.588
V_{charge} (V)	0.7	1.1	0.8

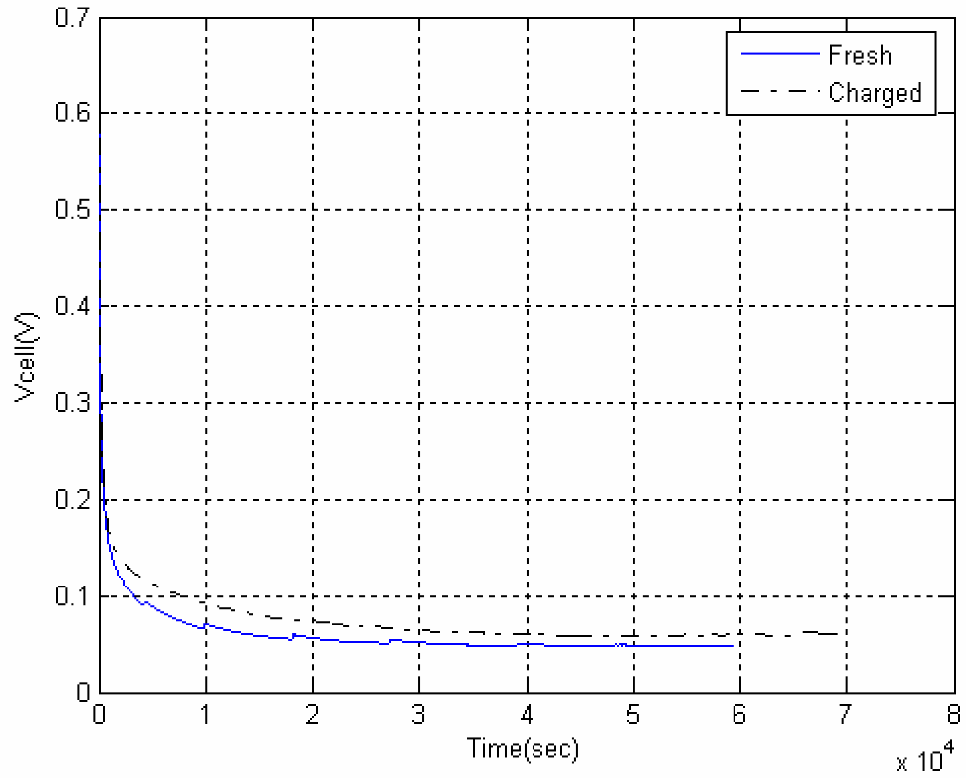

Figure 35: Graphite-Lead cell (E0GP1) resistive load (9.92KΩ) discharge as fresh / new cell and after 3 hour charging at 0.7V

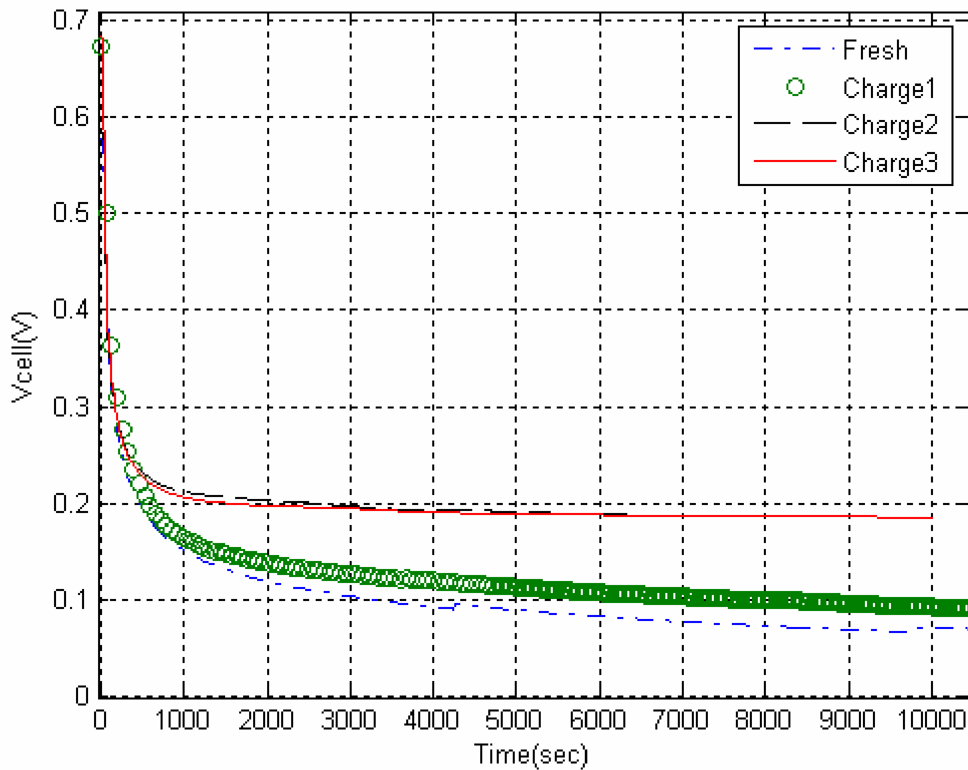

Figure 36: Graphite-Lead cell (E0GP1) resistive load (9.92KΩ) discharge as fresh / new cell and after subsequent charging

Table 9: Comparison of properties of cell E0GP1, E6GP1 (missing fresh cell data) and E7GP1 when new (fresh) and after multiple voltage charging at their respective voltages. The three cells have electrolyte with varying pH, E0GP1 (4pH), E6GP1 (1pH) and E7GP1 (5pH)

		Fresh Cell	Charge 1	Charge 2	Charge 3
E0GP1	Charging Time (h)	0	3	2	4
	Start Voltage (V)	0.527	0.672	0.682	0.682
	End Voltage (V)	0.048	0.0584	0.186	0.185
	Discharge Time (h)	16.48	19.51	2.53	2.77
	Capacity (mA.h)	0.72	0.73	7.9	7.1
E6GP1	Charging Time (h)	--	$2^{1/2}$	$2^{1/2}$	$2^{1/2}$
	Start Voltage (V)	--	1.102	1.103	1.100
	End Voltage (V)	--	0.243	0.824	0.832
	Discharge Time (h)	--	22.68	22.57	20.44
	Capacity (mA.h)	--	1.9	2.1	1.9
E7GP1	Charging Time (h)	0	3	3	3
	Start Voltage (V)	0.588	0.702	0.753	0.733
	End Voltage (V)	0.334	0.358	0.365	0.352
	Discharge Time (h)	22.75	21.56	16.91	15.46
	Capacity (mA.h)	0.847	0.874	0.707	0.639

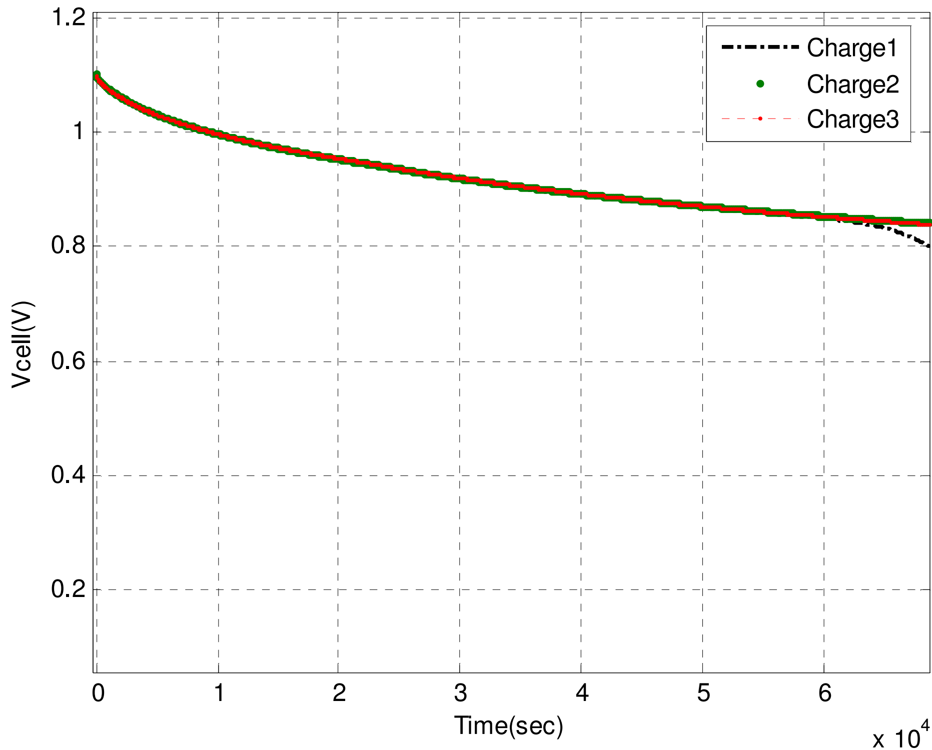

Figure 37: Graphite-Lead cell (E6GP1) resistive load (9.92KΩ) discharge after subsequent charging

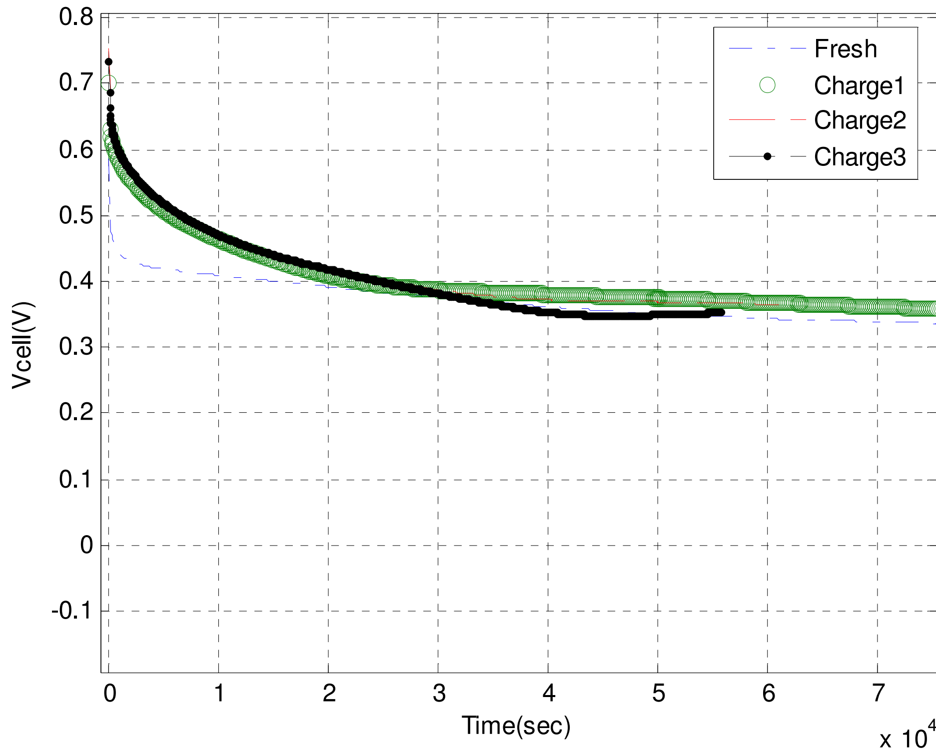

Figure 38: Graphite-Lead cell (E7GP1) resistive load (9.92KΩ) discharge as fresh / new cell and after subsequent charging

2.9.3 Discussion

The open circuit voltage of the Graphite-Lead cell is lower than their Graphite-Zinc counterpart this might be due to the difference of the electrochemical potential of the two electrodes. From the various discharge plots in this section it is evident that the Graphite-Lead cell can be voltage charged. However, the cell requires a few charging cycles to establish a reproducible voltage drive. One would expect this from traditional lead acid batteries which require a few charging cycles to be initialized. Comparing E0GP1 to its Graphite-Zinc counterpart (E0GZ), the capacity of the Graphite-Lead cell is lower than that of a Graphite-Zinc. This does not hold true if the comparison is made between E0GZ cells and the E6GP1 cell, which has a high capacity. This observation differs from standard lead-acid battery operations, which

traditionally have the lowest energy density among modern rechargeable batteries [29]. This points to the conclusion that although the reaction in my cells mimic that of a lead-acid battery, there is a fundamental difference that not only enables a respectful cell capacity but also a relatively fast charging (2 hours). Lead-acid batteries do not lend themselves to fast charging and their charging time is typically 8 to 16 hours. The next section looks at a conventional lead-acid cell and contrasts its chemistry to the interactions within my cells.

2.10 Electro-Chemistry of Rechargeable Cells

2.10.1 Lead Acid

Lead-acid cells use as anode a sponge metallic lead (Pb) and as cathode lead dioxide (PbO_2) with an electrolyte made of dilute mixture of aqueous sulfuric acid (H_2SO_4). During discharge, both electrode turn into lead sulfate ($PbSO_4$). The common chemistry of lead-acid battery half-cell reactions are as follows:

- Positive plate — Cathode (reduction)

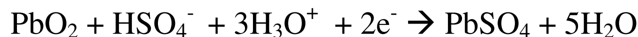

$$PbO_2 + HSO_4^- + 3H_3O^+ + 2e^- \rightarrow PbSO_4 + 5H_2O$$

- Negative plate — Anode (oxidation)

$$Pb + HSO_4^- + H_2O \rightarrow PbSO_4 + H_3O^+ + 2e^-$$

In the lead-acid cell, there is a shedding of the active material. As the cell discharges, the lead dioxide at the positive plate is converted to lead sulfate, the lead sponge at the negative plate is also converted to lead sulfate and the sulfuric acid electrolyte is converted to water. Connection of a resistive load allows electrons to flow from negative to positive plates. This motion would reduce the charge available for transport and the voltage drop across the cell; but, chemical reactions are able to

continue generating new electrons and enable the external load to be driven. With current flowing out of the cell, there are resistive drops at the electrode surface (surface lead-sulfate interface). With the sulfate layer forming on the electrodes further chemistry issues can be expected as the activation energy of the reaction is bound to change since the energy needed for the movement of reacting species through the electrodes surfaces (sulfate layer) increases. Charging reverses the process by forcing electrons back into the cell; whereby, reversing the chemical reactions, converting the lead sulfate back into the respective lead dioxide, lead sponge and sulfuric acid; in a sense, converting electrical energy into stored chemical energy.

2.10.2 Ruthenium Oxide

Normal battery reagents are typically well defined, 3-dimensional phases. Therefore, their conversion from one oxidation state to another continues ideally at a singular potential until relatively all of one phase is transformed to another [30]. Hydrous Ruthenium oxide based redox reaction are 2-dimensional and rely on a Faradaic processes in which a monolayer or quasi-monolayer of electrochemically reactive species can be electrosorbed or electrodesorbed with charge transfer [30]. This reaction ascribes to a series of reversible redox processes with simultaneous exchange of electrons and protons according to the following equation:

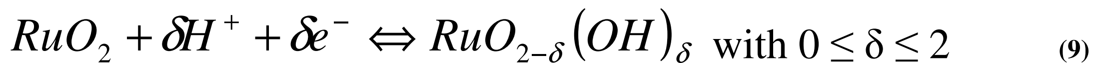

$$RuO_2 + \delta H^+ + \delta e^- \Leftrightarrow RuO_{2-\delta}(OH)_\delta \text{ with } 0 \le \delta \le 2 \quad \textbf{(9)}$$

The proton conductivity is influenced by the amount of water chemically bound at the surface of the ruthenium oxide particles as the water provides a pathway for H^+ [31]. The use the powdery hydrous form of ruthenium oxide ($RuO_2.H_2O$) as opposed to

ruthenium dioxide (RuO_2) increases the wettability of the ruthenium particles and the proton conductivity since there is no bulk material that needs to be penetrated.

The reaction of Ru_2 is in essence a surface reaction that covers the entire range of Ru^{2+}, Ru^{3+}, Ru^{4+} oxidation states. During the redox reactions, the oxygen-ruthenium bonds stretch and contract in a manner consistent to the oxidation state [32]. The bond elongation for oxidation state Ru^{3+} are large enough for a water molecule to fit comfortably. In a sense, the redox reaction of $RuO_2.H_2O$ consists of the adsorption/desorption of hydronium ions [32-34].

2.11 Competitive Technologies

Attempts have been made to create flexible energy cell. Flexible energy storage devices based on carbon nanotube impregnated paper has been introduced by Pushparaj at Rensselaer Polytechnic Institute [8]. However, the presented cell has a moderate capacity while it utilizes highly toxic compounds notably their room temperature ionic liquid (RTIL) 1-butyl, 3-methylimidazolium chloride and lithium hexaflurophasphate (LiPF6). In Refs. [8] the cells is falsely claimed to be safe and environmentally friendly. As for my cell, they are truly environmentally friendly and safe as they contained small ($5/30^{th}$ of a milliliter) and weakly acidic electrolyte and the Ruthenium oxide and activate carbon are inert.

I can compare the performance of my Graphite-Zinc cells to a hearing-aid battery that was discharged across a 1K load for three days (see Figure 39). During this discharge, the 1.5 V open circuit potential of this battery falls to nearly 0.21 volts after 10.6 hours and does not recover. It should be noted that the hearing aid battery is in no way rechargeable. The capacity the hearing-aid battery exhibits up to that point

is 15.10 mA.hr, or 80.2545 J. Measuring the cell volume at 0.095cm^3 and estimating the active weight at 0.3 grams, the corresponding gravitic and volumetric capacities are 5033 mA.hr/kg and 158.95 mA.hr/cm^3 respectively. my results presented for cell E0GZ12 at the end of sub-section 2.8.2 (~5240 mA.h/kg and 8.25 mA.h/cm^3) are quite comparable. However, it should be noted that my cell is far from being depleted at the end of the measurement cited in sub-section 2.8.2 and depicted in Figure 33 and can be recharge multiple time leading to a total capacity far greater than that of the hearing aid battery.

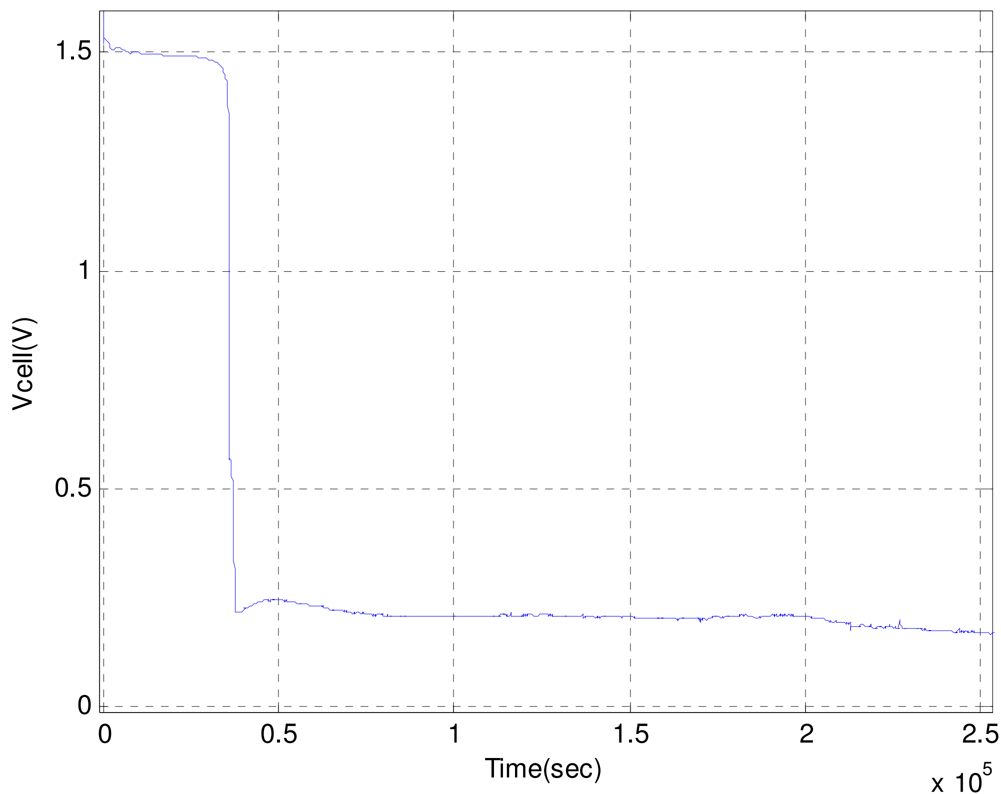

Figure 39: Resistive load (1KΩ) discharge of a 1.5V hearing aid battery

Further comparison can be drawn to small rechargeable batteries such as the Lithium Manganese cell (ML1220) from Panasonic, which has a 3V rating. The

Lithium cell represents state of the art as far rechargeable cell are concerned. The comparison is based on a calculation method that measures voltage across a known load (here 993 ohms) during discharge and disregards the first ten seconds of measurement (for stability purposes). Then, the time require for the battery/cell to fall to 90% of the V(t=10 sec.) value is identified and the current drown from the battery/cell is integrated over the given time. This offers a one-to-one comparison between a rechargeable commercial cell and my cells thereby overcoming ambiguity introduced by manufacturer ratings. The resulting characteristics of the Lithium cell and my Graphite-Zinc and Graphite-Lead cells are compared in Table 10.

The normalized capacity is obtained by recognizing that the cell chemistries dictate the open-circuit potential, which is rated at 3 V for the Li:ion cell and ~1.10 V for my Ruthenium oxide cells. The load as well as the previous discharge history determines the overpotential drop the cells will display when load is connected. I normalized the results from the Li:ion battery by dividing its discharge potential by the ratio of the loaded potentials measured at V(t=10 sec.) during discharges of both cells. The volume of my cells were determined for active volume only and the weight estimate does not include the weight of the backing graphite sheet and the packaging material, a polycarbon plastic named Lexan. This extra weight is reduced via the implementation of folded cells that use laminate plastic for external packing (to be introduced in the next paragraph). It should be noted that the Lithium cell was fresh (no prior discharge or charging). The Graphite-Zinc cell had previously undergone ~184 hours of discharge across various higher loads, yielding 4.39 mA.hr. The Graphite-Lead cell had previously undergone ~65 hours of discharge across various

higher loads, yielding 6.520 mA.hr. When discharged across a higher load, the batteries provide a lower current and therefore display less capacity. Although the raw cost of my cell is much high (cost of ruthenium oxide), the cost of ruthenium oxide will decline when commercial volume is reached.

Table 10: Lithium cell comparison to Graphite-Zinc and Graphite-Lead cells

Compare 100%-to-90% discharge period	**Li:MnO2** **(Commercial from Panasonic)**	**RuOx:Zn** **(In-house built, in development)**	**RuOx:Pb** **(In-house built, in development)**
mA.hr (raw)	0.9584	0.2201	0.558
mA.hr (normalized)	0.3378	0.2201	0.558
mA.hr/gr (raw)	1.1980	0.2201	0.558
mA.hr/gr (normalized)	0.4222	0.2201	0.558
open-circuit potential	3 V (rated)	~1.10 V/1.15 V (measured)	~1.10 V (measured)
cost ($/cm2)	$2.4 (on sale)	$5 (raw cost)	$5 (raw cost)
mechanical design	sealed and non-flexible	flexible depending on casing design	flexible depending on casing design
weight/volume	0.8 gr / 0.25 cm3 (specification)	~0.1 gr / ~0.32 cm3 (manufacture-dependent)	~4 gr / ~0.32 cm3 (manufacture-dependent)
toxicity or raw materials	-highly caustic -risk of esophogic rupture	- eye irritant	- eye irritant

To reduce the overall volume of my cells and the weight of the packaging, a folded cell structure was adopted. The cell has the same chemistry as the other Graphite-Zinc cells. The main difference is that the size of the graphite electrode is cut in half but the same amount of paste and electrolyte is used. The Graphite sheet is sandwich between the zinc sheet with the Ruthenium oxide and activated carbon paste on both sides. The filter paper is also wrapped around the graphite electrode to isolate it from the zinc electrode. The cell is sealed using a thin and light laminating sheet. The cell structure is illustrated in Figure 40. The folded cell maintains a V_{OC} of ~1.1V and displays the same driving capability as my regular Graphite-Zinc cells. A resistive load discharge of the folded cell is shown in Figure 41. Over a 15 hour discharge it delivered 0.519mA.hr. This capacity is comparable to the best Lexan packaged Graphite-Zinc cell recorded during this thesis work with the added benefit of being flexible.

I have generated a low weight (less than 0.5g) battery cell that is flexible and rechargeable. Certainly there are other thin flexible battery commercially available; especially the NanoEnergy™ manufactured by Front Egde Technology who claim that NanoEnergy™ is the world's thinnest rechargeable battery; however, this cell has reliability issue and a capacity (0.1 mA.h—according to their website) far lower than result recorded with my cells.

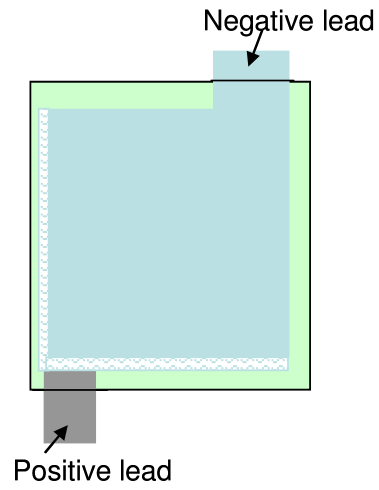

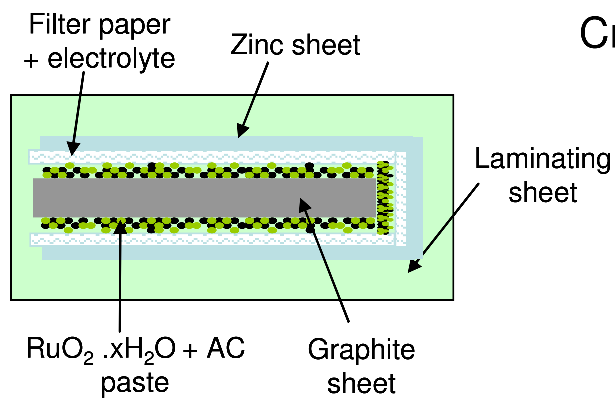

Figure 40: Structure of folded Graphite-Zinc cell (E0FD)

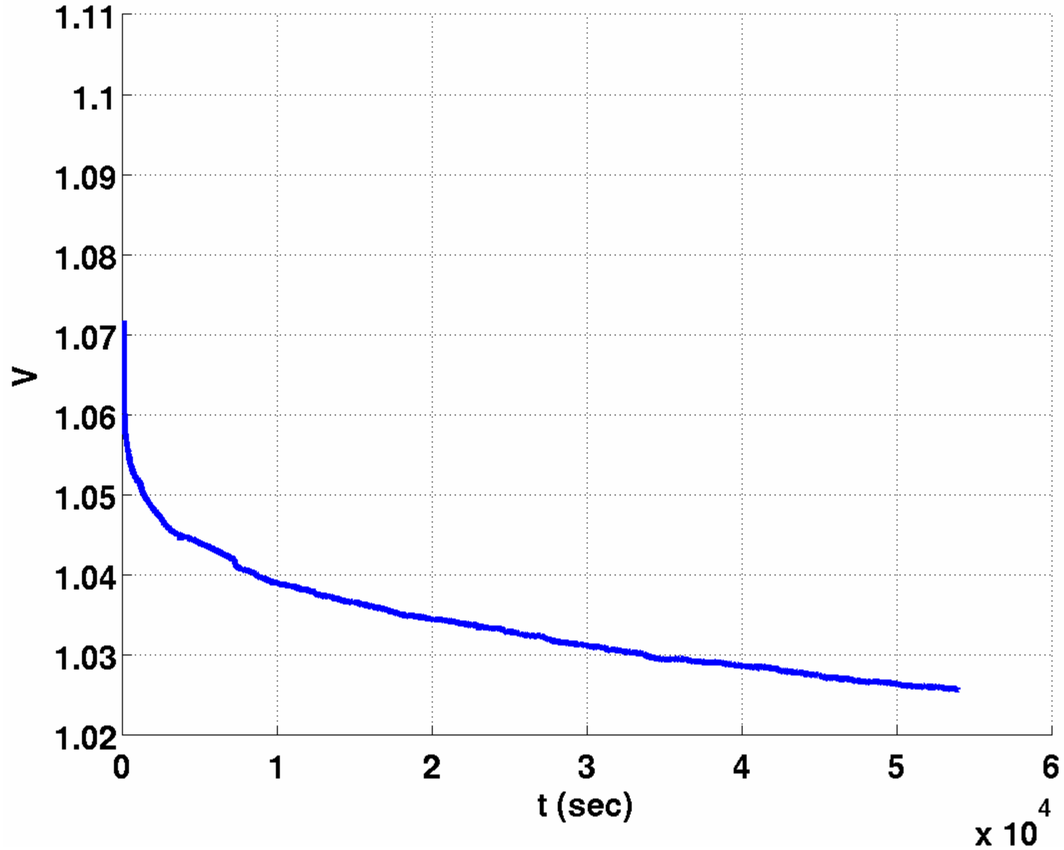

Figure 41: Resistive load (29.83KΩ) discharge of folded Graphite-Zinc cell (E0FD1)

2.12 Conclusion

Throughout this Chapter, the objective has been to develop an electrochemical energy cell that enables efficient energy storage and delivery within a compact volume. The cell is to meet energy storage specifications for low-power ad hoc distributed networks as well as be rechargeable, light weight and flexible. The solutions investigated for this objective centered on an electrochemical cell utilizing a powdery mixture of hydrated ruthenium oxide and activated carbon with a ratio of 10:1 by weight. I determined that that the composition of the powdery mix affects the characteristics of the cell; the ratio mentioned earlier offers the best characteristics [1].

Beside the powdery mixture, the electrode materials as well as the packaging scheme were investigated as follows:

- Electrode material: gold coated glass-silicon die; gold coated aluminum; graphite-zinc and graphite-lead.

- Cell sealing: Acid resistant paint, Lexan sheets equipped with adhesive surface and thin laminating sheets.

- Electrolyte: sulfuric acid or a mixture of solution (Ethylene Glycol, Ammonium Hydroxide, Boric acid, phosphorous acid, DI water and nitric acid in various ratio).

- Filter paper: glass fiber

All these parts and packaging approaches were combined to form four general class of electrochemical cell:

- Gold coated glass slide cells: Showed mostly capacitive behavior with weak redox reaction

- Gold coated aluminum cells: Showed mostly battery behavior due to electrolyte corroding underlying aluminum material. The corrosion effect is easily mitigated by the use of neutral pH electrolytes

- Graphite-Zinc cells: Strong battery behavior with some rechargeability

- Graphite-Lead cells: Good redox reaction and capacitor behavior.

The most promising cell is the Graphite-Zinc cell (electrolyte E0 family). It displays both current and voltage charging capabilities. Furthermore, the cell has a high and constant voltage potential that is reproducible from cell to cell. In addition, the folding of the cells enables a decrease in the cells' volume and weight while the capacity is unchanged (the volumetric and gravitic capacity are increased).

Throughout this chapter, various electrochemical energy cells structures have been presented to show the viability of powder ruthenium oxide and activated carbon use as electrode material. This study contributes to the knowledge base in the field of electrochemical energy cells as it deviates from the conventional use/deposition of these materials when applied as electrode; notably, sputtering, evaporation or pressed with a binder. The presented approach was used to fabricate a variety of cells that have interesting properties. I have, in effect, generated:

1. A flexible electrochemical cell (battery)
2. A battery storing high specific energy density
3. A battery that can be made to be conformal to the surface of any electronics package
4. A method for the fabrication of said battery
5. The materials system for such a battery

CHAPTER 3: DUAL UV-WAVELENGHT IMAGING ARRAY

3.1 Major Contribution

This chapter introduces and executes a process flow for the fabrication of a simultaneous dual UV-wavelength detector array. The design of this array is enabled by the development of my novel fabrication process flow that depends on a modified lift-off process, a patented confined epitaxy growth method for III-nitride semiconductors and a creative detector staking approach. These guiding principles pave the way for the following contribution to the field:

- My presented lift-off lithography process applied to the conditioning/patterning of the area needed for active $Al_xGa_{1-x}N$ growth demonstrates the importance of the confined epitaxial growth process in the quality improvement of grown $Al_xGa_{1-x}N$ layers [4, 5, 35].

- My presented fabrication process flow for the generation of an array of dual UV-wavelength detectors demonstrates simultaneous dual UV-wavelength band detection. This is the first demonstration of such capability, uncovered by the research described in this thesis.

- My lift-off lithography process in conjunction with my presented UV detector device structure (the stacking of two $Al_xGa_{1-x}N$ active layers) offers a road map for the development of other devices based on $Al_xGa_{1-x}N$ alloys

3.2 Introduction

Many objects radiate in the ultraviolet (UV) spectral region, corresponding to short wavelength; these objects include among others, the sun, stars, flames and even biological agents. The ability to characterize UV emission spectra can yield important insight into the nature of the emission source. There are an increasing number of applications that require the use of sensors capable of detecting light in the ultraviolet spectral region. Such application include earth resources management (weather prediction, water purification, pollution monitoring and crop data acquisition), planetary remote sensing, missile plume detections for early missile treat warning, space-to-space-communication, solar astronomy, flame detection, engine monitoring, biological/chemical battlefield reagent detectors [36-39]. Throughout this thesis work, the term UV-wavelength and color/UV color will be used interchangeably.

$Al_xGa_{1-x}N$ alloy has been demonstrated to be an excellent semiconductor for UV detection applications [40]. The alloy peak absorption wavelengths can be changed by adjusting the mole-fraction of aluminum present; yielding a “spectrally tunable” semiconductor. Commercial UV photodetectors are presently available [41]. However, these devices require the use of extra optical filters to eliminate the visible and infra-red part of the incident light, which blinds the detector; consequently, complicating the detection system and reducing the sensitivity of the system by decreasing the number of signal photons reaching the UV sensor [42, 43]. The aforementioned system complexity is alleviated by the use of $Al_xGa_{1-x}N$ hetero-junction device structures. For these devices, the cut-off wavelength of their response spectra can be tuned from, practically, 250nm to 365nm while the hetero-junction

provides bandwidth modulation capability [44]. $Al_xGa_{1-x}N$ hetero-junction devices represent the standard for semiconductor based UV detectors. These detectors are capable of detecting a specified UV frequency range, in other word, single UV “color detection” is enabled.

The ability to detect two UV-wavelengths simultaneously greatly improves the effectiveness of UV detection systems. A number of visible-blind (unaffected by visible light) UV photodetectors based on photoconductive and junction devices have been reported [36-46]. However, these detectors are susceptible to background brightening (noise), especially when used in space, due to the UV radiation coming from the sun. Although present devices are visible-blind, they are not truly solar-blind since sunlight does contain UV radiation components. Therefore, the background of the imaging field is brightened, inhibiting discrimination between the signal contributed by the source being detected and the UV contribution from solar light. One would think that the problem does not pertain to detection at the earth surface since the earth’s atmosphere absorbs photons from the sun with wavelengths shorter than, approximately, 300nm. By so doing, the earth’s atmosphere acts as a “filter” for most solar UV radiation [43]; however, the UV range covers all frequencies shorter than 400nm so the photons between the wavelengths of 300nm and 400nm will be sensed by the detector without discrimination from the signal of interest.

Most objects radiating in the UV range have a very specific UV emission ratio. Thus, the use of a dual UV-wavelength photodetectors is a solution to overcoming the discrimination obstacle. By sensing in two spectral bands, the two signals obtained from the two sensors can be used to eliminate the background corruption from the

presented frame base on the signal ratio between the two detector cells. A dual UV-wavelength band detector would give rise to a detector system less susceptible to solar UV radiation corruption and more resistant to falls positive induced by solar contribution. In addition, dual UV-wavelength band detectors would make possible the simultaneous detection and differentiation of two UV radiation (even from the same source).

One would think that two single UV-wavelength band detector could be easily implemented to enable dual UV-wavelength band sensing. In such a setup, additional electronics would be needed to synchronize both detectors with respect to time and position. To overcome the need for time and position matching algorithm, both detector types need to placed on the same chip and operated by the same code.

Wide band-gap detector materials such as $Al_xGa_{1-x}N$ alloys are subject to large background leakage current. This leakage current results from the internal defect structure of the nitride, notably dislocation and grain boundaries. Epitaxialy grown GaN layers have dislocation concentration of 10^9-10^{10} cm^{-2} due to the low-angle grains present in these epitaxial layers [47]. Since the current transport is the result of defect tunneling, which is weakly temperature dependent, the background leakage current problem can only be resolved by considerably decreasing the defect concentration in the detector material. As a result, a substantial reduction in current leakage can only be obtained with an improved material growth technique that yields lower defect concentration.

Currently, III-V nitride (III-N) semiconductors are mostly grown on either sapphire or silicon carbide (SiC) substrates by metal organic chemical vapor

deposition (MOCVD). Given that SiC is not UV transparent, sapphire wafer is the substrate of choice for UV detector fabrication. When growing UV detector structures, double-side polished sapphire substrates are employed and a thin, low temperature AlN nucleation layer is used to help reduce extended defect (dislocation) densities resulting from the large lattice mismatch between the substrate and the film [48]. The lattice constant ‘a’ for $Al_xGa_{1-x}N$ varies between 3.12 and 3.18 (see Figure 42) whereas the lattice constant ‘a’ of sapphire and SiC are about 4.75 and 3.07, respectively.

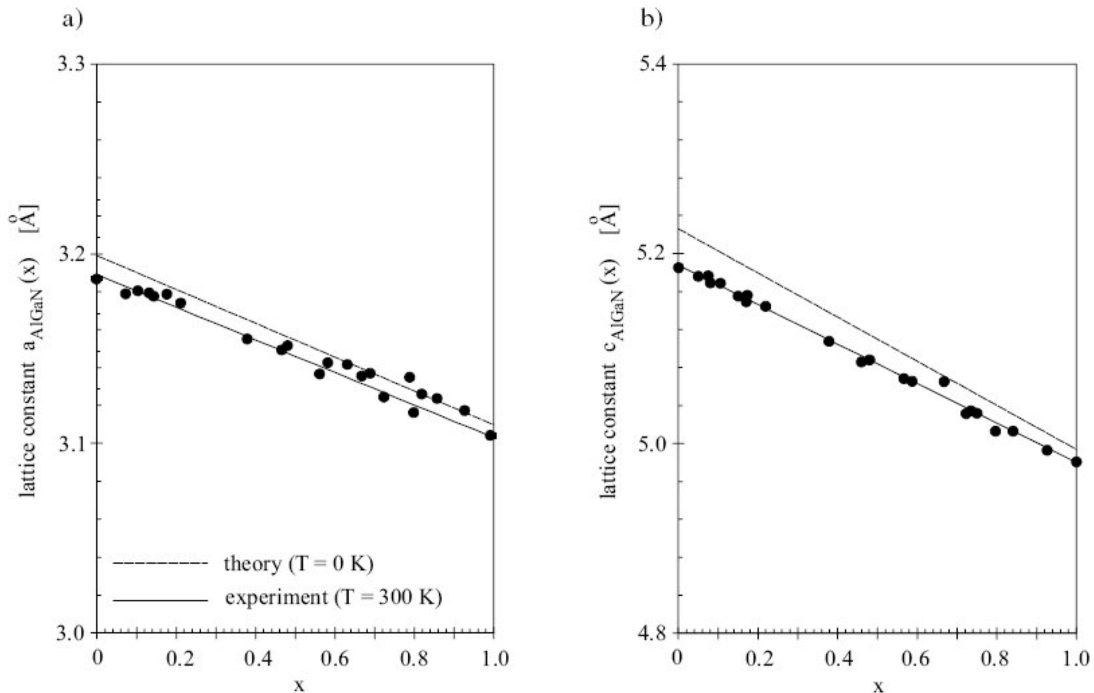

Figure 42: (a) and (b) Lattice constant ‘a’ and ‘c’ for $Al_xGa_{1-x}N$ random alloys measured by high resolution X-ray diffraction at room temperature (solid lines) and calculated for T=0K (dashed lines) (from M. E. O. Ambacher).

These dislocations act as leakage paths in III-V nitride materials and significantly increase reverse leakage currents even for detectors operating at low bias. For the high aluminum mole fraction films needed to detect some of the shorter

UV wavelengths, additional measures are required to keep dislocation densities low and avoid cracking of the films.

Presently, there is no high yield method to permit the creation of an interspersed dual UV color detector array based on III-N materials. Even when all these considerations can be met, it is very challenging to grow two-color detectors in a “stacked” fashion (multiple layers of AlGaN with decreasing aluminum mole fraction from substrate to surface). A confined epitaxy (CE) growth approach, patented jointly by University of Maryland and the Naval Research Laboratory (NRL), is employed to realize dual UV-wavelength band detectors in III-V nitride semiconductor as opposed to the more traditional approach of stacked junctions. Therefore, the creation of an enabling process for this novel growth process, applied towards the fabrication of UV detectors with greater performance, would be presented in this chapter.

When creating a novel process for fabricating UV detectors it is important to examine other UV detector structures and recognizing that the various detectors can be implemented with various material combinations [49-53]. UV detectors are mostly photovoltaic elements since they exhibit a photo-effect when carriers are optically injected into the vicinity of their built-in potential barriers [40]. Although UV detectors, independently of their material composition, display these photovoltaic characteristic, they can still be grouped into three categories based on their modes of operation:

- Photoconductive detectors
- p-n and p-i-n junction photodiodes

- Schottky barrier and metal-semiconductor-metal photodiodes

After presenting a brief review of the aforementioned photodetectors, the structure of my novel dual-color UV imaging array will be examined. Then, the confined epitaxy growth method is presented. The description of the device fabrication flow is offered followed by the device characterization results. Finally, closing remarks conclude this Chapter.

3.3 Background

3.3.1 Photodetectors figures of merit

The current response of photodetectors is determined by the quantum efficiency η and by the photoelectric gain g. Quantum efficiency is a measure of the detectors ability to match with radiations to be detected. In general, it quantifies the number of electron-hole pairs generated per total incident radiation, while internal quantum efficiency η_o describes the efficiency of the radiation photons that made it into the material (not reflected) [40]. Photoelectric gain is a value that describes how well the generated electron-hole pairs contribute to the created photoconductive current. In other words, it is the number of carriers reaching the device electrodes / contacts per each generated pairs and can be expressed as

$$g = \frac{\tau}{t_t} \tag{10}$$

Where t_t is the transit time of electrons between ohmic contacts and τ is the excess carrier lifetime [40]. The spectral current responsivity for photodetectors, which is the ratio of photocurrent per incident power, is defined as

$$R_\lambda = \frac{\lambda\eta}{hc} qg \tag{11}$$

Where, λ is the wavelength, η is the quantum efficiency, h is Plank's constant, c is the speed of light, q is the electron charge and g is the gain of the detector [54]. Responsivity is expressed in units of amperes per watts (A/W). Another figure of merit of importance is detectivity, D*, which characterizes normalized signal to noise performance of detectors and can be defined as

$$D^* = \frac{R_i (A_o \Delta f\ )^{1/2}}{I_n} \tag{12}$$

Where R_i is the responsivity, A_o the optical area, I_n the current noise (from generation and recombination), and Δf is the frequency band [40].

3.3.2 Photoconductive detectors

These devices are basically radiation-sensitive resistors and are sometimes called photodetectors; their general structure is pictured on Figure 43. When a radiation is incident on such a device, photons with energy (*hv*) greater than the bandgap energy of the semiconductor constituting the device are absorbed and generate electron-hole pairs; as a result, the conductivity of the semiconductor is changed. The change in conductivity can be measured via electrodes attached to the sample while the photoconductor is operated in a constant current or voltage circuit [55]. Photoconductor materials have an internal quantum efficiency of unity which means that all photon absorbed contribute to the photoconductive process. It should be noted that the surfaces of the detector materials have reflection coefficients r_1 and r_2 for the front and backside of the materials; hence, some radiation might be lost

through reflections. As for the noise mechanism in a photoconductor, they are attributed to two fundamental mechanisms.

On the one hand, the noise is dominated by generation-recombination (G-R) noise, which is most prominent at intermediate operation frequencies. G-R noise is related to the random generation of free carriers by the crystal vibrations and their ensuing random recombination [56]. In the absence of external bias in the form of fluctuating voltage or current, the random thermal motion of charge carrier in the crystal, not due to a change in the total number of these charge carriers, yields the Johnson-Nyquist noise [40]. In other words, the change in the velocities of free carriers associated with their random thermal motion yield the Johnson-Nyquist noise.

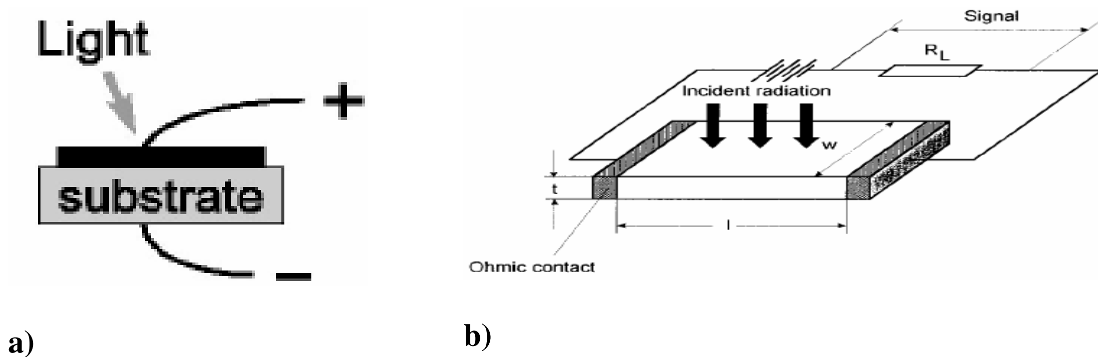

a) **b)**

Figure 43: (a) Open circuit voltage of photoconductive photodiode (from J. Yamaura), (b) geometry and bias of a photoconductor (from M. Razeghi).

3.3.3 Schottky barrier and metal-semiconductor-metal (MSM) photodiodes

Schottky barrier and metal-semiconductor-metal (MSM) photodiode devices are shown in Figure 44 and are characterized by metal-semiconductor contacts, where a thin layer of metal is deposit on a semiconductor. In the case of Schottky barriers, Figure 44(a), one contact is made ohmic while the other is a Schottky barrier/contact

and the current is conducted between the two contacts via the n^--GaN layer. When photons, with energy greater than the bandgap energy of the n^--GaN layer, are incident on the sapphire surface, the photons generate electron-hole pairs within the absorption layer. These electrons give rise to a drift current, when they reach the Schottky contact. The other semiconductor-metal based detector is the MSM photodiode illustrated in Figure 44(b) which is comprised of Schottky/metal contacts arranged in interdigitated patterns and the photocurrent flows from one contact to the other via the AlGaN layer. The thin metal layer exhibits a high UV radiation transmission; consequently, the UV radiation is absorbed near the metal/semiconductor interface where generated carriers are efficiently collected by the depletion region [40]. The electrostatic barrier between the two materials is due to their difference in work functions. Schottky photodiodes display some advantages over p-n and p-i-n junction photodiodes. Schottky photodiodes have less fabrication complexity (do not involve any high-temperature diffusion step) and increased response speed since the current transport is due mainly to majority carrier as opposed to minority carriers, as it is the case in p-n or p-i-n junction photodiodes [41]. Furthermore, the device performance depends on its geometry, such as distance between interdigitated lines (MSM Schottky detectors) or Schottky contact area (Schottky barrier detectors), and its noise spectra exhibits 1/f behavior between 10Hz and 25KHz [57]. Schottky photodetectors, also, posses good external efficiency, about 50%; as well as high gain and low dark current [41, 58].

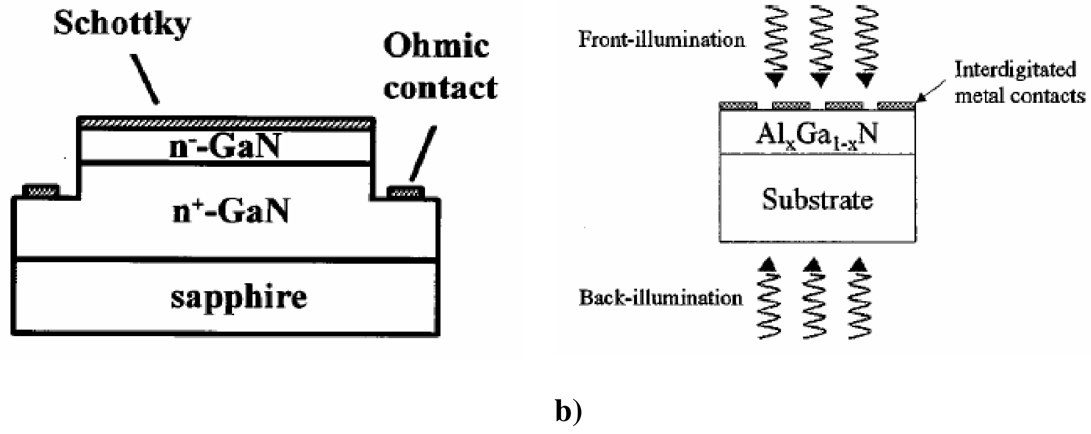

Figure 44: Device structure of (a) a vertical Schottky barrier detector (from Q. Chen), (b) a MSM Schottky detector showing incident light under front and back illumination (from M. Razeghi).

3.3.4 p-n or p-i-n junction photodiodes

P-n or p-i-n junction photodiodes are mostly referred to as photodiodes; they are composed of an abrupt p-n or a p-i-n semiconducting hetero/homo-junction. Figure 45(a) displays a typical p-n junction operation and Figure 45(b) illustrates a p-i-n junction photodiode. In the case of this p-n junction photodiode, the radiation is incident on the front side of the device where the photons possessing energy greater than the bandgap energy of the semiconductor generate electron-hole pairs on either side of the junction. The generated charges then diffuse through the semiconductor. The carriers generated one diffusion length from the space charge region are able to diffuse to the latter region where they are swept to the other side of the junction due to the built in and applied electric field. The generated minority carriers become majority carriers once they are swept across the junction and a photocurrent is created [59]. The same mechanism applies for p-i-n junction photodiode with the difference (in this case) that the radiation is incident on the backside to the devices (sapphire surface—see Figure 45(b)). The photodiode can be operated at any point of its I-V

characteristics. Reverse bias operation is usually used for very high frequency applications to reduce the RC time constant of the devices [55].

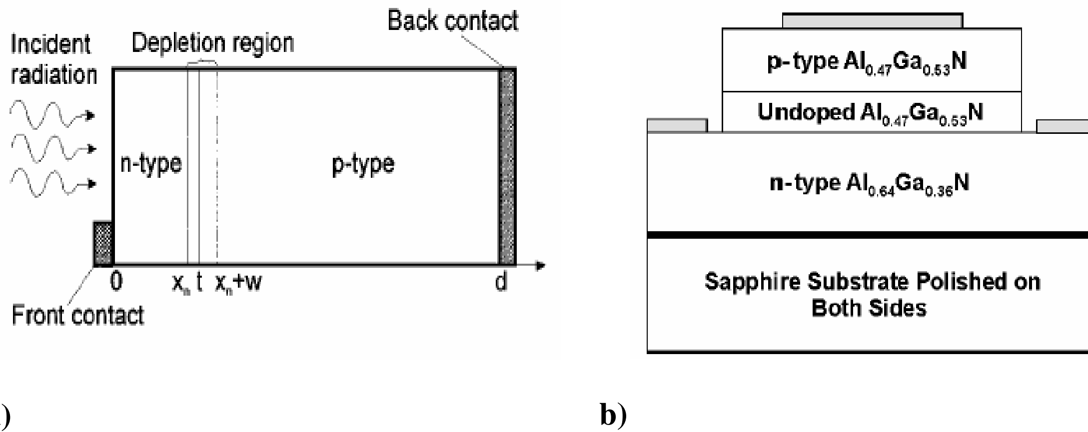

a) **b)**

Figure 45: Schematic representation of (a) p-n junction photodiode (from M Razeghi), (b) p-i-n junction photodiode (from J. D. Brown).

The quantum efficiency of photodiodes is related to the thickness of the illuminated area. As the illuminated region of the junction is made sufficiently thin, the generated carriers easily reach the potential barrier via diffusion. Moreover, the response time of the photodiodes is established by three events; the time needed by carriers to diffuse to the junction depletion region, the time required for the carriers to transit across the depletion region, and the RC time constant associated with the junction capacitance and the parallel combination of the load and diode resistance [60]. As a consequence, the response time of photodiodes is reduced by applying a reverse bias; the latter bias reduces the decay time due to the decrease of the device capacitance [61]. The main noise mechanism in photodiodes is shot noise in the current passing through the diode [40]. Photodiodes display very low dark current

level especially at reverse bias since the depletion layer is quite wide; as a result, leakage current is reduced [41].

3.3.5 Focal plane arrays

In order to utilize any of the previously described UV photodetectors in an UV detector array for imaging purposes, the read out circuitry need to be accounted for in the fabrication technology. A typical approach is to have the device function under backside (i.e. Sapphire surface) illumination to enable the read out circuitry to be connected to the front side. The first report of a successful fabrication and characterization of a GaN based UV photodetector array occurred in 1997, it was a 8x8 GaN Schottky photodiode array [62]. This work was an encouraging first step in the development of UV imaging arrays. The improvement in material growth [63], enabling enhanced material uniformity over 2-in diameter wafers, fostered further development of focal plane array [52, 64-66], refer to Figure 46 for illustration.

In addition, the dimension of the arrays have increased such that p-i-n based photodiodes detector arrays now range from 32x32 [64, 65] too 256x256 [66], while an improved 8x8 Schottky barrier detector array has also been described [52]. Since the progress in p-n and p-i-n based UV photodiode arrays have always been for single wavelength detection; the implementation of a Dual UV-wavelength band detectors will provide an increase in functionality of such an UV imaging system. This system would utilize back-illuminated and p-n photodiodes structures, which have been well understood and characterized [58, 67-69].

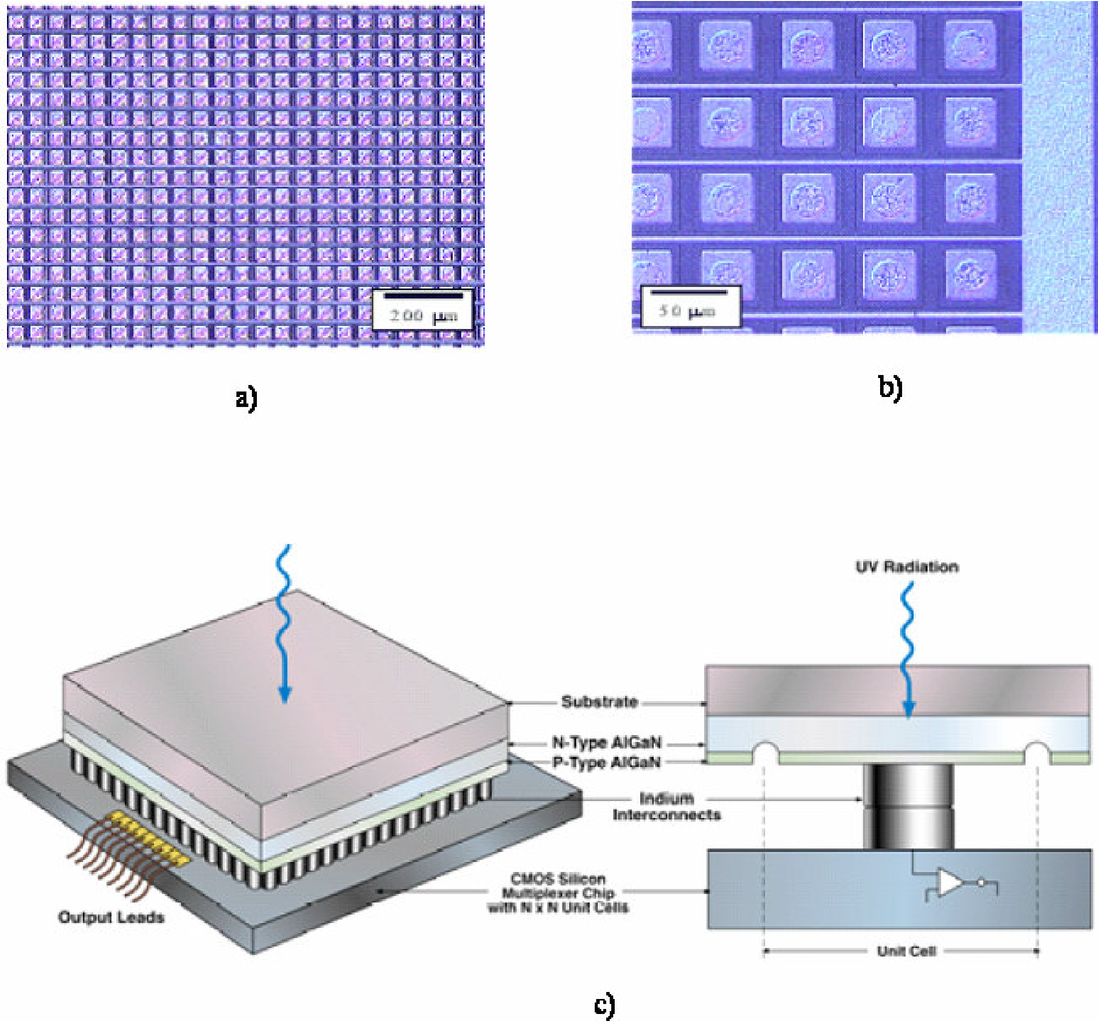

Figure 46: Imaging array, (a) and (b) pictures of a 32x32 GaN/AlGaN photodiode array (from J. D. Brown), (c) hybrid UV Focal Plane Array (FPA), indium bump interconnects to a silicon CMOS read out integrated circuit (from P. Lamarre).

3.4 Structure of Dual-Color UV Imaging Array

3.4.1 Pixel Composition

This thesis project is based on the use of the $Al_xGa_{1-x}N$ confined epitaxy growth method to grow an array of $Al_xGa_{1-x}N$ islands with neighboring pixels using different hetero-structures as shown in Figure 47. Two types of pixels, A pixels (red) and B pixels (blue) are fabricated on the same wafer. The B pixels are grown on continuous layer of $Al_{0.4}Ga_{0.6}N$ covering the double side polished sapphire substrate; while, the A pixels ($Al_yGa_{1-y}N$) are grown on top of the $Al_xGa_{1-x}N$ island used for pixel B. The two growths are accomplished using confined epitaxy growth techniques. The two types of pixels have a p-n / p-i-n like structure. The p layers which for each pixel refer to the layer closer to the top metal contact have a thickness of 0.5µm and are doped p-type while the n-doped layer is the layer in contact with the sapphire wafer and it has a thickness of 1µm.

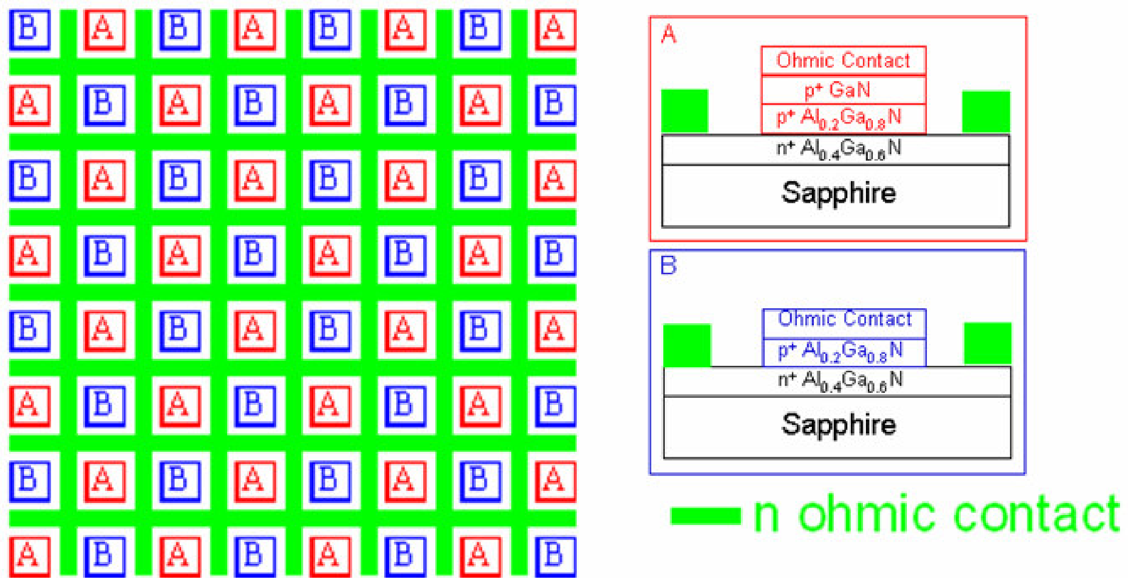

Figure 47: Structure of two-color UV photodiode arrays with one band in UVa and the other band in UVb. The "A" pixel will respond to one band and "B" pixels will respond to another band. The green grid lines are the n-Ohmic contacts.

The chosen pixel thickness was based on absorption calculations described in Appendix A. It was determine that all incidents photon in the UV range, which make it into the material, would be totally absorbed at 0.5μm thickness as can be seen from the absorption curves of Figure 48 (see Appendix A for calculation details). The stoichiometry (i.e. the x and y values of the AlGaN layers) of the layers can be adjusted according to the frequencies that are to be detected. Along the same lines, the stoichiometry of the underlying $Al_xGa_{1-x}N$ layer can be adjusted to generate specific wavelength band sensitivity. The relationship between the stoichiometry of a layer and the optimal detectable wavelength is shown in Figure 49, where the aluminum mole fraction establishes the onset of the cut-off wavelength.

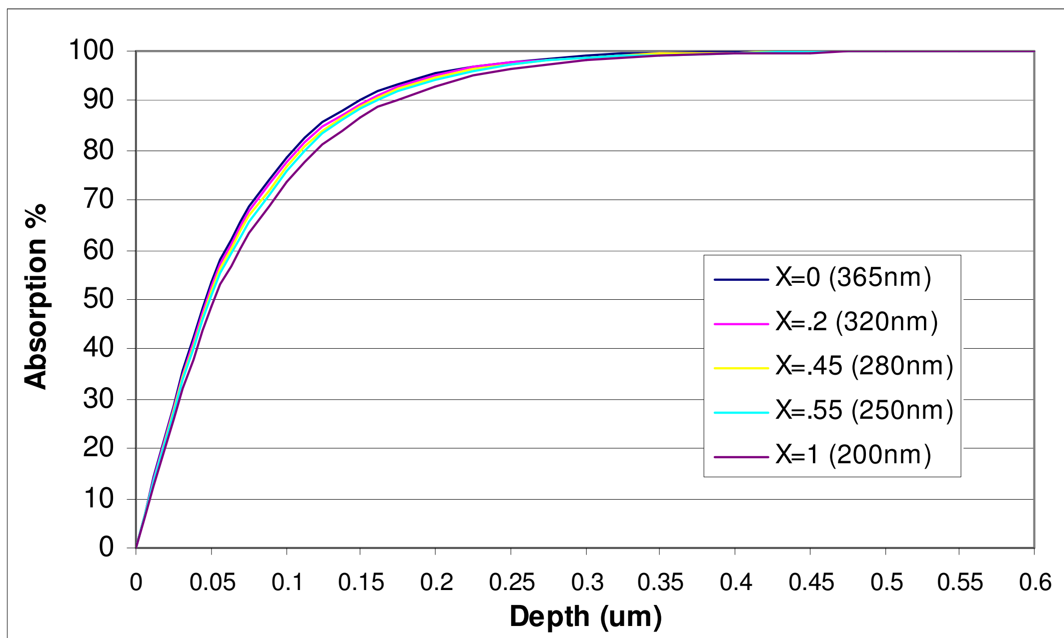

Figure 48: Absorption percentage as a function Al mole fraction and thickness of $Al_xGa_{1-x}N$ layer.

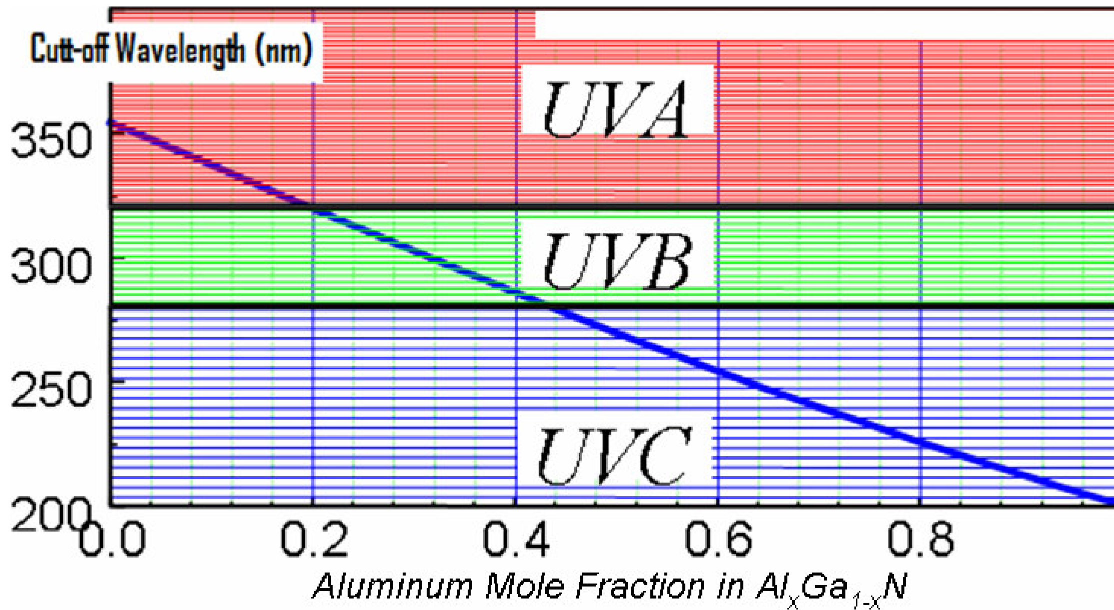

Figure 49: Aluminum Mole Fraction in $Al_xGa_{1-x}N$ (from F. Yun).

The most important thing in setting the stoichiometry is to recognize that the $Al_xGa_{1-x}N$ layer closes to the substrate or continuous/buffer layer must act as high-pass filter for the incident wavelength (photon energy is inversely proportional to wavelength). This bottom layers sets the lowest wavelength that can be detected. On the other hand, the top most layer (A pixel layer $Al_yGa_{1-y}N$) sets the upper limit on the wavelength that can be detected. The stoichiometry of the $Al_xGa_{1-x}N$ layer used for the B pixel should then be between those two to enable dual-color detection. The two UV wavelength band imaging array presented in this thesis are designed to respond to UVa and UVb wavelength. A pixels are designed to respond to UVa radiation and “B pixels are designed to respond to UVb radiation. For A pixels, x and y are 0 and 2, respectively, while for B pixels, x is 0.2.

Back-illumination is used and photons are injected from the sapphire side. When the wavelengths of incident photons are shorter than the cut-off wavelength of bottom layer (incident energy > bandgap), most of the photons will be absorbed in this layer

because of the very high absorption coefficient of $Al_xGa_{1-x}N$, $>10^5$/cm. Since the carriers generated in the bottom layer will mostly be shielded from the top contact by the very high doping in the top layer, the photo-response / UV induced noise is very weak. When the wavelength is longer than the cut-off (incident energy < bandgap) of the top layer, no photon absorption occurs in the detectors and there is no photo-response. Only the photon between the cut-off wavelength of the bottom and top layers can be intercepted and collected effectively. Therefore, an intrinsic bandpass filter forms naturally for the selected bands. The bandwidth can be tuned according to the application requirements. In this thesis, the chosen stoichiometries sets the detection bands to approximately (320nm-355nm) for pixel A and (280nm-320nm) for pixel B.

3.4.2 $Al_xGa_{1-x}N$ Growth Technique

There is an extremely high, by semiconductor standards, vertical threading dislocation in III-nitride semiconductor materials. With no commercially viable native substrate technology on the horizon, heteroepitaxy and their associated extended defects will continue to hinder the application of the material to promising device technological areas. The origin of defects found within $Al_xGa_{1-x}N$ films is mechanical stress in the growth. When the stress exceeds some critical level, the crystal strains resolve themselves as defects—largely threading dislocations. The confined epitaxy (CE) technique used in this thesis work, on an appropriate scale, is a good approach to reduce extended defect densities in the active regions of vertically conducting AlGaN devices.

This approach is significantly different from common metal-organic vapor phase epitaxy (MOVPE) and molecular beam epitaxy, which are growth techniques commonly employed for $Al_xGa_{1-x}N$ thin films. In common growth methods, two techniques yield $Al_xGa_{1-x}N$ films with reduced dislocation density; lateral epitaxial overgrowth (LEO) and pendeoepitaxy (PE) both making use of MOVPE. The idea in both approaches is as follows:

- **Lateral Epitaxial Overgrowth (LEO)** involves the masking of a continuous III-nitride surface with either a silicon dioxide or a silicon nitride film/mask. Then, the deposit material grows vertically within the patterned area till the top of the mask then laterally over the mask as can be seen in Figure 50(a) [63]. The dislocation density in the overgrown part of the film is quite reduced compare to the original "seed" area. In order to take advantage of the reduction in defect concentration, devices must be placed in these overgrown areas.

- **Pendeoepitaxy (PE)** is also an overgrowth process with the difference that the desired active layer pattern is etched directly into the substrate/buffer film forming a stripe "seed". The $Al_xGa_{1-x}N$ film is grown vertically and laterally off the striped area as illustrated in Figure 50(b). Once again, it is the laterally grown part of the film that displays a decrease in dislocation density [63]. However, only a small fraction (lateral portion) of the grown film is suitable for device fabrication.

Although both methods offer a decrease in dislocation density, the grown films are suspended and the topology of the wafer surface becomes considerably non-

planar. Furthermore, the devices have to be fabricated on top of this topography; consequently, these approaches are inefficient for any integrated device manufacturing technology. Hence, a growth process more suitable for easy integration in common fabrication processes has to be considered; confined epitaxy (CE).

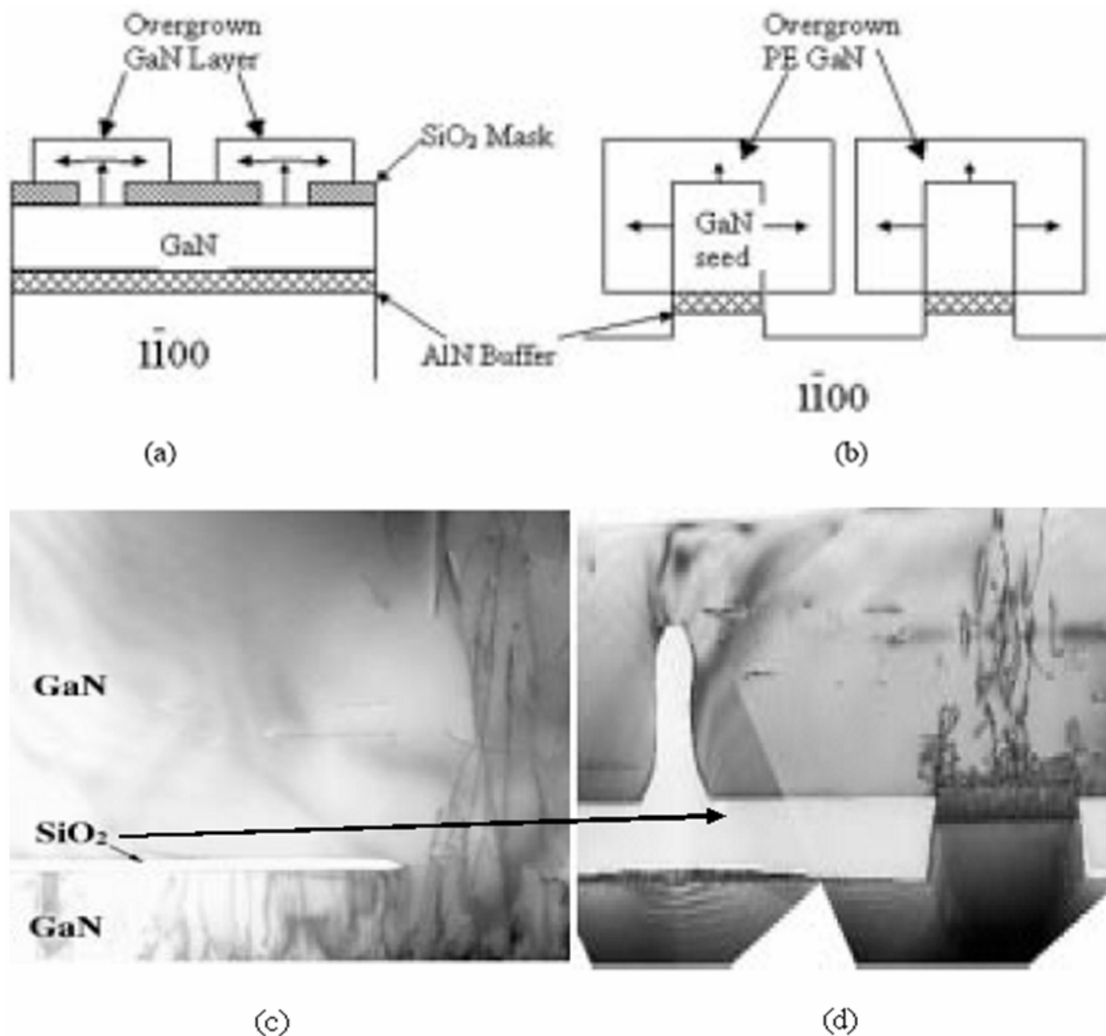

Figure 50: Schematic of growth technique (from R. F.Davis) of (a) LEO growth through a window in SiO2 and laterally over the mask. (b) PE growth from GaN seed laterally off the sidewalls and vertically off the stripe. (c) TEM of LEO GaN film. (d) TEM of PE grown GaN film.

The procedure for growing low defect regions by confined epitaxy is as follows: a conventional, GaN film is deposited on an entire *a*-plane sapphire wafer. This film is then patterned with resist such that only the areas in which confined epitaxial growth is to occur are covered. The wafer is then blanketed by a layer of reactive sputtered silicon dioxide of about 500nm thickness. A lift-off technique is subsequently employed to remove oxide from the areas in which III-N is to be grown. A dilute sulfuric acid etch can then be used to clean up any residual resist left in the epitaxy openings.

In the case of growth on *r*-plane sapphire, the oxide mask is formed with the same lift-off technique directly on the sapphire substrate. Before introduction into the chemical vapor deposition reactor for CE growth, the sample is solvent cleaned. The nitride will not grow on the oxide—only on the UV window layer (epitaxy openings). The crystallite is grown out to the edge of the oxide window with no lateral growth taking place. Instead, the edges of the grown films are slanted inward (see Figure 51). The crystal never gets large enough to achieve strains sufficient to form dislocations.

The confined epitaxy growth approach patented jointly by the Naval Research Laboratory (NRL) and the University of Maryland is utilized in this thesis as a way to realize two-color UV detector arrays with III-V nitride semiconductors. Confined epitaxy has demonstrated several advantages over the more traditional approach of stacked junctions growth described previously in this chapter. By using confined epitaxy growth, a considerable strain reduction is achieved in the material grown relative to a continuous film. This reduction in strain is partially due to the size of film and the slant on their edges.

Micro-Raman measurements show a reduction in strain of over 50% in the selectively grown region as seen in Figure 52. The shift to the left (red and green curve relative to blue) observed in Figure 52 identifies a decrease in strain; since the curve for the 10 and 20µm mesa are getting closer to the strain free curve (black curve). In addition, a significant reduction in threading dislocation densities has been demonstrated with nearly an order of magnitude improvement from the mid-10^9 cm^{-2} range to the mid-10^8 cm^{-2} range over only 0.15µm thick layer of grown $Al_xGa_{1-x}N$ as can be observed in Figure 51. Since these defects have been identified as preferred vertical leakage paths in this material system, such reductions will have a significant impact on the performance of vertical devices, e.g. UV detectors [5].

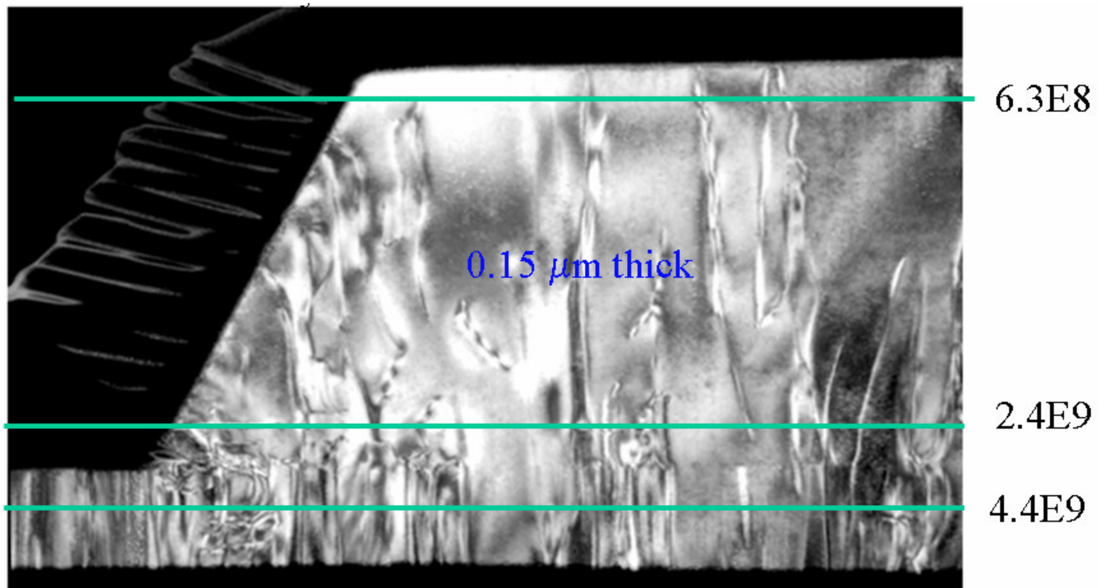

Figure 51: Dark-filed XTEM micrograph of dislocation structure in confined epitaxy grown homoepitaxially on a continuous GaN film on sapphire. Dislocation density reduction from $4.4*10^9/cm^2$ to $6.3*10^8/cm^2$

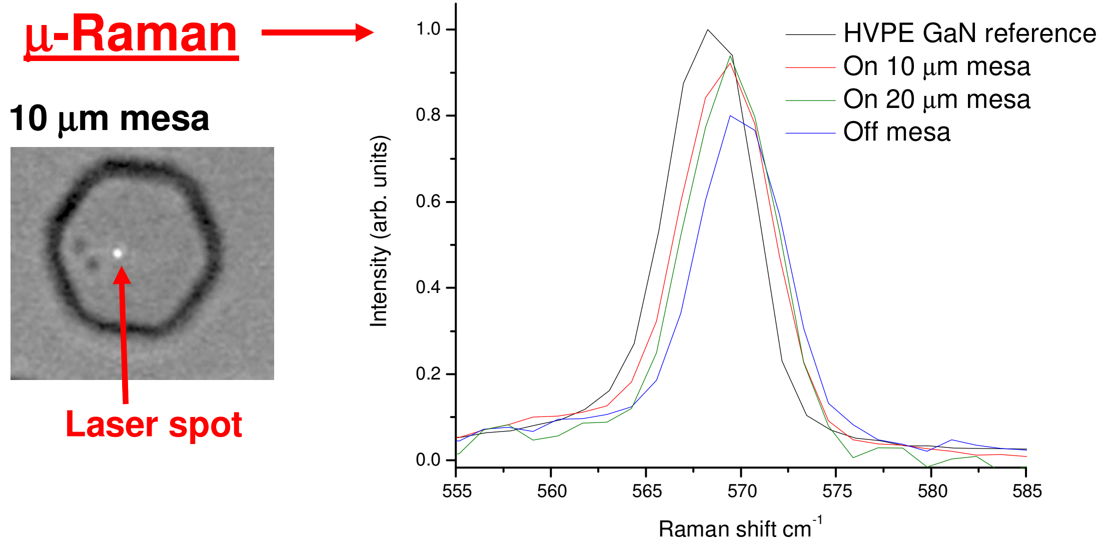

Figure 52: MicroRaman data showing strain reduction in selectively grown GaN material. Blue curve is for continuous GaN layer beneath the selective epitaxy region and black curve is for a free-standing GaN substrate (presumably strain free). Selectively grown mesas show approximately 50% reduction in strain. Inset shows laser spot size relative to selectively grown mesa size. (Data courtesy of Orest Glembocki, NRL)

Confined epitaxy growth in combination with the lift off process is believed to be the only way to achieve high-performance, two-color UV detectors employing the III-V nitride family of semiconductors [4, 5, 35]. It enables the growth of high aluminum mole fraction material with reduced strain to allow thicker absorption regions without fear of high dislocation densities. Confined epitaxy growth in combination with lift-off lithography permits the creation of devices without the need for plasma etching which induces layer interface damages that lead to increased leakage and higher contact resistance.

3.4.3 Lift-Off Process

"Lift-Off" lithography is a method used to make metallic patterns on a substrate for noble metal thin films which are difficult to etch with conventional methods. In the case of this work, "lift-off" is used to pattern an insulator (oxide). However, the general idea is still the same and is illustrated in Figure 53. First, a pattern is defined on a substrate using, in my case, positive photoresist (Shipley-1813) and a sacrificial lift-off layer (LOL-2000) [70]. LOL-2000 lift-off layer is a non-photosensitive film that dissolves in photoresist developer in a controlled way [71]. Then, everything around the patterns of interest (hexagonal pixels) is stripped and an insulating film is deposit all over the wafer, covering the area stripped and those still containing photoresist as illustrated in Figure 53(d).

The actual lift-off occurs when the film covering the photoresist/LOL-2000 layers (hexagonal patterns) is removed with solvent, in effect, lifting off part of the insulator and leaving only the film deposit on the previously exposed substrate as can be seen in Figure 53(e). Finally, the fabrication process continues with the growth of an $Al_xGa_{1-x}N$ film on the hexagonal patterns using confined epitaxy growth method. The quality of the $Al_xGa_{1-x}N$ film will impact the effectiveness of the diode pixels as it will dictate the defect concentration; hence, leakage current.

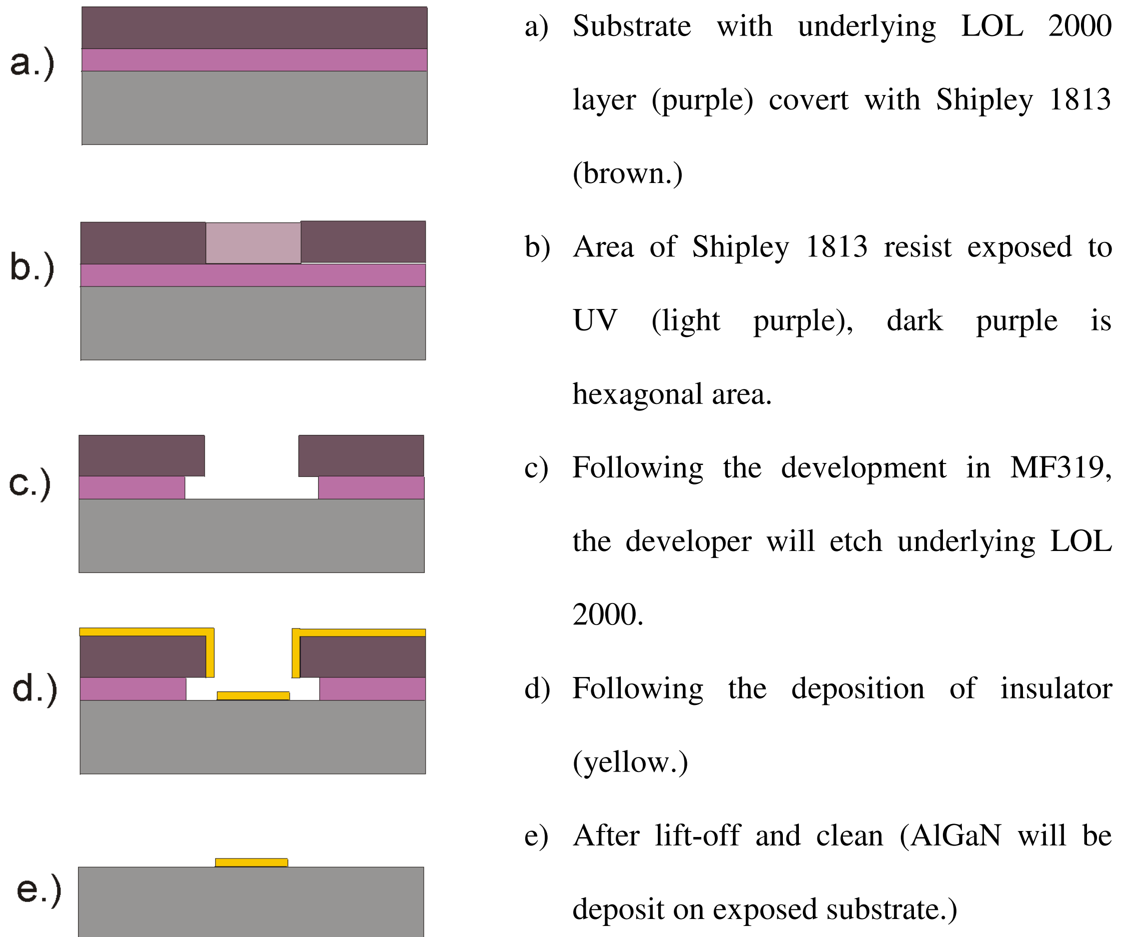

Figure 53: General two layer lift-off procedure (from Stanford Nanofabrication).

3.4.4 System Assembling

One of the major considerations in the design of the detector array is the way the system is assembled. The detector array is used in backside illuminated mode. The light is incident on one side of the double side polished sapphire wafer while the active devices and read-out electronics are placed on the other side. The read-out integrated circuit (ROIC) used is the 256 x 256 PICNIC chip from Rockwell

(Teledyne). The chosen ROIC fixes the minimum size of the detector pixels since the ROIC is bump bounded right on top of the detector array. The ROIC square pixel size is 50μm on each side while the confined epitaxy growth technique utilized in this thesis requires the use of hexagonal pixels (matches the crystal structure of $Al_xGa_{1-x}N$) of size less than 30μm. The 30μm limitation on the size of hexagonal pixel structure is due to the fact that the stress in the grown film increases as the $Al_xGa_{1-x}N$ grown films gets larger; as a result, the defect concentration is proportional to the pixel size [5].

Once the sensor detects a UV signal in the frequencies of interest, a current is generated. The goal of the read out circuitry is to generate a voltage, in response to the current output of the photodiode, and stream it out to a data acquisition unit. This is accomplished via the Rockwell PICNIC 256x256 ROIC. The properties of the ROIC are tabulated in Table 11, where SFD refers to source follower inputs. The output of each pixel is indium bonded to the input of one source follower. The display unit constitutes the final stage of the UV imaging array. The ensuing voltage will be streamed out via 4 output ports. The streamed signal is collected and displayed.

Table 11: Rockwell PICNIC chip properties (from Rockwell)

Parameter	Specification
Detector technology	HgCdTe (PACE)
Detector input circuit	SFD
Readout mode	Ripple (per quadrant)
Pixel readout rate	Up to 200kHz
Pixel format	256 x 256
Pixel Pitch	40 μm
Fill factor	>90
Output ports	4 total (1 per quadrant)
Spectral range	0.9 - 2.5μm
Quantum Efficiency @ 2.3μm	>75%
Read noise: multiple sample	<20
Dark current	<0.2 e-/sec (@77K)
Well capacity	200,000 e-
Pixel operability	>99%

3.5 Fabrication Process Flow

I fabricated from ground up the detector system presented so far. The design starts with a double side polished sapphire wafers. The entire masks needed to fabricate the detector array were all designed. The masks were then employed to generate a fabrication process flow for the detector array. This section presents the details of the creation of a dual UV-wavelength band detector array. I will first present the lithographic mask used in the fabrication. Then, a fabrication process flow will be shown followed by a description and explanation of some of the processing steps.

3.5.1 Mask Design

The main consideration in the mask design was that positive photoresist was to be used and that the hexagonal area used for color pixels active film growth were not to be exposed during lithography. The hexagonal shape of the $Al_xGa_{1-x}N$ mesa was chosen because it accommodates the hexagonal crystal structure of the alloy thereby also reducing strains in the film. The mask system was composed of six masks. Starting from the mask used for the lowest layer, the six created masks are:

Mask #1, Color 1 Hex: Comprised of arrays (256x256) of hexagonal patterns used to define the area that will contain pixel B (light blue layer in Figure 54). This is the larger one of the two types of hexagonal islands.

General characteristics of the mask:

- First used mask
- Mask used to pattern area where color 1 ($Al_{.2}Ga_{.8}N$) will be grown
- Mask used for LOL 2000 lift off
- Dark field mask (do not expose drown area / drown area covered with chrome on the mask)

Mask #2, Color 2 Hex: Comprised of arrays (128x128) of hexagonal patterns used to define the area that will contain pixel A (layer made out of black crossed lines in Figure 54). Patterns in this mask are located on top of every other pixel B pattern from Mask #1.

General characteristics of the mask:

- Second used mask

- Mask used to pattern area where color 2 (GaN) will be grown
- Mask used for LOL 2000 lift off
- Dark field mask (do not expose drown area / drown area covered with chrome on the mask)

Mask #3, n-metallization: Comprised of crossing lines through and around the 256x256 pixels used to define the area for metallic contact to the underlying n-type $Al_{.2}Ga_{.8}N$ (green layer in Figure 54).

General characteristics of the mask:

- Third used mask
- Mask used to etch all oxides (create trench down to n-layer)
- Mask used to perform n-metallization lift-off
- Light field mask (expose drown area / drown area uncovered on the mask)

Mask #4, via: Comprised of arrays (256x256) of square patterns used to define via necessary to gain access to the underlying hexagonal detector layers (dark grey layer in Figure 54).

General characteristics of the mask:

- Fourth used mask
- Mask used to wet etch via to color 1 & 2 detector surfaces
- Mask used to delimitate areas for p-metallization
- Light field mask (expose drown area / drown area uncovered on the mask)

Mask #5, Contact Pads: Comprised of arrays (256x256) of square patterns used to define p-type ohmic contact to the hexagonal detectors (dark blue layer in Figure 54).

General characteristics of the mask:

- Last used mask (at UMCP)
- Mask used for p-metallization (onto color 1 & 2)
- Mask used to lift-off p-metallization
- Mask used after via has been wet etched
- Light field mask (expose drown area / drown area uncovered on the mask)

Mask #6, Indium Bump: Comprised of arrays (256x256) of square patterns used to define indium bump location for hybridization with the ROIC (light grey layer in Figure 54).

General characteristics of the mask:

- Last mask of entire process (used by Rockwell/Teledyne)
- Mask used to deposit indium bumps
- Used with negative photo resist (exposed area stays)
- Dark field mask (do not expose drown area / drown area covered with chrome on the mask)

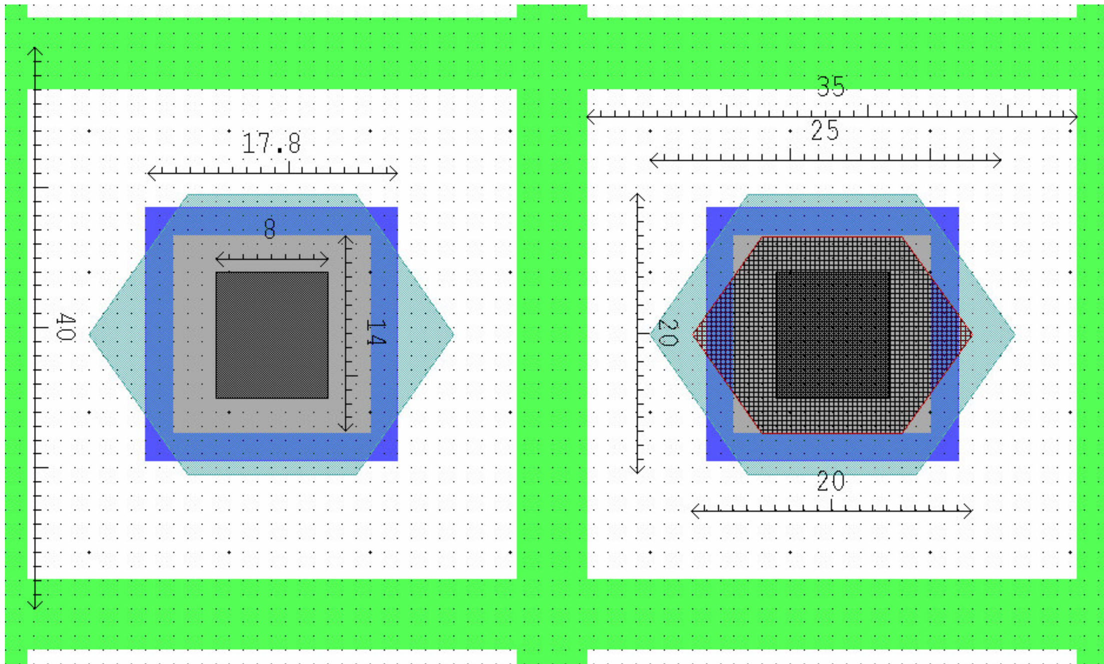

Figure 54: GDS image of two pixels (pixel B on the left and pixel A on the right) with all dimensions in µm.

3.5.2 Fabrication Steps

The fabrication steps for the creation of dual UV-wavelength band detector array dies starts with a 2" double side polished sapphire wafer. Phase I of the fabrication steps is illustrated in Figure 55. Phase I covers the deposition of all the active layers to be used for the detectors. The fabrication steps of phase I commences with a double side polished sapphire wafer on which a buffer/seed layer of $Al_{.4}Ga_{.6}N$ is grown as shown in Figure 55(a). Then LOL 2000 and photoresist are spun on the seed layer and subsequently patterned to uncover the surroundings of the hexagonal areas to be used for color 1, see Figure 55(b) and (c). Once the seed layer is selectively uncovered, an oxide film is sputtered on the wafer then the LOL 2000 and photoresit are lifted-off to reveal hexagonal windows to the seed layer. In these

windows, the active layer for color 1 ($Al_{.2}Ga_{.8}N$) is grown, these steps are presented in Figure 55(d)-(f).

The patterning of color 2 is illustrated in Figure 55(g) - (k). Color 2 material (GaN) is grown selectively over half of the $Al_{.2}Ga_{.8}N$ areas. First, LOL 2000 and photoresist are spun on the wafer then subsequently patterned to uncover the surroundings of the hexagonal areas to be used for color 2, Figure 55(g) and (h) illustrate these steps. Once half of the color 1 ($Al_{.2}Ga_{.8}N$) areas are selectively uncovered, an oxide film is sputtered on the wafer as shown in Figure 55(i). After that, the LOL 2000 and photoresit are lifted-off to reveal hexagonal windows to the underlying $Al_{.2}Ga_{.8}N$ layer; in these windows, the active layer for color 2 (GaN) is grown as presented in Figure 55(j) and (k). Phase I is completed with a sputtered layer of oxide to seal all the detectors; this is illustrated in Figure 55(l). The latter step sets the stage for phase II of the fabrication process.

Phase II of the fabrication process centers around the metallization steps. This phase starts with all the active areas covered by oxide as in Figure 55(l) and Figure 56(a). A combination of LOL 2000 and photoresist (Shipley 1813) is used to mask/pattern the wafer as well as enable lift-off of the evaporated metals. Once again, the process calls for successive layers of LOL 2000 and photoresist to be spun on the wafer for lift-off application as shown in Figure 56(b). Wet etching is then used to create via to the n-doped seed layer (see Figure 56(c)); subsequently, ohmic contacts are made to the n-doped layer by evaporating layers of Ti/Al/Ti/Au and patterning them through lift-off, the steps are presented in Figure 56(d) and (e). The same process steps are then conducted to create ohmic contacts to the p-type AlGaN alloy

as illustrated in Figure 56 (f) and (g). Phase II is concluded with the deposition of indium bumps to be used for read out IC hybridization. This later step is conducted by a vendor (Teledyne).

Once received by Teledyne, the wafer is processed for flip chip bonding as illustrated in Figure 57. First, my wafer is masked such as to expose my metal pad (see Figure 57(a)). Then, solder dots are deposited on each of the metal pads (see Figure 57(b). Following that, the wafer is diced and the chips are flipped and positioned so that the solder balls are facing connectors on the read out circuitry (see Figure 57 (c), (d) and (e)). The solder balls are then remelted, usually using ultrasound, (see Figure 57(f)). Finally, the mounted chip is “underfilled” using an electrically-insulating adhesive (see Figure 57(g) and (h)). What I receive back from Teledyne is a FPGA (read out integrated circuit—ROIC) bonded to my detector array. The entire package has a structure similar to the illustration in Figure 58. At this point the imager is ready for system testing.

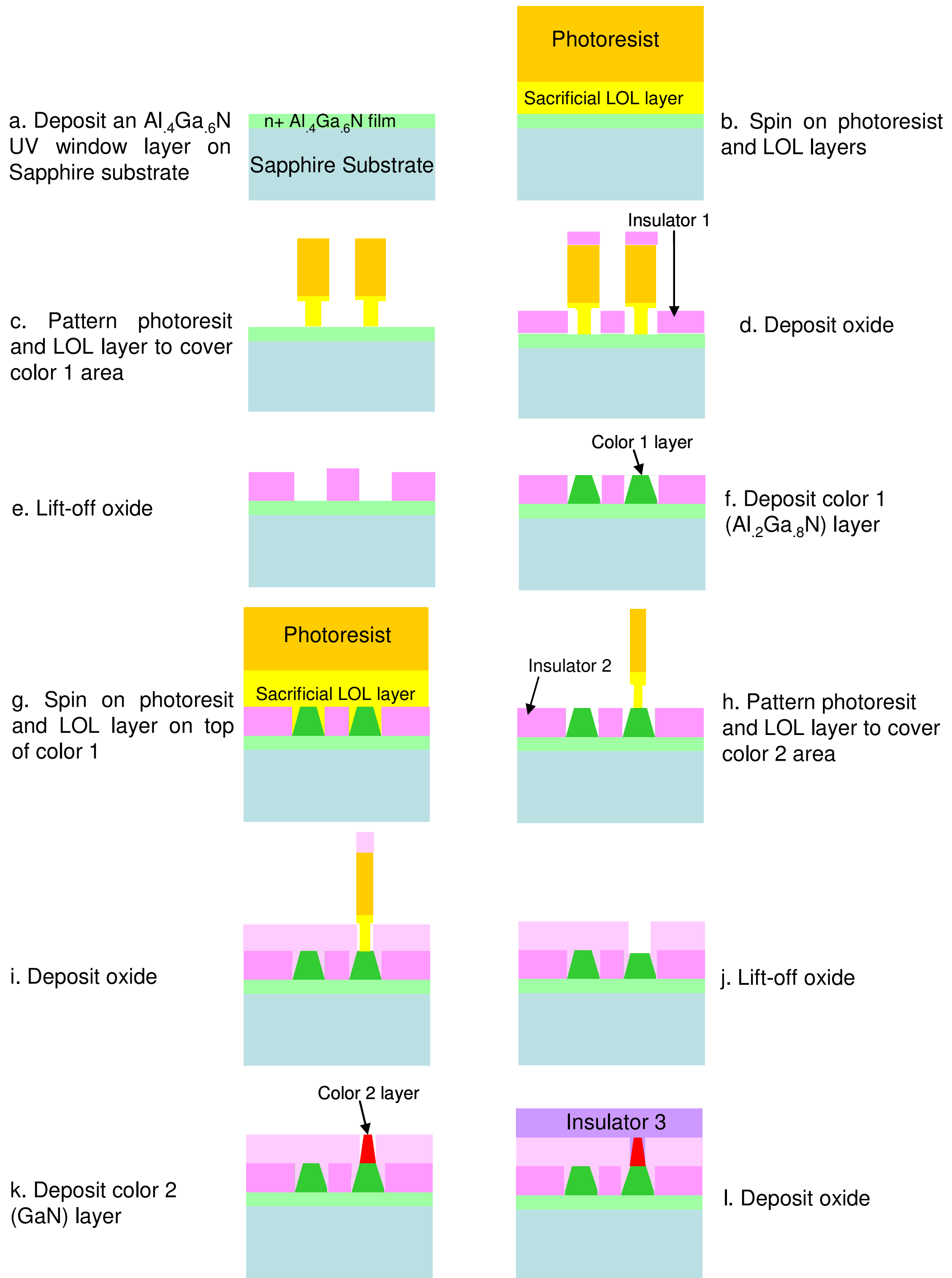

Figure 55: Phase I of processing flow

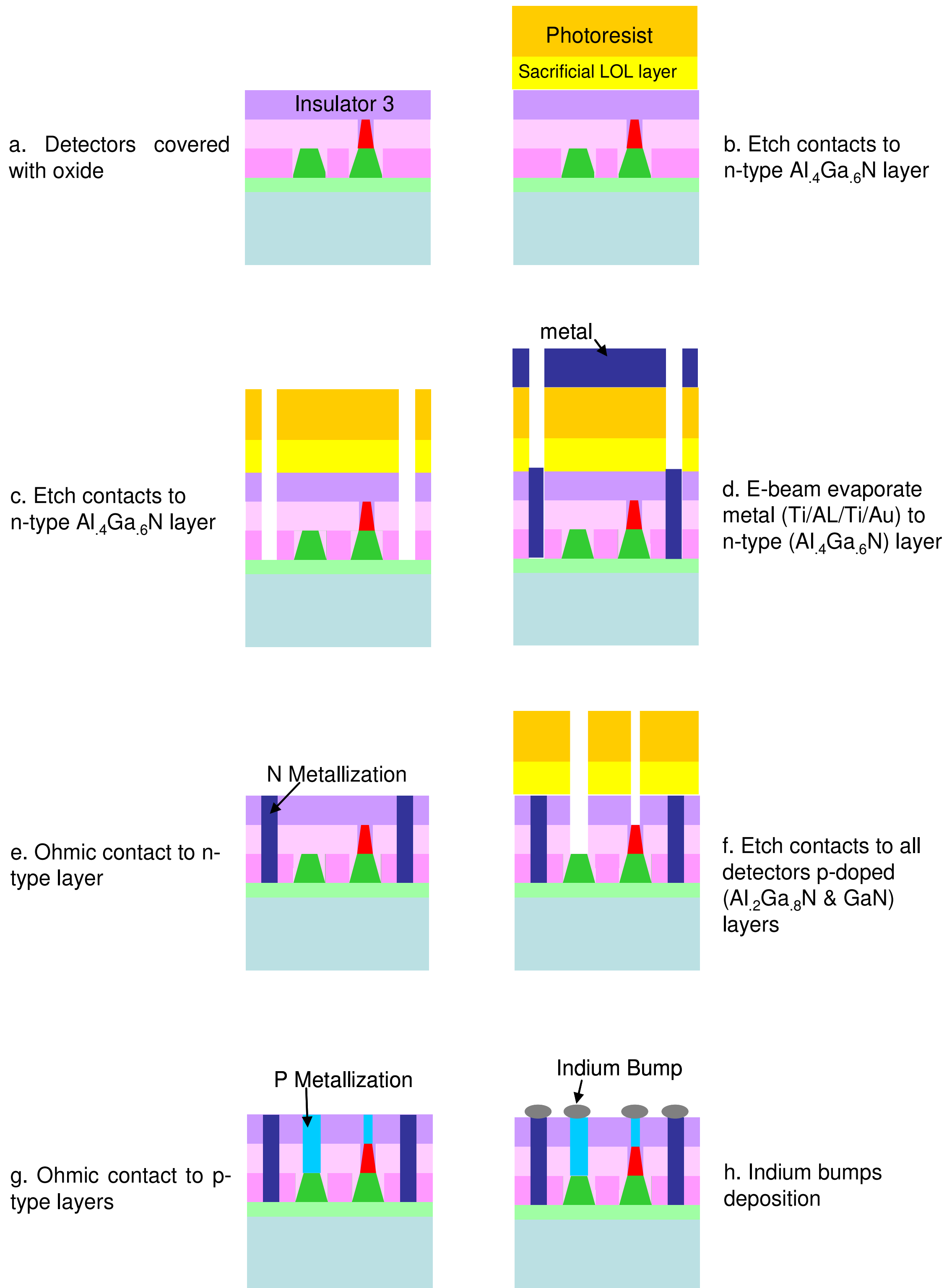

Figure 56: Phase II of processing flow

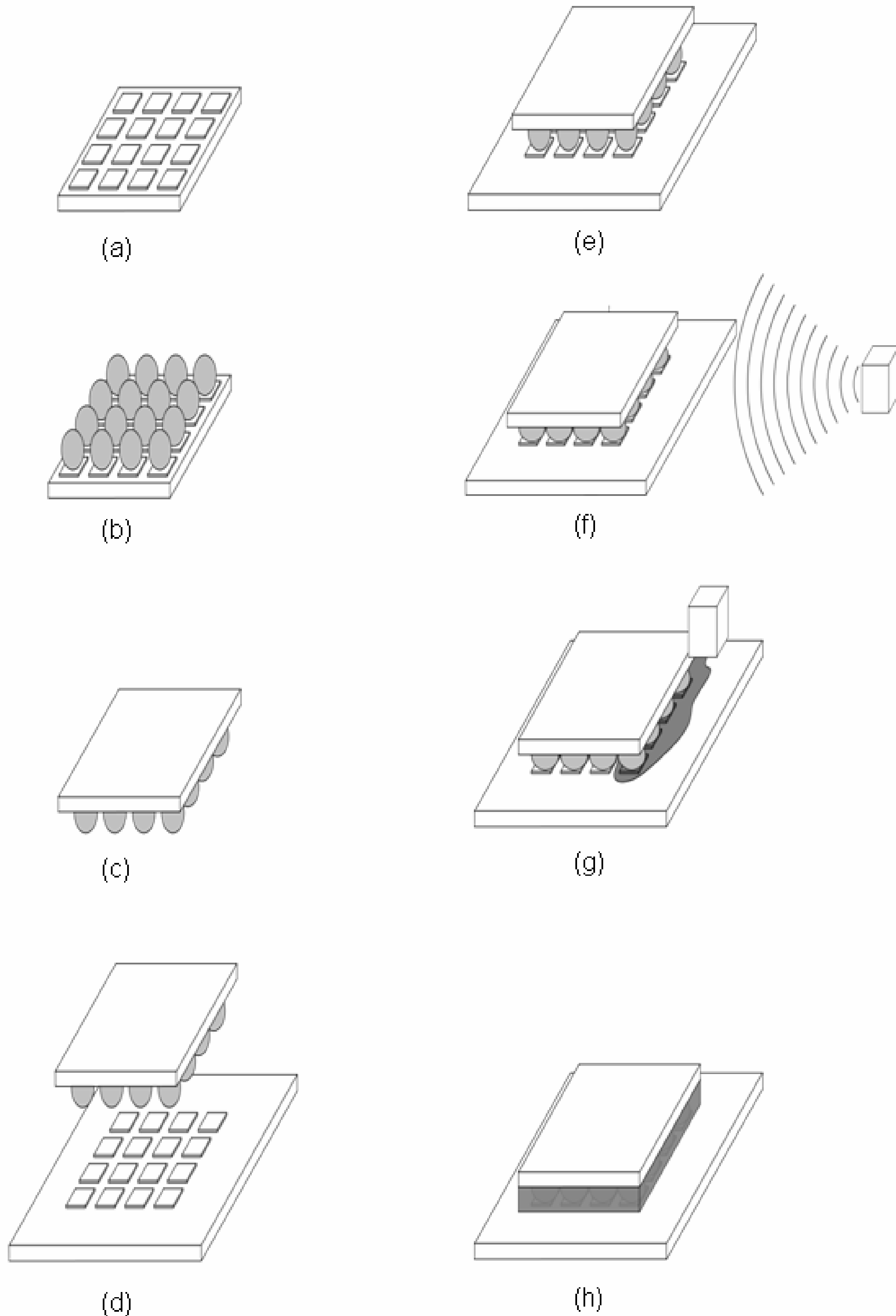

Figure 57: Schematic of flip chip bonding (from Wikepidia); (a) pads are metalized on the surface of the chips; (b) solder dots are deposited on each of the pads; (c), (d) and (e) chips are flipped and positioned so that the solder balls are facing connectors on the external circuitry; (f)solder balls are then remelted; (g) and (h) mounted chip is "underfilled"

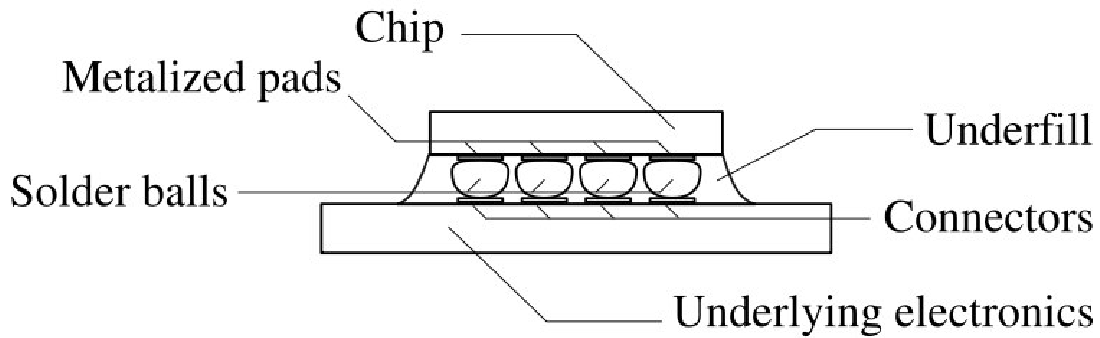

Figure 58: Cross section schematic of a typical flip chip mounting (from Wikepidia).

3.5.3 Processing Guide

This sub-section offers the processing details and explanation for the process flow outlined in the previous sub-section. The exact duration of all the process steps are detailed in Appendix B. In phase I, the processing flow requires the use of LOL 2000 and positive photoresit (Shipley 1813) for patterning and lift-off purposes. The photoresist is spun at 4000rpm; however, the LOL 2000 is spun at 1500rpm, since LOL 2000 is quite fluid. Spining LOL 2000 at 1500rpm yields a layer with only about 350nm thickness. Hence, two layers of LOL 2000 need to be spun one on the other to generate a total LOL 2000 film thickness of ~700nm. This thickness facilitate a successful lift-off of a 0.5µm thick film of sputtered oxide. Both LOL 2000 films are softbaked individually. The fist layer is sofbaked for 5min and the second layer for 7min. The later layer is softbaked longer to permit good heat absorption throughout the total film.

The size of the hexagonal detector used for color 2 are much smaller than the size of the hexagonal detector used for color 1. This is done because color 2 detectors have to fit over the area used for color 1. This is most apparent with the process wafer, see Figure 59. Figure 59 shows a picture of a portion of an array post phase I

of the fabrication process flow. Pixel A is the smaller hexagonal that fits on top of a bigger hexagonal (pixel B).

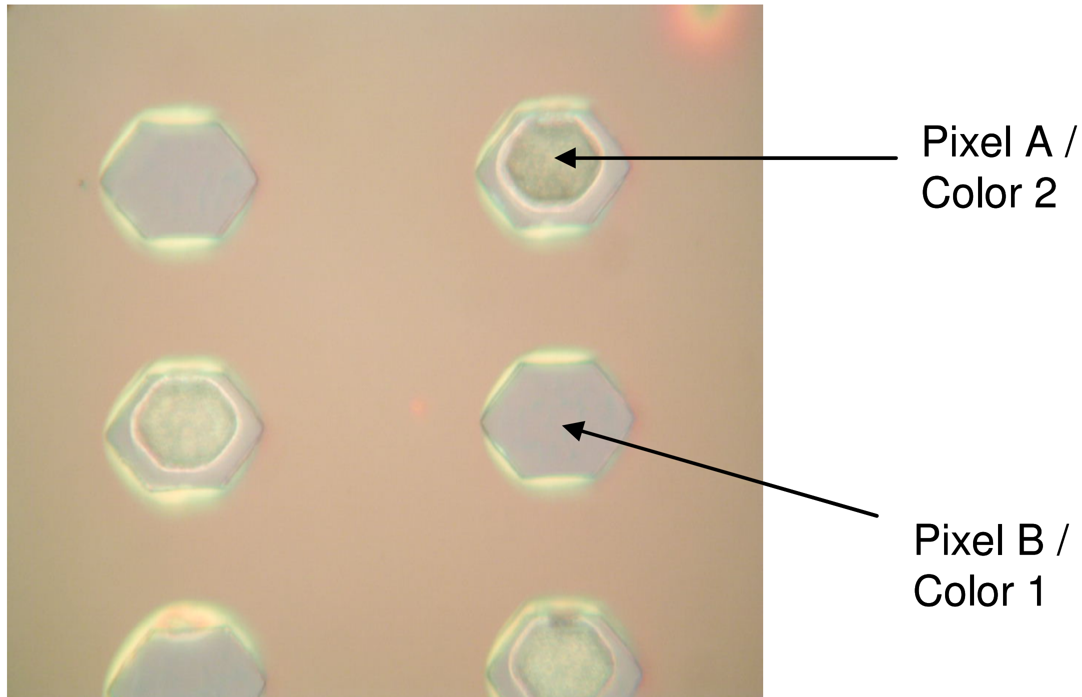

Figure 59: Micrograph of detector pixels after completion of Phase I of the fabrication process flow

In phase II, the processing flow demands that the etching through the oxide is done via wet etch. Wet etching ensures that there is no interface damage. The metal contacts are pattern via lift-off. For the contact to the n-doped alloy (n-metallization), the photoresist used for wet etching is also used to lift-off the metal. The n-metallization contact is generated by stacking multiple metal layers. Starting with the metal layer in contact with the n-doped alloy, the deposit contact was made of Ti(20nm)/Al(45nm)/Ti(100nm)/Au(450nm). The entire thickness of the different metal layers should be less than 700nm (thickness of LOL 2000) to ensure that I will have a successful lift-off.

Annealing in nitrogen is better than annealing in air. Longer anneal result in slower decrease; however, long anneal could lead to some nitrogen migration in the layer. The Ti/Al/Ti/Au metallization sequence and thicknesses are carefully designed. The first Ti layer is used to assure adhesion and to react with residual surface oxide by forming TiO_2 (an oxide that has lower bandgap, 3.05eV than $Al_{.4}Ga_{.6}N$). The Al layer interacts with nitrogen in $Al_{.4}Ga_{.6}N$ and result in formation of Ohmic contact to the $Al_{.4}Ga_{.6}N$. With the Ti/Al combination low-resistance contact is obtained after Al diffuses through the surface Ti layer. The anneal time is reduced for thinner Ti layer. The second Ti layer forms a oxygen barrier by interacting with the Al beneath it during anneal to form $TiAl_3$ which acts as an oxygen diffusion barrier to inhibit formation of surface oxides of Al or Ti [72]. A 600°C anneal for 30 sec in an N_2 environment was conducted.

Metals with high work function were usually chosen to form the ohmic contact on p-type GaN in order to obtain low-resistance electrodes for devices, these metals included Au, Ni, Pt and Pd [73]. Presently, the contacts are primarily made by associating those metals with Au such as Ni/Au, Pt/Au, Pt/Ni/Au. The ohmic contact to the p-doped AlGaN alloys (p-metallization) is obtained by using a film of Ni(50nm)/Au(450nm). The contact was annealed at 500°C in an N_2 environment for 5min. Once the n-metallization and p-metallization steps are completed, as shown in Figure 60, the wafers are ready for the indium bump deposition, die dicing and hybridization to the read-out IC. After this processes, full system testing can commence.

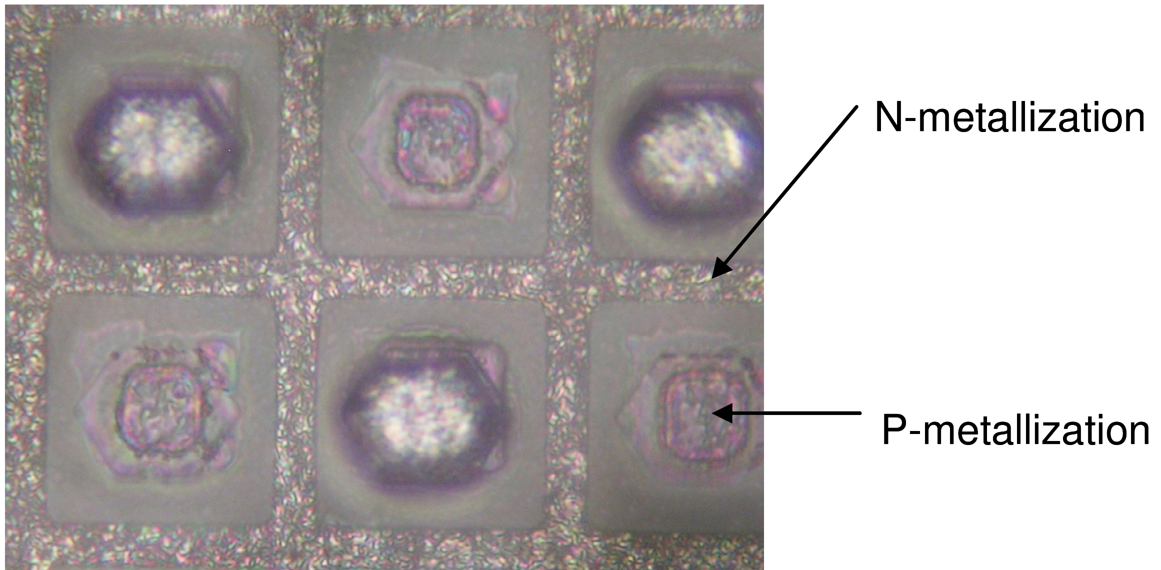

Figure 60: Micrograph of detector pixels after completion of Phase II of the fabrication process flow

3.6 Testing

This section covers characterization efforts used to evaluate the fabricated detector array. The array of detectors is tested electrically and optically by examining single pixels. Then, the imager is evaluated by testing the operation of the entire array and the read out circuitry.

3.6.1 Electrical Evaluation

From an electrical testing standpoint, a current versus voltage (IV) analysis and a detector noise measurement are conducted for a set of detector pixels. For the I-V measurements, a low-noise probe station and a parameter analyzer are used to measure DC current as voltage is swept across the devices. The test enables to determinate if the detector shows diode like behavior, its turn-on voltage as well as the dark current level. Figure 61 shows IV plots for color 1 and color 2 detectors where current is expressed as current density. The area of tested pixel is $3.14*10^{-4}$

cm^2. Both types of detectors demonstrate diode like behavior. The characteristics of the two types of detectors are described in Table 12. The leakage current at 1.5V reverse bias is of 10µA/cm^2 and 0.15µA/cm^2 for color 1 and color 2 detectors; respectively.

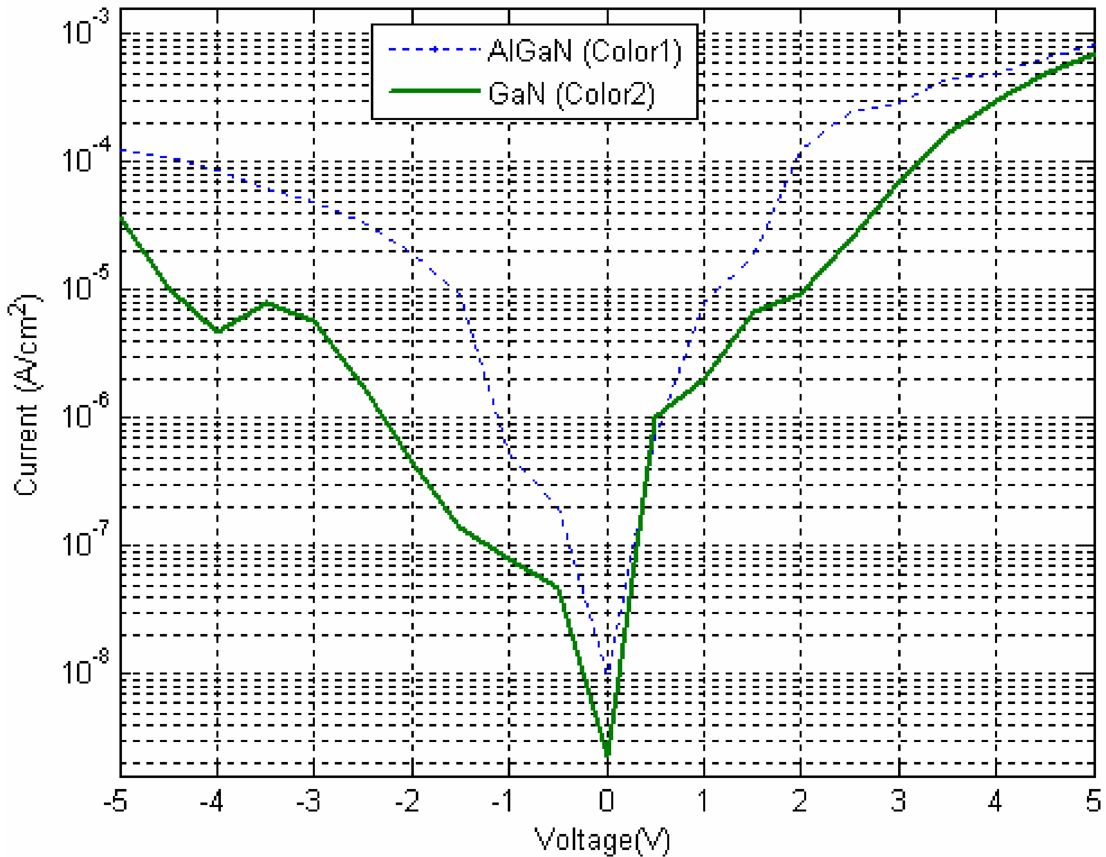

Figure 61: Current vs. Voltage plots of Color 1 and Color 2 pixels

Table 12: Characteristics of detectors

Noise Level (A)	Signal Level (A)	S/N ratio
$46.9*10^{-9}$	$237*10^{-9}$	5.04

3.6.2 Optical Evaluation

The detector pixels are tested optically for spectral responsivity. Spectral responsivity measurements is completed on a select group of detector pixels utilizing a xenon lamp as a UV source and the UV wavelength is selected by a monochromator

calibrated with a UV-enhanced Si photodetector. Varying the incident light wavelength from 300nm till about 400nm enables the determination of the detection band of the various pixels; thereby, demonstrating the systems ability to detect two different frequencies. The setup for such measurements is schematically represented in Figure 62 .

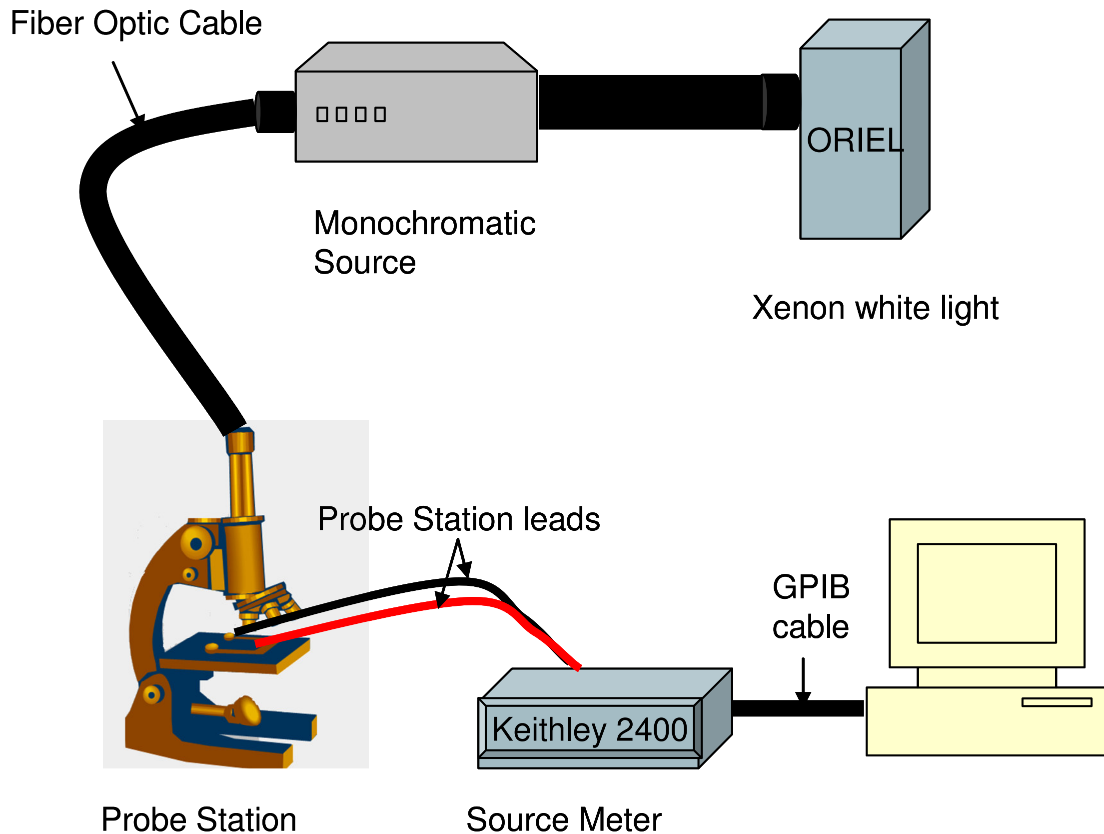

Figure 62: Setup of optical evaluation of pixels

IV curve of the different detectors reveals (as expected) a change in current level between the IV curves recorded with UV-light illuminating the detector and in absence of the UV-light (current referred to as dark current). The difference between the illuminated and non-illuminated diode is better observed when the diode is

reversed bias since in this regime the current does not increase as rapidly as it is the case in forward (positive) bias in response to change in voltage. Figure 63 shows the difference between the IV curve of the detector while illuminated with UV-light and in absence of illumination.

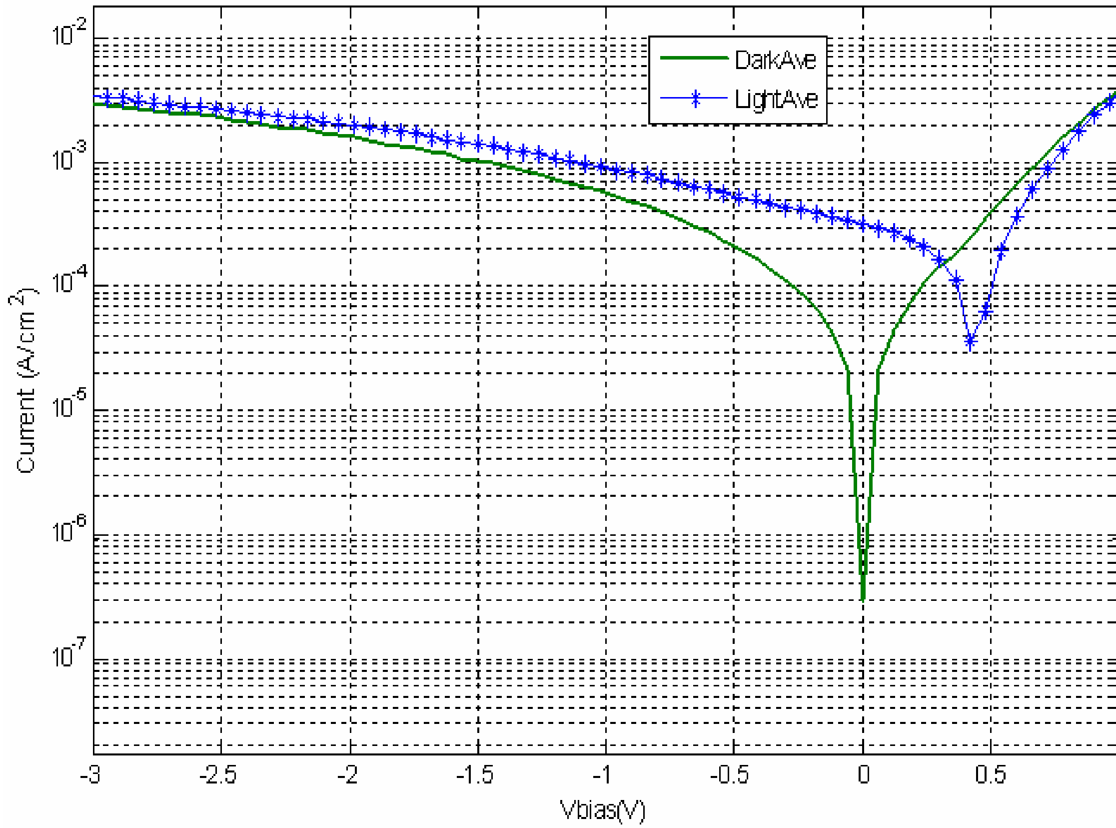

Figure 63: IV characteristics of diodes in absence (dark) and presence (light) of UV-illumination.

The difference in current between the UV illumination induced current and the dark current for both types of detectors (color 1 and color 2) are plotted in Figure 65 and Figure 64. The figures show the current at 1.5V reverse bias with the wavelength of the incident light varied from 300 – 400nm (limitations imposed by available setup). Figure 64 shows the spectral response from the $Al_{.2}Ga_{.8}N$ layer (color 1). There is a peaked response at the expected 320 nm wavelength, indicative of band-to-

band absorption at the nominal 3.4eV bandgap. The GaN layer (color 2) structure indicated absorption close to 360nm. The low-energy peak around 325nm is from absorption in the lower $Al_{.2}Ga_{.8}N$ layer which is believed to be due to some contamination during the GaN layer growth. This places the response of the 2-color array at UVA and in a spectral region just entering UVB. Thus, dual-color detection has successfully been demonstrated. The spectrum response display in Figure 64 and Figure 65 is in good agreement with common response plots in literature both in shape and in range (0.12 A/W for Color1 and 0.05 A/W for Color2). After the peak absorption wavelength is reached, the responsivity decreases with shorter wavelength because the mean penetration depth goes down at lower frequency; hence, less photons are absorbed. This commonly occure with relatively small layers [36].

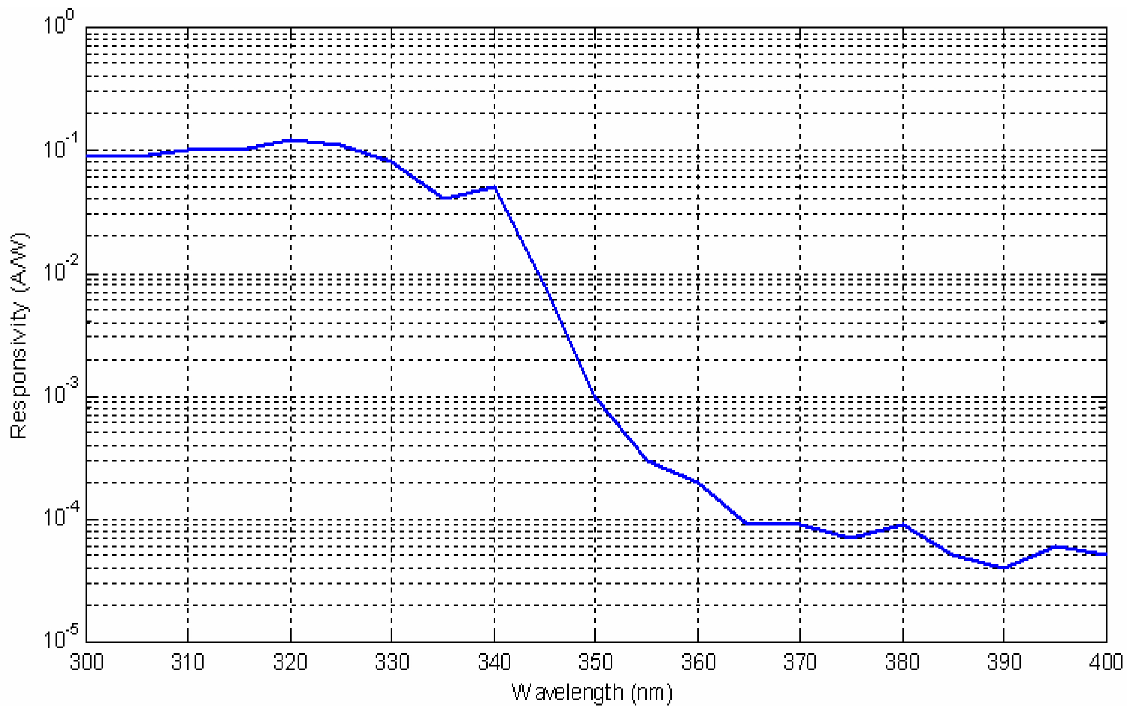

Figure 64: $Al_{.2}Ga_{.8}N$ detector (Color 1) current at various UV-wavelengths with diodes biased at -1.5V

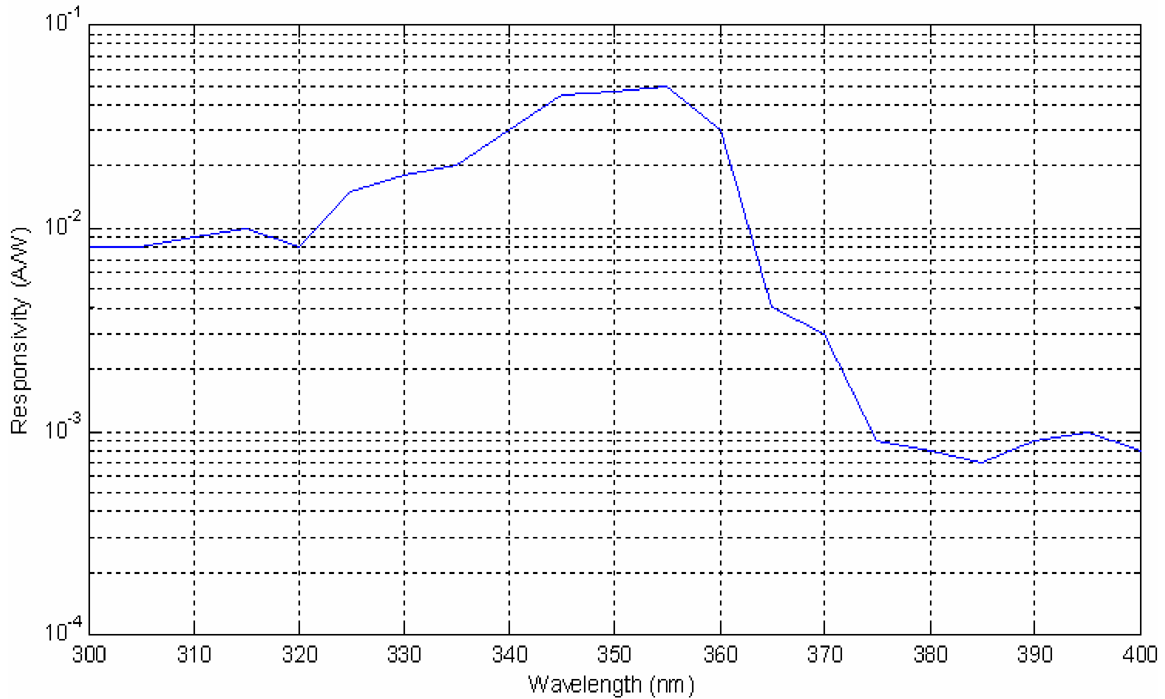

Figure 65: GaN detector (Color 2) current at various UV-wavelengths with diodes biased at -1.5V

3.6.3 Imager Evaluation

Once the entire system is assembled (as shown in Figure 58), the array imaging capability is tested. Figure 66 illustrates the setup used for imager evaluation. My flip chip is position such that the backside of the array faces the UV source and the function generator and data acquition unit are connected to the read out integrated circuit (ROIC). The function generator produces the clock signals necessary to operate the ROIC. The response signals from the detector pulled out by the data acquisition unit and set to the frame grabber. The frame grabber in conjunction with the software on the computer displays the response of the array as an image on the screen. The UV light source is used to generate light patterns to project onto the array. The resulting images are observed on the display. The UV light used is in the

two frequency bands of interest to show the simultaneous dual band imaging aptitude of the detector system.

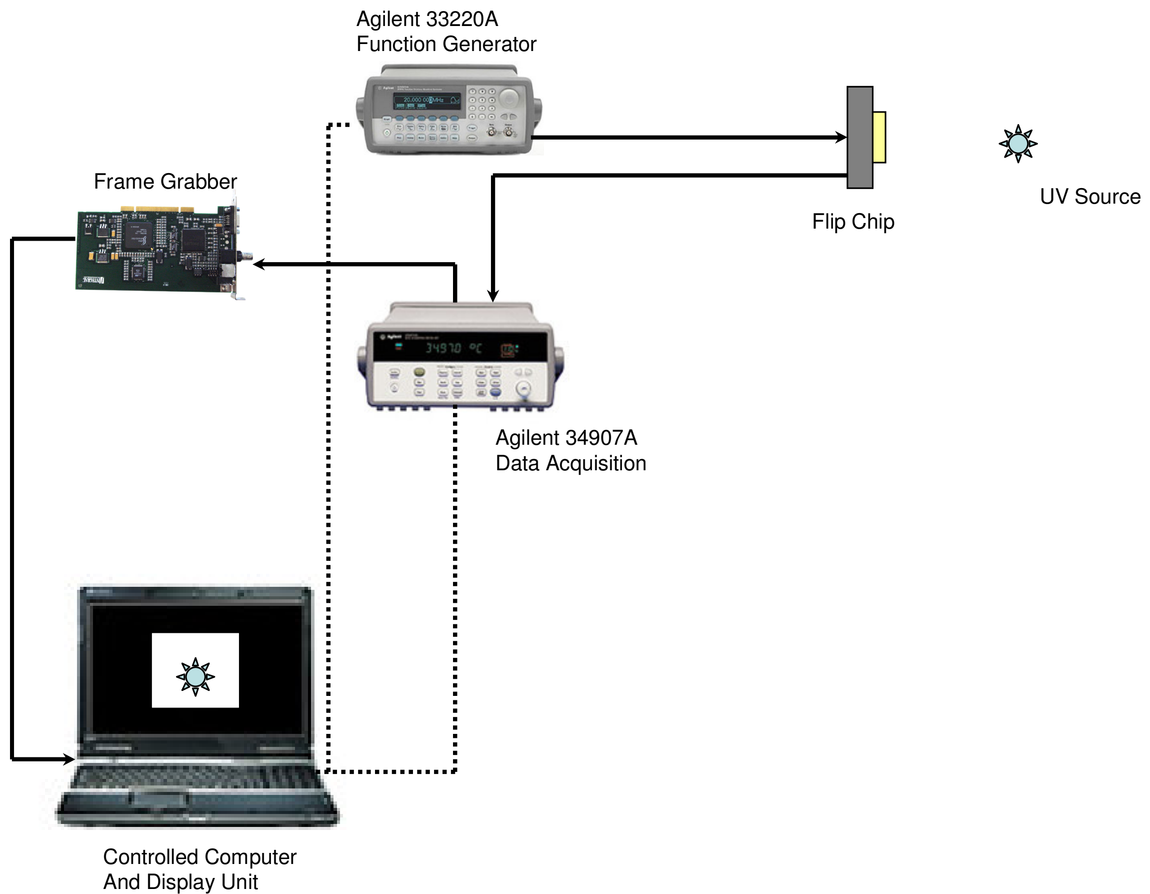

Figure 66: System setup for imager evaluation

3.7 Conclusion

This chapter offers a clear roadmap to the creation of a dual UV-wavelength detector array where detections of both are done simultaneously. This is the first demonstration of such capability. A group NASA Goddard Space Flight Center has reported to have fabricated a dual band ultraviolet photodetector [74]. However, the detection in that system is in no way simultaneous. The detection of both bands is done with a single detector. The band to be detected is set by the bias across their detector. For color 1 detection the detector is forward bias while for color 2 detection

the detector is reverse bias. The detection in such a setup is not simultaneous. Furthermore, the sample rate of the system is slowed by the requirement that the photodetector bias be switch. On the other hand, my detector array functions at a set bias across both type of diodes. This enables the detection to be truly simultaneously.

I have presented the growth mechanism involved in the confined epitaxial growth approach. This growth mechanism enables the stacking of active layers with varying stoichiometry; hence, detectors sensitivity can be tuned different/specific UV-wavelength bands. I have developed and implemented a process flow to make use of the confined epitaxial growth approach. The fabrication process does not make use of any dry etching their by reducing defects to my active layers. Ultimately, this contributes to the reduction in leakage current [5]. Finally, electrical evaluations have revealed that the fabricated detectors display diode behaviors. Furthermore, they display sensitivity to certain predetermined UV-wavelength bands. In a sense, low reverse leakage diode arrays with two-color spectral sensitivities (UVA and UVB) have been constructed and tested.

CHAPTER 4: SUB-WAVELENGTH LITHOGRPHY TECHNOLOGY

4.1 Major Contribution

This chapter introduces a mask based on inexpensive and effective array of sub-wavelength apertures for use in a conventional stepper for far field imaging. A multitude of square patterns are shown in this chapter to establish some of the mechanisms involve in this sub-wavelength transmission phenomenon. The guiding principles of the construction and calibration of the mask lay the ground for the following contribution to the field:

- I developed a mask writing technique where a beam writer is presented with a smaller writing area without requiring the shrinkage of the expected printed pattern or the loss of resolution [1, 6, 75].
- I used and demonstrated the first far-field imaging capability of an array of sub-wavelength apertures [7].

4.2 Introduction

Mask making is an expensive process whether a raster-scan or a vector-scan tool is used. In the case of a raster-scan tool, a beam sweeps across the mask and writes the desired patterns addressing all pixels in the field. For a vector-scan tool, a beam moves to the target shape and those pixels to be exposed are addressed. Both cases require many tiny pixel exposures made serially over a long period of time. It requires that patterns be written serially and that each pixel be addressed. Given the

writing mechanism, reducing the overall area that needs to be written for a given pattern would decrease the time required to write the mask and hence increase the throughput of a tool that cost 10s of millions of dollars. In this study, I demonstrate how sub-wavelength aperture array illumination reduces the number of exposure sites by 1 to 2 orders of magnitude while maintaining control over critical dimensions.

A way to reduce the number of pixels that need to be addressed during mask writing is to substitute conventional mask with an array of holes that would resolve as a single pattern. Conventional mask are made out of clear and opaque regions where the clear region follows exactly the shape of the pattern to be printed. On the other hand, in the case of the array of holes, the contour of the array would be identical to the desired pattern. This mask is referred to as a "Dot Array" mask. Figure 67 illustrates the difference between a conventional mask and a "Dot Array" mask.

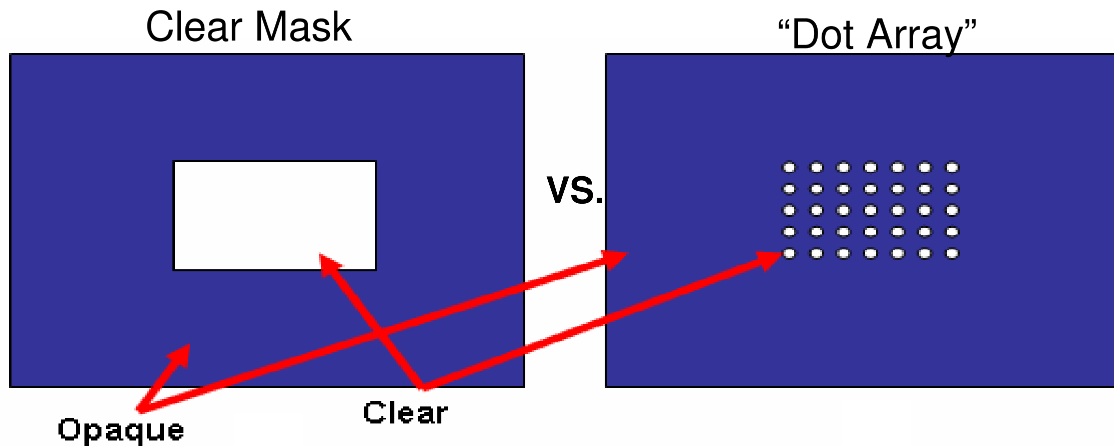

Figure 67: Conventional mask versus "Dot Array" mask

In the "Dot Array" mask, the fill-factor (fraction of area actually addressed) is reduced over that of a conventional mask (where a continuous clear pattern must be generated). A smaller fill-factor will reduce the over-all fabrication time, especially when a rastered-Gaussian beam addressing technique is used. By reducing the size of

the holes, the fill-factor is further increased. The diameter of the holes can be reduced to below wavelength of the incident light (sub-wavelength).

This chapter is devoted to presenting the first experimental evidence that plasmonic excitation in metal films perforated with regular arrays of sub-wavelength apertures can produce high resolution far-field radiation patterns of sufficient intensity to expose photoresist when propagated through the optical system of a conventional stepper. A review of the mechanism involved in the interaction between incident light and apertures in a metal film is presented, followed by a description of the mask fabrication method. Then the experimental setup and the exposure results are presented. A discussion section will follow and the chapter will close with concluding remarks.

4.3 Background

The mechanisms of interaction between light and a hole in an opaque screen has been the object of curiosity and technology application for centuries. Grimaldi first described diffraction from a circular aperture thereby establishing the foundation of classical optics in the seventeenth century [76]. Although, the work done involved apertures much larger than the wavelength of the incident light, their interaction remained the source of scientific study and debates centuries thereafter. In the twentieth century, the interest shifted to subwavelength apertures. In the 1940s, Bethe was able to offer a theoretical description of light at a given wavelength (λ) impinging on a circular aperture of radius (r) much smaller than the wavelength [77]. The analysis was done for the case of an idealized perfect metal sheet infinitely thin. Bethe established dependency of the transmission spectrum of visible light through a

subwavelength hole with regards to r and λ. According to the relationship, transmission spectrum T (λ) is proportional to $(r/\lambda)^4$ as illustrated in Figure 68.

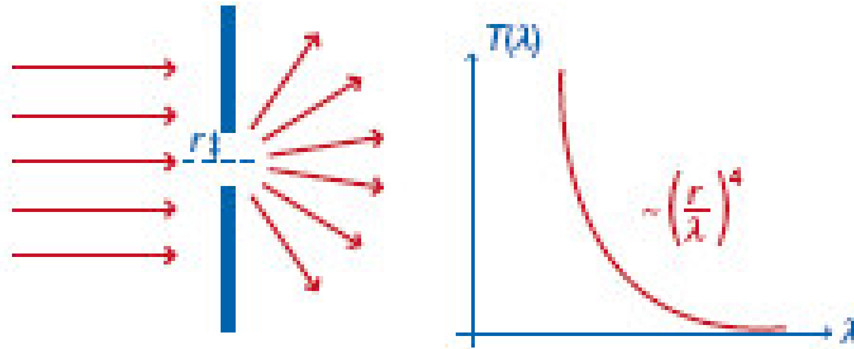

Figure 68: Diffraction and typical transmission spectrum of visible light through a subwavelength hole in an infinitely thin perfect metal film (from H. A. Bethe).

Bethe gave the first description of light diffraction through a hole much smaller than λ; however, a real aperture is characterized by a depth and therefore should have waveguide properties. The lateral dimension of the waveguide (ie. metal film thickness) sets the wavelength at which light can no longer propagate through the aperture (cutoff wavelength λ_c). For incident wavelength larger than the cutoff, there should be no transmission. Nevertheless, the cutoff point is not sharply defined in the case of metal films. Whether the aperture was regarded as a hole or a waveguide, Bethe's prediction that the optical transmission would be very weak became the reasoning behind challenges related to the miniaturization of optical elements.

Given this prediction, the publication of extraordinary transmission through an array of subwavelength hole in a optically opaque metal film generated substantial interest in the foundation of this phenomenon [78]. It is commonly believed that light incident on a metal thin film establishes an oscillation in the mobile charge density (ripples in the "Fermi sea"). These ripples, or plasmon excitations in the metal foil,

give rise to an evanescent mode of re-radiation electromagnetic fields that decay exponentially into the space perpendicular to the surface that has been exploited.

In recent years, the foundation of the extraordinary transmission phenomenon has been under debate [79, 80]. Most of the research focus has been placed on understanding and controlling the interaction between light and metals by introducing nanostructures (single hole, arrays of holes, slits, dimples and others) on the length scales smaller than the wavelength of the light involved. Many studies have been performed to characterize the unusual transmission, in the optical [81, 82], infrared [83], microwave [84] and terahertz range [85-87]. In this chapter, I am going to look at light transmission through a single aperture, then the transmission though an array of holes followed by a review of the effect of hole shapes. In closing a discussion of the mechanism responsible for the transmission phenomenon will be presented.

4.3.1 Single aperture

In accordance with classical optics, the light transmission through a subwavelength aperture is very small. However, when this aperture is surrounded by symmetric corrugations, the transmission through the subwavelength aperture is enhanced [88]. The transmission effect of a single aperture surrounded by an array of dimples has also been analyzed [89, 90]. Both setups yield an enhancement in transmission with the transmission enhancement due to the corrugations being much higher than that due to the dimples as illustrated in Figure 69.

The surface plasmon (SP) responsible for the transmission phenomenon results from the incident light exciting standing waves of charge displacement at the metal surface. There are two standing-wave modes which differ by the distribution of the

electromagnetic fields. For Mode 1 the charge distribution is located in the in-plane of the metal. For Mode 2 most of the electromagnetic field is located in the grooves or dimples as shown in Figure 70. Mode 2 yields stronger coupling between the front and back of the metal film since the electromagnetic field is maximal at the grooves or dimples as well as at the central aperture.

There is a momentum difference (G) between wave vector of the incident light and that of the evanescent waves at which the SP modes resonates. One way of providing the needed momentum, that enables coupling between the incident light and the SP wave, is via the use of periodic arrays [80]. In one dimension, G is a multiple of $2\pi/P$ where P is the periodicity of the structure (spacing between corrugations or dimples). The relationship between the periodicity of the array and the momentum difference points towards an optimal periodicity for maximum transmission. The next sub-section analysis what happens when the dimples of Figure 70 are replaced by holes such that I in effect have an array of holes.

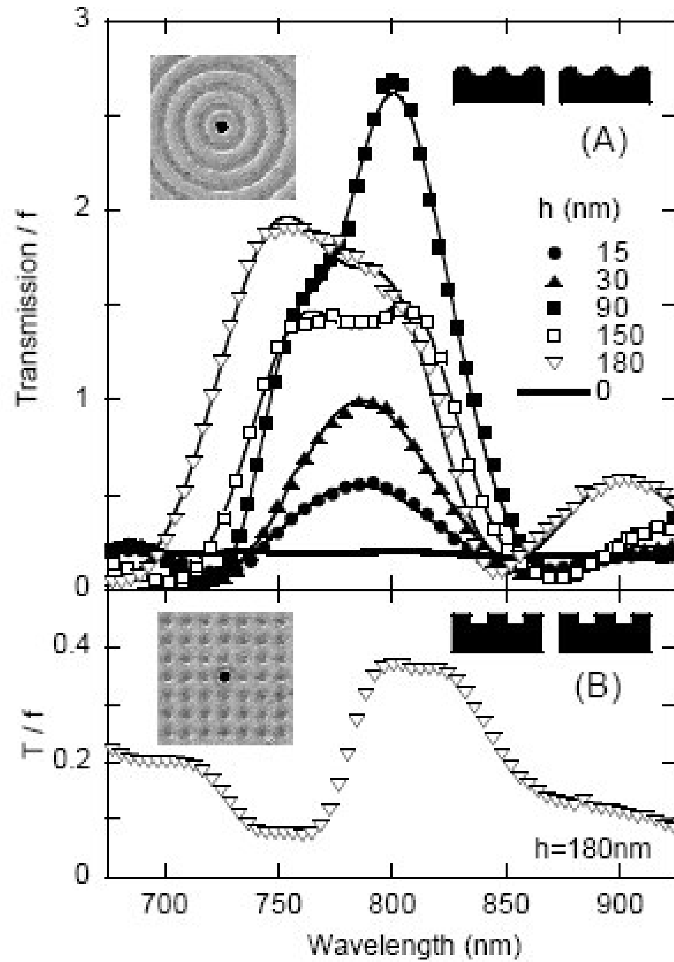

Figure 69: Transmission spectraof a single aperture (d= 440nm) surrounded by (A) rings with sinusoidal cross section and (B) a square array of dimples (h=180nm). Left insets, focus ion beam images of typical samples; right insets, cross sections of the hole and corrugation (from T. Thio).

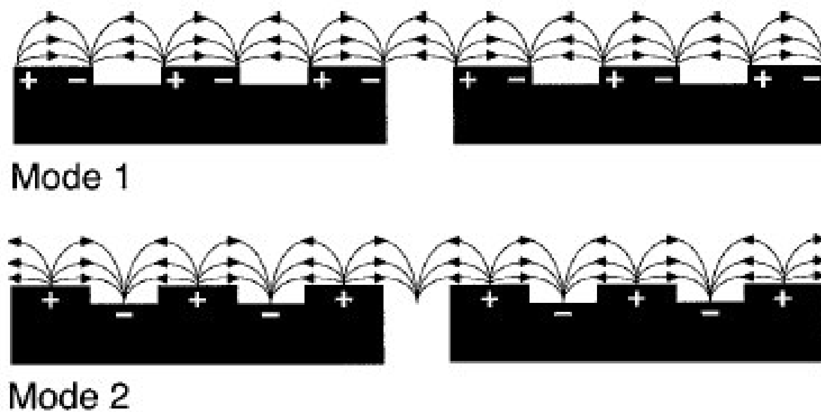

Figure 70: Real-space model of charge displacement at the metal surface and associated electric fields of SP modes at level crossing (from T. Thio).

4.3.2 Array of holes

The transmission process can be divided into three steps: coupling of light and SPs on incidence surface, transmission through the holes to the secondary surface and re-emission from the secondary surface. One interesting feature of the hole arrays is the fact that each hole on the output surface acts like a new point source for light [80]. The evanescent mode of the re-radiation has been exploited for contact printing [91]. In this application, the array of apertures is used as a mask to expose photoresist spun on a wafer. Figure 71 and Figure 72 show the lithographic setup and an AFM image of such transferred pattern.

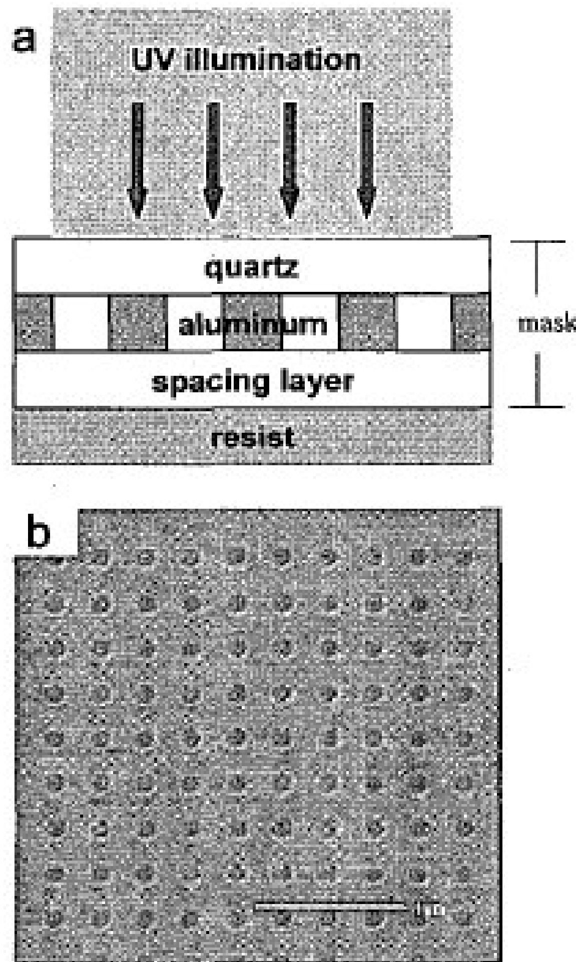

Figure 71: Contact printing application (a) Schematic of the lithographic setup. (b) Image of hole array fabricated by Focused Ion Beam etching. The diameter of the holes is 160nm and the lattice constant is 320nm (from Srituravanich).

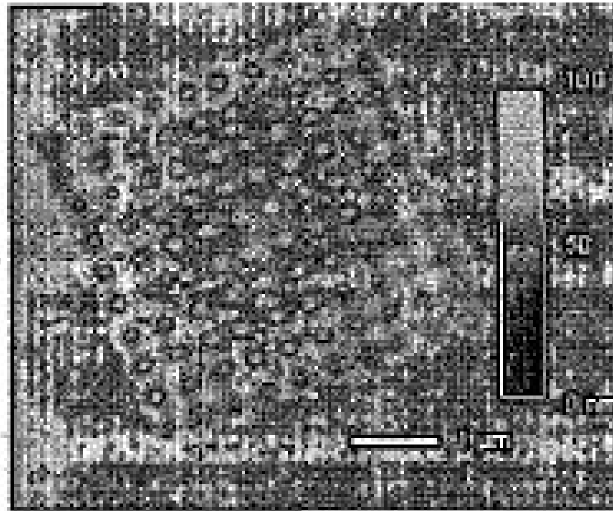

Figure 72: AFM image of the transferred dot array pattern (from Srituravanich).

If a collimated beam impinges on the input surface, the radiation of each of the point sources construct a plane wave through classical interference as light travels away from the output surface. As a result, the far field beams resemble plane waves-like propagation [92]. In a periodic arrangement of subwavelength holes in a metal film the transmitted fraction of the incident light exceeds the open air fraction of the film, for certain wavelengths. This extraordinary transmission is not merely due to the periodic structure. Changes in the shape of the subwavelength apertures can greatly affect the extraordinary transmission [93, 94]. The next sub-section investigates the effect of aperture shape on the transmission spectrum.

4.3.3 Effect of aperture shape

As the shape of the hole is modified, there is a change in localized SP and of the cutoff frequency of the hole. Hence, the transmission spectrum is changed [80]. The hole shape effect was experimentally examined [93, 94]; the metal type and thickness as well as the periodicity of the array were kept constant to insure no change in surface plasmon while the aperture arrays were varied (circular vs. rectangular

aperture). A spectral shift was observed as presented in Figure 73. The shift is due to the change in *localized shape resonance* in the individual holes.

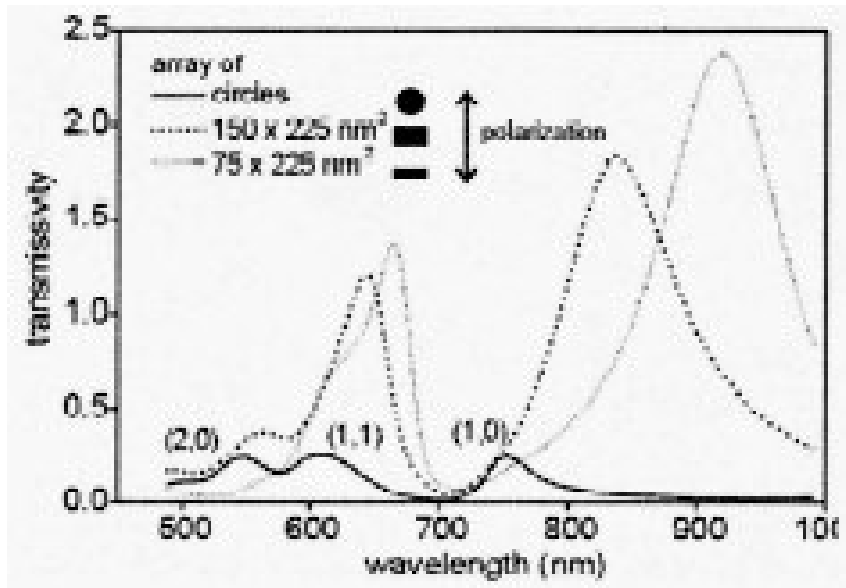

Figure 73: Measured transmissivity (transmission divided by open air fraction) spectra for 3 different hole arrays (from K. L. Van der Molen).

The surface plasmon is maximum on the metal surface and the electromagnetic field decays exponentially if you move perpendicular to the surface. The shape and periodicity of the hole array has a strong influence on the extraordinary transmission. “shape resonance” is used to explain the difference in transmission spectra at a given periodicity [95].

4.3.4 Transmission mechanism

The exact mechanism behind the extraordinary transmission phenomenon that is observed when light is shined on a single sub-wavelength hole surrounded by corrugation or dimples or when light is shined on an array of sub-wavelength apertures is not truly understood. However, the effects of the different components of the transmission have been identified. The transmission phenomenon is affected by:

- The size and shape of the aperture: Responsible for the localized surface plasmon
- The periodicity of the array of apertures or corrugation / dimples around a single hole: Enables coupling of light and surface plasmon by providing momentum difference between the two waves

- The thickness of the metal film: The thicker the metal the more the aperture behaves as a wave guide. If the metal film is too thin (much smaller than the wavelength of the incident light) the assumption of an opaque metal is false [96].

- The type of metal: The wavelength of the surface plasmon resonance varies with metal. The closer the chosen metal is to the “ideal metal”, the greater the enhancement [88].

- The quality of the metal film: Defects and unevenness on metal film shifts the wavelength at which optimal coupling occurs.

All the aforementioned parameters affect the transmission phenomenon of subwavelength apertures. Multiple models exist based on surface plasmon coupling and on diffraction theories. However, the diffraction theory models, which are not based on Maxwell’s equations but instead on wave models are not the solution. Models that neglect the size and shape of the aperture should be regarded with skepticism [97, 98].

Understanding transmission through subwavelength apertures in metal films could open the door to multiple applications of the surface plasmon effect. Possible application will include among others, single molecule fluorescence in biology, enhanced vibrational spectroscopy of molecular monolayers and ultrafast photodetectors for optoelectronics [80]. I am interested in using the phenomenon to do projection lithography. To obtain a good transmission contrast, the metal must be opaque (optically thick). The film thickness must be several times the skin-depth (penetration depth in the metal at which incoming light intensity has been reduced by 1/e) of the metal. Typically, the skin-depth is of the order of 20nm for noble metals (at optical wavelengths the skin depth of silver is about 25nm). This would enable the array of holes to be used as mask. The application of interest in this thesis work is the possibility of SP-activated lithography masks usage for subwavelength feature patterning.

4.4 Mask Fabrication and Experiment

To study the effectiveness of using arrays of sub-wavelength apertures to generate masks, I fabricated my own masks. The masks were fabricated via focus ion beam (FIB) milling. The next sub-section will introduce the FIB tool used and its capabilities and the subsequent sub-section will present the different patterns fabricated on my masks and the aim of these patterns.

4.4.1 FIB Tools

I used a FEI Dualbeam 620 [99], which consists of a scanning electron microscope (SEM) and a focus ion beam (FIB) system, to mill the arrays of apertures. The principle configuration of the dual beam is given in Figure 74. The equipment

offers the facility to rotate the target holder by 360° and to tilt it by $\theta = 52°$ relative to the directions of both beams and the surface normal of the holder, if the sample is positioned in the eucentric point E. In Figure 74, the angle θ_{max} is the fixed angle between the FIB and the SEM optical axes [99]. A schematic of the full system is presented in Figure 75.

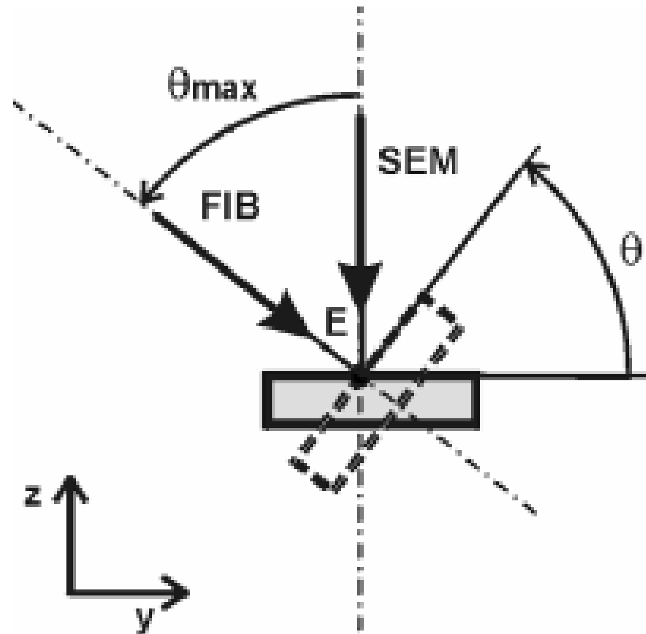

Figure 74: Schematic view of the axes of the SEM and the FIB optical columns relative to the sample normal in a Dualbeam 620. The angle θ is the tilt angle between the optical axes of the SEM, θ_{max} is the fixed angle between the optical axes of the FIB and SEM colums and E the eucebtric point (from F. Machalett)

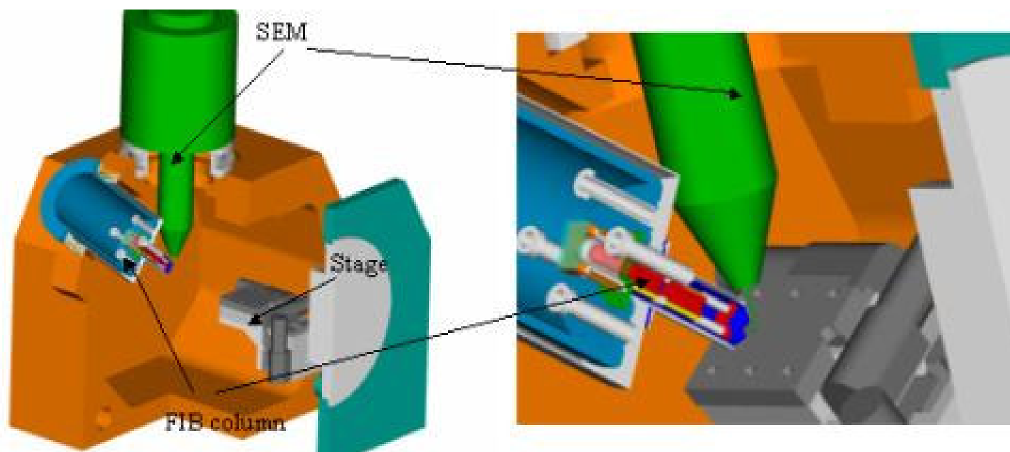

Figure 75: Schematic diagram of the FIB/SEM dual beam system (from T. Kalvas).

Stream files are used as the design tool by the DualBeam 620 system to define patterns. Stream files are created as a text file to address the patterning Digital to Analog Converter (DAC) directly and produce custom pattern files. The patterning field of view on the tool is divided into horizontal and vertical rows of 4096 pixels because a 12-bit DAC is used. Each pixel can be addressed / written to. This offers great flexibility as the system accepts xy data from a text file. The upper left pixel (on the screen) X,Y coordinate is 0,0 and the lower right pixel X,Y coordinate is 4095, 4095.

The following example of a stream file will mill 9 equally spaced holes on my mask (a 3 by 3 array):

```
s
1000
9
40000    2000  2000
40000    2000  2300
40000    2000  2600
40000    2300  2000
40000    2300  2300
40000    2300  2600
40000    2600  2000
40000    2600  2300
40000    2600  2600
```

The file must begin with an "s" indicating a stream file. The second line defines the number of loops the pattern will mill, where one loop has the beam visiting each of the 9 pixels one time. The third line indicates the total number of x, y coordinates, in this example it is 9. The 40000 figure represents dwell time in nanoseconds. The dwell time can be controlled for each individual pixel [100]. For my experiment, the dwell time is kept constant over all pixels. When a stream file is open by the DualBeam 620, the pattern is downloaded to the image screen and the displayed mill

time is calculated from the looptime and the total number of loops [101]. Starting on line 4, the number in the second and third column represent the x,y coordinates of each pixel to be milled.

Instrument settings such as beam current and magnification are incorporated at the design stage. When I mill my holes, each hole is addressed as a unique pixel. Figure 76 shows the FIB milling of a single pixel with the FIB represented by the red arrow and the sputtered material by the grey arrows. The resulting trench when milling a single pixel in a single pass at long dwell time is to a first order approximation similar to a V-profile (FIB profile).

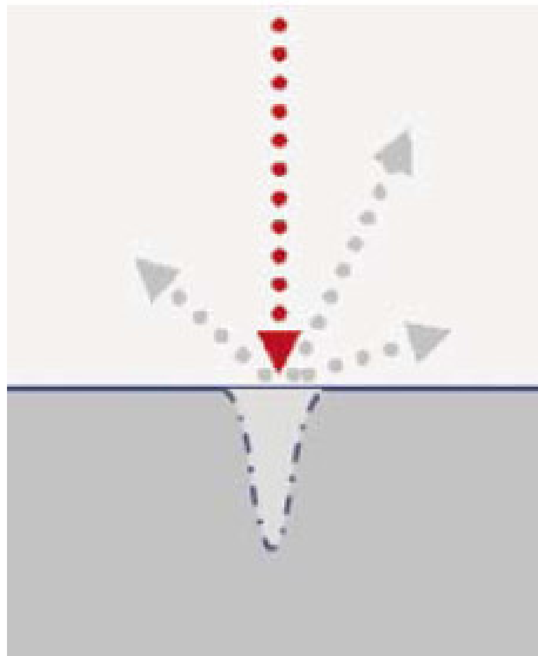

Figure 76: FIB milling on one position for a prolonged dwell time (from O. Wilhelmi).

The spacing between pixels is determined by the magnification used. Hence, to obtain a predetermine spacing between two holes, the number of pixels for the spacing as well as the required magnification need to be calculated. In the example listed earlier, the spacing between neighboring holes is 300 pixels. At that set pixel

number between holes, the distance (in nanometers) between neighboring holes is determined by the following relationship

$$\frac{1}{Kx} \alpha D \qquad \textbf{(13)}$$

α identifies a proportionality relationship; consequently, there is an inverse proportionality relationship linking the distance between holes (*D* in nm) and the display magnification (*Kx*) used on the tools' screen. Table 13 offers a sample of some of the physical spacing calculation as they relate to the chosen number of pixels (spacing between holes' location on the stream file) and display magnification.

Table 13: Magnification calculation

Number of Pixels	Magnification	Physical Spacing (nm)
300	$43*10^3$	300
300	$26*10^3$	500
150	$21.5*10^3$	300
100	$43*10^3$	100

4.4.2 Mask Patterns

The fabricated masks were designed to explore the effects of hole spacing, array size as well as the influence of correctional holes used in a manner similar to anchors and serifs to improve image transfer fidelity. In addition, defective arrays were generated to observe the technique's defect tolerance.

The masks are fabricated as follows: first, a 100nm thick Ag film is thermally evaporated on a 6" X 6" quartz substrate and then an array of cylindrical holes is milled using a focused ion beam. The sizes of the arrays (total number of holes) are varied, from 3x3 to 10x10; in addition, the hole spacing (center-to-center) is varied from 200nm to 320nm. The diameter of the milled holes is kept constant at

100nm.Table 14 summarized all the display magnification used to write all the patterns in the mask at the desired hole spacing.

Table 14: Magnification used to write patterns

Pixels between holes coordinates	Holes Center-Center Spacing (nm)	Magnification (*Kx*)
150	200	$32.25*10^3$
150	220	$29.3*10^3$
150	240	$26.87*10^3$
150	260	$25*10^3$
150	280	$23*10^3$
150	300	$21.5*10^3$
150	320	$20*10^3$

Figure 77 shows SEM images of a few milled arrays. Figure 77 (a) presents the image of a 10x10 array with 320nm hole spacing, and Figure 77 (b) shows a 3x3 array with 280nm hole spacing. The vertical slit like appearance of the columns in the array in the latter figure is due to the astigmatism of the beam during milling; however, the exit aperture at the bottom of the metal film is circular (to the best of our ability to conduct SEM image deep into the milled apertures). Figure 77 (c)-(d) demonstrates the modifications that can be done to a conventional square array to square-up the array; in Figure 77 (c), a single hole is placed diagonal to each corner of the array while in Figure 77 (d) the single hole is replaced by a 3x3 array of holes. The additional apertures in both cases have hole spacing (center-to-center) identical to those of the main array to which they are attached.

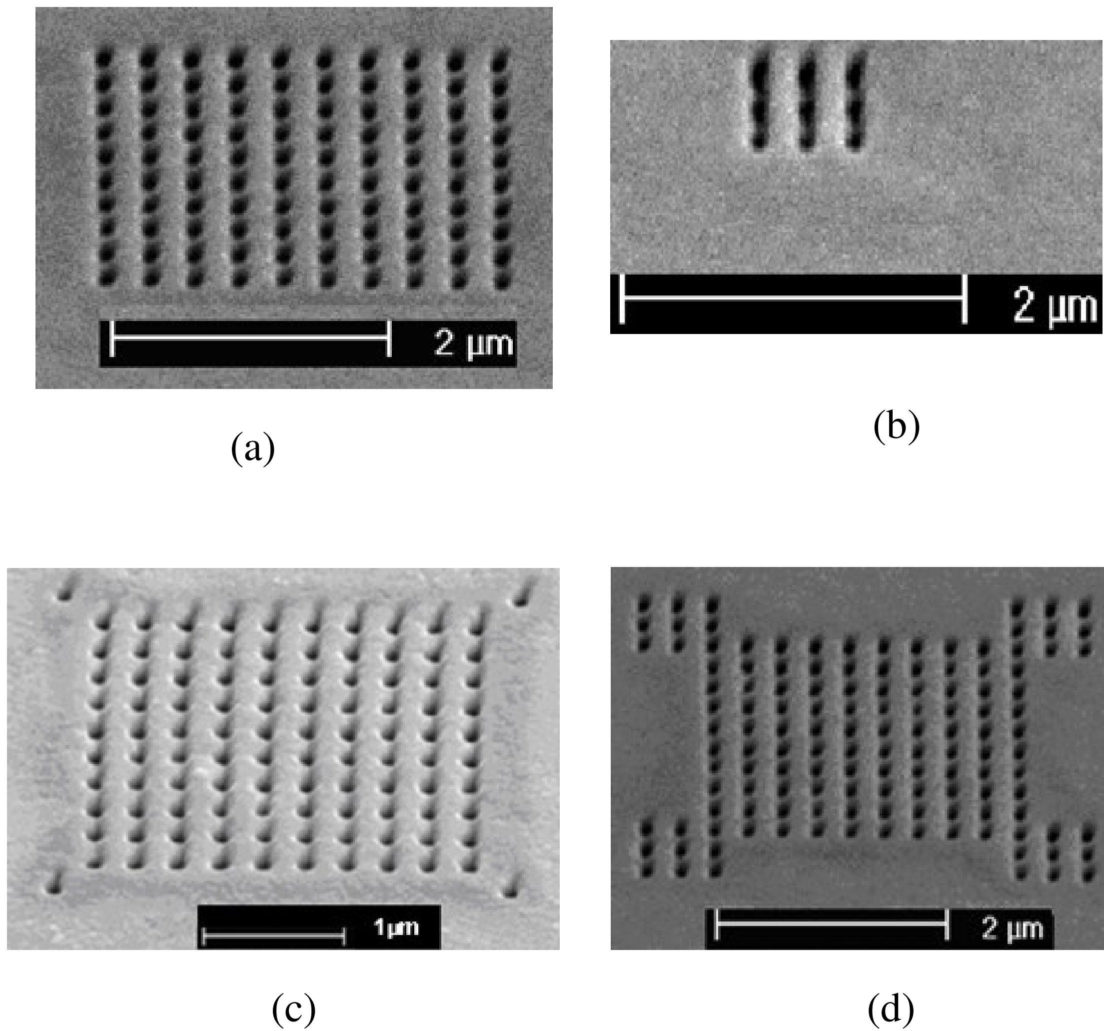

Figure 77: SEM images of arrays of sub-wavelength apertures; (a) Array of a 10x10 apertures with 320nm hole spacing; (b) array of 3x3 apertures with 280nm hole spacing; (c) array of 10x10 apertures with single correctional hole with 300nm hole spacing; (d) array of 10x10 apertures with 3x3 array of correctional holes all with 300nm hole spacing

4.5 Results

Using a 248nm mercury exposure source, the masks are imaged via a 4x projection printing tool (ASML QML full field stepper configured for 0.25µm resolution, 248nm light source and 0.7 numerical aperture (NA)), on a 0.78µm-thick UV26 photoresist spun on a silicon wafer. An illustration of the stepper is shown on

Figure 78. The exposure was done at various focuses and intensities. The excitation wavelength corresponds to a charge excitation above the surface plasmon resonance. Contrary to the case of a free electron gas where a propagating mode would not exist at frequencies above the surface plasmon resonance, a real propagating mode is created in the silver film for frequencies above the surface plasmon resonance [102]. For each hole spacing arrangement, the array of holes is expected to form a square with the following equation describing the linear dimension, T, of the square structure:

$$T = 0.25[(x-1)*d + D] \tag{14}$$

where d represents the hole spacing, D is the diameter of the holes (100 nm) and x is the number of holes in a line of the square array (i.e., $x = 10$ in a 10 by 10 array).

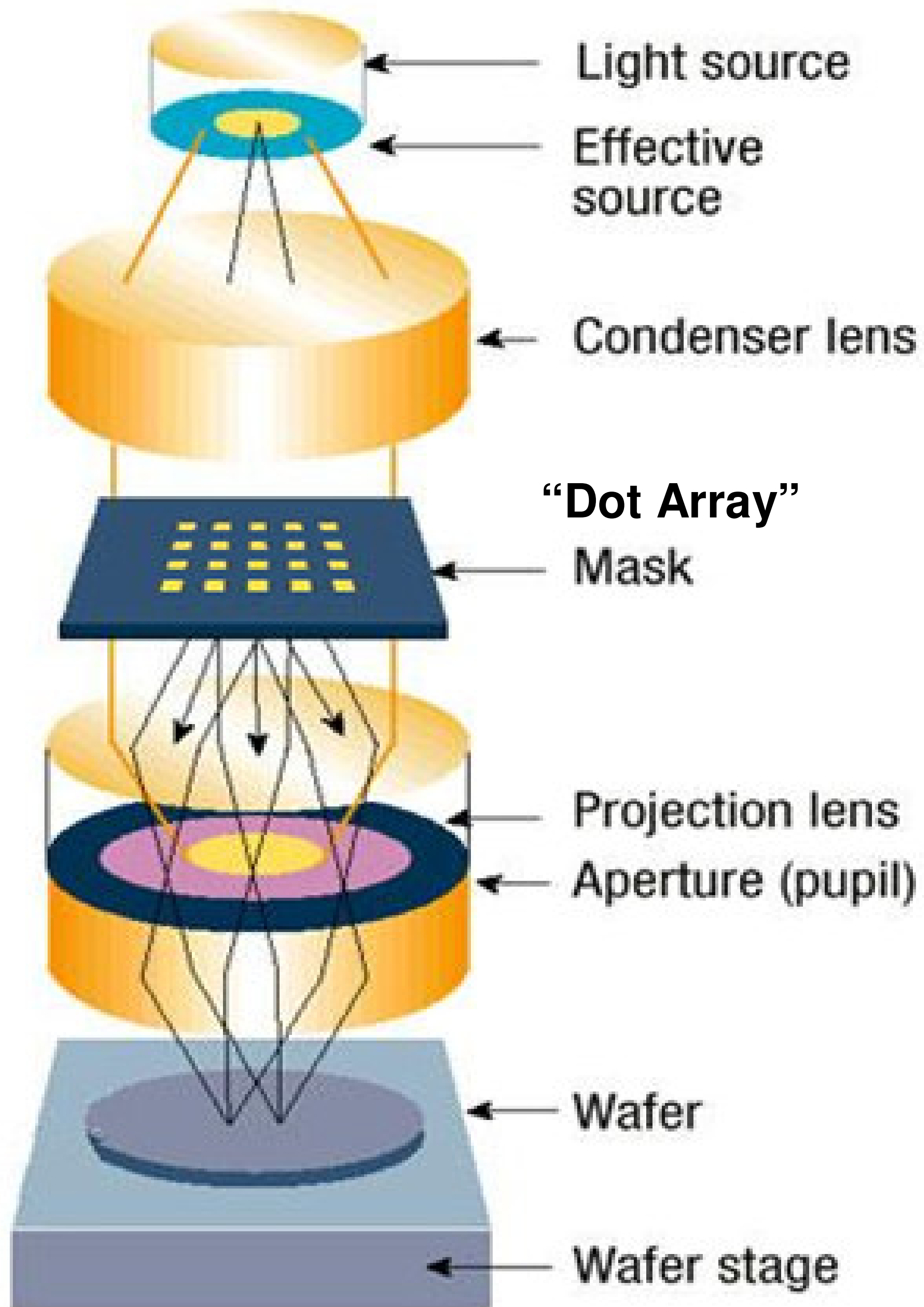

Figure 78: Illustration of ASML QML Stepper

Once the mask is projected on a wafer coated with UV26 photoresist, the resolved patterns are captured via SEM images and measured. The measured dimension is compared to its expected value, T, also referred to as the nominal critical dimension (nominal CD), as calculated using Equation 5. For a 10x10 array with 300nm hole spacing, the array size on the mask is 2.8 μm by 2.8 μm, with an expected 4x projected image of 0.7 μm x 0.7 μm. SEM images of resolved arrays are shown in Figure 79. The patterns printed as squares with some corner rounding. Dimensions of the resolved patterns compare well:

• For Figure 79 (a); Nominal x,y: 655nm, 655nm; Obtained x,y: 676nm, 672nm

• For Figure 79 (b); Nominal x,y: 415nm, 415nm; Obtained x,y: 409nm, 403nm

• For Figure 79 (c); Nominal x,y: 255nm, 255nm; Obtained x,y: 280nm, 260nm

Thus, using a 248nm exposure source, I was able to successfully image contact window patterns with features as small as 260nm as shown in Figure 79 (c). I tried to go beyond the physical limitation of the optical system used to print features with sizes much smaller than the wavelength of the exposure source. This was accomplished via the exposure of 3 x 3 arrays (see Figure 77(b) for SEM image of the array). The 3x3 arrays printed had aperture spacing of 280nm and 220nm. The printed patterns compare as follows:

• For Figure 80 (a); Nominal x,y: 165nm, 165nm; Obtained x,y: 187.5nm, 187.5nm

• For Figure 80(b); Nominal x,y: 135nm, 135nm; Obtained x,y: 110.2nm, 96.56nm

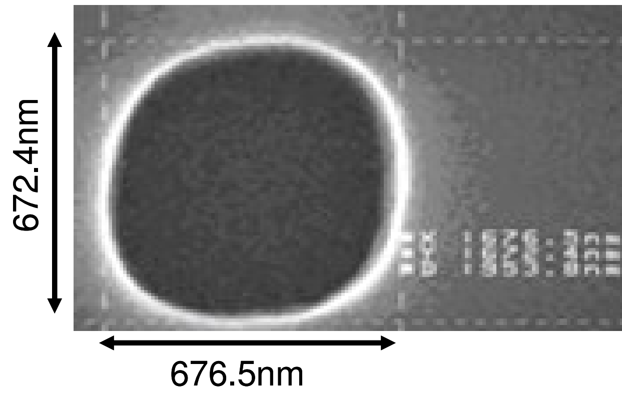

(a)

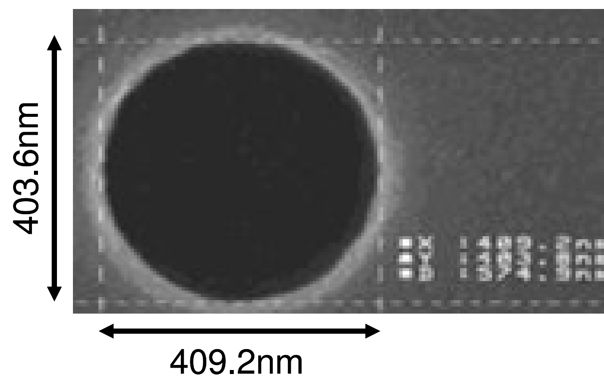

(b)

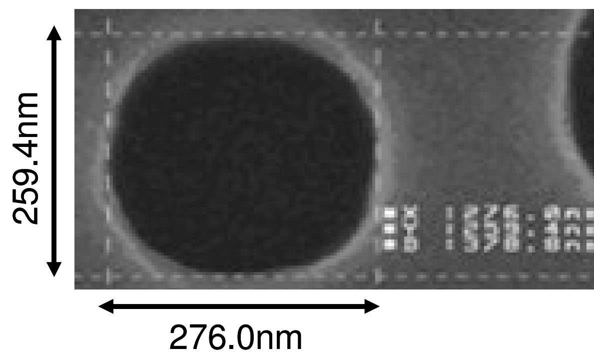

(c)

Figure 79: SEM image of resolved pattern with X and Y measurement; (a) resolved 10x10 array with 280nm hole spacing x = 676.5nm; y = 672.4nm; (b) resolved 7x7 array with 260nm hole spacing x = 409.2nm; y = 603.6nm; (c) resolved 5x5 array with 220nm hole spacing x = 276.0nm; y = 259.4nm

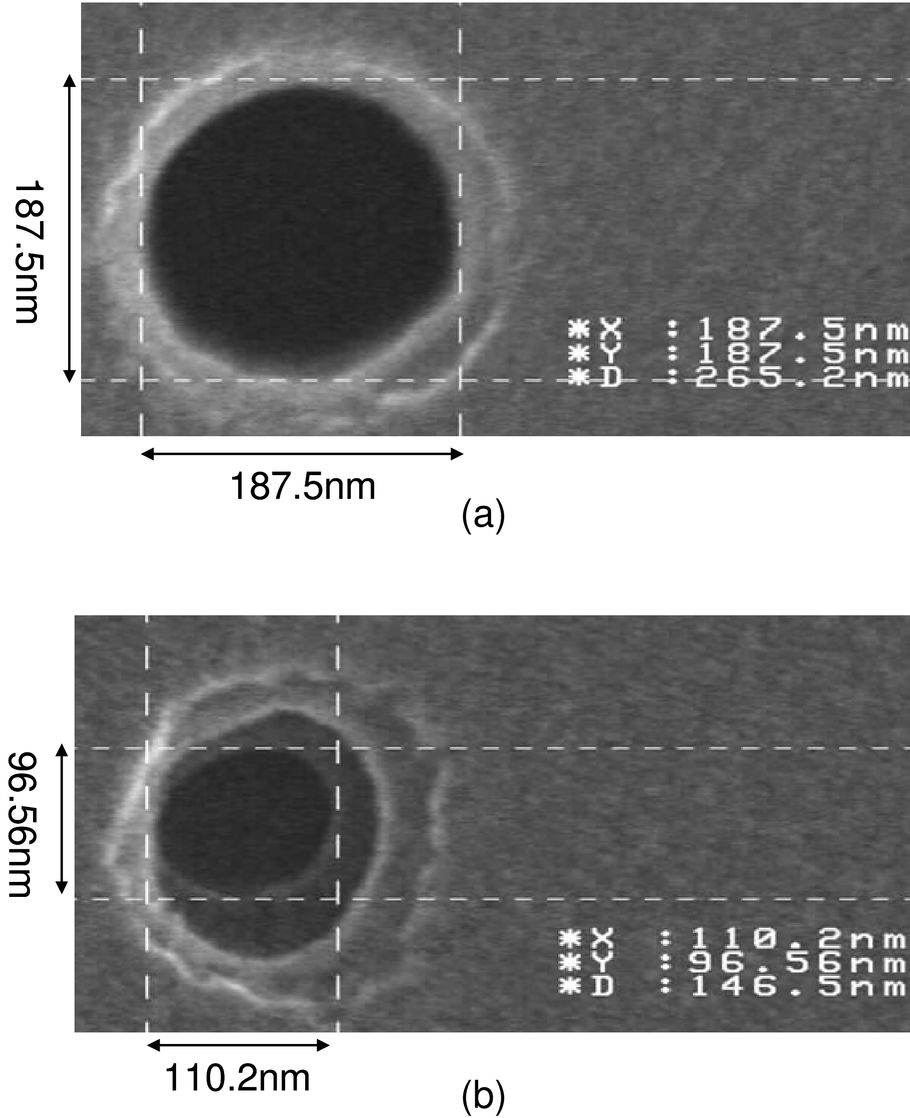

Figure 80: SEM image of resolved pattern with X and Y measurement; (a) resolved 3x3 array with 280nm hole spacing x = 187.5nm; y = 187.5nm; (b) resolved 3x3 array with 220nm hole spacing x = 110.2nm; y = 96.56nm

An attempt to sharpen the rounded corners in Figure 79 was done with the use of the patterns shown in Figure 77(c)-(d). The added pixels were implemented to fill-in the corners of the squares; however, the pattern with the single aperture placed diagonal to each corner of the arrays edges was unsuccessful in squaring the corners.

On the other hand, the pattern with the 3x3 array at the corners improved the features linearity as can be observed in Figure 81 where the resolved patterns of 10x10 arrays with and without the correctional 3x3 array are compared.

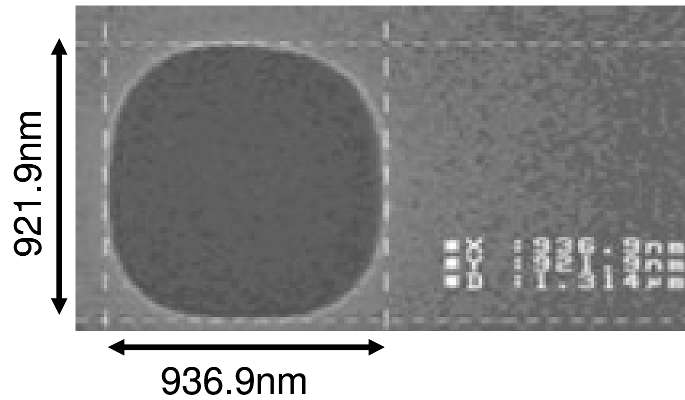

(a)

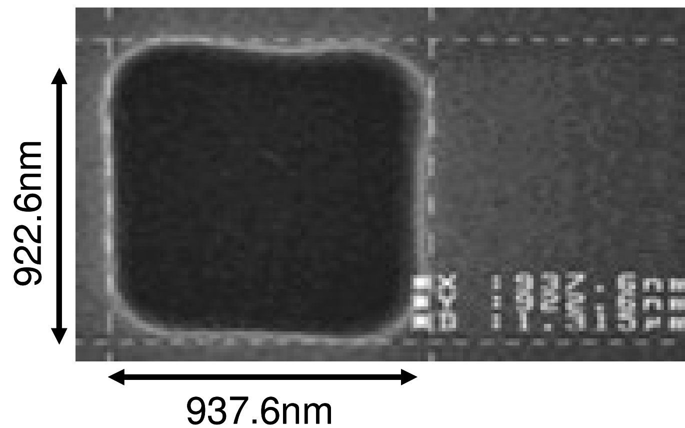

(b)

Figure 81: Effect of correctional holes on edge acuity; (a) resolved 10x10 array with an added single diagonal aperture; (b) resolved 10x10 array with an added 3x3 correctional array

A study of the mask pattern stability as a function of exposure dose demonstrates the exposure system stability. As expected, the exposed feature size increases and saturates as the applied exposure dose is increased. For proper

exposure, the sizes of the exposed patterns are dictated by the hole spacing and array sizes. In other words, matching between exposed feature sizes and the expected nominal CDs (which is related to the amount of light transmitted) varies as a function of hole spacing and light dose, as shown in Figure 82.

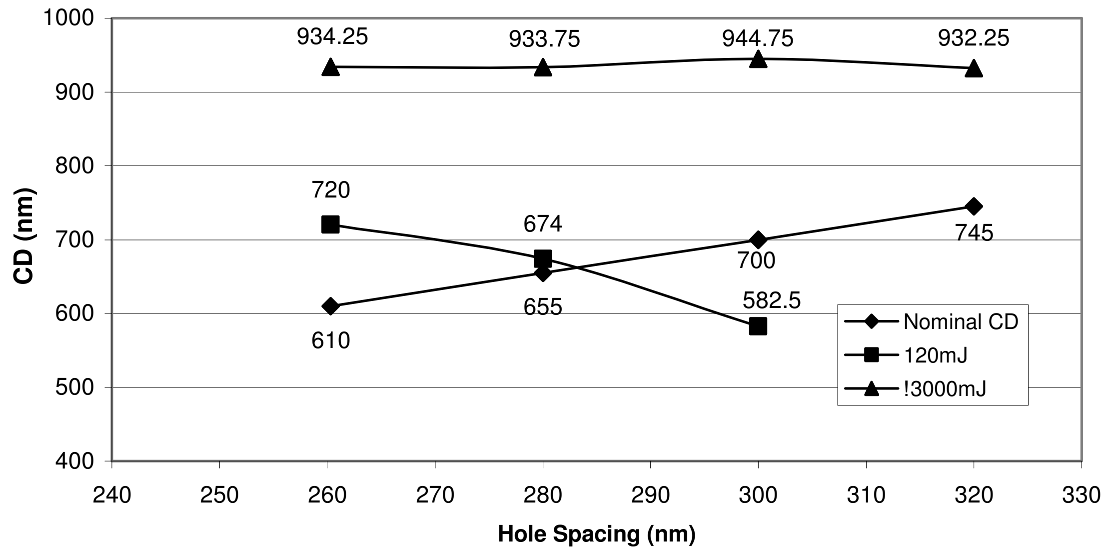

Figure 82: Feature size stability analysis, feature size vs. hole spacing in 10x10 arrays at different doses

The stability of the image pattern was also studied by off-setting the image plane from its focus position. Just like traditional masks, the dot matrix mask is also affected by focus offsets of the lens system. Changing the focus by + or - 0.3μm leads to changes in the size of the exposed features, as seen in Figure 83.

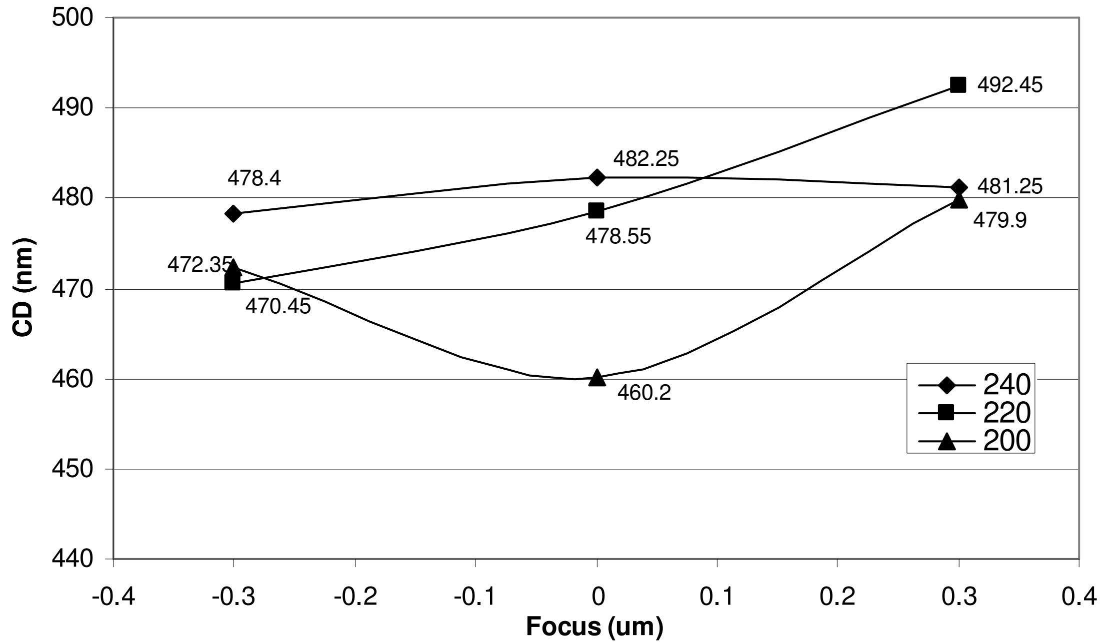

Figure 83: Feature size stability analysis, feature size vs. focus of 7x7 arrays with varying hole spacing (nm)

The collective nature of the electromagnetic excitation emanating from the mask aperture was tested by taking 10x10 arrays with 240nm hole spacing and omitting a set of random holes in the array. Figure 84 shows SEM images of the mask where the arrays in Figure 84 (a-c) are randomly missing 10, 20 and 30 apertures, respectively. These patterns where all successfully exposed with no discontinuity as presented in Figure 84 (d-f) for 10, 20 and 30 missing apertures, respectively. The dimension of the resolved patterns compares favorably with the expected dimensions obtained from Equation 14 as follows:

• For Figure 84 (d); Nominal x,y: 565nm, 565nm; Obtained x,y: 586nm, 581nm

• For Figure 84 (e); Nominal x,y: 565nm, 565nm; Obtained x,y: 495nm, 492nm

• For Figure 84 (f); Nominal x,y: 565nm, 565nm; Obtained x,y: 461nm, 460nm

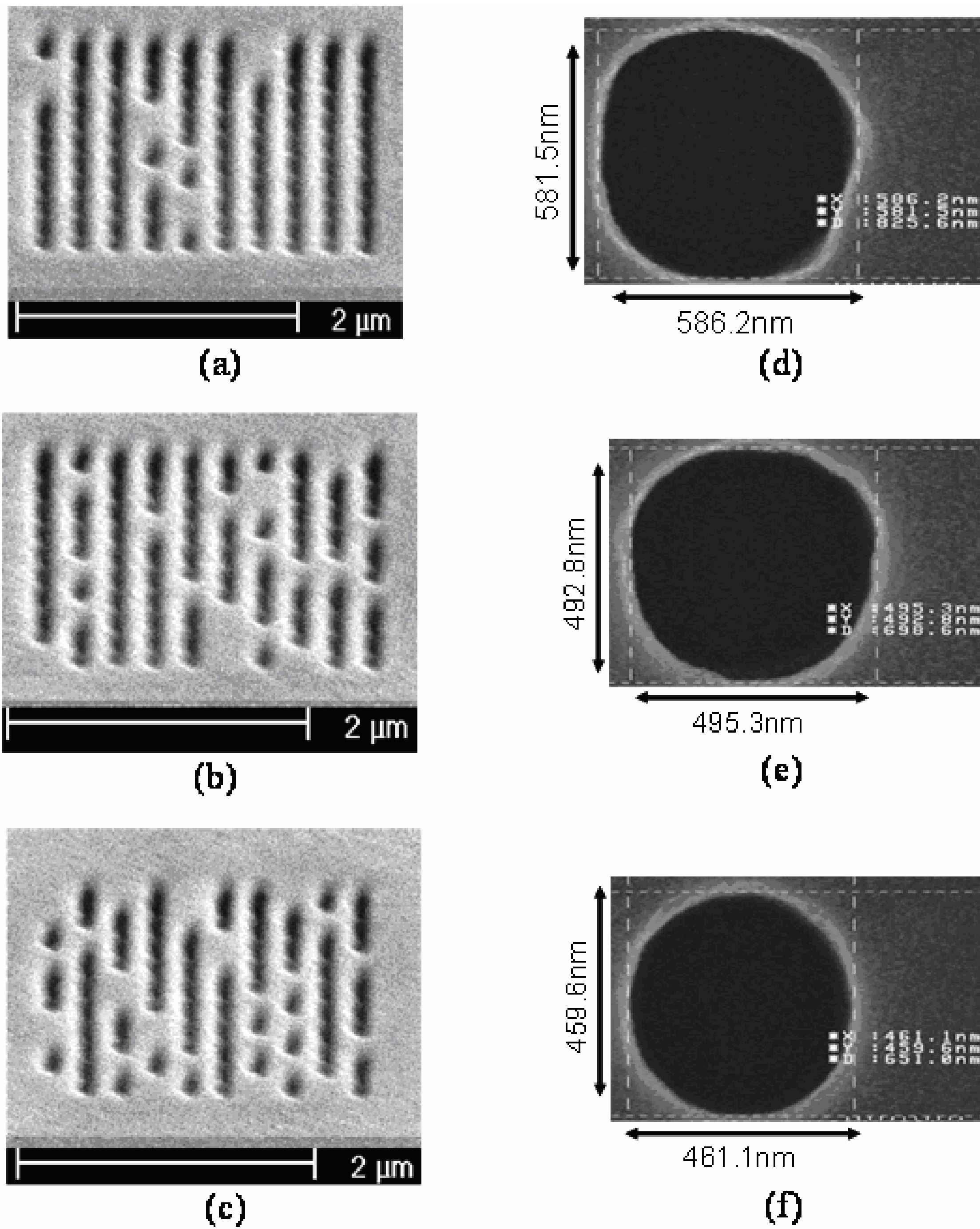

Figure 84: SEM images of 10x10 arrays with 240nm hole spacing and missing apertures; (a) Mask of 10x10 array missing 10 apertures; (b) Mask of 10x10 array missing 20 apertures; (c) Mask of 10x10 array missing 40 apertures; (d) resolved pattern missing 10 apertures; (e) resolved pattern missing 20 apertures; (f) resolved pattern missing 30 apertures

While there is some slight deformation of the shape, no unexposed photoresist is found in the resolved pattern and, for the most part, the feature boundary size is quite close to that obtained from defect free arrays. Some deformation is evident, but all the apertures are fully cleared and would be useful at the resolution limit of the tool employed. It should be noted that higher NA tools are expected to provide higher resolution. Not only do the above results prove that the dot matrix mask is based on a collective effect of the sub-wavelength apertures, it also shows a certain amount of defect resilience.

4.6 Discussion

Through this study, I have proven that a dot matrix mask structure can be used for far field imaging. Conventional optics would suggest that the transmission through a sub-wavelength aperture would be extremely small; however, that is not what was observed experimentally. My far-field emission was strong enough to pattern UV26 photoresist of 0.78μm thickness. I believe that plasma excitation in the silver film together with the localized excitation of the cavity modes due to the sub-wavelength apertures are responsible for the transfer of the excitation from one side of the sample to the other side. Figure 85 illustrate how the combination of the silver film and the aperture collects the electromagnetic energy into a surface plasmon. This surface plasmon propagates along the plane and interacts with localized Plasmon (located at the apertures). An antenna-like effect takes place at the aperture openings on the back side of the mask, producing light radiation. When the apertures of the array subsequently radiate, there is constructive interference between the apertures and transmission enhancement [103]. My observation is supported by a simulation

conducted for a slit flanked by 10 grooves on each side. Figure 86 shows the resulting contour plot which displays a spatial dependence of the component of the Poynting vector along the radial direction [104].

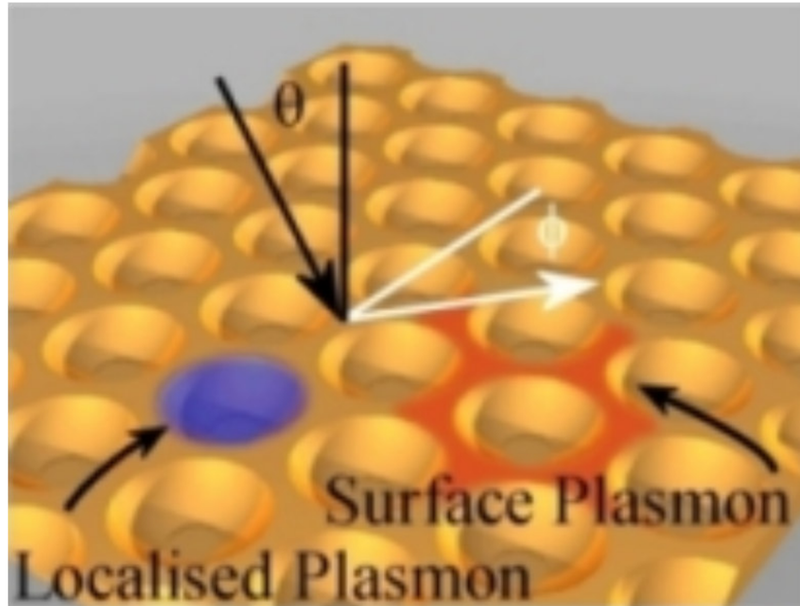

Figure 85: Illustration of Plasmon coupling to sub-wavelength apertures (from W. L. Barnes).

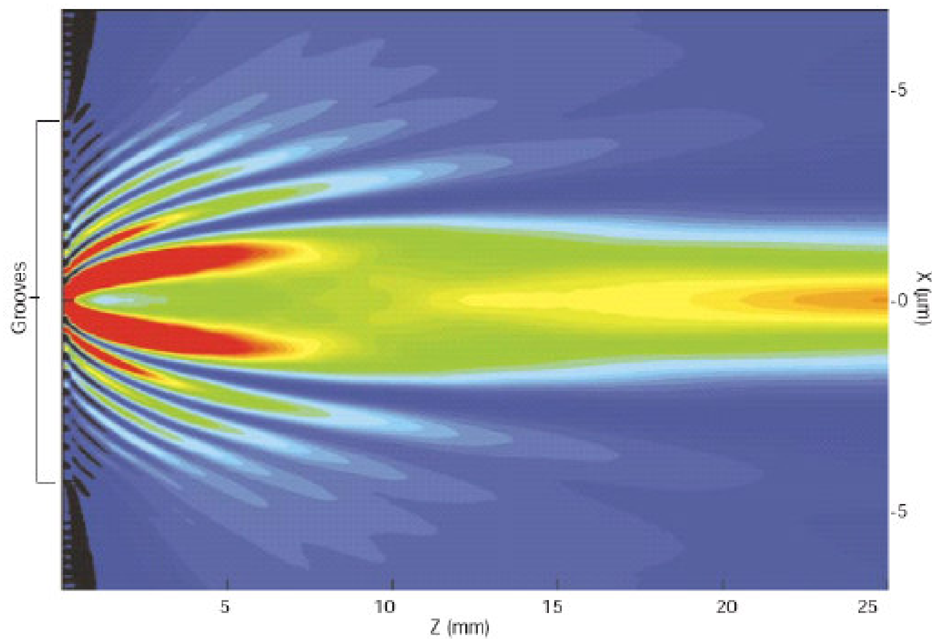

Figure 86: Calculated pattern of light emerging from a single slit surrounded by a finite array of grooves (from W. L. Barnes).

The excited plasma in the silver field is in effect an electric field. Modeling the electric field over the metal film and the apertures offers more insight as to what interaction is responsible for the experimental observations. Finite Difference Time Domain (FDTD) analyses were conducted to examine the electric field behavior at the silver layer due to the incident wave. Furthermore, the simulation covers the coupling of the induced field with the aperture and finally how it radiates at the back side. Figure 87 shows the results of the 2-dimensional FDTD electric field simulations. The simulation was conducted in 2-dimensions (x and z). In Figure 87 the light is shining down on the silver film. The silver film side on which the light impinges is identified by the coordinate 0.0 in the vertical direction. The thickness of the simulated silver is 120nm. There are two holes in the silver film at -0.25µm and 0.25µm in the horizontal coordinates; each hole has a diameter of 100nm.

Figure 87(a) presents the resulting electric field in the x-direction (along the surface of the silver film). There is a strong electric field (plasma excitation) on the front side of the silver film as well as in the apertures. The electric field along the silver film on the back side is weak reflecting the lack of plasma along the surface of the film on the backside. Figure 87 (b) shows the resulting electric field in the z-direction (perpendicular to the silver film). The electric field in this direction on the light incident side of the silver film and inside the apertures is low. However, on the back side of the silver film, the electric field is large representing the radiated wave that is gathered by the optical lenses of the stepper. Figure 87 (c) offers a view of the magnitude of the electric field in both directions on either side of the silver film.

This study demonstrates that an array of sub-wavelength holes can be used to expose the photoresist on a wafer at 4x reduction using a conventional stepper. The presented approach was targeting 250nm technology given the limitation of the optical tools. However, with 3 x 3 array of apertures I was able to print features half that size (down to 110nm).

I believe that this approach can successfully be applied for feature technologies (45nm-65nm) with the use of more powerful optical tools having higher numerical apertures. In this study I have shown that pattern corner sharpening can be accomplished with resolution assisting patterning. The use of superior optical tools is expected to sharpen the corner rounding of exposed patterns as would be required for next generation design rules. The dose required for optimal exposure is about 3 times greater than a conventional dose while the required mask writing time could be as much as 10 to 100 times shorter than that required for conventional masks writing approaches, raster-scan and vector-scan tools. Although, vector-scan tools are the faster of the previous two, the fact that I address fewer pixels still makes the described approach much faster.

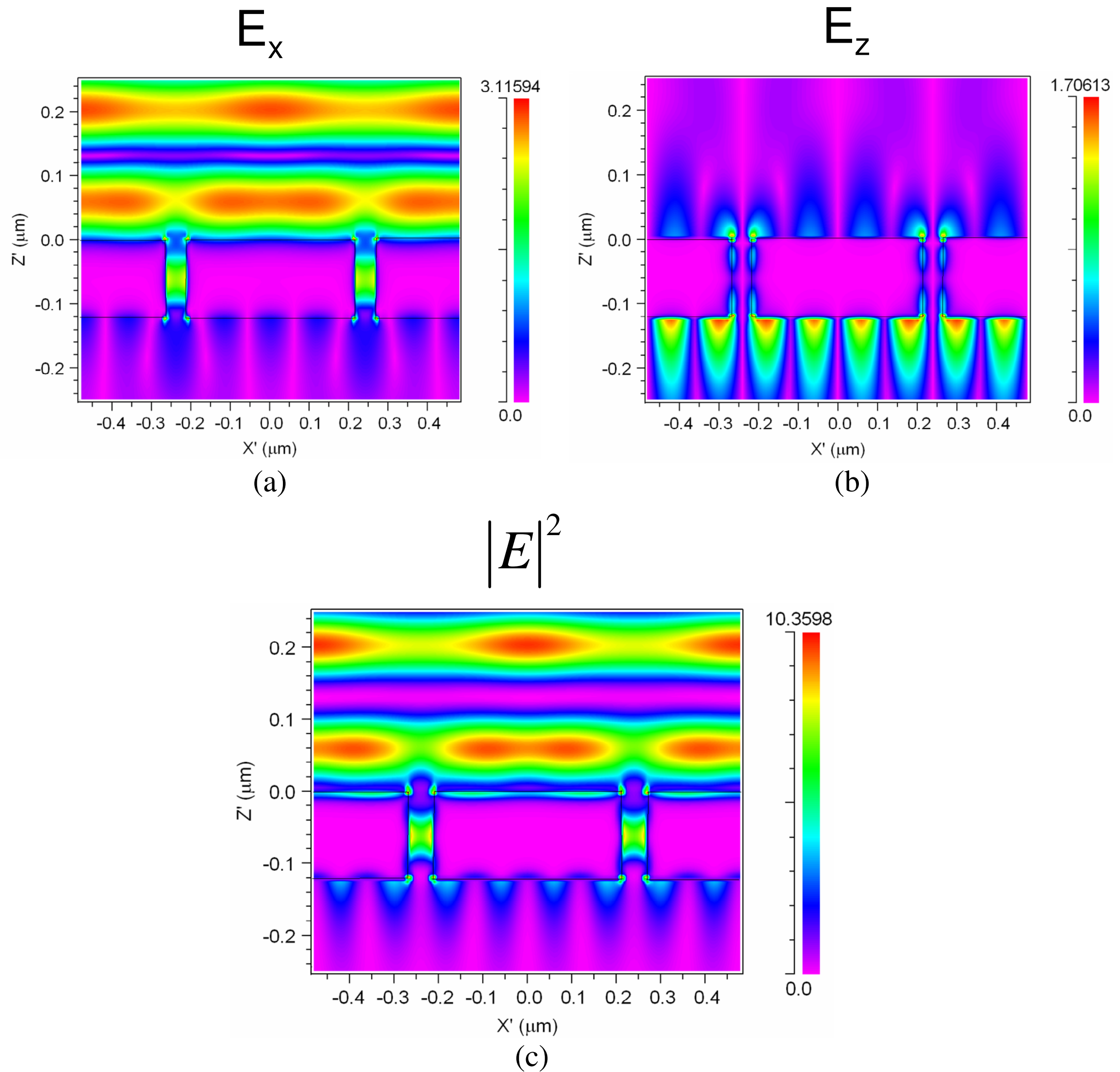

Figure 87: FDTD simulation of the electric field around the silver field; (a) electric field in the x-direct (along the silver field); (b) electric field in the z-direction (perpendicular to the silver film); (c) electric field magnitude

4.7 Conclusion

I describe the ion-beam fabrication of an optical proximity corrected (OPC) mask with a significantly reduced fill-factor over those masks manufactured using current direct-write technologies. For this novel mask, I prove that the absence of one, or a few, apertures does not seriously degrade the far field pattern (image) created by the collective scattering from the many subwavelength apertures. The image exhibits good edge acuity and robustness against many of the normally encountered mask defects.

The understanding of what happens when light travels through nano-apertures is generally incomplete [103]. However, I can point to a collective effect based on plasmonic interactions. Light incident on the mask generate plasmon waves on the silver surface. These waves propagate in the plane of the mask. Furthermore, when these waves encounter and are scattered at apertures in the metal film, they can turn back into a freely propagating optical wave [96]. I then capture these waves via the lenses and use them to expose my photoresist. The absence of up to 30% of the apertures still allows useful printing of the affected features; there are neither individual holes being printed nor any discontinuity in the exposed pattern. The image still exhibits good edge acuity and robustness against many of the normally encountered mask defects for the targeted 250nm features.

My results demonstrate that a mask containing a two-dimensional array of sub-wavelength apertures can be used to expose a photoresist with the same resolution as a clear aperture mask of the same size as the array, only requiring a slightly longer

exposure time. Therefore, this discovery points to a new way of making photolithographic masks with a writing time reduced by the fill factor of the array, which can be 10 to 100 times smaller. I expect that this observation might revolutionize the way that present lithographic masks are made. For this approach to be applied to state-of-the art design rules (45nm - 65nm) would necessitate the use of higher NA optical tools. I anticipate that my results will be applicable to systems with higher numerical aperture, allowing for extension to higher feature resolution. Of course, changing the exposure wavelength may affect the coupling of the incident beam to the plasmonic excitation modes.

CHAPTER 5: CONCLUSION

5.1 Summary of Accomplishments

5.1.1 Electrochemical energy cell

The electrochemical energy cell research work I conducted in this thesis had as objective the development of an efficient energy storage and delivery cell within a compact volume. The cell is to meet energy storage specifications for low-power ad hoc distributed networks as well as be rechargeable. The solutions I investigated in this thesis centered on an electrochemical cell utilizing a powdery mixture of hydrated ruthenium oxide and activated carbon with a ratio of 10:1 by weight. I found that the composition of the powdery mix affects the characteristics of the cell; the ratio mentioned earlier offers the best characteristics.

I investigated multiple electrode materials (gold coated glass / silicon die; gold coated aluminum; graphite / zinc and graphite / lead), packaging approaches (cell sealed with acid resistant paint and Lexan sheets equipped with adhesive service) and electrolyte composition (sulfuric acid or a mixture of solution). The performances of the various devices were evaluated. The studies on the fabrication of the novel electrochemical energy cell yielded great results:

- Gold coated glass slide cells: Showed mostly capacitive behavior with weak redox reaction

- Gold coated aluminum cells: Showed mostly battery behavior due to electrolyte corroding underlying aluminum material. This is easily remediate with the use of a weakly acidic electrolyte.

- Graphite-Zinc cells: Showed strong battery behavior with rechargeability capability

- Graphite-Lead cells: Showed good redox reaction and capacitor behavior.

where the most promising cell is the Graphite-Zinc cell (electrolyte E0 family). It displays both current and voltage charging capabilities. Furthermore, the cell has a high/constant voltage potential that is reproducible from cell to cell with a shelf life of more than eighth months and counting. The cell family is implemented via the use of asymmetric electrodes, the asymmetry both in material and electrolyte interface. The electrode materials are zinc and graphite. The Graphite electrode is covered with a mix of hydrated ruthenium oxide and activated carbon, both in powder form. The electrolyte is made of a solution of ethylene glycol, ammonium hydroxide, boric acid and nitric acid. A glass fiber filter paper is used as separator and the entire cell is contained within a Lexan package.

To reduce the overall volume of my cells and the weight of the packaging, I adopted a folded cell structure. The cell has the same chemistry as the other Graphite-Zinc cells. The main difference is that the size of the graphite electrode is cut in half but the same amount of paste and electrolyte is used. The Graphite sheet is sandwich between the zinc sheet with the Ruthenium oxide and activated carbon paste on both sides. The filter paper is also wrapped around the graphite electrode to isolate it from the zinc electrode. The cell is sealed using a thin and light laminating sheet. The folded cell maintains a V_{OC} of ~1.1V and displays the same driving capability as my

regular Graphite-Zinc cells with a greater gravitic and volumetric capacity. Furthermore, the cell is flexible.

5.1.2 Dual UV-wavelength detector array

The III-V nitrides have been established as outstanding materials for optoelectronic applications in both detection and emission. Commercial light emitting diodes have found wide ranging applications. III-N based detectors have been the focus of many department of defense (DoD) and NASA programs for detection in the blue/UV region of the electromagnetic spectrum. To date, these programs have focused on single wavelength detection. It has been demonstrated that detection at two wavelengths simultaneously can enhance the operation of such systems for static and dynamic imaging applications. Currently, there is no high yield method to permit the creation of an interspersed two-color imager based on III-N materials. Etching of these materials is notoriously difficult and often results in damaged surfaces that lead to leakage in junctions that have been etched through. A method to enable two-color imaging detectors in the nitrides would be tremendously useful.

Through the dual UV-wavelength detector array work presented in this thesis, I offer a clear roadmap to the creation of a dual UV-wavelength detector array, where two-color detection is done simultaneously. The growth mechanism involved in the confined epitaxial growth approach is introduced. This growth mechanism enables the stacking of active layers with varying stoichiometry; hence, detectors can be tuned to be sensitive to a variety of UV-wavelength band pairs. I executed my developed process flow, which makes use of the confined epitaxial growth approach

and does not comprise any dry etching step. Thereby reducing defects to the active layers; defects that are commonly associated with larger leakage/dark currents.

Finally, electrical evaluation of my fabricated detectors proves the diode nature of the detectors; While, spectral sensitivity curves demonstrate dual UV-wavelength sensitivity of the detector array. To sum up the work done, I constructed and tested low reverse leakage diode arrays with two-color spectral sensitivities (UVA and UVB).

5.1.3 Sub-wavelength lithography technique

The subwavelength transmission phenomenon has only recently received significant attention in the theoretical physics community. Light incident on a metal thin film establishes oscillation in the mobile charge density (ripples in the “Fermi sea”.) These ripples, in turn, excite cavity modes in circular apertures in thin films. These cavity modes acts as intense light sources, drawing energy from their surroundings on which light is incident. The net transmission is far greater than the aperture area alone would dictate. In this thesis work, the incorporation of this technique in photolithographic mask design to provide an inexpensive method for performing high resolution photolithographic work in a university or in a small business environment is examined.

I describe the ion-beam fabrication of an optical proximity corrected (OPC) mask with a significantly reduced fill-factor over those masks manufactured using current direct-write technologies. For my novel mask, I prove that the absence of one, or a few, apertures does not seriously degrade the far field pattern (image) created by the collective scattering from the many subwavelength apertures. The image exhibits

good edge acuity and robustness against this type of normally encountered mask defects.

The understanding of what happens when light travels through nano-apertures is generally incomplete [103]. However, I can point to a collective effect based on plasmonic interactions. Light incident on the mask generate plasmon waves on the silver surface. These waves propagate in the plane of the mask. Furthermore, when these waves encounter and are scattered at apertures in the metal film, they can turn back into a freely propagating optical wave [96]. I then capture these waves via the lenses and use them to expose the photoresist. The fabricated mask is proven to be defect resilient as patterns with missing apertures still print with no discontinuity in the resist.

The pattern fill factor is more than an order of magnitude smaller than the ratio of the mask clear area divided by the total mask area of a conventional mask. This leads to a significant increase in mask making throughput. Contact window arrays were exposed with critical dimensions down to 110nm using 248nm incident radiation. While the exposure intensity are higher (somewhat less than three times more energy is required on the mask), the image pattern appears to be a cooperative effect of scattering from multiple apertures. If the array is defective, meaning that it contains a small number of unopened apertures, the pattern still prints as a coherent, cleared feature.

5.2 Unique Contribution

My electrochemical energy cell research work presented in this thesis touches upon an area not much explored; that of using hydrated ruthenium oxide and activated carbon as electrode materials in powder form. My research work, furthermore, contributes to the work done in the field of UV detector fabrication and characterization as well as in the area of $Al_xGa_{1-x}N$ alloy film growth which would enhance the performance of III-nitride dependent devices. In addition, my research conducted on the array of sub-wavelength apertures for lithography applications adds to the knowledge pool in sub-wavelength aperture far-field imaging work. These different research endeavors offer unique contributions along the following lines:

Electrochemical Energy Cell

The various presented electrochemical energy cells show the viability of powdery ruthenium oxide and activated carbon usage as electrode material [1-3]. This deviates from the conventional use/deposition of these materials when applied as electrode; notably, sputtering or evaporation. A thin, flexible electrochemical cell (battery) that can be easily integrated into a general flexible electronics matrix has been developed and presented. The contribution claims are these:

a) I have created electrodes that have a high surface area as power is generated at the electrode surface [1].

b) I implemented the cells with an electrolyte that is as close to pH-neutral (7) as possible to prevent rapid dissolution of the electrode materials or package sealing materials while favoring the needed redox reactions [3].

c) I have enabled the reaction chemistry to proceed as close to equilibrium as possible to allow electrically driven reversibility (re-charging).

d) I have targeted the weight and volume of the cells to be as light and low volume as possible.

I achieved (a) through the use of nano-particulate RuO_x as a cathode material. I assure permeability of the RuO_x mass by compounding it with graphite nano-particles. This also lowers the internal resistance of the cell. The compound forms a screenable conducting paste that can be applied as a thin film over a flexible substrate (like polypropylene).

To accomplish (b), I use an ethylene glycol base to which I add a buffered HNO_3 solution. The buffering and dilution process creates a pH 5 mixture. This is electrolyte applied as droplets over the RuO_x/activated carbon paste, forming a gel-like mixture. A counter-electrode of either zinc or lead is pressed over the gel. The RuOx/electrolyte/metal foil cell has an electrochemistry close to that of a lead-acid battery and the redox reaction responsible for power generation is close to equilibrium, allowing for electrically driven re-charging. This also satisfies requirement (c). A second plastic sheet is placed over the whole assemblage and the assemblage is sealed. All the materials used are flexible. The resulting RuOx/graphite-electrolyte-metal foil cell is thinner than 0.5mm, and a typical zinc anode cell weighs less than 1g – satisfying requirement (d).

Dual UV-Wavelength Imaging Array

My simultaneous dual UV-wavelength detector array is introduced. This thesis outlines my fabrication process flow to generate the detector array and implements the process flow to generate a detector array. The design of this array is enabled by my development of this novel fabrication process flow that depends on a modified lift-off process, a patented confined epitaxy growth method for III-nitride semiconductors and a creative detector staking approach. These guiding principles pave the way for the following contribution to the field:

- My presented lift-off lithography process applied to the conditioning/patterning of the area needed for active $Al_xGa_{1-x}N$ demonstrates the importance of the confined epitaxial growth process in the quality improvement of grown $Al_xGa_{1-x}N$ layers [4, 5, 35].

- My presented fabrication process flow for the generation of an array of dual UV-wavelength detectors demonstrates simultaneous dual UV-wavelength band detection. This is the first demonstration of such capability, uncovered by the research described in this thesis.

- My lift-off lithography process in conjunction with my presented UV detector device structure (the stacking of two $Al_xGa_{1-x}N$ active layers) offers a road map for the development of other devices based on $Al_xGa_{1-x}N$ alloys such as high power electronics that require high band gap semiconductors ($Al_xGa_{1-x}N$ among others)

Sub-Wavelength Litography Technology

Our results demonstrate that a mask containing a two-dimensional array of sub-wavelength apertures can be used to expose a photoresist with the same resolution as a clear aperture mask of the same size as the array, only requiring slightly larger exposure energy [6, 7, 75]. I created a mask based on an inexpensive and effective array of sub-wavelength aperture for use in a conventional stepper demonstrates far field imaging capabilities. The guiding principles of the construction and calibration of my mask lay the ground for the following contribution to the field:

- I developed of a mask writing technique where a beam writer is presented with a smaller writing area without requiring the shrinkage of the expected printed pattern or the loss of resolution.
- I used and demonstrated the first far-field imaging capability of an array of sub-wavelength apertures.

5.3 Future Work

The following sub-sections will briefly comment on areas for future work based on this PhD dissertation.

5.3.1 Electrochemical energy cell

Throughout the electrochemical energy cell discussion within this dissertation, the emphasis was in developing a cell that could store and deliver electrochemical energy within a compact volume. This idea could be stretch further were one would then increase the flexibility of the cell. Thin sheet of zinc (~0.003”) do exist. One can envision arc sputtering the graphite onto a soft plastic and thereby improve the cell’s flexibility.

5.3.2 Dual UV-wavelength detector array: Reduced leakage and Avalanche diodes

The discussion on dual UV-wavelength detector array presented in this research was primarily concerned with the design of the device structure for dual color detection and the creation of an appropriately fabrication flow to enable the use of the confined epitaxial growth method. However, the generated leakage current / defects in the active layers are tied to the size of my hexagonal detectors and their nature (p-n/p-i-n diodes).

The devices size can be kept as described in this thesis for color 1 with color 2 patterns omitted. This setup would be used to fabricate a different type of UV detector. Instead of growing a simple $Al_xGa_{1-x}N$ layer to make a p-n/p-i-n diode, a layered structure of $Al_xGa_{1-x}N$ film can be grown to make avalanche photodiode (APD). The pixel size would be the same and the mask 2 would be eliminated. Another avenue would be to try dual-color detection with APDs.

The area of the active layer of the detectors can be reduced while keeping a relatively identical pixel size. This can be done via the investigation of what could be considered mini-pixels. Such a setup is presented in Figure 88 were Figure 88(a) has larger hexagonal than Figure 88(b); however, the set of pixels still occupy the same area as the original color 1 hexagonal described in this thesis. Hence, the same electronics (ROIC) can be used.

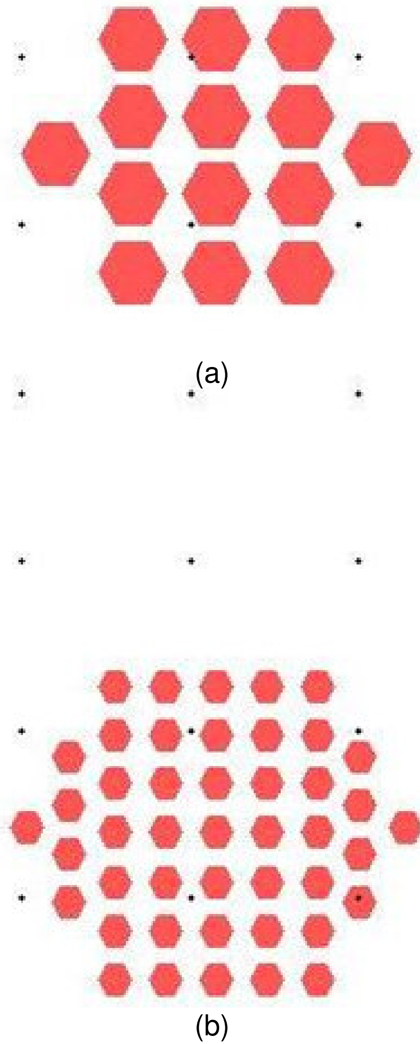

Figure 88: Mini-pixel layout; (a) approximately 6µm across; (b) approximately 3µm across

5.3.3 Sub-wavelength lithography technique

The discussion on sub-wavelength lithography technique presented in this research was mainly concern with demonstrating far-field imaging capabilities of the novel mask structure. It would be of interest to establish an in-depth simulation tool to understand/predict some of the behaviors. Furthermore, a stepper with better numerical aperture could be used to push the resolution capabilities/critical dimension limits of the mask structure.

Appendix A: $Al_xGa_{1-x}N$ absorption thickness calculations

Growth and doping of $Al_xGa_{1-x}N$ alloys films via confined epitaxy is controllable for thin layer (less than 0.5μm). As a result, it is of great importance to verify that an $Al_xGa_{1-x}N$ alloys layer of that thickness would effectively absorb the UV wavelength of interest. The absorption depth of $Al_xGa_{1-x}N$ alloys is based on their stoichiometry as well as the thickness of the layer. This appendix section presents the calculation necessary to estimate absorption percentage for five $Al_xGa_{1-x}N$ alloys having the following stoichiometry: x = 0, 0.2, 0.45, 0.55 and 1.

When gamma and x rays pass through matter they are attenuated mainly by photoelectric absorption, incoherent scattering and coherent scattering. The probabilities of these exchanges occurring per unit depth of penetration are called cross sections, and the total attenuation cross section μ is related to the aforementioned mechanisms by

$$\mu = \tau + \sigma_I + \sigma_C \qquad \text{(A1)}$$

Incoherent scattering (σ_I) collisions may be divided into scattering (σ_C) and absorption (σ_a) components such that

$$\sigma_I = \sigma_S + \sigma_a \qquad \text{(A2)}$$

Attenuation follows the exponential law

$$I = I_o \exp(-\mu * x) \qquad \text{(A3)}$$

Where I and I_o are intensities at a depth x and at the surface, respectively; μ is the absorption coefficient given here in μm^{-1} such that the absorption in a given alloy of fraction f_1, f_2 and f_3 is given by

$$\mu_{medium} = \rho_{alloy}\left[\left(\frac{\mu}{\rho}\right)_1 wf_1 + \left(\frac{\mu}{\rho}\right)_2 wf_2 + \left(\frac{\mu}{\rho}\right)_3 wf_3\right] \quad \text{(A4)}$$

Where ρ_{alloy} is the density of the alloy divided by Avocadros' Number, $(\mu/\rho)_1$ is the mass attenuation coefficient of each component of the alloy (i.e. Aluminum, Gallium or Nitride) and *wf* represents the weight fraction of each component of the alloy.

I first determine the mass attenuation coefficient of Al, Ga and N [105]; the values a tabulated in Table A1. For each $Al_xGa_{1-x}N$ alloy of interest, I determine the total mass of the alloy per mole (M_T), the weight fraction which represents the distribution by weight in the alloy. Furthermore, I determine the lattice constant of the crystal of each allow (a and c) and the volume of the lattice (Volume = a^2c). From the previous parameter values, I determine the alloys' density (ρ_{alloy}). All the parameters mentioned above are tabulated in Table A2.

The μ_{medium} values of Table A2 are inserted into a normalized version of Equation A3 to obtain an absorption profile as a function of distance into the $Al_xGa_{1-x}N$ alloy of interest. The resulting plots are shown both in Figure 48 and Figure A1. These figures clearly show that for the alloys under consideration, all the photons of interest are absorbed within 0.5μm of alloy film.

Table A1: Mass attenuation coefficient

Elements	Aluminum	Gallium	Nitride
(μ/ρ) (cm²/g)	$4.45*10^4$	$1.2*10^5$	$6.14*10^4$

Table A2: Summary of absorption calculations

Alloy		GaN	$Al_{.2}Ga_{.8}N$	$Al_{.45}Ga_{.55}N$	$Al_{.55}Ga_{.45}N$	AlN
M_T (g/mole)		84	75.4	64.65	60	41
wf	Al	0	.08	.19	.25	.66
	Ga	.83	.74	.6	.53	.34
	N	.17	.18	.21	.22	0
Lattice (Å)	a	3.19	3.17	3.16	3.15	3.11
	c	5.19	5.15	5.10	5.07	4.98
Volume (cm^3)		$5.27*10^{23}$	$5.18*10^{23}$	$5.09*10^{23}$	$5.03*10^{23}$	$4.82*10^{23}$
ρ (g/cm^3)		$1.59*10^{24}$	$1.46*10^{24}$	$1.27*10^{24}$	$1.19*10^{24}$	$8.5*10^{23}$
μ_{medium} (cm^{-3})		15.40	14.90	14.55	14.29	13.31

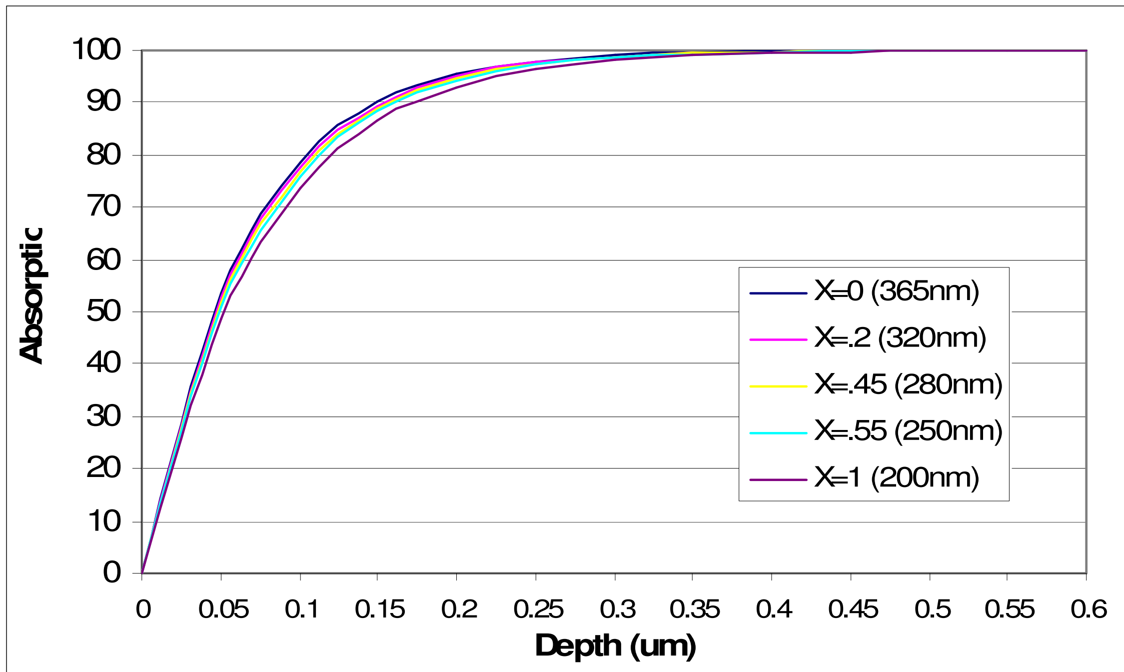

Figure A1: Absorption as a function of depth of penetration and the $Al_xGa_{1-x}N$ alloy stoichiometry

Appendix B: Fabrication Process for Dual-Color UV Detector Array

I. Generate hexagonal for color 1 layer (use positive resist)

a. Clean wafer

i. Acetone bath 3min

ii. Methanol bath 3min

iii. DI rinse 5min

iv. Dip in BHF (1:10) for 15 sec

v. DI rinse 10min

vi. N2 blow dry

vii. Bake wafer for 45 min at 120°C

b. Condition wafer for coating

i. Dehydration: hotplate 120°C for 5min

ii. Dispense HMDS over entire wafer and wait 15sec

iii. Spin for 45sec @1500rpm

c. Spin-on LOL 2000 @ 1500 rpm for 45sec => 300nm layer

d. Soft bake @ ~120 ^{o}C for 5 min

e. Let sample cool for $1^{1/2}$min

f. Spin-on LOL 2000 @ 1500 rpm for 45sec => additional 300nm layer

g. Soft bake @ ~120 ^{o}C for 7 min

h. Let wafer cool for 1 min

i. Spin-on photoresist (Shipley 1813) @ 4000 rpm for 45sec

j. Soft bake @ ~100 ^{o}C for 2 min

k. Expose PR with 18mJ/cm^2 (8mW/cm^2)—for 10sec (use Mask# 1)

l. Develop in MF 319 for 20sec

m. Deposit oxide on uncovered area (around hex patterns)—done by Hionix

n. Lift-off LOL 2000 and photoresit (to free up hexagonal patterns)

    i. Place glass holder with wafers in ultrasonic bath of MicroChem Nano Remover PG (OR NMP- Microposit Remover 1165)

    ii. Degas for 5min at room temp

    iii. Ultrasonicate wafer for 70min @ 50°C

    iv. Rinse in DI water

    v. N2 blow dry

o. Grow AlGaN layer—done at NRL

=> The wafer has hexagonal AlGaN patterns delimitated by an oxide.

II. Generate hexagonal for color 2 layer (use positive resist)

a. Spin-on LOL 2000 @ 1500 rpm for 45sec

b. Soft bake @ ~150 ^{o}C for 5 min

c. Let sample cool for 1$^{1/2}$min

d. Spin-on LOL 2000 @ 1500 rpm for 45sec => additional 300nm layer

e. Soft bake @ ~120 ^{o}C for 7 min

f. Let wafer cool for 1 min

g. Spin-on photoresist (Shipley 1813) @ 400 rpm for 45sec

h. Soft bake @ ~100 ^{o}C for 2 min

i. Expose PR with 8mW/cm^2 for 10sec (use Mask# 2)

j. Develop in MF 319 for 20sec

k. Deposit oxide on uncovered area (around hex patterns)—done by Hionix

l. Lift-off LOL 2000 and photoresist (to free up hexagonal patterns)

m. Grow GaN layer—done at NRL

=> The wafer has hexagonal GaN patterns on AlGaN patterns delimitated by an oxide.

III. Cover all active devices/detectors

a. Grow a third layer of oxide—done by Hionix

=> The wafer is totally covered of oxide.

IV. Generate n-metallization to contact underlying n-type layer (Ohmic contact desired, use positive resist and evaporate Ti/Al/Ti/Au).

a. Spin-on LOL 2000 @ 1500 rpm for 45sec

b. Soft bake @ ~150 ^{o}C for 5 min

c. Let sample cool for $1^{1/2}$min

d. Spin-on LOL 2000 @ 1500 rpm for 45sec => additional 300nm layer

e. Soft bake @ ~120 ^{o}C for 7 min

f. Let wafer cool for 1 min

g. Spin-on photoresist (Shipley 1813) @ 400 rpm for 45sec

h. Soft bake @ ~100 ^{o}C for 2 min

i. Expose PR with 8mW/cm^2 for 10sec (use Mask# 3)

j. Develop in MF 319 for 20sec

k. Wet etch oxide (in 50:1 BOE ~ 90sec)—to expose underlying n-layer

l. E-beam evaporate metal Ti(20nm)/Al(45nm)/Ti(100nm)/Au(450nm)—to generate Ohmic contact.

m. Lift-off metal in MicroChem Nano Remover PG

    i. Ultrasonicate wafer for 70min @ 50°C

    ii. Rinse in DI water

    iii. N2 blow dry

n. Anneal metal at 600°C for 30sec (in a N_2 atmosphere)

=> Wafer has ohmic contact to the n-doped alloy layer

V. Generate holes to frontal surface of detector hexagonal (for p-metallization, use positive resist)

a. Spin-on photoresist (Shipley 1813) @ 4000 rpm for 45sec

b. Soft bake @ ~100 ^{o}C for 2 min

c. Expose PR with 8mW/cm^2 for 10sec (use Mask# 4)

d. Develop in MF 319 for 20sec

e. Wet etch oxide (in 10:1 BOE ~ 3min)—to expose surface of detectors

f. Strip-off PR with Acetone (can also clean wafer ultrasonic bath for 5min)

=> The wafer has square holes over each detector. Next, the holes will be filled with metal.

VI. Generate p-metallization and pads to be used for Indium bump binding (use positive resist and evaporate Ni/Au)

a. Spin-on LOL 2000 @ 1500 rpm for 45sec

b. Soft bake @ ~150 ^{o}C for 5 min

c. Let sample cool for 1$^{1/2}$min

d. Spin-on LOL 2000 @ 1500 rpm for 45sec => additional 300nm layer

e. Soft bake @ ~120 ^{o}C for 7 min

f. Let wafer cool for 1 min

g. Spin-on photoresist (Shipley 1813) @ 400 rpm for 45sec

h. Soft bake @ ~100 ^{o}C for 2 min

i. Expose PR with 8mW/cm^2 for 10sec (use Mask# 5)

j. Develop in MF 319 for 20sec

k. Wet etch oxide (in 50:1 BOE ~ 90sec)—to expose underlying n-layer

l. E-beam evaporate metal Ni(50nm)/Au(450nm)—to generate Ohmic contact.

m. Lift-off metal in MicroChem Nano Remover PG

   i. Ultrasonicate wafer for 70min @ 50°C

   ii. Rinse in DI water

   iii. N2 blow dry

n. Anneal metal at 500°C for 5min (in a N_2 atmosphere)

=> Wafer has ohmic contact to the p-doped alloy layers

VII. Deposit Indium for bumps (use Mask# 6)—done at Rockwell / Teledyne

=> The wafer has square pads (bigger than previous via holes) that will accommodate Indium bumps.

Bibliography

[1] Y. Ngu, M. Peckerar, M. Kbheis, D. Lowy, N. Goldsman, G. Metze, and L. Tender, "An Electrochemical Cell with Capacitance-Enhanced Double Layer," *ECS Transactions*, vol. 3, pp. 77-85, 2007.

[2] Y. Ngu, M. Peckerar, N. Goldsman, M. Kbheis, and G. Metze, "A Capacitance-Enhanced Double Layer Electrochemical Cell," *ECS Meeting Abstracts*, vol. 602, pp. 203, 2006.

[3] Y. Ngu, M. Peckerar, Z. Dilli, and N. Goldsman, "High capacitance battery for powering distributed networks node devices," presented at International Semiconductor Device Research Symposium (ISDRS), College Park, MD, 2007.

[4] C. R. Eddy, M. Mastro, N. Bassim, M. Twigg, R. Henry, R. Holm, J. Culbertson, O. Glembocki, J. D. Caldwell, P. Neudeck, A. Trunek, J. A. Powell, M. Peckerar, Y. Ngu, F. Yan, and S. Babu, "Approaches to Reduced-Defect Active Regions for III-N Devices," *ECS Transactions*, vol. 3, pp. 117-125, 2006.

[5] C. R. Eddy, R. T. Holm, R. L. Henry, M. E. Twigg, N. D. Bassim, L. M. Shirey, O. J. Glembocki, J. C. Culbertson, F. K. Perkins, M. C. Peckerar, Y. Ngu, and F. Yan, "Improved GaN materials and devices through confined epitaxy," *Applied Physics Letters*, vol. 90, pp. 162101-1621, 2007.

[6] Y. Ngu, M. Peckerar, M. Dagenais, J. Barry, and B. R. Dutt, "Lithography, plasmonics, and subwavelength aperture exposure technology," *Journal of Vacuum Science & Technology B: Microelectronics and Nanometer Structures*, vol. 25, pp. 2471-2475, 2007.

[7] Y. Ngu, M. Peckerar, X. Liu, M. Dagenais, M. Messina, and J. Barry, "Lithography, Plasmonics and Sub-wavelength Aperture Exposure Technology," presented at International Conference on Electron, Ion, and Photon Beam Technology and Nanofabrication (EIPBN), Denver, CO, 2007.

[8] Victor L. Pushparaj and A. K. Manikoth M. Shaijumon, Saravanababu Murugesan, Lijie Ci, Robert Vajtai, Robert J. Linhardt, Omkaram Nalamasu, and Pulickel M. Ajayan, "Flexible energy storage devices based on nanocomposite paper," *PNAS*, vol. 104, pp. 13574-13577, 2007.

[9] M. Dell, Rand,JAD,, "Understanding batteries," 2001.

[10] Vincent, Colin Scrosati,,Bruno, "Modern batteries," 1997.

[11] "Battery (electricity)," in *Wikipedia*: http://en.wikipedia.org/wiki/Battery_(electricity), 2008.

[12] P. M. Deeley, *Electrolytic Capacitors: Theory, Construction, Characteristics and Applications*: http://www.FaradNet.com, 1996.

[13] S. A. Merryman and Z. Chen, "Ruthenium Oxide Electrochemical Super Capacitor Optimization For Pulse Power Applications," NASA MArshall Space FlightCenter 2000.

[14] B. E. Conway, *Electrochemical supercapacitors*, 1999.

[15] B. E. Conway, "Proceedings of the Symposium on Electrochemical Capacitors," 1996.

[16] Wikepidia, "Adsorption," http://en.wikipedia.org/wiki/Adsorption, 2008.

[17] B. E. Conway, "Electrical Double-Layer and Ion Adsorption Behavior at Solid–Solution Interfaces," *Encyclopedia of Surface and Colloid Science*, pp. 1908 - 1931, 2006.

[18] M. Matsumoto, "Electrocapillarity and double layer structure," *Surfactant science series*, vol. 76, pp. 87-99, 1998.

[19] J. P. Zheng and T. R. Jow, "A new charge storage mechanism for electrochemical capacitors," *Journal of the Electrochemical Society*, vol. 142, pp. L6-8, 1995.

[20] Wikipedia, "Underpotential deposition," http://en.wikipedia.org/wiki/Underpotential_deposition, 2008.

[21] B. E. Conway, V. Birss, and J. Wojtowicz, "The role and utilization of pseudocapacitance for energy storage by supercapacitors," *Journal of Power Sources*, vol. 66, pp. 1-14, 1997.

[22] H. Kim and B. N. Popov, "A mathematical model of oxide/carbon composite electrode for Supercapacitors," *Journal of the Electrochemical Society*, vol. 150, pp. A1153-60, 2003.

[23] J. M. Miller, B. Dunn, T. D. Tran, and R. W. Pekala, "Deposition of ruthenium nanoparticles on carbon aerogels for high energy density supercapacitor electrodes," *Journal of the Electrochemical Society*, vol. 144, pp. L309-11, 1997.

[24] E. Frackowiak and F. Beguin, "Carbon materials for the electrochemical storage of energy in capacitors," *Carbon*, vol. 39, pp. 937-950, 2001.

[25] J. P. Zheng and T. R. Jow, "High energy and high power density electrochemical capacitors," *Journal of Power Sources*, vol. 62, pp. 155-159, 1996.

[26] J. P. Zheng, P. J. Cygan, and T. R. Jow, "Hydrous ruthenium oxide as an electrode material for electrochemical capacitors," *Journal of the Electrochemical Society*, vol. 142, pp. 2699-2703, 1995.

[27] T. R. Jow and J. P. Zheng, "Electrochemical capacitors using hydrous ruthenium oxide and hydrogen inserted ruthenium oxide," *Journal of the Electrochemical Society*, vol. 145, pp. 49-52, 1998.

[28] C. B. Arnold, R. C. Wartena, K. E. Swider-Lyons, and A. Pique, "Direct-write planar microultracapacitors by laser engineering," *Journal of the Electrochemical Society*, vol. 150, pp. A571-5, 2003.

[29] I. Buchmann, "Can the lead-acid battery compete in modern times?," BatteryUniversity.com, 2003.

[30] B. E. Conway, "Transition from `supercapacitor' to `battery' behavior in electrochemical energy storage," *Journal of the Electrochemical Society*, vol. 138, pp. 1539-1548, 1991.

[31] O. Barbieri, M. Hahn, A. Foelske, and R. Kotz, "Effect of electronic resistance and water content on the performance of RuO/sub 2/ for supercapacitors," *Journal of the Electrochemical Society*, vol. 153, pp. A2049-54, 2006.

[32] T. Lister, Y. Chu, H. You, and Z. Nagy, "Reduction of the ruthenium dioxide (100) surface: origin of ultracapacitance," Argonne National Laboratory 1999.

[33] T. E. Lister, Y. V. Tolmachev, Y. Chu, W. G. Cullen, H. You, R. Yonco, and Z. Nagy, "Cathodic activation of RuO2 single crystal surfaces for hydrogen-evolution reaction," *Journal of Electroanalytical Chemistry Special issue in memory of Professor M.J. Weaver*, vol. 554-555, pp. 71-76, 2003.

[34] S. Hadzi-Jordanov, H. Angerstein-Kozlowska, M. Vukovic, and B. E. Conway, "Reversibility and growth behavior of surface oxide films at ruthenium electrodes," *Journal of the Electrochemical Society*, vol. 125, pp. 1471-1480, 1978.

[35] C. R. Eddy, M. Mastro, N. Bassim, M. Twigg, R. Henry, R. Holm, J. Culbertson, O. Glembocki, J. D. Caldwell, P. Neudeck, A. Trunek, J. A. Powell, M. Peckerar, Y. Ngu, F. Yan, and S. Babu, "Approaches to Reduced-Defect Active Regions for III-N Devices," *ECS Meeting Abstracts*, vol. 602, pp. 1539, 2006.

[36] M. Razeghi and A. Rogalski, "Semiconductor ultraviolet detectors," presented at Proceedings of the SPIE - The International Society for Optical Engineering, USA, 1996.

[37] A. M. Streltsov, K. D. Moll, A. L. Gaeta, P. Kung, D. Walker, and M. Razeghi, "Pulse autocorrelation measurements based on two- and three-photon conductivity in a GaN photodiode," *Applied Physics Letters*, vol. 75, pp. 3778-3780, 1999.

[38] M. P. Ulmer, M. Razeghi, and E. Bigan, "Ultraviolet detectors for astrophysics, present and future," presented at Proceedings of the SPIE - The International Society for Optical Engineering, USA, 1995.

[39] J. D. Brown, J. Li, P. Srinivasan, J. Matthews, and J. F. Schetzina, "Solar-blind AlGaN heterostructure photodiodes," *MRS Internet Journal of Nitride Semiconductor Research*, vol. 5S1, 2000.

[40] M. Razeghi and A. Rogalski, "Semiconductor ultraviolet detectors," *Journal of Applied Physics*, vol. 79, pp. 7433-7473, 1996.

[41] M. Razeghi, "Short-wavelength solar-blind detectors-status, prospects, and markets," *Proceedings of the IEEE*, vol. 90, pp. 1006-1014, 2002.

[42] M. Badila, G. Brezeanu, J. Millan, P. Godignon, M. L. Locatelli, J. P. Chante, A. Lebedev, P. Lungu, G. Dinca, V. Banu, and G. Banoiu, "Lift-off technology for SiC UV detectors," presented at Diamond and Related Materials, Switzerland, 2000.

[43] M. A. Khan, M. S. Shur, Q. Chen, J. N. Kuznia, and C. J. Sun, "Gated photodetector based on GaN/AlGaN heterostructure field effect transistor," *Electronics Letters*, vol. 31, pp. 398-400, 1995.

[44] S. J. Pearton, R. J. Shul, and F. Ren, "A review of dry etching of GaN and related materials," *MRS Internet Journal of Nitride Semiconductor Research*, vol. 5S1, 2000.

[45] R. McClintock, A. Yasan, K. Mayes, D. Shiell, S. R. Darvish, P. Kung, and M. Razeghi, "High quantum efficiency AlGaN solar-blind p-i-n photodiodes," *Applied Physics Letters*, vol. 84, pp. 1248-1250, 2004.

[46] S. K. Zhang, W. B. Wang, I. Shtau, F. Yun, L. He, H. Morkoc, X. Zhou, M. Tamargo, and R. R. Alfano, "Backilluminated GaN/AlGaN heterojunction ultraviolet photodetector with high internal gain," *Applied Physics Letters*, vol. 81, pp. 4862-4864, 2002.

[47] S. D. Lester, F. A. Ponce, M. G. Craford, and D. A. Steigerwald, "High dislocation densities in high efficiency GaN-based light-emitting diodes," *Applied Physics Letters*, vol. 66, pp. 1249-1251, 1995.

[48] U. K. Mishra, P. Parikh, and Y.-F. Wu, "AlGaN/GaN HEMTs-an overview of device operation and applications," *Proceedings of the IEEE*, vol. 90, pp. 1022-1031, 2002.

[49] M. Liu and H. K. Kim, "Ultraviolet detection with ultrathin ZnO epitaxial films treated with oxygen plasma," *Applied Physics Letters*, vol. 84, pp. 173-175, 2004.

[50] W. Yang, R. D. Vispute, S. Choopun, R. P. Sharma, T. Venkatesan, and H. Shen, "Ultraviolet photoconductive detector based on epitaxial Mg/sub 0.34/Zn/sub 0.66/O thin films," *Applied Physics Letters*, vol. 78, pp. 2787-2789, 2001.

[51] A. Ohtomo, M. Kawasaki, Y. Sakurai, Y. Yoshida, H. Koinuma, P. Yu, Z. K. Tang, G. K. L. Wong, and Y. Segawa, "Room temperature ultraviolet laser emission from ZnO nanocrystal thin films grown by laser MBE," presented at Materials Science & Engineering B (Solid-State Materials for Advanced Technology), Switzerland, 1998.

[52] S. Dake, H. Gaorong, S. Y. Au, G. Weikun, and I. K. Sou, "High-responsivity ZnS Schottky barrier photodiode array for ultraviolet imaging," *Chinese Journal of Semiconductors*, vol. 23, pp. 892-896, 2002.

[53] E. Arama, I. Ababii, V. Zhitar, and T. Shemyakova, "UV detectors based on Zn/sub x/In/sub 2/S/sub 3+x/ and related compounds," in *2003 International Semiconductor Conference. CAS 2003 Proceedings (IEEE Cat. No.03TH8676)*, Vol. 1 ed. USA, Piscataway, NJ: IEEE Electron Devices Soc, 2003, pp. 147.

[54] E. Sandvik, K. Mi, F. Shahedipour, R. McClintock, A. Yasan, P. Kung, and M. Razeghi, "Al/sub x/Ga/sub 1-x/N for solar-blind UV detectors," presented at Journal of Crystal Growth, Netherlands, 2001.

[55] J. Yamaura, Y. Muraoka, T. Yamauchi, T. Muramatsu, and Z. Hiroi, "Ultraviolet light selective photodiode based on an organic-inorganic heterostructure," *Applied Physics Letters*, vol. 83, pp. 2097-2099, 2003.

[56] D. Walker, X. Zhang, A. Saxler, P. Kung, J. Xu, and M. Razeghi, "Al/sub x/Ga/sub 1-x/N(0<x<1) ultraviolet photodetectors grown on sapphire by metal-organic chemical-vapor deposition," *Applied Physics Letters*, vol. 70, pp. 949-951, 1997.

[57] G. Smith, M. J. Estes, J. Van Nostrand, T. Dang, P. J. Schreiber, H. Temkin, and J. Hoelscher, "UV Schottky-barrier detector development for possible Air Force applications," presented at Proceedings of the SPIE - The International Society for Optical Engineering, USA, 1999.

[58] Q. Chen, J. W. Yang, A. Osinsky, S. Gangopadhyay, B. Lim, M. Z. Anwar, M. A. Khan, D. Kuksenkov, and H. Temkin, "Transparent Schottky barrier detectors on GaN for visible-blind ultraviolet detection," *Applied Physics Letters*, vol. 70, pp. 2277-2279, 1997.

[59] Chuang, Shun, *Physics of optoelectronic devices*, 1995.

[60] E. Monroy, E. Munoz, F. J. Sanchez, F. Calle, E. Calleja, B. Beaumont, P. Gibart, J. A. Munoz, and F. Cusso, "High-performance GaN p-n junction photodetectors for solar ultraviolet applications," *Semiconductor Science and Technology*, vol. 13, pp. 1042-1046, 1998.

[61] C. Pernot, A. Hirano, M. Iwaya, T. Detchprohm, H. Amano, and I. Akasaki, "Solar-blind UV photodetectors based on GaN/AlGaN p-i-n photodiodes," *Japanese Journal of Applied Physics, Part 2 (Letters)*, vol. 39, pp. L387-9, 2000.

[62] B. W. Lim, S. Gangopadhyay, J. W. Wang, A. Osinsky, Q. Chen, M. Z. Anwar, and M. A. Khan, "8x8 GaN Schottky barrier photodiode array for visible-blind imaging," *Electronics Letters*, vol. 33, pp. 633-634, 1997.

[63] R. F. Davis, A. M. Roskowski, E. A. Preble, J. S. Speck, B. Heying, J. A. Freitas, Jr., E. R. Glaser, and W. E. Carlos, "Gallium nitride materials - progress, status, and potential roadblocks," *Proceedings of the IEEE*, vol. 90, pp. 993-1005, 2002.

[64] J. D. Brown, Z. Yu, H. Matthews, S. Harney, J. Boney, J. Schetzina, J. D. Benson, K. W. Dang, C. Terrill, T. Nohava, W. Yang, and S. Krishnankutty, "Visible-blind UV digital camera based on a 32Ã—32 array of GaN/AlGaN p-i-n photodiodes," *MRS Internet Journal of Nitride Semiconductor Research*, vol. 4S1, 1999.

[65] B. Yang, K. Heng, T. Li, C. J. Collins, S. Wang, R. D. Dupuis, J. C. Campbell, M. J. Schurman, and I. T. Ferguson, "32Ã—32 ultraviolet Al/sub 0.1/Ga/sub 0.9/N/GaN p-i-n photodetector array," *IEEE Journal of Quantum Electronics*, vol. 36, pp. 1229-1231, 2000.

[66] P. Lamarre, A. Hairston, S. P. Tobin, K. K. Wong, A. K. Sood, M. B. Reine, M. Pophristic, R. Birkham, I. T. Ferguson, R. Singh, C. R. Eddy, Jr., U. Chowdhury, M. M. Wong, R. D. Dupuis, P. Kozodoy, and E. J. Tarsa, "AlGaN UV focal plane arrays," presented at Physica Status Solidi A, Germany, 2001.

[67] N. Biyikli, T. Kartaloglu, O. Aytur, I. Kimukin, and E. Ozbay, "High-performance solar-blind AlGaN Schottky photodiodes," *MRS Internet Journal of Nitride Semiconductor Research*, vol. 8S1, 2003.

[68] N. Biyikli, O. Aytur, I. Kimukin, T. Tut, and E. Ozbay, "Solar-blind AlGaN-based Schottky photodiodes with low noise and high detectivity," *Applied Physics Letters*, vol. 81, pp. 3272-3274, 2002.

[69] A. Osinsky, S. Gangopadhyay, B. W. Lim, M. Z. Anwar, M. A. Khan, D. V. Kuksenkov, and H. Temkin, "Schottky barrier photodetectors based on AlGaN," *Applied Physics Letters*, vol. 72, pp. 742-744, 1998.

[70] S.-C. Chang, J. M. Kempisty, R. P. Manginell, J. T. Borenstein, L. P. Lee, and P. J. Hesketh, "Lift-off methods for MEMS devices," in *BioMEMS and Bionanotechnology. Symposium (Materials Research Society Proceedings Vol.729)*, R. P. Manginell, J. T. Borenstein, L. P. Lee, and P. J. Hesketh, Eds. USA, Warendale, PA: Mater. Res. Soc, 2002, pp. 47-56.

[71] B. Nilsson, "Photolithography Liftoff," Shipley: http://fy.chalmers.se/assp/snl/public/wproc/LOL2000_Liftoff.html, 1999.

[72] J. Yun, K. Choi, K. Mathur, V. Kuryatkov, B. Borisov, G. Kipshidze, S. Nikishin, and H. Temkin, "Low-resistance Ohmic contacts to digital alloys of n-AlGaN/AlN," *IEEE Electron Device Letters*, vol. 27, pp. 22-24, 2006.

[73] C. H. Kuo, J. K. Sheu, G. C. Chi, Y. L. Huang, and T. W. Yeh, "Low-resistance Ni/Au ohmic contact to Mg-doped of Al0.15Ga0.85N/GaN superlattices," *Solid-State Electronics*, vol. 45, pp. 717-720, 2001.

[74] S. Aslam, "Dual Band Ultraviolet AlGaN Photodetectors for Space Applications," presented at Internal Semiconductor Device Research Symposium, College Park, MD, 2007.

[75] Y. Ngu, M. Peckerar, X. Liu, M. Dagenais, M. Messina, and J. Barry, "Lithography, Plasmonics and Sub-wavelength Aperture Exposure Technology," presented at Optical Society of America - CLEO/QELS, Baltimore, MD, 2007.

[76] F. M. Grimaldi, *Physico-mathesis de Lumine, Coloribus, et Iride*, pp. 9, 1665.

[77] H. A. Bethe, "Theory of diffraction by small holes," *Phys. Rev.*, vol. 66, pp. 163-182, 1944.

[78] T. W. Ebbesen, H. J. Lezec, H. F. Ghaemi, T. Thio, and P. A. Wolff, "Extraordinary optical transmission through sub-wavelength hole arrays," *Nature*, vol. 391, pp. 667-669, 1998.

[79] J.-B. Masson and G. Gallot, "Coupling between surface plasmons in subwavelength hole arrays," *Physical Review B (Condensed Matter and Materials Physics)*, vol. 73, pp. 121401-1211, 2006.

[80] C. Genet and T. W. Ebbesen, "Light in tiny holes," *Nature*, vol. 445, pp. 39-46, 2007.

[81] W. L. Barnes, W. A. Murray, J. Dintinger, E. Devaux, and T. W. Ebbesen, "Surface plasmon polaritons and their role in the enhanced transmission of

light through periodic arrays of subwavelength holes in a metal film," *Physical Review Letters*, vol. 92, pp. 107401/1, 2004.

[82] A. Dogariu, A. Nahata, R. A. Linke, L. J. Wang, and R. Trebino, "Optical pulse propagation through metallic nano-apertures," presented at Applied Physics B (Lasers and Optics), Germany, 2002.

[83] Q. Cao and P. Lalanne, "Negative role of surface plasmons in the transmission of metallic gratings with very narrow slits," *Physical Review Letters*, vol. 88, pp. 057403/1, 2002.

[84] S. S. Akarca-Biyikli, I. Bulu, and E. Ozbay, "Enhanced transmission of microwave radiation in one-dimensional metallic gratings with subwavelength aperture," *Applied Physics Letters*, vol. 85, pp. 1098-1100, 2004.

[85] D. Qu and D. Grischkowsky, "Observation of a new type of THz resonance of surface plasmons propagating on metal-film hole arrays," *Physical Review Letters*, vol. 93, pp. 196804/1, 2004.

[86] F. Miyamaru and M. Hangyo, "Finite size effect of transmission property for metal hole arrays in subterahertz region," *Applied Physics Letters*, vol. 84, pp. 2742-2744, 2004.

[87] H. Cao and A. Nahata, "Resonantly enhanced transmission of terahertz radiation through a periodic array of subwavelength apertures," *Optics Express*, vol. 12, 2004.

[88] T. Thio, H. J. Lezec, T. W. Ebbesen, K. M. Pellerin, G. D. Lewen, A. Nahata, and R. A. Linke, "Giant optical transmission of sub-wavelength apertures: physics and applications," presented at Nanotechnology, UK, 2002.

[89] T. Thio, K. M. Pellerin, R. A. Linke, H. J. Lezec, and T. W. Ebbesen, "Enhanced light transmission through a single subwavelength aperture," *Optics Letters*, vol. 26, pp. 1972-1974, 2001.

[90] T. Thio, H. J. Lezec, and T. W. Ebbesen, "Strongly enhanced optical transmission through subwavelength holes in metal films," presented at Physica B, Netherlands, 2000.

[91] W. Srituravanich, N. Fang, C. Sun, Q. Luo, and X. Zhang, "Subwavelength nanolithography using surface plasmons," in *2003 Third IEEE Conference on Nanotechnology. IEEE-NANO 2003. Proceedings (Cat. No.03TH8700)*, vol. 2 ed. USA, Piscataway, NJ: IEEE Nanotechnol. Council, 2003, pp. 609.

[92] M. W. Docter, L. T. Young, O. M. Piciu, A. Bossche, P. F. A. Alkemade, P. M. van den Berg, and Y. Garini, "Measuring the wavelength-dependent divergence of transmission through sub-wavelength hole-arrays by spectral imaging," *Optics Express*, vol. 14, 2006.

[93] K. L. Van der Molen, K. J. Klein Koerkamp, F. B. Segerink, N. F. Van Hulst, S. Enoch, and L. Kuipers, "Shape resonances in extraordinary transmission," in *2005 European Quantum Electronics Conference (IEEE Cat. No. 05TH8796)*. USA, Piscataway, NJ: IEEE, 2005, pp. 339.

[94] K. L. Van der Molen, F. B. Segerink, N. F. Van Hulst, and L. Kuipers, "Influence of hole size on the extraordinary transmission through subwavelength hole arrays," *Applied Physics Letters*, vol. 85, pp. 4316-4318, 2004.

[95] S. Mei, L. Rong-Juan, L. Zhi-Yuan, C. Bing-Ying, Z. Dao-Zhong, Y. Hai-Fang, and J. Ai-Zi, "The influence of hole shape on enhancing transmission through subwavelength hole arrays," *Chinese Physics*, vol. 15, pp. 1591-1594, 2006.

[96] T. D. Visser, "Plasmons at work?," *Nature Physics*, vol. 2, pp. 509-510, 2006.

[97] M. Bai and N. Garcia, "Transmission of light by a single subwavelength cylindrical hole in metallic films," *Applied Physics Letters*, vol. 89, pp. 141110-1411, 2006.

[98] N. Garcia and M. Bai, "Theory of transmission of light by sub-wavelength cylindrical holes in metallic films," *Optics Express*, vol. 14, 2006.

[99] "FEI Dualbeam 620," FEI Company, 7451 N. E. Evergreen Parkway, Hillsboro, OR 97124-5830, USA.

[100] O. Wilhelmi, "Nanofabrication and rapid prototyping with DualBeam instruments," http://www.feicompany.com/Portals/_default/PDFs/content/2007_05_nanofabrication_AN.pdf, 2007.

[101] "FEI DualBeam 620 User Manual."

[102] J. A. Dionne, L. A. Sweatlock, H. A. Atwater, and A. Polman, "Planar metal plasmon waveguides: frequency-dependent dispersion, propagation, localization, and loss beyond the free electron model," *Physical Review B (Condensed Matter and Materials Physics)*, vol. 72, pp. 75405-71, 2005.

[103] T. Thio and H. J. Lezec, "Diffracted evanescent wave model for enhancement and suppression of optical transmission of subwavelength hole arrays," in *2005 Quantum Electronics and Laser Science Conference (QELS) (IEEE Cat. No. 05CH37696)*, Vol. 2 ed. USA, Piscataway, NJ: IEEE, 2005, pp. 1088.

[104] W. L. Barnes, A. Dereux, and T. W. Ebbesen, "Surface plasmon subwavelength optics," vol. 424, pp. 824-830, 2003.

[105] J. W. Robinson, *Handbook of Spectroscopy Volume 1*: CRC Press, 1974.